

**PREPARATION AND STRUCTURAL INVESTIGATIONS  
ON ZIRCONOLITE AND PYROCHLORE BASED  
CERAMICS: POTENTIAL MATERIALS FOR NUCLEAR  
BACK END APPLICATION**

*By*

**MOHSIN JAFAR**

**CHEM01201404019**

**Bhabha Atomic Research Centre, Mumbai**

*A thesis submitted to the*

*Board of Studies in Chemical Sciences*

*In partial fulfillment of requirements*

*for the Degree of*

**DOCTOR OF PHILOSOPHY**

*of*

**HOMI BHABHA NATIONAL INSTITUTE**



**January 2021**

Government of India  
Bhabha Atomic Research Centre  
Chemistry Division

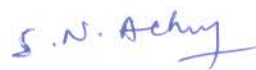
Ref: HBNI/BARC/Ph.D./ CHEM01201404019

Date: 26/07/2021

**Sub:** Certification regarding incorporation of corrections suggested by the examiners for the Ph.D. Thesis of Shri Mohsin Jafar (CHEM01201404019), in Chemical Sciences, HBNI.

Name of Candidate:	Mr. Mohsin Jafar
Enrollment Number:	CHEM01201404019
Title of the Thesis:	Preparation and structural investigations on zirconolite and pyrochlore based ceramics: Potential materials for nuclear back end application

This is to certify that, all the corrections suggested by the reviewers for the Ph.D. Thesis of Shri Mohsin Jafar (**Enrollment No.:** CHEM01201404019) are incorporated in the final Thesis.


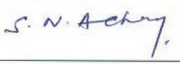

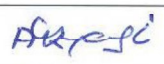

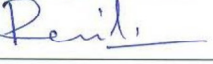
  
Dr. S. N. Achary  
Ph.D. Guide

Dean  
HBNI

# Homi Bhabha National Institute<sup>1</sup>

## Recommendations of the Viva Voce Committee

As members of the Viva Voce Committee, we certify that we have read the dissertation prepared by Shri Mohsin Jafar entitled "Preparation and structural investigations on zirconolite and pyrochlore based ceramics: Potential materials for nuclear back end application" and recommend that it may be accepted as fulfilling the thesis requirement for the award of Degree of Doctor of Philosophy.

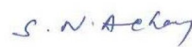
Chairman – Dr. C. P. Kaushik		24/04/2021
Guide / Convener – Dr. S. N. Achary		24/04/2021
Examiner - Dr. A. Chowdhury		24/04/2021
Member 1- Dr. A. K. Tyagi		24/04/2021
Member 2- Dr. S. Kannan		24/04/2021
Member 3- Dr. R. Mishra		24/04/2021

Final approval and acceptance of this thesis is contingent upon the candidate's submission of the final copies of the thesis to HBNI.

I/We hereby certify that I/we have read this thesis prepared under my/our direction and recommend that it may be accepted as fulfilling the thesis requirement.

Date: 24/04/2021

Place: Mumbai



Signature

(Dr. S. N. Achary)

Guide

<sup>1</sup> This page is to be included only for final submission after successful completion of viva voce.

## STATEMENT BY AUTHOR

This dissertation has been submitted in partial fulfilment of requirements for an advanced degree at Homi Bhabha National Institute (HBNI) and is deposited in the Library to be made available to borrowers under rules of the HBNI.

Brief quotations from this dissertation are allowable without special permission, provided that accurate acknowledgement of source is made. Requests for permission for extended quotation from or reproduction of this manuscript in whole or in part may be granted by the Competent Authority of HBNI when in his or her judgment the proposed use of the material is in the interests of scholarship. In all other instances, however, permission must be obtained from the author.

*Mohsin Jafar*  
Mohsin Jafar



## DECLARATION

I, hereby declare that the investigation presented in the thesis has been carried out by me. The work is original and has not been submitted earlier as a whole or in part for a degree / diploma at this or any other Institution / University.

*Mohsin Jafar*

Mohsin Jafar

## List of Publications arising from the thesis

### Journal

1. Phase Evolution and Microstructural Studies in  $\text{CaZrTi}_2\text{O}_7$ – $\text{Nd}_2\text{Ti}_2\text{O}_7$  System, **M. Jafar**, P. Sengupta, S. N. Achary, A. K. Tyagi, *J. Am. Ceram. Soc.*, **2014**, 97, 609-616.
2. Phase evolution and microstructural studies in  $\text{CaZrTi}_2\text{O}_7$  (zirconolite)– $\text{Sm}_2\text{Ti}_2\text{O}_7$  (pyrochlore) system, **M. Jafar**, P. Sengupta, S. N. Achary, A. K. Tyagi, *J. Eur. Ceram. Soc.*, **2014**, 34, 4373-4381.
3. Phase evolution studies in  $\text{CaZrTi}_2\text{O}_7$ – $\text{RE}_2\text{Ti}_2\text{O}_7$  (RE=  $\text{Nd}^{3+}$ ,  $\text{Sm}^{3+}$ ) system: Futuristic Ceramic Host Matrices for Nuclear Waste Immobilization, **M. Jafar**, S.N. Achary, A. K. Tyagi, *AIP Conf. Proc.*, **2014**, 1591, 55-57.
4. Preparation and structure of uranium incorporated  $\text{Gd}_2\text{Zr}_2\text{O}_7$  compounds and their thermodynamic stabilities under oxidizing and reducing conditions, **M. Jafar**, S. B. Phapale, B. P. Mandal, R. Mishra, A. K. Tyagi, *Inorg. Chem.*, **2015**, 54, 9447-9457.
5. X-ray diffraction and Raman spectroscopic investigations on  $\text{CaZrTi}_2\text{O}_7$ – $\text{Y}_2\text{Ti}_2\text{O}_7$  system: Delineation of phase fields consisting of potential ceramic host materials, **M. Jafar**, S. N. Achary, N. P. Salke, A. K. Sahu, R. Rao, A. K. Tyagi, *J. Nucl. Mater.*, **2016**, 475, 192-199.
6. High temperature crystallographic and thermodynamic investigations on synthetic calzirtite ( $\text{Ca}_2\text{Zr}_5\text{Ti}_2\text{O}_{16}$ ), **M. Jafar**, S. B. Phapale, S. N. Achary, R. Mishra, A. K. Tyagi, *J Alloys Compd.*, **2016**, 682, 284-293.
7. High temperature crystallographic and thermodynamic investigations on synthetic zirconolite ( $\text{CaZrTi}_2\text{O}_7$ ), **M. Jafar**, S. B. Phapale, S. N. Achary, R. Mishra, A. K. Tyagi, *J. Therm. Anal. Calorim.*, **2018**, 131, 2709-2718.
8. Implication of aliovalent cation substitution on structural and thermodynamic stability of  $\text{Gd}_2\text{Ti}_2\text{O}_7$ : Experimental and theoretical investigations, **M. Jafar**, S. B. Phapale, S. Nigam, S. N. Achary, R. Mishra, C. Majumder, A. K. Tyagi, *J Alloys Compd.* (Accepted).

9. Enthalpy variation of  $Gd_2Zr_2O_7$  as a function of temperature, **M. Jafar** et al. (minor revision in *J Alloys Compd.*).
10. Solubility studies of  $Gd_2O_3$  in BBS glass structure, **M. Jafar** et al. (To be communicated).
11. Structural and stability analysis of uranium and cerium incorporated  $Gd_2Zr_2O_7$ , **M. Jafar** et al. (To be communicated)

## Conferences

1. Thermodynamic Stability of  $Gd_{2-x}U_xZr_2O_{7+δ}$  ( $0.0 \leq x \leq 0.15$ ), **M. Jafar**, B. P. Mandal, S. Phapale, R. Mishra and A. K. Tyagi, ISMC - 2014
2. Phase Evolution in  $CaZrTi_2O_7$ - $Y_2Ti_2O_7$  System, **M. Jafar**, S. N. Achary and A. K. Tyagi, SSPS-2015
3. High Temperature Crystallographic and Thermodynamic Investigations of Calzirtite ( $Ca_2Zr_5Ti_2O_{16}$ ), **M. Jafar**, S. Phapale, S. N. Achary, R. Mishra and A. K. Tyagi, THERMANS-2016

### Best poster award

4. High Temperature Crystallographic and Thermodynamic Investigations of Zirconolite ( $CaZrTi_2O_7$ ), **M. Jafar**, S. Phapale, S. N. Achary, R. Mishra and A. K. Tyagi, ISMC-2016
5. Impact of  $Gd_2O_3$  on barium borosilicate (BBS) glass network, **M. Jafar**, R. K. Mishra, S. N. Achary, V. Sudarsan, C. P. Kaushik, A. K. Tyagi, ISMC-2018
6. Effect of thermal annealing on thermodynamic stability of  $Gd_2Zr_2O_7$ , **M. Jafar**, B. P. Mandal, S. Phapale, R. Mishra and A. K. Tyagi, THERMANS-2018
7. Structure and thermodynamic stability of  $Gd_{2-2x}Ca_xZr_xTi_2O_7$  ( $x=0.00, 0.10, 0.20, 0.30$  and  $0.40$ ): Experimental and theoretical study, **M. Jafar**, S. Phapale, S. Nigam, R. Mishra, S. N. Achary, A. K. Tyagi, THERMANS-2020

*Mohsin Jafar*

MOHSIN JAFAR

*Dedicated to the Almighty  
and my family  
whose grace, love and support  
sustained me throughout*

## ACKNOWLEDGEMENTS

First and foremost, I would like to acknowledge my supervisor, **Dr. S. N. Achary**, Head, Nuclear and Energy Materials Section, Chemistry Division for his constant guidance and support. I am highly indebted to him for his sound advice and scientific understanding. I also thank **Dr. A. K. Tyagi**, Associate Director, Chemistry group and Head, Chemistry Division for his never ending enthusiasm and inspiring discussions. I express sincere gratitude to **Dr. C. P. Kaushik**, chairman of doctoral committee for his unending help in carrying out some experiments using his facilities. Moreover, I thank **Dr. V. K. Jain**, ex-chairman of doctoral committee for his support and encouragement. I express sincere gratitude to **Dr. S. Kannan** and **Dr. R. Mishra**, for their positive comments and support during annual review meetings. I am also thankful to **Bhabha Atomic Research Centre** and **Department of Atomic Energy** for providing me with sound infrastructure for my research work. In addition to this, I am thankful to all my collaborators **Dr. P. Sengupta, Dr. R. Rao, Dr. N. Shelke, Dr. A. K. Sahu, Dr. B. P. Mandal, Dr. M. Roy, Dr. S. Nigam, Dr. C. Majumder, Dr. R. K. Mishra, Dr. A. Kumar** and **Mr. S. Phapale**. Moreover, I bestow my heartfelt thanks to **Dr. K. Bhattacharyya, Dr. M. Anitha, Dr. D. Sahoo, Dr. C. Nayak** and **Mr. S. Kaity** for their help in carrying out some of my experiments.

Additionally, I thank my colleagues **Dr. D. Dutta, Dr. V. Gupta, Dr. A. Singhal, Dr. S. J. Patwe, Dr. R. Shukla, Dr. O. D. Jayakumar, Mr. K. S. Rao** and **Mrs. A. V. Ghadge** for their scientific inputs and help. My heartfelt thanks goes to **Dr. Farheen Sayad, Dr. V. Kotari, Dr. Jerina Majeed, Dr. Pooja Sawant, Dr. P. Anita Kumari, Dr. Deepa Dutta, Ms. K. Halankar**, for their help at different stages of my

doctoral studies. All the staff of Chemistry Division are also thanked for their active support during this tenure.

I also extend my thanks to all my training school friends both from BARC, and IGCAR training schools for creating a friendly atmosphere and help. I thank others also, whose name might not have appeared, but has helped me in the progress of my research work.

Finally, I thank my wife **Afsana**, daughter **Inaaya** and **my parents and other family members** for their unconditional love and support during some turbulent patches in my life during my PhD tenure. Finally, I thank **The Almighty** for everything that was bestowed to me.

**MOHSIN JAFAR**



# CONTENTS

	Page No.
<b>SUMMARY</b>	xv
<b>SYNOPSIS</b>	xvi-xxv
<b>LIST OF FIGURES</b>	xxvi-xxx
<b>LIST OF TABLES</b>	xxxi-xxxii
<b>LIST OF ABBREVIATIONS</b>	xxxiii-xxxiv
 <b>CHAPTER 1 INTRODUCTION</b>	 <b>1-30</b>
<b>1.1. Introduction</b>	2
<b>1.2. Nuclear Energy</b>	3
1.2.1. Boiling Water Reactor (BWR)	4
1.2.2. Pressurized Water Reactor (PWR)	4
1.2.3. Pressurized Heavy Water Reactor (PHWR)	5
1.2.4. Gas Cooled Reactor (GCR)	5
1.2.5. Vodo-Vodyanoi Energetichesky Reactor (VVER)	5
1.2.6. Liquid Metal Cooled Fast Breeder Reactor (LMCFBR / FBR)	6
<b>1.3. Indian Nuclear Energy Programme</b>	6
<b>1.4. Futuristic Nuclear Fuels In Indian Scenario</b>	9
<b>1.5. Nuclear Waste</b>	10
1.5.1. Constituents of LLW	11
1.5.2. Constituents of ILW	12
1.5.3. Constituents of HLW	12
<b>1.6. Management Strategy of HLW</b>	13
<b>1.7. Disposal of HLW</b>	14
<b>1.8. Nuclear HLW Immobilization Matrices</b>	16
<b>1.9. Glass Matrices</b>	17

1.9.1. Phosphate based glasses	17
1.9.2. Borosilicate based glasses	18
1.9.3. Glass ceramics or glass composites	19
<b>1.10. Limitations of Glass Matrices</b>	<b>19</b>
<b>1.11. Crystalline Matrices</b>	<b>20</b>
1.11.1. Apatites	21
1.11.2. Sodium Zirconium Phosphate (NZP)	22
1.11.3. Zircon	22
1.11.4. Monazite	22
1.11.5. Hollandite	23
1.11.6. Perovskite	23
1.11.7. Zirconolite	24
1.11.8. Pyrochlore	26
<b>1.12. Surrogate Nuclear Materials</b>	<b>27</b>
1.12.1. Surrogate for Plutonium	27
1.12.2. Surrogate for Americium	28
<b>1.13. Scope of the thesis</b>	<b>29</b>
<b>CHAPTER 2 SYNTHESIS METHODS AND INSTRUMENTAL TECHNIQUES</b>	<b>31-61</b>
<b>2.1. Introduction</b>	<b>32</b>
<b>2.2. Synthesis Methods</b>	<b>33</b>
2.2.1. Solid state method	33
2.2.2. Gel combustion method	36
2.2.3. Melt quench method	38
<b>2.3. Instrumental Techniques</b>	<b>39</b>
2.3.1. X-ray diffraction (XRD)	39
2.3.2. Raman spectroscopy	47
2.3.3. X-ray absorption fine structure (XAFS)	50
2.3.4. Calvet oxide melt calorimeter	52
2.3.5. Thermogravimetric analysis coupled with differential thermal analysis (DTA)	55

	2.3.6. Scanning electron microscopy (SEM)	56
	2.3.7. Electron probe micro analyzer (EPMA)	59
	2.3.8. X-ray photoelectron spectroscopy (XPS)	59
CHAPTER 3	<b>STRUCTURE AND THERMODYNAMIC PROPERTIES OF POTENTIAL WASTE IMMOBILIZATION LATTICES IN Ca-Zr-Ti-O SYSTEM: CALZIRTITE AND ZIRCONOLITE</b>	<b>62-97</b>
	3.1. Introduction	63
	3.2. Experimental Methods	65
	3.3. Results and Discussions	66
	3.3.1. Structural studies of calzirtite ( $\text{Ca}_2\text{Zr}_5\text{Ti}_2\text{O}_{16}$ )	66
	3.3.2. Structural studies of zirconolite ( $\text{CaZrTi}_2\text{O}_7$ )	76
	3.3.3. Standard molar enthalpy of formation of calzirtite and zirconolite	81
	3.3.4. Enthalpy increment and heat capacity measurements of calzirtite and zirconolite	86
	3.3.5. Construction of thermodynamic tables for calzirtite and zirconolite	89
	3.3.6. Standard Gibbs free energy of formation of calzirtite and zirconolite	91
	3.4. Conclusions	96
CHAPTER 4	<b>PHASE EVOLUTION AND MICROSTRUCTURAL STUDIES IN <math>\text{CaZrTi}_2\text{O}_7</math> (ZIRCONOLITE)-<math>\text{RE}_2\text{Ti}_2\text{O}_7</math> (PYROCHLORE) (RE= <math>\text{Nd}^{3+}</math>, <math>\text{Sm}^{3+}</math> and</b>	<b>98-132</b>

	<b>Y<sup>3+</sup>) RELATED SYSTEMS</b>	
<b>4.1.</b>	<b>Introduction</b>	<b>99</b>
<b>4.2.</b>	<b>Experimental Methods</b>	<b>101</b>
<b>4.3.</b>	<b>Results and Discussions</b>	<b>102</b>
	<b>4.3.1. Phase evolution studies</b>	<b>102</b>
	<b>4.3.2. Microstructural studies</b>	<b>123</b>
<b>4.4.</b>	<b>Conclusions</b>	<b>130</b>
<b>CHAPTER 5</b>	<b>STRUCTURE AND THERMODYNAMIC STABILITY OF Ca AND Zr CO-SUBSTITUTED Gd<sub>2</sub>Ti<sub>2</sub>O<sub>7</sub> PYROCHLORE SYSTEM: EXPERIMENTAL AND THEORETICAL STUDY</b>	<b>133-151</b>
<b>5.1.</b>	<b>Introduction</b>	<b>134</b>
<b>5.2.</b>	<b>Experimental Methods</b>	<b>135</b>
<b>5.3.</b>	<b>Results and Discussions</b>	<b>137</b>
	<b>5.3.1. Structural studies</b>	<b>137</b>
	<b>5.3.2. Calorimetric studies</b>	<b>143</b>
	<b>5.3.3. Computational results</b>	<b>146</b>
<b>5.4.</b>	<b>Conclusions</b>	<b>151</b>
<b>CHAPTER 6</b>	<b>STRUCTURE AND THERMODYNAMIC STUDIES ON PARENT AND ACTINIDE SUBSTITUTED Gd<sub>2</sub>Zr<sub>2</sub>O<sub>7</sub></b>	<b>152-202</b>
<b>6.1.</b>	<b>Introduction</b>	<b>153</b>
<b>6.2.</b>	<b>Experimental Methods</b>	<b>154</b>
<b>6.3.</b>	<b>Results and Discussions</b>	<b>159</b>
<b>Part A</b>	<b>Structural And Thermodynamic Studies On Pristine Gd<sub>2</sub>Zr<sub>2</sub>O<sub>7</sub></b>	<b>159</b>
	<b>(i) Powder XRD studies</b>	<b>159</b>

	(ii) Raman spectroscopic studies	163
	(iii) EXAFS studies	165
	(iv) Calorimetric studies	168
<b>Part B</b>	<b>Structural And Thermodynamic Studies On Uranium Incorporated <math>Gd_2Zr_2O_7</math></b>	<b>172</b>
	(i) Powder XRD studies	172
	(ii) XPS studies	181
	(iii) SEM studies	182
	(iv) Calorimetric studies	184
<b>Part C</b>	<b>Structural And Thermodynamic Studies On Uranium And Cerium Co- Incorporated <math>Gd_2Zr_2O_7</math></b>	<b>191</b>
	(i) Powder XRD studies	191
	(ii) XPS studies	195
	(iii) Calorimetric studies	196
<b>6.4.</b>	<b>Conclusions</b>	<b>202</b>
<b>CHAPTER 7</b>	<b>MISCELLANEOUS ACTIVITIES PERTAINING TO NUCLEAR WASTE IMMOBILIZATION</b>	<b>203-214</b>
<b>7.1.</b>	<b>Introduction</b>	<b>204</b>
<b>7.2.</b>	<b>Synthesis strategy</b>	<b>205</b>
<b>7.3.</b>	<b>Experimental Methods</b>	<b>206</b>
<b>7.4.</b>	<b>Results and Discussions</b>	<b>208</b>
<b>7.5.</b>	<b>Conclusions</b>	<b>213</b>
<b>CHAPTER 8</b>	<b>SUMMARY AND FUTURE SCOPE</b>	<b>215-220</b>
<b>8.1.</b>	<b>Summary</b>	<b>216</b>
<b>8.2.</b>	<b>Future Scope</b>	<b>220</b>
	<b>REFERENCES</b>	<b>221-244</b>

## **SUMMARY**

As an efficient alternative to fossil fuels and minimum greenhouse emission, nuclear energy comes as a consented source. Worldwide, including India, Nuclear energy plays and is expected to play a pivotal role in the energy sector. This is being achieved by varieties of nuclear reactors. In India, currently number of nuclear reactors are serving as power source. However, immobilization of nuclear high level waste in geological repositories is an important field of ongoing research in nuclear energy industry. Ceramic matrices viz. titanates, zirconates, etc. are considered as potential matrices for immobilization of nuclear waste in repositories. In view of this, structural and thermodynamic stability studies of titanates and zirconates with zirconolite and pyrochlore structures have been investigated. Detailed structural and microstructural studies were carried out on varieties of compositions to unearth their potential use as waste matrices. A single phasic pyrochlore domain was elucidated which can incorporate up to 40 mol % of diverse ions inside the structure without undergoing phase separation. The effects of incorporation of diverse ions in to the pyrochlore structure was ascertained by detailed structural and thermodynamic stability studies (both theoretical and experimental). In addition, thermodynamic stabilities of uranium and uranium-cerium incorporated zirconate pyrochlore were also studied and it was concluded that both uranium and cerium need to be immobilized in higher oxidation state within ceramic lattice. Also, a novel glass formulation for incorporation of excess gadolinium containing waste was also designed as part of this thesis.



## **SYNOPSIS**

Increasing power consumption by a rapidly growing population for better life choices due to advancement in science and technology is depleting non-renewable energy resources such as coal, petroleum, etc. In addition to this, contribution of these fuels in global warming also makes mankind to think of utilizing non-renewable sources of energy for a better future. Production of power from nuclear reaction is considered as one of the best methodology because of its high power density and zero emission of greenhouse gases. Nuclear fuel cycle involves a series of processes starting from mining of uranium ores, ore processing, fuel fabrication, fuel installation in a reactor and reprocessing of spent fuel. One of the toughest challenges of this cycle involves safe disposal of obtained nuclear waste [1]. Safe disposal of nuclear waste is a protocol bound process that takes care of aspects of human health and environmental protection for present and future generations [2]. It is a fact that nuclear waste is generated in all steps of nuclear fuel cycle. However, the major precaution is required for reprocessing of spent nuclear fuel which consists of survived or non-fissioned uranium, plutonium along with minor actinides such as neptunium, americium, etc.

In the current scenario, waste immobilization matrix used worldwide is borosilicate glasses [3]. However, low solubility of minor actinides, chances of possible devitrification, etc. are some of the questions that bothers researchers worldwide [4-6]. Keeping this in mind, Ringwood et al. proposed ceramic composites consisting of mineral analogous titanates termed as SYNROC as potential ceramic waste immobilization matrices [6]. SYNROC mainly consists of phases such as zirconolite, pyrochlore, perovskite along with minor phases such as rutile, hollandite, etc. [7-10]. The primary objective of this thesis involves the a) phase evolution studies of composite having zirconolite and pyrochlore type structures as constituent phases and b) processing conditions optimization and thermodynamic stability of single phasic pyrochlore related lattice with simulated and actinide loaded compositions. The results of the studies carried in these aims are presented in

this thesis. This thesis consists of eight chapters and the brief outlines of these chapters are as follows:

## **Chapter 1: Introduction**

This chapter covers the importance of Indian nuclear energy program and its journey from different stages for self-sustainability. As India has adopted the policy of closed nuclear fuel cycle, different contents and type of nuclear waste has been discussed and their present processing strategies have been discussed in brief. A more detailed description has been carried out on high level nuclear waste, their management protocol and different types of glasses or glass-ceramics which are presently being investigated or practiced. Discussion has also been carried out on the potential application of zirconolite, pyrochlore and host of other ceramic matrices regarding their application for nuclear high level waste or minor actinide immobilization. Finally, the aspect of importance of surrogate elements has also been discussed as it is one of the main pillar strategies adopted in various research laboratories worldwide to mimic the of minor actinides, and then the scope of the work pertaining to this thesis is mentioned.

## **Chapter 2: Synthesis methods and instrumental techniques**

A brief description of methodology adopted for synthesis of various ceramic and glass-ceramic phases, instrumental techniques used for phase characterizations and property measurement studies are present in this chapter. Synthesis of the materials have been carried out mainly by three techniques viz. solid-state synthesis, gel combustion and melt-quench technique. Solid state synthesis has been employed for synthesis of zirconolite and other titanate based ceramics whereas gel combustion technique has been used for synthesis of zirconate based ceramics. Melt quench technique has been used for preparation of glass and glass ceramics. Phase purity and

characterization were carried out primarily by powder X-ray diffraction technique while Raman spectroscopy or extended X-ray absorption fine structure (EXAFS) techniques were used depending on their requirements. Microstructural studies were carried out by secondary electron imaging (SEM) or electron probe micro analyzer (EPMA) technique. Thermodynamic property measurements were carried out by high temperature Calvet calorimeter or differential thermal calorimeter (DTA) whereas oxidation state was characterized by X-ray photoelectron spectroscopy (XPS). A brief discussion of the above mentioned techniques are given in this chapter.

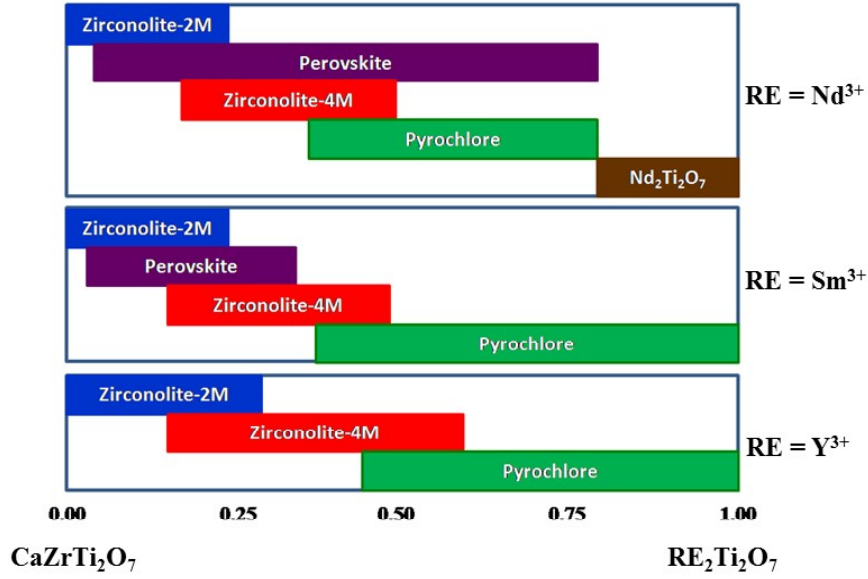
### **Chapter 3: Structure and thermodynamic properties of potential waste immobilization lattices in Ca-Zr-Ti-O system: Calzirtite and Zirconolite.**

This chapter explains the preparation, detailed structural characterization (room and high temperature) and thermodynamic stability of calzirtite ( $\text{Ca}_2\text{Zr}_5\text{Ti}_2\text{O}_{16}$ ) and zirconolite ( $\text{CaZrTi}_2\text{O}_7$ ) lattice. Both of these lattices are prepared by solid state reaction and characterized by a combination of variable temperature X-ray diffraction (XRD) and high temperature calorimetric studies. Calzirtite is found to crystallize in tetragonal lattice with space group  $I4_1/acd$  having unit cell parameters:  $a = 15.2113(1)$ ,  $c = 10.1139(1)$  Å. The average coefficient of lattice thermal expansion of calzirtite in between of 300 K to 1473 K are found to be  $\alpha_a = \alpha_b = 12.72 \times 10^{-6}/\text{K}$  and  $\alpha_c = 9.21 \times 10^{-6}/\text{K}$ , and the average volume thermal expansion coefficient is  $30.79 \times 10^{-6}/\text{K}$ . Zirconolite was found to crystallize in a monoclinic structure having  $C2/c$  space group with unit cell parameters  $a = 12.4413(2)$ ,  $b = 7.2700(1)$ ,  $c = 11.3744(2)$  Å,  $\beta = 100.557(2)^\circ$ . The observed lattice thermal expansion coefficient of zirconolite was found to be as:  $\alpha_a = 12.45 \times 10^{-6}/\text{K}$ ,  $\alpha_b = 9.34 \times 10^{-6}/\text{K}$  and  $\alpha_c = 11.21 \times 10^{-6}/\text{K}$ . Structural studies revealed the fact that zirconolite structure is amenable to Ti and Zr distribution among its cationic sites whereas a small intermixing is only allowed in calzirtite lattice. Lower volume thermal coefficient of expansion of calzirtite as compared to zirconolite also

indicates rigidity of the polyhedra present in calzirtite which does not help for its consideration as a waste immobilization lattice. Standard molar enthalpy of formation of zirconolite and calzirtite at 298 K is found to be  $-3716.49 \pm 4.12$  kJ and  $-8964.16 \pm 12.59$  mol<sup>-1</sup>, respectively. It was also observed that calzirtite can decompose to zirconolite lattice at  $\sim 1750$  K.

#### **Chapter 4: Phase evolution and microstructural studies in CaZrTi<sub>2</sub>O<sub>7</sub> (zirconolite)-RE<sub>2</sub>Ti<sub>2</sub>O<sub>7</sub> (pyrochlore) (RE= Nd<sup>3+</sup>, Sm<sup>3+</sup> and Y<sup>3+</sup>) related systems**

In continuation with the earlier chapter where it was shown that zirconolite acts as a better immobilization matrix over calzirtite, extensive phase studies of CaZrTi<sub>2</sub>O<sub>7</sub> (zirconolite)-RE<sub>2</sub>Ti<sub>2</sub>O<sub>7</sub> (pyrochlore) (RE= Nd<sup>3+</sup>, Sm<sup>3+</sup> and Y<sup>3+</sup>) system, to mimic SYNROC related phases was carried out. An extensive study on phase evolution with all rare earth cations being too time and cost intensive, a systematic selection of rare earths based upon their availability and ionic radii was considered to minimize the experiments. Hence studies are carried out with neodymium (surrogate of americium), samarium and yttrium titanate as they have considerable difference in their ionic radii. All the nominal compositions Ca<sub>1-x</sub>Zr<sub>1-x</sub>RE<sub>2x</sub>Ti<sub>2</sub>O<sub>7</sub> ( $0.0 \leq x \leq 1.0$ ) were prepared by solid state method of synthesis. Structural and microstructural studies were carried out by powder X-ray diffraction and SEM or EPMA, respectively. This system has been found to contain mainly four phase fields (i) monoclinic zirconolite (comprising of 2M and 4M), (ii) cubic perovskite (not for Y<sup>3+</sup> series), (iii) cubic pyrochlore and (iv) monoclinic Nd<sub>2</sub>Ti<sub>2</sub>O<sub>7</sub> types (for Nd<sup>3+</sup> series) as shown in **Figure 1**. Solubility of trivalent lanthanides in zirconolite lattice, range of perovskite phase field, etc. were found to vary as a function of ionic radii of the rare earth ion. Microstructural studies reveal the absence of cracks and fissures among the phase boundary in composite ensembles. These results indicate that CaZrTi<sub>2</sub>O<sub>7</sub>-RE<sub>2</sub>Ti<sub>2</sub>O<sub>7</sub> system can act as potential matrices for immobilization of nuclear HLW.



**Figure 1:** Phase evolution in  $\text{CaZrTi}_2\text{O}_7$   $\text{RE}_2\text{Ti}_2\text{O}_7$  ( $\text{RE} = \text{Nd}^{3+}$ ,  $\text{Sm}^{3+}$  and  $\text{Y}^{3+}$ ) system.

## Chapter 5: Structure and thermodynamic stability of Ca and Zr co-substituted $\text{Gd}_2\text{Ti}_2\text{O}_7$ pyrochlore system: Experimental and theoretical study

The detailed phase evolution study carried out in chapter 4 revealed the existence of a cubic pyrochlore phase with significant incorporation of dopant ion of different charge and size. In order to understand, the detailed structural implication upon incorporation of aliovalent ions in pyrochlore lattice,  $\text{Ca}^{2+}$  and  $\text{Zr}^{4+}$  is simultaneously incorporated in a pyrochlore  $\text{Gd}_2\text{Ti}_2\text{O}_7$  lattice. The nominal compositions in the studied range  $\text{Gd}_{2-2x}\text{Ca}_x\text{Zr}_x\text{Ti}_2\text{O}_7$  ( $0.0 \leq x \leq 0.4$ ) are prepared by solid state method and characterized in detail by powder X-ray diffraction, Raman spectroscopy and theoretical studies. Moreover, the variation of thermodynamic stability with increasing incorporation of aliovalent ions is also an important parameter which needs to be understood for their practical usage. Hence high temperature calorimetric technique is employed to understand the variation in stability of these compositions. From a combination of the structural studies, it is observed that about 40 mol% of  $\text{Gd}^{3+}$  in  $\text{Gd}_2\text{Ti}_2\text{O}_7$  can be replaced by  $\text{Ca}^{2+}$  and  $\text{Zr}^{4+}$  cations.

However, a systematic decrease in superstructure peak of pyrochlore is observed with increasing substitution which refers to a gradual disordering within the lattice. Theoretical studies revealed that greater amount of disorder is possible at Gd site rather than Ti site which leads to a reduction in the intensity of superstructure peak with increasing x values. Calorimetric studies revealed that standard molar enthalpy of formation of pyrochlore as a function of x is found to decrease by about 3.5% upon incorporation of 40 mol% of aliovalent cations which can be considered as negligible loss in stability. Hence, these type of titanate pyrochlore can be considered as promising ones for immobilization of nuclear HLW.

## **Chapter 6: Structure and thermodynamic studies on parent and actinide substituted**

### **Gd<sub>2</sub>Zr<sub>2</sub>O<sub>7</sub>**

Among zirconate based pyrochlore, Gd<sub>2</sub>Zr<sub>2</sub>O<sub>7</sub> is considered as one of the most potential matrix for incorporation of minor actinides [11, 12]. However, rapid processing of this composition pertaining to its consideration as waste immobilization matrix needs to be carried out. This chapter consists of three parts. Part A of this chapter deals exclusively deals with structural findings and variation of thermodynamic stability of Gd<sub>2</sub>Zr<sub>2</sub>O<sub>7</sub> with annealing temperature. Information gained from part A is utilized to find out the processing conditions and environment requirement for immobilization of uranium in Gd<sub>2</sub>Zr<sub>2</sub>O<sub>7</sub> and they are mentioned in part B. Part C deals with simultaneous incorporation of urania-ceria (surrogate for plutonia) in to the lattice of Gd<sub>2</sub>Zr<sub>2</sub>O<sub>7</sub>.

All the nominal compositions were prepared by gel combustion mode of synthesis followed by calcination and annealing at higher temperature. Calcined Gd<sub>2</sub>Zr<sub>2</sub>O<sub>7</sub> powders were annealed successively at 1373 K, 1473 K, 1573 K and 1673 K for 8 h in air, and the variation of structural and thermodynamic stability is found out. It is observed that Gd<sub>2</sub>Zr<sub>2</sub>O<sub>7</sub> transforms from defect fluorite to pyrochlore structure in the studied temperature range. Pure defect fluorite and pyrochlore



phase was observed at 1373 K and 1673 K, respectively whereas mixture of these two phases was observed in between these two temperatures. The standard molar enthalpies of formation of  $\text{Gd}_2\text{Zr}_2\text{O}_7$  phase obtained by annealing at 1373 K, 1473 K, 1573 K and 1673 K are found to be  $-4014.50 \pm 17.08$ ,  $-3977.74 \pm 17.04$ ,  $-3944.52 \pm 17.01$ ,  $-4059.27 \pm 17.07 \text{ kJ.mol}^{-1}$ , respectively. Thus, it is revealed that stability of compound decreases from 1373 K to 1573 K followed by an increase at 1673 K. Hence, it could be inferred that processing of  $\text{Gd}_2\text{Zr}_2\text{O}_7$  at either 1373 K or 1673 K for 8 h is better.

Hence for phase characterization, uranium incorporated  $\text{Gd}_2\text{Zr}_2\text{O}_7$  i.e.  $\text{Gd}_{2-x}\text{U}_x\text{Zr}_2\text{O}_{7+\delta}$  ( $0.0 \leq x \leq 0.25$ ) was annealed at 1373 K in air and  $\text{Ar:H}_2$  atmosphere, respectively. The conditions for processing of uranium (oxidized and reduced form) and consequent stability variation were studied and they are presented in this part. It is observed that a greater amount of uranium ( $x=0.25$ ) can be immobilized in  $\text{Gd}_2\text{Zr}_2\text{O}_7$  lattice in reducing environment as compared to air heated samples where the solubility is reduced to  $x=0.15$ . Oxidation state studies carried out by XPS studies revealed that uranium in air heated compositions exist in +6 oxidation state whereas samples heated at  $\text{Ar:H}_2$  atmosphere revealed uranium to exist in +4 oxidation state. Thermodynamic stability studies are carried out on uranium substituted gadolinium zirconates  $\text{Gd}_{2-x}\text{U}_x\text{Zr}_2\text{O}_{7+\delta}$  ( $0.0 \leq x \leq 0.15$ ) heated in both air and  $\text{Ar:H}_2$  in a bid to understand the role of stability with oxidation state of uranium. Clearly it could be evidenced that uranium in +6 oxidation state stabilizes the matrix significantly as compared to that in +4 oxidation state. The obtained results thereby helped to delineate proper conditions for incorporation of simultaneous urania-ceria in  $\text{Gd}_2\text{Zr}_2\text{O}_7$  respectively.

Nominal compositions with stoichiometry  $\text{Gd}_{2-x}\text{Ce}_x\text{Zr}_{1.9}\text{U}_{0.1}\text{O}_{7+\delta}$  ( $0.0 \leq x \leq 0.50$ ) is prepared by gel combustion followed by calcination and annealing at 1173 K for 8 h in air (obtained from part A and B). It is observed that no secondary phases are present in the compositions within the studied range. Thermodynamic stability studies revealed that incremental incorporation of ceria increases

the standard molar enthalpy of formation of the nominal compositions. Thus the studies from this chapter provided considerable insight regarding the immobilization of uranium and minor actinides in  $\text{Gd}_2\text{Zr}_2\text{O}_7$  lattice and their processing conditions.

## **Chapter-7: Miscellaneous activities pertaining to nuclear waste immobilization**

The advent of  $\text{PuO}_2$  based fuel in Indian nuclear program resulted to wastes with excess gadolinium salts which are added to spent fuel to make them proliferation resistant. Hence, necessary research regarding the solubility of gadolinia in borosilicate glasses became a necessity. Literature reports suggest low solubility,  $\sim 1.5$  mol% of gadolinium, in waste glasses prepared at around 1573 K [13-14]. Hence, studies on a series of glass compositions based on barium borosilicate glass were carried out to increase the solubility as well as to reduce the processing temperature. The composition with 50:20:20:10 ratio of  $\text{SiO}_2$ :  $\text{B}_2\text{O}_3$ :  $\text{Na}_2\text{O}$ :  $\text{BaO}$  is zeroed down to be the base glass for incorporation of gadolinium. Loading of gadolinia starting from 0 to 10 mol% were carried out by melt-quench technique. Crystalline peaks are found to be present in glasses with more than loading of 6 mol% of gadolinia. Differential thermal analysis results revealed that incorporation of Gd increase the glass transition temperature ( $T_g$ ) up to 5 mol% thereby acting as glass former while decrease the  $T_g$  from 6 mol% onwards thereby acting as a network modifier. Secondary electron imaging studies led to arrive at the conclusion that glass based on this formulation can actually incorporate Gd to the extent of 5 mol% or 21 wt% which is considerably higher than reported literatures.

## **Chapter 8: Summary and future scope**

This thesis gives an account of the parameters required for a ceramic matrix to be qualified as a potential waste immobilization matrix. Role of crystal structure in designing a nuclear waste

immobilization matrix is emphasized from the structural studies obtained from powder XRD data. Satisfactory flexibility present in crystal structure is further probed from thermodynamic stability point of view to emphasize upon long term behaviour of these matrices. Preference of an open structure over a rigid one and its effects are concluded in this thesis. Different phase fields pertaining to SYNROC based phases identified in this study are promising for future usages. Moreover, existence of cubic pyrochlore phases that can stabilize even after incorporation of 40 mol% of aliovalent cations is really worthwhile to mention from the angle of nuclear waste immobilization. Moreover, rapid processing conditions of  $Gd_2Zr_2O_7$  base matrix along with their phase constituent, the incorporation of uranium and cerium in its oxidized form are important information which will cater to the use of these types of ceramic matrices in future.

However, the structural and thermodynamic stability are not the only parameters to qualify a matrix for waste immobilization. Leaching of radioactivity and ion irradiation stability of these matrices also need to be carried out in future to comment on their actual usage. Moreover, SYNROC type phases require hot isostatic pressing during sintering phase for densification which is another parameter needs further attention.

## **References:**

- [1] R.L. Orbach, The Achilles Heel of Nuclear Energy, Disposal of Spent Fuel, The Energy Institute, The University of Texas at Austin, November 23, 2009.
- [2] The Principles of radioactive waste management, safety Fundamentals, Safety Series No. 111-F, IAEA, Vienna 1995.
- [3] M. I. Ojovan and W. E. Lee, An Introduction to Nuclear Waste Immobilization. pp. 213–67, Elsevier Ltd, Oxford, UK, 2005.

- [4] D. Caurant, O. Majérus, P. Loiseau, I. Bardez, N. Baffier, J.L. Dussossoy, J. Nucl. Mater. 354, 143–162 (2006).
- [5] P. Loiseau, D. Caurant, O. Majerus, N. Baffier, C. Fillet, J. Mater. Sci. 38, 843-852(2003).
- [6] A.E. Ringwood, S.E. Kesson, N.G.Ware, W. Hibberson, Nature 278, 219-223(1979).
- [7] R. C. Ewing, Proc. Natl Acad. Sci. USA, 96, 3432–9 (1999).
- [8] E. R. Vance, G. R. Lumpkin, M. L. Carter, D. J. Cassidy, C. J. Ball, R. A. Day, and B. D. Begg J. Am. Ceram. Soc., 85, 1853-1859 (2002).
- [9] R. C. Ewing, W. J. Weber, and J. Lian, J. Appl. Phys. 95, 5929-5971 (2004).
- [10] M.A. Subramanian, G. Aravamudan, G.V. Subba Rao, Prog. Solid State Chem. 15, 55-143 (1983).
- [11] B.P. Mandal, M. Pandey, A. K. Tyagi, J. Nucl Mater., 406, 238-243 (2010).
- [12] E. R. Vance, Mater Res Soc Symp Proc. 985, 135–140 (2007).
- [13] Y. Zhang, A. Navrotsky, H. Li, L. Li, L. L. Davis and D. M. Strachan, J. Non-Cryst. Solids, 296, 93-101 (2001).
- [14] L. Li, H. Li, M. Qian and D. M. Strachan, J. Non-Cryst. Solids, 281, 189-197 (2001).

## LIST OF FIGURES

Fig 1.1.	Schematic diagram of the generation of transuranic radionuclides in a uranium fueled nuclear power reactor.	4
Fig 1.2.	A schematic diagram of closed nuclear fuel cycle practiced by India	7
Fig 1.3.	A schematic diagram of Indian three stage nuclear power programme	8
Fig 1.4.	Schematic diagram of a multi-barrier system of nuclear waste storage in a DGR	15
Fig 1.5.	Crystal structure of zirconolite -2M polytype ( $\text{CaZrTi}_2\text{O}_7$ )	24
Fig 1.6.	Crystal structure of zirconolite -4M polytype	25
Fig 1.7.	Crystal structure of pyrochlore showing distorted $\text{AO}_8$ and $\text{BO}_6$ polyhedra	26
Fig 2.1.	Schematic diagram of X-ray diffraction	41
Fig 2.2..	Schematic diagram of a typical powder X-ray diffractometer	43
Fig 2.3.	Diagram showing the schematic of Bragg-Brentano geometry	44
Fig 2.4.	Different goodness of fit parameters associated with Rietveld refinement	47
Fig 2.5.	Schematic representation of Raman Scattering	48
Fig 2.6.	Schematic diagram showing the three distinct zones of XAFS	50
Fig 2.7.	Depiction of different phenomena occurring on interaction of electron beam with sample	58
Fig 2.8.	Schematic diagram of different parts of a XPS instrument	61
Fig 3.1.	Rietveld refinement plot of powder XRD data of calzirtite sample recorded at ambient tempetraure. The vertical line indicate Bragg postions for tetragonal calzirtite (1 <sup>st</sup> row) and monolinc $\text{ZrO}_2$ (2 <sup>nd</sup> row)	69
Fig 3.2.	Typical crystal strcture of tetragonal calzirtite. The $\text{Zr}_2\text{O}_7$ , $\text{CaO}_8$ , $\text{TiO}_6$ polyhedra are shown along with vacant anion site	70
Fig 3.3.	Rietveld refinement plot of powder XRD data of calzirtite sample recorded at 1473 K. The vertical line indicate Bragg postions for calzirtite (1 <sup>st</sup> row) and zirconia (2 <sup>nd</sup> row) <sup>126</sup>	73
Fig 3.4.	Variation of unit cell parametrs of calzirtite as a function of temperature	75
Fig 3.5.	Rietveld refinement plot of powder XRD data of zirconolite recored at 300 K. The vertical line indicate Bragg postions for zirconolite (1 <sup>st</sup> row) and base metal platinum used as sample holder (2 <sup>nd</sup> row)	77
Fig 3.6.	Rietveld refinement plot of powder XRD data of zirconolite recored at 1273 K. The vertical line indicate Bragg postions for zirconolite (1 <sup>st</sup> row) and base metal platinum used as sample holder (2 <sup>nd</sup> row)	78
Fig 3.7.	Variation of unit cell parametrs of zirconolite as a function of	79

	temperature	
Fig 3.8.	Varation of unit cell volume of calzirtite and zirconolite with temperature. The unit cell volume of calzirtite is divided by 2 for proper scaling	81
Fig 3.9.	Normalized heat flow signal after dropping the sample in liquid Na <sub>2</sub> O + MoO <sub>3</sub> (3:4 molar ratio) solvent maintained at 986 K	83
Fig 3.10.	Plot of H <sub>T</sub> –H <sub>298.15</sub> as a function of temperature for Ca <sub>2</sub> Zr <sub>5</sub> Ti <sub>2</sub> O <sub>16</sub> (s) and CaZrTi <sub>2</sub> O <sub>7</sub> (s) measured in the temperature range 324 to 986 K together with the enthalpy increment data for CaZrTi <sub>2</sub> O <sub>7</sub> (s) reported by Pöml et al	88
Fig 3.11	Plot of heat capacities of calzirtite Ca <sub>2</sub> Zr <sub>5</sub> Ti <sub>2</sub> O <sub>16</sub> (s) and zirconolite CaZrTi <sub>2</sub> O <sub>7</sub> (s) as a function of temperature	89
Fig 3.12.	Plot of Standard Gibbs free energy of Ca <sub>2</sub> Zr <sub>5</sub> Ti <sub>2</sub> O <sub>16</sub> (s) and CaZrTi <sub>2</sub> O <sub>7</sub> (s) as a function of temperature	95
Fig 4.1.	: Final refinement plot of the powder XRD data of CaZrTi <sub>2</sub> O <sub>7</sub> (2M-zirconolite phase)	104
Fig 4.2.	Final refinement plots of the powder XRD data of Nd <sub>2</sub> Ti <sub>2</sub> O <sub>7</sub> composition	106
Fig 4.3.	Final refinement plots of the powder XRD data of Sm <sub>2</sub> Ti <sub>2</sub> O <sub>7</sub> composition	107
Fig 4.4.	Final refinement plots of the powder XRD data of Y <sub>2</sub> Ti <sub>2</sub> O <sub>7</sub> composition	108
Fig 4.5.	Representative XRD patterns of Ca <sub>1-x</sub> Zr <sub>x</sub> Nd <sub>2x</sub> Ti <sub>2</sub> O <sub>7</sub> compositions	110
Fig 4.6.	Representative XRD patterns of Ca <sub>1-x</sub> Zr <sub>x</sub> Sm <sub>2x</sub> Ti <sub>2</sub> O <sub>7</sub> compositions. Signature peaks are marked in figure as “up arrow” pyrochlore and “down arrow” 4M-zirconolite	111
Fig 4.7.	Representative XRD patterns of Ca <sub>1-x</sub> Zr <sub>x</sub> Y <sub>2x</sub> Ti <sub>2</sub> O <sub>7</sub> (0.00 ≤ x ≤ 1.00) compositions. Signature peaks are marked in figure as “*” 2M-zirconolite and “#” 4M-zirconolite.	112
Fig 4.8.	Final refinement plots of the powder XRD data of Ca <sub>0.80</sub> Zr <sub>0.80</sub> Zr <sub>0.40</sub> Ti <sub>2</sub> O <sub>7</sub> composition. Vertical lines are Bragg positions for 4M-zirconolite, perovskite and 2M-zirconolite structures (top to bottom). (R <sub>p</sub> = 11.0 %, R <sub>wp</sub> = 14.7 %, χ <sup>2</sup> = 2.63)	119
Fig 4.9.	Final refinement plots of the powder XRD data of Ca <sub>0.50</sub> Zr <sub>0.50</sub> Nd <sub>1.00</sub> Ti <sub>2</sub> O <sub>7</sub> composition. Vertical lines are Bragg positions for cubic pyrochlore phase (upper) and perovskite phase (lower). (R <sub>p</sub> = 12.7 %, R <sub>wp</sub> = 16.1 %, χ <sup>2</sup> = 2.51).	120
Fig 4.10.	Final refinement plots of the powder XRD data of Ca <sub>0.40</sub> Zr <sub>0.40</sub> Sm <sub>1.20</sub> Ti <sub>2</sub> O <sub>7</sub> composition. (R <sub>p</sub> : 17.9 %, R <sub>wp</sub> : 25.0 %, χ <sup>2</sup> : 1.50).	120
Fig 4.11.	Variations of normalized volume (V/Z) of different observed phases with nominal compositions. (Z-I: Zirconolite-2M (Z = 8); Z-II: zirconolite-4M (Z = 16); Per: Perovskite (Z = 2); Py: cubic pyrochlore (Z = 8); NT: monoclinic Nd <sub>2</sub> Ti <sub>2</sub> O <sub>7</sub> (Z= 8). For proper scaling of perovskite phase Z = 2 has been used	121
Fig 4.12.	Representative BSE images of 6 different bulk compositions with	124



	constituent phase assemblages. Grain pull-outs are polishing defects	
Fig 4.13.	Representative qualitative x-ray images showing elemental distribution patterns among different phases of $\text{Ca}_{0.60}\text{Zr}_{0.60}\text{Nd}_{0.80}\text{Ti}_2\text{O}_7$ bulk composition	125
Fig 4.14.	Representative BSE images for $\text{Ca}_{1-x}\text{Zr}_{1-x}\text{Sm}_{2x}\text{Ti}_2\text{O}_7$ compositions. ( $x = 0.10$ (a). $0.50$ (b) and $0.60$ (c)). Dark black regions are polishing grain pull-outs defect.	128
Fig 4.15.	X-ray images of $\text{Ca}_{0.50}\text{Zr}_{0.50}\text{Sm}_{1.00}\text{Ti}_2\text{O}_7$ ( $x=0.50$ ). (Two phase system consisting of zirconolite and pyrochlore)	129
Fig 4.16.	SEM images of compositions with $x = 0.25, 0.40$ and $0.50$ in two different resolutions (left column: 150 KX and right column: 5 KX magnifications)	131
Fig 4.17.	Phase evolution in $\text{CaZrTi}_2\text{O}_7$ (zirconolite)- $\text{RE}_2\text{Ti}_2\text{O}_7$ (pyrochlore) ( $\text{RE} = \text{Nd}^{3+}, \text{Sm}^{3+}$ and $\text{Y}^{3+}$ ) system	132
Fig 5.1.	Powder X-ray diffraction patterns of the series $\text{Gd}_{2-2x}\text{Ca}_x\text{Zr}_x\text{Ti}_2\text{O}_7$ ( $0.0 \leq x \leq 0.4$ )	138
Fig 5.2.	Relative peak intensity (%) of (111) superstructure peak with respect to the strongest (222) peak of pyrochlore structure	138
Fig 5.3.	Rietveld refinement plot of $\text{Gd}_{1.6}\text{Ca}_{0.2}\text{Zr}_{0.2}\text{Ti}_2\text{O}_7$ ( $x=0.2$ )	140
Fig 5.4.	Raman spectra of the nominal compositions of the series $\text{Gd}_{2-2x}\text{Ca}_x\text{Zr}_x\text{Ti}_2\text{O}_7$ ( $0.0 \leq x \leq 0.4$ )	142
Fig 5.5.	Normalized heat flow curves for nominal compositions of the series $\text{Gd}_{2-2x}\text{Ca}_x\text{Zr}_x\text{Ti}_2\text{O}_7$ ( $0.0 \leq x \leq 0.4$ )	144
Fig 5.6.	Plot of standard molar enthalpy of formation of $\text{Gd}_{2-2x}\text{Ca}_x\text{Zr}_x\text{Ti}_2\text{O}_7$ ( $0.0 \leq x \leq 0.4$ )	145
Fig 5.7.	Structure of $\text{GdO}_8$ and $\text{TiO}_6$ polyhedra in doped and undoped $\text{Gd}_2\text{Ti}_2\text{O}_7$	150
Fig 6.1.	Powder X-ray diffraction patterns of $\text{Gd}_2\text{Zr}_2\text{O}_7$ sintered at 1373 K, 1473 K, 1573 K and 1673 K	160
Fig 6.2.	Powder X-ray diffraction patterns $\text{Gd}_2\text{Zr}_2\text{O}_7$ sintered at 1373 K, 1473 K, 1573 K and 1673 K in the $2\theta$ range of $10-30^\circ$ , showing superstructure peaks observed at $2\theta \sim 14.5^\circ$ and $28.2^\circ$	161
Fig 6.3.	Rietveld refinement plot of $\text{Gd}_2\text{Zr}_2\text{O}_7$ sintered at 1373 K, 1473 K, 1573 K and 1673 K. Figure a, b: Top and bottom vertical lines indicate Bragg positions for defect fluorite and pyrochlore type phase respectively. Figure c, d: top and bottom vertical lines indicate Bragg positions for pyrochlore and defect fluorite phase respectively	162
Fig 6.4.	Raman spectra of $\text{Gd}_2\text{Zr}_2\text{O}_7$ sintered at 1373 K, 1473 K, 1573 K and 1673 K respectively	165
Fig 6.5.	Normalized heat flow curves for $\text{Gd}_2\text{Zr}_2\text{O}_7$ sintered at 1373 K, 1473 K, 1573 K and 1673 K respectively	169
Fig 6.6.	Powder XRD patterns of $\text{Gd}_{2-x}\text{U}_x\text{Zr}_2\text{O}_{7+\delta}$ ( $0.0 \leq x \leq 0.25$ ) samples calcined at 873 K for 1 h	173
Fig 6.7.	Representative Rietveld refinement plots for the nominal	174

	compositions in the series $\text{Gd}_{2-x}\text{U}_x\text{Zr}_2\text{O}_{7+\delta}$ ( $0.0 \leq x \leq 0.25$ ) heated in reducing atmosphere	
Fig 6.8.	Powder XRD patterns of $\text{Gd}_{2-x}\text{U}_x\text{Zr}_2\text{O}_{7+\delta}$ ( $0.0 \leq x \leq 0.25$ ) samples annealed in Ar : $\text{H}_2$ (92:8) at 1373 K for 8 h. All the compositions were found to crystallize in defect fluorite structure	176
Fig 6.9.	Powder XRD patterns of $\text{Gd}_{2-x}\text{U}_x\text{Zr}_2\text{O}_{7+\delta}$ ( $0.0 \leq x \leq 0.25$ ) after heat treatment in air at 1373 K for 8 h. Asterisks indicate unidentified minor secondary phase	177
Fig 6.10.	Variation of unit cell parameter upon substitution of U at Gd site in $\text{Gd}_{2-x}\text{U}_x\text{Zr}_2\text{O}_{7+\delta}$ (reduced and oxidized samples)	178
Fig 6.11a.	High temperature-XRD pattern of $\text{Gd}_{1.95}\text{U}_{0.05}\text{Zr}_2\text{O}_{7+\delta}$ . Solid line has been used to show the shift in peak position with variation in temperature	179
Fig 6.11b.	High temperature-XRD pattern of $\text{Gd}_{1.75}\text{U}_{0.25}\text{Zr}_2\text{O}_{7+\delta}$ . Asterisk indicated the segregation of secondary phase	179
Fig 6.12.	Variation of unit cell parameters of nominal compositions $\text{Gd}_{2-x}\text{U}_x\text{Zr}_2\text{O}_{7+\delta}$ ( $0.00 \leq x \leq 0.25$ ) with temperature	181
Fig 6.13.	X-ray photoelectron spectra of uranium ( $4f_{7/2}$ ) of reduced and oxidized sample having nominal composition $\text{Gd}_{1.85}\text{U}_{0.15}\text{Zr}_2\text{O}_{7+\delta}$	182
Fig 6.14.	BSE images of (a) $x=0.15$ (c) $x=0.20$ (e) $x=0.25$ and SE images of (b) $x=0.15$ (d) $x=0.20$ (f) $x=0.25$ nominal compositions heated in static air respectively	183
Fig 6.15.	Representative heat flow signals for dissolution of $\text{Gd}_{2-x}\text{U}_x\text{Zr}_2\text{O}_{7+\delta}$ ( $0.0 \leq x \leq 0.15$ ) nominal compositions (a) reduced and (b) oxidized compounds (normalized to 10 mg each) in liquid $\text{Na}_2\text{O} + \text{MoO}_3$ (3:4 molar ratio) dropped from room temperature to liquid solvent 986 K	185
Fig 6.16.	The enthalpy of formation of $\text{Gd}_{2-x}\text{U}_x\text{Zr}_2\text{O}_{7+\delta}$ (both oxidized and reduced samples)	190
Fig 6.17.	Powder XRD patterns of $\text{Gd}_{2-x}\text{Ce}_x\text{Zr}_{1.9}\text{U}_{0.1}\text{O}_{7+\delta}$ ( $0.0 \leq x \leq 0.50$ ) samples calcined at 873 K for 1 h	192
Fig 6.18.	Powder XRD patterns of $\text{Gd}_{2-x}\text{Ce}_x\text{Zr}_{1.9}\text{U}_{0.1}\text{O}_{7+\delta}$ ( $0.0 \leq x \leq 0.50$ ) samples annealed at 1373 K for 8 h in air	192
Fig 6.19.	Powder XRD patterns of $\text{Gd}_{1.8}\text{Ce}_{0.2}\text{Zr}_{1.9}\text{U}_{0.1}\text{O}_{7+\delta}$ ( $x=0.20$ ) samples annealed at 1373 K for 8 h in air	194
Fig 6.20.	X-ray photoelectron spectra of cerium ( $3d_{5/2}$ ) of sample having nominal composition $\text{Gd}_{1.8}\text{Ce}_{0.2}\text{Zr}_{1.9}\text{U}_{0.1}\text{O}_{7+\delta}$	195
Fig 6.21.	X-ray photoelectron spectra of uranium ( $4f_{7/2}$ ) of sample having nominal composition $\text{Gd}_{1.8}\text{Ce}_{0.2}\text{Zr}_{1.9}\text{U}_{0.1}\text{O}_{7+\delta}$	196
Fig 6.22.	Normalized heat flow signals for dissolution of $\text{Gd}_{2-x}\text{Ce}_x\text{Zr}_{1.9}\text{U}_{0.1}\text{O}_{7+\delta}$ ( $0.0 \leq x \leq 0.5$ ) nominal compositions (normalized to 10 mg each) in liquid $\text{Na}_2\text{O} + \text{MoO}_3$ (3:4 molar ratio) dropped from room temperature to liquid solvent 986 K	197
Fig 6.23.	Variation of standard molar enthalpy of formation of $\text{Gd}_{2-x}\text{Ce}_x\text{Zr}_{1.9}\text{U}_{0.1}\text{O}_{7+\delta}$ ( $0.0 \leq x \leq 0.5$ )	199
Fig 7.1.	Powder XRD patterns of the prepared glass formulations. “*” marks the peaks corresponding to the crystalline phase	209

	$\text{Gd}_{4.67}(\text{SiO}_4)_3\text{O}$	
Fig 7.2.	DTA curves of the prepared glass formulations	210
Fig 7.3.	BSE images of glass formulation Gd-5.0 (top) and Gd-6.0 (bottom). Segregated phases are clearly observed in Gd-6.0	211

## LIST OF TABLES

Table 1.1.	Classification of nuclear waste in accordance with radioactivity	11
Table 1.2.	List of fission products and transuranic elements present in HLW	13
Table 1.3.	General comparison between glass and ceramic matrices for nuclear HLW immobilization	21
Table 1.4.	Table showing the similarity in properties between $\text{CeO}_2$ and $\text{PuO}_2$	28
Table 3.1.	Refined structural parameters of calzirtite at ambient conditions	69
Table 3.2.	The observed bond lengths ( $\text{\AA}$ ) of calzirtite at ambient temperature	71
Table 3.3.	Refined structural parameters of calzirtite at 1473 K	72
Table 3.4.	The observed inter-atomic distances ( $\text{\AA}$ ) of calzirtite at 1473 K	74
Table 3.5.	Refined structural parameters of zirconolite at ambient conditions	76
Table 3.6.	The molar enthalpies of dissolution of $\text{Ca}_2\text{Zr}_5\text{Ti}_2\text{O}_{16}(\text{s})$ (Calzirtite), $\text{CaZrTi}_2\text{O}_7(\text{s})$ , $\text{CaO}(\text{s})$ , $\text{ZrO}_2(\text{s})$ and $\text{TiO}_2(\text{s})$ in 6g of $\text{Na}_2\text{O} + \text{MoO}_3$ 3:4 molar ratio at $T = 986 \text{ K}$	85
Table 3.7.	Thermo chemical cycles for derivation of standard molar enthalpies of formation of $\text{Ca}_2\text{Zr}_5\text{Ti}_2\text{O}_{16}(\text{s}, 298\text{K})$ , Calzirtite) and $\text{CaZrTi}_2\text{O}_7(\text{s}, 298\text{K})$ , Zirconolite) $\text{MO}_x(\text{sln}) = \text{dilute solution of species } \text{MO}_x \text{ in 6g liquid } \text{Na}_2\text{O} + \text{MoO}_3 \text{ 3:4 molar solvent maintained at } 986 \text{ K}$	86
Table 3.8.	Enthalpy increment ( $H_T - H_{298}$ ) values for $\text{Ca}_2\text{Zr}_5\text{Ti}_2\text{O}_{16}(\text{s})$ and $\text{CaZrTi}_2\text{O}_7(\text{s})$	87
Table 3.9.	Thermodynamic data for calzirtite ( $\text{Ca}_2\text{Zr}_5\text{Ti}_2\text{O}_{16}, \text{s}$ )	92
Table 3.10.	Thermodynamic data for zirconolite ( $\text{CaZrTi}_2\text{O}_7, \text{s}$ )	93
Table 4.1.	Refined structural parameters of zirconolite $\text{CaZrTi}_2\text{O}_7$ ( $x=0.00$ )	103
Table 4.2.	Refined structural parameters of $\text{Nd}_2\text{Ti}_2\text{O}_7$ ( $x=1.00$ ) for RE= $\text{Nd}^{3+}$ series	105
Table 4.3.	Refined structural parameters of $\text{Sm}_2\text{Ti}_2\text{O}_7$ ( $x=1.00$ ) for RE= $\text{Sm}^{3+}$ series	107
Table 4.4.	Refined structural parameters of $\text{Y}_2\text{Ti}_2\text{O}_7$ ( $x=1.00$ ) for RE= $\text{Y}^{3+}$ series	107
Table 4.5.	Summary of phases identified in $\text{Ca}_{1-x}\text{Zr}_{1-x}\text{Nd}_{2x}\text{Ti}_2\text{O}_7$ and their unit cell parameters	113
Table 4.6.	Summary of phases identified in $\text{Ca}_{1-x}\text{Zr}_{1-x}\text{Sm}_{2x}\text{Ti}_2\text{O}_7$ and their unit cell parameters	114
Table 4.7.	Summary of phases identified in $\text{Ca}_{1-x}\text{Zr}_{1-x}\text{Y}_{2x}\text{Ti}_2\text{O}_7$ and their unit cell parameters	115
Table 4.8.	Phase and compositions (at %) observed at various nominal	126

	bulk compositions for $\text{Nd}^{3+}$ series. (balance oxygen or mention as “y”)	
Table 4.9.	Phase and compositions (at %) observed at various representative compositions for $\text{Sm}^{3+}$ series	129
Table 4.10.	Atomic (metal) ratio as estimated from point mode EDX analyses of some representative compositions <sup>1</sup>	130
Table 5.1.	Ionic radii of the constituent ions at different coordination number	139
Table 5.2.	Refinement parameters of the series $\text{Gd}_{2-2x}\text{Ca}_x\text{Zr}_x\text{Ti}_2\text{O}_7$ ( $0.0 \leq x \leq 0.4$ )	141
Table 5.3.	Heat of Dissolution of $\text{Gd}_{2-2x}\text{Ca}_x\text{Zr}_x\text{Ti}_2\text{O}_7$ ( $0.0 \leq x \leq 0.4$ ) and their component oxides	147
Table 5.4.	Thermochemical cycles for enthalpy of formation of $\text{Gd}_{2-2x}\text{Ca}_x\text{Zr}_x\text{Ti}_2\text{O}_7$ ( $0.0 \leq x \leq 0.4$ )	148
Table 6.1.	Refined phase fraction and unit cell parameters of $\text{Gd}_2\text{Zr}_2\text{O}_7$ sintered at 1373 K, 1473 K, 1573 K and 1673 K	164
Table 6.2.	Table depicting average Zr-O bond length of $\text{Gd}_2\text{Zr}_2\text{O}_7$ sintered at 1373 K, 1473 K, 1573 K and 1673 K	167
Table 6.3.	Table depicting average Gd-O bond length of $\text{Gd}_2\text{Zr}_2\text{O}_7$ sintered at 1373 K, 1473 K, 1573 K and 1673 K. [Defect fluorite model]	168
Table 6.4.	Table depicting average Gd-O bond length of $\text{Gd}_2\text{Zr}_2\text{O}_7$ sintered at 1373 K, 1473 K, 1573 K and 1673 K respectively. [Pyrochlore model]	168
Table 6.5.	Heat of Dissolution of $\text{Gd}_2\text{Zr}_2\text{O}_7$ sintered at 1373 K, 1473 K, 1573 K and 1673 K and their component oxides	170
Table 6.6.	Thermochemical cycles for enthalpy of formation of $\text{Gd}_2\text{Zr}_2\text{O}_7$ sintered at 1373 K, 1473 K, 1573 K and 1673 K	171
Table 6.7.	Rietveld refined parameters of $\text{Gd}_{2-x}\text{U}_x\text{Zr}_2\text{O}_{7+\delta}$ ( $0.0 \leq x \leq 0.25$ ) compositions after annealing at Ar :H <sub>2</sub> (92:8) at 1373 K for 8h	175
Table 6.8.	Heat of dissolution of $\text{Gd}_{2-x}\text{U}_x\text{Zr}_2\text{O}_{7+\delta}$ (oxidized/reduced) and their component oxides	186
Table 6.9.	Thermochemical cycle for enthalpy of formation of $\text{Gd}_{2-x}\text{U}_x\text{Zr}_2\text{O}_{7+\delta}$ (oxidized/reduced)	188
Table 6.10.	Rietveld refined parameters of $\text{Gd}_{2-x}\text{Ce}_x\text{Zr}_{1.9}\text{U}_{0.1}\text{O}_{7+\delta}$ ( $0.0 \leq x \leq 0.50$ ) compositions after annealing at 1373 K for 8h in air.	193
Table 6.11.	Heat of dissolution of $\text{Gd}_{2-x}\text{Ce}_x\text{Zr}_{1.9}\text{U}_{0.1}\text{O}_{7+\delta}$ ( $0.0 \leq x \leq 0.5$ ) and their component oxides	198
Table 6.12.	Thermochemical cycles for enthalpy of formation of $\text{Gd}_{2-x}\text{Ce}_x\text{Zr}_{1.9}\text{U}_{0.1}\text{O}_{7+\delta}$ ( $0.0 \leq x \leq 0.5$ )	200
Table 7.1a.	Compositions in mol% of synthesized borosilicate glass	207
Table 7.1b.	Compositions in wt% of synthesized borosilicate glass	207
Table 7.2.	Table showing the lifetime with the mode of decay in the prepared glass formulations	213

## LIST OF ABBREVIATIONS

BARC	Bhabha Atomic Research Centre
HBNI	Homi Bhabha National Institute
NFC	Nuclear Fuel Cycle
HLW	High Level Waste
BWR	Boiling Water Reactor
PWR	Pressurized Water Reactor
PHWR	Pressurized Heavy Water Reactor
GCR	Gas Cooled Reactor
VVER	Vodo-Vodyanoi Energetichesky Reactor
LMCFBR / FBR	Liquid Metal Cooled Fast Breeder Reactor
MOX	Mixed Oxide Fuel
FBTR	Fast Breeder Test Reactor
IGCAR	Indira Gandhi Centre for Atomic Research
AHWR	Advanced Heavy Water Reactor
MSBR	Molten Salt Breeder Reactor
INPRO	International Project on Innovative Nuclear Reactors and Fuel Cycles
GIF	Generation IV International Forum
MICANET	European Union led Michelangelo network
IAEA	International Atomic Energy Agency
IMF	Inert Matrix Fuel
LLW	Low Level Waste
ILW	Intermediate Level Waste
HLW	High Level Waste
NSDF	Near Surface Disposal Facility
DGR	Deep Geological Repository
SSSSF	Solid State Storage and Surveillance Facility
EBS	Engineered Barrier System
$T_g$	Glass Transition Temperature
NBS	Sodium Borosilicate Glass
BBS	Barium Borosilicate Glass
SYNROC	Synthetic Rock
ASDF	Actinide Separation Demonstration Facility
NZP	Sodium Zirconium Phosphate
XRD	X-ray Diffraction
XAFS	X-Ray Absorption Fine Structure
TG-DTA	Thermogravimetric Analysis coupled with Differential Thermal Analysis
SEM	Scanning Electron Microscopy
EPMA	Electron Probe Micro Analyzer
XPS	X-Ray Photoelectron Spectroscopy
HMTA	Hexa Methylene Tetra Amine
JCPDS	Joint Committee on Powder Diffraction Standards
FWHM	Full Width at Half Maximum
CCD	Charge Coupled Device

XANES	X-Ray Absorption Near Edge Structure
EXAFS	Extended X-Ray Absorption Fine Structure
SE	Secondary Electron
BSE	Back Scattered Electron
FEG	Field Emission Gun
WDS	Wavelength Dispersive Spectroscopy
CL	Cathodoluminescence
EDS	Energy Dispersive Spectroscopy
ESCA	Electron Spectroscopy For Chemical Analysis
ppt	Parts per Thousand
ppm	Parts per Million
BE	Binding Energy
RSF	Relative Sensitivity Factor
HT-XRD	High Temperature X-ray Diffraction
DFT	Density Functional theory
VASP	Vienna Ab-initio Simulation Package
PAW	Projector Augmented Wave
PBE	Perdew–Burke–Ernzerhof

# CONTENTS

	Page No.
<b>SUMMARY</b>	xv
<b>SYNOPSIS</b>	xvi-xxv
<b>LIST OF FIGURES</b>	xxvi-xxx
<b>LIST OF TABLES</b>	xxxi-xxxii
<b>LIST OF ABBREVIATIONS</b>	xxxiii-xxxiv
 <b>CHAPTER 1 INTRODUCTION</b>	 <b>1-30</b>
<b>1.1. Introduction</b>	2
<b>1.2. Nuclear Energy</b>	3
1.2.1. Boiling Water Reactor (BWR)	4
1.2.2. Pressurized Water Reactor (PWR)	4
1.2.3. Pressurized Heavy Water Reactor (PHWR)	5
1.2.4. Gas Cooled Reactor (GCR)	5
1.2.5. Vodo-Vodyanoi Energetichesky Reactor (VVER)	5
1.2.6. Liquid Metal Cooled Fast Breeder Reactor (LMCFBR / FBR)	6
<b>1.3. Indian Nuclear Energy Programme</b>	6
<b>1.4. Futuristic Nuclear Fuels In Indian Scenario</b>	9
<b>1.5. Nuclear Waste</b>	10
1.5.1. Constituents of LLW	11
1.5.2. Constituents of ILW	12
1.5.3. Constituents of HLW	12
<b>1.6. Management Strategy of HLW</b>	13
<b>1.7. Disposal of HLW</b>	14
<b>1.8. Nuclear HLW Immobilization Matrices</b>	16
<b>1.9. Glass Matrices</b>	17



1.9.1. Phosphate based glasses	17
1.9.2. Borosilicate based glasses	18
1.9.3. Glass ceramics or glass composites	19
<b>1.10. Limitations of Glass Matrices</b>	<b>19</b>
<b>1.11. Crystalline Matrices</b>	<b>20</b>
1.11.1. Apatites	21
1.11.2. Sodium Zirconium Phosphate (NZP)	22
1.11.3. Zircon	22
1.11.4. Monazite	22
1.11.5. Hollandite	23
1.11.6. Perovskite	23
1.11.7. Zirconolite	24
1.11.8. Pyrochlore	26
<b>1.12. Surrogate Nuclear Materials</b>	<b>27</b>
1.12.1. Surrogate for Plutonium	27
1.12.2. Surrogate for Americium	28
<b>1.13. Scope of the thesis</b>	<b>29</b>
<b>CHAPTER 2 SYNTHESIS METHODS AND INSTRUMENTAL TECHNIQUES</b>	<b>31-61</b>
<b>2.1. Introduction</b>	<b>32</b>
<b>2.2. Synthesis Methods</b>	<b>33</b>
2.2.1. Solid state method	33
2.2.2. Gel combustion method	36
2.2.3. Melt quench method	38
<b>2.3. Instrumental Techniques</b>	<b>39</b>
2.3.1. X-ray diffraction (XRD)	39
2.3.2. Raman spectroscopy	47
2.3.3. X-ray absorption fine structure (XAFS)	50
2.3.4. Calvet oxide melt calorimeter	52
2.3.5. Thermogravimetric analysis coupled with differential thermal analysis (DTA)	55

	2.3.6. Scanning electron microscopy (SEM)	56
	2.3.7. Electron probe micro analyzer (EPMA)	59
	2.3.8. X-ray photoelectron spectroscopy (XPS)	59
CHAPTER 3	<b>STRUCTURE AND THERMODYNAMIC PROPERTIES OF POTENTIAL WASTE IMMOBILIZATION LATTICES IN Ca-Zr-Ti-O SYSTEM: CALZIRTITE AND ZIRCONOLITE</b>	<b>62-97</b>
3.1.	Introduction	63
3.2.	Experimental Methods	65
3.3.	Results and Discussions	66
	3.3.1. Structural studies of calzirtite ( $\text{Ca}_2\text{Zr}_5\text{Ti}_2\text{O}_{16}$ )	66
	3.3.2. Structural studies of zirconolite ( $\text{CaZrTi}_2\text{O}_7$ )	76
	3.3.3. Standard molar enthalpy of formation of calzirtite and zirconolite	81
	3.3.4. Enthalpy increment and heat capacity measurements of calzirtite and zirconolite	86
	3.3.5. Construction of thermodynamic tables for calzirtite and zirconolite	89
	3.3.6. Standard Gibbs free energy of formation of calzirtite and zirconolite	91
3.4.	Conclusions	96
CHAPTER 4	<b>PHASE EVOLUTION AND MICROSTRUCTURAL STUDIES IN <math>\text{CaZrTi}_2\text{O}_7</math> (ZIRCONOLITE)-<math>\text{RE}_2\text{Ti}_2\text{O}_7</math> (PYROCHLORE) (RE= <math>\text{Nd}^{3+}</math>, <math>\text{Sm}^{3+}</math> and</b>	<b>98-132</b>

	<b>Y<sup>3+</sup>) RELATED SYSTEMS</b>	
<b>4.1.</b>	<b>Introduction</b>	<b>99</b>
<b>4.2.</b>	<b>Experimental Methods</b>	<b>101</b>
<b>4.3.</b>	<b>Results and Discussions</b>	<b>102</b>
	<b>4.3.1. Phase evolution studies</b>	<b>102</b>
	<b>4.3.2. Microstructural studies</b>	<b>123</b>
<b>4.4.</b>	<b>Conclusions</b>	<b>130</b>
<b>CHAPTER 5</b>	<b>STRUCTURE AND THERMODYNAMIC STABILITY OF Ca AND Zr CO-SUBSTITUTED Gd<sub>2</sub>Ti<sub>2</sub>O<sub>7</sub> PYROCHLORE SYSTEM: EXPERIMENTAL AND THEORETICAL STUDY</b>	<b>133-151</b>
<b>5.1.</b>	<b>Introduction</b>	<b>134</b>
<b>5.2.</b>	<b>Experimental Methods</b>	<b>135</b>
<b>5.3.</b>	<b>Results and Discussions</b>	<b>137</b>
	<b>5.3.1. Structural studies</b>	<b>137</b>
	<b>5.3.2. Calorimetric studies</b>	<b>143</b>
	<b>5.3.3. Computational results</b>	<b>146</b>
<b>5.4.</b>	<b>Conclusions</b>	<b>151</b>
<b>CHAPTER 6</b>	<b>STRUCTURE AND THERMODYNAMIC STUDIES ON PARENT AND ACTINIDE SUBSTITUTED Gd<sub>2</sub>Zr<sub>2</sub>O<sub>7</sub></b>	<b>152-202</b>
<b>6.1.</b>	<b>Introduction</b>	<b>153</b>
<b>6.2.</b>	<b>Experimental Methods</b>	<b>154</b>
<b>6.3.</b>	<b>Results and Discussions</b>	<b>159</b>
<b>Part A</b>	<b>Structural And Thermodynamic Studies On Pristine Gd<sub>2</sub>Zr<sub>2</sub>O<sub>7</sub></b>	<b>159</b>
	<b>(i) Powder XRD studies</b>	<b>159</b>

	(ii) Raman spectroscopic studies	163
	(iii) EXAFS studies	165
	(iv) Calorimetric studies	168
<b>Part B</b>	<b>Structural And Thermodynamic Studies On Uranium Incorporated <math>Gd_2Zr_2O_7</math></b>	<b>172</b>
	(i) Powder XRD studies	172
	(ii) XPS studies	181
	(iii) SEM studies	182
	(iv) Calorimetric studies	184
<b>Part C</b>	<b>Structural And Thermodynamic Studies On Uranium And Cerium Co- Incorporated <math>Gd_2Zr_2O_7</math></b>	<b>191</b>
	(i) Powder XRD studies	191
	(ii) XPS studies	195
	(iii) Calorimetric studies	196
<b>6.4.</b>	<b>Conclusions</b>	<b>202</b>
<b>CHAPTER 7</b>	<b>MISCELLANEOUS ACTIVITIES PERTAINING TO NUCLEAR WASTE IMMOBILIZATION</b>	<b>203-214</b>
<b>7.1.</b>	<b>Introduction</b>	<b>204</b>
<b>7.2.</b>	<b>Synthesis strategy</b>	<b>205</b>
<b>7.3.</b>	<b>Experimental Methods</b>	<b>206</b>
<b>7.4.</b>	<b>Results and Discussions</b>	<b>208</b>
<b>7.5.</b>	<b>Conclusions</b>	<b>213</b>
<b>CHAPTER 8</b>	<b>SUMMARY AND FUTURE SCOPE</b>	<b>215-220</b>
<b>8.1.</b>	<b>Summary</b>	<b>216</b>
<b>8.2.</b>	<b>Future Scope</b>	<b>220</b>
	<b>REFERENCES</b>	<b>221-244</b>

## LIST OF FIGURES

	Description	Page no.
Fig 1.1.	Schematic diagram of the generation of transuranic radionuclides in a uranium fueled nuclear power reactor.	4
Fig 1.2.	A schematic diagram of closed nuclear fuel cycle practiced by India	7
Fig 1.3.	A schematic diagram of Indian three stage nuclear power programme	8
Fig 1.4.	Schematic diagram of a multi-barrier system of nuclear waste storage in a DGR	15
Fig 1.5.	Crystal structure of zirconolite -2M polytype ( $\text{CaZrTi}_2\text{O}_7$ )	24
Fig 1.6.	Crystal structure of zirconolite -4M polytype	25
Fig 1.7.	Crystal structure of pyrochlore showing distorted $\text{AO}_8$ and $\text{BO}_6$ polyhedra	26
Fig 2.1.	Schematic diagram of X-ray diffraction	41
Fig 2.2..	Schematic diagram of a typical powder X-ray diffractometer	43
Fig 2.3.	Diagram showing the schematic of Bragg-Brentano geometry	44
Fig 2.4.	Different goodness of fit parameters associated with Rietveld refinement	47
Fig 2.5.	Schematic representation of Raman Scattering	48
Fig 2.6.	Schematic diagram showing the three distinct zones of XAFS	50
Fig 2.7.	Depiction of different phenomena occurring on interaction of electron beam with sample	58
Fig 2.8.	Schematic diagram of different parts of a XPS instrument	61
Fig 3.1.	Rietveld refinement plot of powder XRD data of calzirtite sample recorded at ambient tempetraure. The vertical line indicate Bragg postions for tetragonal calzirtite (1 <sup>st</sup> row) and monolinc $\text{ZrO}_2$ (2 <sup>nd</sup> row)	69
Fig 3.2.	Typical crystal strcture of tetragonal calzirtite. The $\text{Zr}_2\text{O}_7$ , $\text{CaO}_8$ , $\text{TiO}_6$ polyhedra are shown along with vacant anion site	70
Fig 3.3.	Rietveld refinement plot of powder XRD data of calzirtite sample recorded at 1473 K. The vertical line indicate Bragg postions for calzirtite (1 <sup>st</sup> row) and zirconia (2 <sup>nd</sup> row) <sup>126</sup>	73
Fig 3.4.	Varation of unit cell parametrs of calzirtite as a function of temperature	75
Fig 3.5.	Rietveld refinement plot of powder XRD data of zirconolite recored at 300 K. The vertical line indicate Bragg postions for zirconolite (1 <sup>st</sup> row) and base metal platinum used as sample holder (2 <sup>nd</sup> row)	77
Fig 3.6.	Rietveld refinement plot of powder XRD data of zirconolite recored at 1273 K. The vertical line indicate Bragg postions for zirconolite (1 <sup>st</sup> row) and base metal platinum used as sample holder (2 <sup>nd</sup> row)	78
Fig 3.7.	Varation of unit cell parametrs of zirconolite as a function of temperature	79
Fig 3.8.	Varation of unit cell volume of calzirtite and zirconolite with temperature. The unit cell volume of calzirtite is divided by 2 for proper scaling	81

Fig 3.9.	Normalized heat flow signal after dropping the sample in liquid $\text{Na}_2\text{O} + \text{MoO}_3$ (3:4 molar ratio) solvent maintained at 986 K	83
Fig 3.10.	Plot of $H_T - H_{298.15}$ as a function of temperature for $\text{Ca}_2\text{Zr}_5\text{Ti}_2\text{O}_{16}(\text{s})$ and $\text{CaZrTi}_2\text{O}_7(\text{s})$ measured in the temperature range 324 to 986 K together with the enthalpy increment data for $\text{CaZrTi}_2\text{O}_7(\text{s})$ reported by Pöml et al	88
Fig 3.11	Plot of heat capacities of calzirtite $\text{Ca}_2\text{Zr}_5\text{Ti}_2\text{O}_{16}(\text{s})$ and zirconolite $\text{CaZrTi}_2\text{O}_7(\text{s})$ as a function of temperature	89
Fig 3.12.	Plot of Standard Gibbs free energy of $\text{Ca}_2\text{Zr}_5\text{Ti}_2\text{O}_{16}(\text{s})$ and $\text{CaZrTi}_2\text{O}_7(\text{s})$ as a function of temperature	95
Fig 4.1.	: Final refinement plot of the powder XRD data of $\text{CaZrTi}_2\text{O}_7$ (2M-zirconolite phase)	104
Fig 4.2.	Final refinement plots of the powder XRD data of $\text{Nd}_2\text{Ti}_2\text{O}_7$ composition	106
Fig 4.3.	Final refinement plots of the powder XRD data of $\text{Sm}_2\text{Ti}_2\text{O}_7$ composition	107
Fig 4.4.	Final refinement plots of the powder XRD data of $\text{Y}_2\text{Ti}_2\text{O}_7$ composition	108
Fig 4.5.	Representative XRD patterns of $\text{Ca}_{1-x}\text{Zr}_x\text{Nd}_{2x}\text{Ti}_2\text{O}_7$ compositions	110
Fig 4.6.	Representative XRD patterns of $\text{Ca}_{1-x}\text{Zr}_x\text{Sm}_{2x}\text{Ti}_2\text{O}_7$ compositions. Signature peaks are marked in figure as “up arrow” pyrochlore and “down arrow” 4M-zirconolite	111
Fig 4.7.	Representative XRD patterns of $\text{Ca}_{1-x}\text{Zr}_x\text{Y}_{2x}\text{Ti}_2\text{O}_7$ ( $0.00 \leq x \leq 1.00$ ) compositions. Signature peaks are marked in figure as “*” 2M-zirconolite and “#” 4M-zirconolite.	112
Fig 4.8.	Final refinement plots of the powder XRD data of $\text{Ca}_{0.80}\text{Zr}_{0.80}\text{Zr}_{0.40}\text{Ti}_2\text{O}_7$ composition. Vertical lines are Bragg positions for 4M-zirconolite, perovskite and 2M-zirconolite structures (top to bottom). ( $R_p = 11.0\%$ , $R_{wp} = 14.7\%$ , $\chi^2 = 2.63$ )	119
Fig 4.9.	Final refinement plots of the powder XRD data of $\text{Ca}_{0.50}\text{Zr}_{0.50}\text{Nd}_{1.00}\text{Ti}_2\text{O}_7$ composition. Vertical lines are Bragg positions for cubic pyrochlore phase (upper) and perovskite phase (lower). ( $R_p = 12.7\%$ , $R_{wp} = 16.1\%$ , $\chi^2 = 2.51$ ).	120
Fig 4.10.	Final refinement plots of the powder XRD data of $\text{Ca}_{0.40}\text{Zr}_{0.40}\text{Sm}_{1.20}\text{Ti}_2\text{O}_7$ composition. ( $R_p: 17.9\%$ , $R_{wp}: 25.0\%$ , $\chi^2: 1.50$ ).	120
Fig 4.11.	Variations of normalized volume ( $V/Z$ ) of different observed phases with nominal compositions. (Z-I: Zirconolite-2M ( $Z = 8$ ); Z-II: zirconolite-4M ( $Z = 16$ ); Per: Perovskite ( $Z = 2$ ); Py: cubic pyrochlore ( $Z = 8$ ); NT: monoclinic $\text{Nd}_2\text{Ti}_2\text{O}_7$ ( $Z = 8$ ). For proper scaling of perovskite phase $Z = 2$ has been used	121
Fig 4.12.	Representative BSE images of 6 different bulk compositions with constituent phase assemblages. Grain pull-outs are polishing defects	124
Fig 4.13.	Representative qualitative x-ray images showing elemental distribution patterns among different phases of $\text{Ca}_{0.60}\text{Zr}_{0.60}\text{Nd}_{0.80}\text{Ti}_2\text{O}_7$ bulk composition	125

Fig 4.14.	Representative BSE images for $\text{Ca}_{1-x}\text{Zr}_{1-x}\text{Sm}_{2x}\text{Ti}_2\text{O}_7$ compositions. (x = 0.10 (a). 0.50 (b) and 0.60 (c)). Dark black regions are polishing grain pull-outs defect.	128
Fig 4.15.	X-ray images of $\text{Ca}_{0.50}\text{Zr}_{0.50}\text{Sm}_{1.00}\text{Ti}_2\text{O}_7$ (x=0.50). (Two phase system consisting of zirconolite and pyrochlore)	129
Fig 4.16.	SEM images of compositions with x = 0.25, 0.40 and 0.50 in two different resolutions (left column: 150 KX and right column: 5 KX magnifications)	131
Fig 4.17.	Phase evolution in $\text{CaZrTi}_2\text{O}_7$ (zirconolite)- $\text{RE}_2\text{Ti}_2\text{O}_7$ (pyrochlore) (RE= $\text{Nd}^{3+}$ , $\text{Sm}^{3+}$ and $\text{Y}^{3+}$ ) system	132
Fig 5.1.	Powder X-ray diffraction patterns of the series $\text{Gd}_{2-2x}\text{Ca}_x\text{Zr}_x\text{Ti}_2\text{O}_7$ ( $0.0 \leq x \leq 0.4$ )	138
Fig 5.2.	Relative peak intensity (%) of (111) superstructure peak with respect to the strongest (222) peak of pyrochlore structure	138
Fig 5.3.	Rietveld refinement plot of $\text{Gd}_{1.6}\text{Ca}_{0.2}\text{Zr}_{0.2}\text{Ti}_2\text{O}_7$ (x=0.2)	140
Fig 5.4.	Raman spectra of the nominal compositions of the series $\text{Gd}_{2-2x}\text{Ca}_x\text{Zr}_x\text{Ti}_2\text{O}_7$ ( $0.0 \leq x \leq 0.4$ )	142
Fig 5.5.	Normalized heat flow curves for nominal compositions of the series $\text{Gd}_{2-2x}\text{Ca}_x\text{Zr}_x\text{Ti}_2\text{O}_7$ ( $0.0 \leq x \leq 0.4$ )	144
Fig 5.6.	Plot of standard molar enthalpy of formation of $\text{Gd}_{2-2x}\text{Ca}_x\text{Zr}_x\text{Ti}_2\text{O}_7$ ( $0.0 \leq x \leq 0.4$ )	145
Fig 5.7.	Structure of $\text{GdO}_8$ and $\text{TiO}_6$ polyhedra in doped and undoped $\text{Gd}_2\text{Ti}_2\text{O}_7$	150
Fig 6.1.	Powder X-ray diffraction patterns of $\text{Gd}_2\text{Zr}_2\text{O}_7$ sintered at 1373 K, 1473 K, 1573 K and 1673 K	160
Fig 6.2.	Powder X-ray diffraction patterns $\text{Gd}_2\text{Zr}_2\text{O}_7$ sintered at 1373 K, 1473 K, 1573 K and 1673 K in the $2\theta$ range of $10-30^\circ$ , showing superstructure peaks observed at $2\theta \sim 14.5^\circ$ and $28.2^\circ$	161
Fig 6.3.	Rietveld refinement plot of $\text{Gd}_2\text{Zr}_2\text{O}_7$ sintered at 1373 K, 1473 K, 1573 K and 1673 K. Figure a, b: Top and bottom vertical lines indicate Bragg positions for defect fluorite and pyrochlore type phase respectively. Figure c, d: top and bottom vertical lines indicate Bragg positions for pyrochlore and defect fluorite phase respectively	162
Fig 6.4.	Raman spectra of $\text{Gd}_2\text{Zr}_2\text{O}_7$ sintered at 1373 K, 1473 K, 1573 K and 1673 K respectively	165
Fig 6.5.	Normalized heat flow curves for $\text{Gd}_2\text{Zr}_2\text{O}_7$ sintered at 1373 K, 1473 K, 1573 K and 1673 K respectively	169
Fig 6.6.	Powder XRD patterns of $\text{Gd}_{2-x}\text{U}_x\text{Zr}_2\text{O}_{7+\delta}$ ( $0.0 \leq x \leq 0.25$ ) samples calcined at 873 K for 1 h	173
Fig 6.7.	Representative Rietveld refinement plots for the nominal compositions in the series $\text{Gd}_{2-x}\text{U}_x\text{Zr}_2\text{O}_{7+\delta}$ ( $0.0 \leq x \leq 0.25$ ) heated in reducing atmosphere	174
Fig 6.8.	Powder XRD patterns of $\text{Gd}_{2-x}\text{U}_x\text{Zr}_2\text{O}_{7+\delta}$ ( $0.0 \leq x \leq 0.25$ ) samples annealed in Ar : $\text{H}_2$ (92:8) at 1373 K for 8 h. All the compositions were found to crystallize in defect fluorite structure	176

Fig 6.9.	Powder XRD patterns of $\text{Gd}_{2-x}\text{U}_x\text{Zr}_2\text{O}_{7+\delta}$ ( $0.0 \leq x \leq 0.25$ ) after heat treatment in air at 1373 K for 8 h. Asterisks indicate unidentified minor secondary phase	177
Fig 6.10.	Variation of unit cell parameter upon substitution of U at Gd site in $\text{Gd}_{2-x}\text{U}_x\text{Zr}_2\text{O}_{7+\delta}$ (reduced and oxidized samples)	178
Fig 6.11a.	High temperature-XRD pattern of $\text{Gd}_{1.95}\text{U}_{0.05}\text{Zr}_2\text{O}_{7+\delta}$ . Solid line has been used to show the shift in peak position with variation in temperature	179
Fig 6.11b.	High temperature-XRD pattern of $\text{Gd}_{1.75}\text{U}_{0.25}\text{Zr}_2\text{O}_{7+\delta}$ . Asterisk indicated the segregation of secondary phase	179
Fig 6.12.	Variation of unit cell parameters of nominal compositions $\text{Gd}_{2-x}\text{U}_x\text{Zr}_2\text{O}_{7+\delta}$ ( $0.00 \leq x \leq 0.25$ ) with temperature	181
Fig 6.13.	X-ray photoelectron spectra of uranium ( $4f_{7/2}$ ) of reduced and oxidized sample having nominal composition $\text{Gd}_{1.85}\text{U}_{0.15}\text{Zr}_2\text{O}_{7+\delta}$	182
Fig 6.14.	BSE images of (a) $x=0.15$ (c) $x=0.20$ (e) $x=0.25$ and SE images of (b) $x=0.15$ (d) $x=0.20$ (f) $x=0.25$ nominal compositions heated in static air respectively	183
Fig 6.15.	Representative heat flow signals for dissolution of $\text{Gd}_{2-x}\text{U}_x\text{Zr}_2\text{O}_{7+\delta}$ ( $0.0 \leq x \leq 0.15$ ) nominal compositions (a) reduced and (b) oxidized compounds (normalized to 10 mg each) in liquid $\text{Na}_2\text{O} + \text{MoO}_3$ (3:4 molar ratio) dropped from room temperature to liquid solvent 986 K	185
Fig 6.16.	The enthalpy of formation of $\text{Gd}_{2-x}\text{U}_x\text{Zr}_2\text{O}_{7+\delta}$ (both oxidized and reduced samples)	190
Fig 6.17.	Powder XRD patterns of $\text{Gd}_{2-x}\text{Ce}_x\text{Zr}_{1.9}\text{U}_{0.1}\text{O}_{7+\delta}$ ( $0.0 \leq x \leq 0.50$ ) samples calcined at 873 K for 1 h	192
Fig 6.18.	Powder XRD patterns of $\text{Gd}_{2-x}\text{Ce}_x\text{Zr}_{1.9}\text{U}_{0.1}\text{O}_{7+\delta}$ ( $0.0 \leq x \leq 0.50$ ) samples annealed at 1373 K for 8 h in air	192
Fig 6.19.	Powder XRD patterns of $\text{Gd}_{1.8}\text{Ce}_{0.2}\text{Zr}_{1.9}\text{U}_{0.1}\text{O}_{7+\delta}$ ( $x=0.20$ ) samples annealed at 1373 K for 8 h in air	194
Fig 6.20.	X-ray photoelectron spectra of cerium ( $3d_{5/2}$ ) of sample having nominal composition $\text{Gd}_{1.8}\text{Ce}_{0.2}\text{Zr}_{1.9}\text{U}_{0.1}\text{O}_{7+\delta}$	195
Fig 6.21.	X-ray photoelectron spectra of uranium ( $4f_{7/2}$ ) of sample having nominal composition $\text{Gd}_{1.8}\text{Ce}_{0.2}\text{Zr}_{1.9}\text{U}_{0.1}\text{O}_{7+\delta}$	196
Fig 6.22.	Normalized heat flow signals for dissolution of $\text{Gd}_{2-x}\text{Ce}_x\text{Zr}_{1.9}\text{U}_{0.1}\text{O}_{7+\delta}$ ( $0.0 \leq x \leq 0.5$ ) nominal compositions (normalized to 10 mg each) in liquid $\text{Na}_2\text{O} + \text{MoO}_3$ (3:4 molar ratio) dropped from room temperature to liquid solvent 986 K	197
Fig 6.23.	Variation of standard molar enthalpy of formation of $\text{Gd}_{2-x}\text{Ce}_x\text{Zr}_{1.9}\text{U}_{0.1}\text{O}_{7+\delta}$ ( $0.0 \leq x \leq 0.5$ )	199
Fig 7.1.	Powder XRD patterns of the prepared glass formulations. “*” marks the peaks corresponding to the crystalline phase $\text{Gd}_{4.67}(\text{SiO}_4)_3\text{O}$	209
Fig 7.2.	DTA curves of the prepared glass formulations	210
Fig 7.3.	BSE images of glass formulation Gd-5.0 (top) and Gd-6.0 (bottom). Segregated phases are clearly observed in Gd-6.0	211



## LIST OF TABLES

	Description	Page no.
Table 1.1.	Classification of nuclear waste in accordance with radioactivity	11
Table 1.2.	List of fission products and transuranic elements present in HLW	13
Table 1.3.	General comparison between glass and ceramic matrices for nuclear HLW immobilization	21
Table 1.4.	Table showing the similarity in properties between $\text{CeO}_2$ and $\text{PuO}_2$	28
Table 3.1.	Refined structural parameters of calzirtite at ambient conditions	69
Table 3.2.	The observed bond lengths ( $\text{\AA}$ ) of calzirtite at ambient temperature	71
Table 3.3.	Refined structural parameters of calzirtite at 1473 K	72
Table 3.4.	The observed inter-atomic distances ( $\text{\AA}$ ) of calzirtite at 1473 K	74
Table 3.5.	Refined structural parameters of zirconolite at ambient conditions	76
Table 3.6.	The molar enthalpies of dissolution of $\text{Ca}_2\text{Zr}_5\text{Ti}_2\text{O}_{16}(\text{s})$ (Calzirtite), $\text{CaZrTi}_2\text{O}_7(\text{s})$ , $\text{CaO}(\text{s})$ , $\text{ZrO}_2(\text{s})$ and $\text{TiO}_2(\text{s})$ in 6g of $\text{Na}_2\text{O} + \text{MoO}_3$ 3:4 molar ratio at $T = 986 \text{ K}$	85
Table 3.7.	Thermo chemical cycles for derivation of standard molar enthalpies of formation of $\text{Ca}_2\text{Zr}_5\text{Ti}_2\text{O}_{16}(\text{s}, 298\text{K})$ , Calzirtite) and $\text{CaZrTi}_2\text{O}_7(\text{s}, 298\text{K})$ , Zirconolite) $\text{MO}_x(\text{sln}) = \text{dilute solution of species } \text{MO}_x \text{ in 6g liquid } \text{Na}_2\text{O} + \text{MoO}_3 \text{ 3:4 molar solvent maintained at } 986 \text{ K}$	86
Table 3.8.	Enthalpy increment ( $H_T - H_{298}$ ) values for $\text{Ca}_2\text{Zr}_5\text{Ti}_2\text{O}_{16}(\text{s})$ and $\text{CaZrTi}_2\text{O}_7(\text{s})$	87
Table 3.9.	Thermodynamic data for calzirtite ( $\text{Ca}_2\text{Zr}_5\text{Ti}_2\text{O}_{16}, \text{s}$ )	92
Table 3.10.	Thermodynamic data for zirconolite ( $\text{CaZrTi}_2\text{O}_7, \text{s}$ )	93
Table 4.1.	Refined structural parameters of zirconolite $\text{CaZrTi}_2\text{O}_7$ ( $x=0.00$ )	103
Table 4.2.	Refined structural parameters of $\text{Nd}_2\text{Ti}_2\text{O}_7$ ( $x=1.00$ ) for RE= $\text{Nd}^{3+}$ series	105
Table 4.3.	Refined structural parameters of $\text{Sm}_2\text{Ti}_2\text{O}_7$ ( $x=1.00$ ) for RE= $\text{Sm}^{3+}$ series	107
Table 4.4.	Refined structural parameters of $\text{Y}_2\text{Ti}_2\text{O}_7$ ( $x=1.00$ ) for RE= $\text{Y}^{3+}$ series	107
Table 4.5.	Summary of phases identified in $\text{Ca}_{1-x}\text{Zr}_{1-x}\text{Nd}_{2x}\text{Ti}_2\text{O}_7$ and their unit cell parameters	113
Table 4.6.	Summary of phases identified in $\text{Ca}_{1-x}\text{Zr}_{1-x}\text{Sm}_{2x}\text{Ti}_2\text{O}_7$ and their unit cell parameters	114
Table 4.7.	Summary of phases identified in $\text{Ca}_{1-x}\text{Zr}_{1-x}\text{Y}_{2x}\text{Ti}_2\text{O}_7$ and their unit cell parameters	115
Table 4.8.	Phase and compositions (at %) observed at various nominal bulk compositions for $\text{Nd}^{3+}$ series. (balance oxygen or mention as "y")	126
Table 4.9.	Phase and compositions (at %) observed at various representative compositions for $\text{Sm}^{3+}$ series	129

Table 4.10.	Atomic (metal) ratio as estimated from point mode EDX analyses of some representative compositions <sup>1</sup>	130
Table 5.1.	Ionic radii of the constituent ions at different coordination number	139
Table 5.2.	Refinement parameters of the series $\text{Gd}_{2-2x}\text{Ca}_x\text{Zr}_x\text{Ti}_2\text{O}_7$ ( $0.0 \leq x \leq 0.4$ )	141
Table 5.3.	Heat of Dissolution of $\text{Gd}_{2-2x}\text{Ca}_x\text{Zr}_x\text{Ti}_2\text{O}_7$ ( $0.0 \leq x \leq 0.4$ ) and their component oxides	147
Table 5.4.	Thermochemical cycles for enthalpy of formation of $\text{Gd}_{2-2x}\text{Ca}_x\text{Zr}_x\text{Ti}_2\text{O}_7$ ( $0.0 \leq x \leq 0.4$ )	148
Table 6.1.	Refined phase fraction and unit cell parameters of $\text{Gd}_2\text{Zr}_2\text{O}_7$ sintered at 1373 K, 1473 K, 1573 K and 1673 K	164
Table 6.2.	Table depicting average Zr-O bond length of $\text{Gd}_2\text{Zr}_2\text{O}_7$ sintered at 1373 K, 1473 K, 1573 K and 1673 K	167
Table 6.3.	Table depicting average Gd-O bond length of $\text{Gd}_2\text{Zr}_2\text{O}_7$ sintered at 1373 K, 1473 K, 1573 K and 1673 K. [Defect fluorite model]	168
Table 6.4.	Table depicting average Gd-O bond length of $\text{Gd}_2\text{Zr}_2\text{O}_7$ sintered at 1373 K, 1473 K, 1573 K and 1673 K respectively. [Pyrochlore model]	168
Table 6.5.	Heat of Dissolution of $\text{Gd}_2\text{Zr}_2\text{O}_7$ sintered at 1373 K, 1473 K, 1573 K and 1673 K and their component oxides	170
Table 6.6.	Thermochemical cycles for enthalpy of formation of $\text{Gd}_2\text{Zr}_2\text{O}_7$ sintered at 1373 K, 1473 K, 1573 K and 1673 K	171
Table 6.7	Rietveld refined parameters of $\text{Gd}_{2-x}\text{U}_x\text{Zr}_2\text{O}_{7+\delta}$ ( $0.0 \leq x \leq 0.25$ ) compositions after annealing at Ar :H <sub>2</sub> (92:8) at 1373 K for 8h	175
Table 6.8.	Heat of dissolution of $\text{Gd}_{2-x}\text{U}_x\text{Zr}_2\text{O}_{7+\delta}$ (oxidized/reduced) and their component oxides	186
Table 6.9.	Thermochemical cycle for enthalpy of formation of $\text{Gd}_{2-x}\text{U}_x\text{Zr}_2\text{O}_{7+\delta}$ (oxidized/reduced)	188
Table 6.10.	Rietveld refined parameters of $\text{Gd}_{2-x}\text{Ce}_x\text{Zr}_{1.9}\text{U}_{0.1}\text{O}_{7+\delta}$ ( $0.0 \leq x \leq 0.50$ ) compositions after annealing at 1373 K for 8h in air.	193
Table 6.11.	Heat of dissolution of $\text{Gd}_{2-x}\text{Ce}_x\text{Zr}_{1.9}\text{U}_{0.1}\text{O}_{7+\delta}$ ( $0.0 \leq x \leq 0.5$ ) and their component oxides	198
Table 6.12.	Thermochemical cycles for enthalpy of formation of $\text{Gd}_{2-x}\text{Ce}_x\text{Zr}_{1.9}\text{U}_{0.1}\text{O}_{7+\delta}$ ( $0.0 \leq x \leq 0.5$ )	200
Table 7.1a.	Compositions in mol% of synthesized borosilicate glass	207
Table 7.1b.	Compositions in wt% of synthesized borosilicate glass	207
Table 7.2.	Table showing the lifetime with the mode of decay in the prepared glass formulations	213

**Chapter 8**

**Summary**

**and**

**future scope**

## 8.1. SUMMARY

The aim of the thesis “Preparation and structural investigations on zirconolite and pyrochlore based ceramics: Potential materials for nuclear back end application” is the development of preparation methodology for zirconolite and pyrochlore based ceramics and to understand their potential for immobilization of actinides present in nuclear high level waste. Both zirconolite and pyrochlore phases are being important constituents of SYNROC, the research work in this thesis has been focused on these two phases.

, From the point of view of nuclear waste immobilization, zirconolite ( $\text{CaZrTi}_2\text{O}_7$ ) is a very important mineral analogous phase of the  $\text{CaO-ZrO}_2\text{-TiO}_2$  system. However, another mineral analogous phase with a fluorite related structural arrangement, termed as calzirtite ( $\text{Ca}_2\text{Zr}_5\text{Ti}_2\text{O}_{16}$ ) is also reported in  $\text{CaO-ZrO}_2\text{-TiO}_2$  system. Calzirtite phases are found to coexist with zirconolite in metasomatic calcite-forsterite-magnetite rocks and their nominal composition exhibits a variation in the Zr and Ti content in the lattice. Hence a detailed structural characterization and thermodynamic property evaluation of these two lattices are carried out. Structural studies carried out by combination of room temperature and high temperature X-ray diffraction studies, and revealed that only a feeble amount of Ti and Zr atoms can get exchanged within calzirtite lattice whereas the zirconolite lattice is more amenable for compositional variation. Moreover, low thermal expansion coefficient of calzirtite lattice as compared to zirconolite was observed which also justified to the closed packed nature of calzirtite lattice. These factors clearly indicated that zirconolite can act as a better nuclear waste immobilization matrix as compared to calzirtite. The open structure of zirconolite can easily accommodate cations of various charge and size. Thermodynamic studies carried out on these two lattices revealed that at  $\sim 1775$  K, calzirtite lattice can decompose to yield zirconolite, calcium zirconate and zirconium dioxide respectively.

As the above-mentioned findings ruled out the possibility of calzirtite phase to use as potential nuclear waste immobilization matrix, a detailed structural and micro-structural investigations on zirconolite-pyrochlore ( $\text{CaZrTi}_2\text{O}_7\text{-RE}_2\text{Ti}_2\text{O}_7$ , where RE= rare earth elements) based multiphasic systems were carried out to understand the mutual phase compatibility. Detailed investigations with rare earth based systems being quite tedious, due to their low availability, selected trivalent ions of different ionic radii were only used to carry out the phase evolution study. Extensive structural and microstructural studies carried out in the  $\text{CaZrTi}_2\text{O}_7$  (zirconolite)- $\text{RE}_2\text{Ti}_2\text{O}_7$  (pyrochlore) (RE=  $\text{Nd}^{3+}$ ,  $\text{Sm}^{3+}$  and  $\text{Y}^{3+}$ ) revealed the system to consists of four broad phase fields namely, (i) monoclinic zirconolite (comprising of 2M and 4M), (ii) cubic perovskite (not for  $\text{Y}^{3+}$  series), (iii) cubic pyrochlore, and (iv) monoclinic  $\text{Nd}_2\text{Ti}_2\text{O}_7$  types (for  $\text{Nd}^{3+}$  series). It could be concluded that the phase boundary of cubic perovskite increases with increasing ionic radii of  $\text{RE}^{3+}$  ion. On the contrary, it was observed that solubility of trivalent rare-earth ions in zirconolite (both 2M and 4M) lattice increases with decreasing ionic radii of  $\text{RE}^{3+}$  ion. In all the three studied systems, existence of a single phasic cubic pyrochlore phase was observed. This pyrochlore phase has the ability to incorporate a large amount of heterovalent cations without any major alteration in the crystal structure which is considered as very promising results pertaining to their usage as waste immobilization matrices.

In view of the above results, experimental and theoretical studies were carried out on  $\text{Gd}_{2-2x}\text{Ca}_x\text{Zr}_x\text{Ti}_2\text{O}_7$  ( $0.0 \leq x \leq 0.4$ ) pyrochlore system. to understand the structural perturbations induced by incorporation of one divalent ion ( $\text{Ca}^{2+}$ ) and one tetravalent cation ( $\text{Zr}^{4+}$ ) in place of two trivalent cations ( $\text{Gd}^{3+}$ ) of the titanate pyrochlore lattice. It was clearly observed that these type of titanate based pyrochlore phases are able to accommodate about 40 mol% of diverse cations without major alteration in their crystal structure. Theoretical studies carried out revealed that a small amount of disorder arises around the Gd site due to

incorporation of Ca and Zr which results in decreasing intensity of super-structure peaks with increasing incorporation of diverse cations. However, these incorporated ions are not able to destroy the cubic pyrochlore framework. Thermodynamic stability studies carried out indicates lowering of relative stability of the lattice by only about 3.5% even after incorporation of 40 mol % of heteroatom. These studies indicated that titanate pyrochlore lattices can be potential lattices in terms of their usage as waste immobilization matrices.

On the other hand,  $\text{Gd}_2\text{Zr}_2\text{O}_7$  is considered the most promising zirconate based pyrochlores for immobilization of minor actinides present in nuclear high level waste. However, the optimum processing conditions and incorporation of actinides were not substantially present in literature.  $\text{Gd}_2\text{Zr}_2\text{O}_7$  synthesized by gel-combustion technique was annealed for 8 h at 1373 K, 1473 K, 1573 K and 1673 K respectively. Powder X-ray diffraction studies revealed that transformation from defect fluorite to ordered pyrochlore structure takes place in this temperature range under the studied conditions. Phase pure defect fluorite and ordered pyrochlore structures were found to be stabilized at 1373 K and 1673 K, respectively, whereas mixed products were observed at intermediate temperatures. Thermodynamic stability studies carried out on all the compositions revealed that stability decrease from 1373 K to 1573 K before increasing again at 1673 K. It clearly indicated that  $\text{Gd}_2\text{Zr}_2\text{O}_7$  matrix needs processing at either 1373 K or 1673 K for better phase characteristics. This study helped us in optimization of process conditions for preparation of uranium loaded  $\text{Gd}_2\text{Zr}_2\text{O}_7$ , i.e.  $\text{Gd}_{2-x}\text{U}_x\text{Zr}_2\text{O}_{7+\delta}$  ( $0.0 \leq x \leq 0.25$ ). Multiple oxidation states of uranium posed a question regarding their immobilization in reduced or oxidized form in  $\text{Gd}_2\text{Zr}_2\text{O}_7$  matrix. As a result, uranium incorporation studies were carried out both in air and argon-hydrogen atmosphere at 1373K for 8 h (optimized condition from earlier study). Substantial amount of uranium ( $x=0.25$ ) could be incorporated in  $\text{Gd}_2\text{Zr}_2\text{O}_7$  lattice in reducing environment as compared to air heated samples ( $x=0.15$ ). However, higher loading samples in reducing atmosphere reverted to minor phase

precipitation during heating in ambient conditions. Thermodynamic stability studies carried out on both reducing and air heated samples revealed that immobilization of uranium in reduced state does not alter the stability of uranium incorporated  $\text{Gd}_2\text{Zr}_2\text{O}_7$  whereas the stability for samples heated in air increased significantly in the studied range of composition. These studies revealed that it is always better to immobilize uranium in +6 state in  $\text{Gd}_2\text{Zr}_2\text{O}_7$  lattice. This study was extended further towards the co-incorporation of uranium and cerium in  $\text{Gd}_2\text{Zr}_2\text{O}_7$  matrix. Keeping this in mind, a series with nominal compositions  $\text{Gd}_{2-x}\text{Ce}_x\text{Zr}_{1.9}\text{U}_{0.1}\text{O}_{7+\delta}$  ( $0.0 \leq x \leq 0.5$ ) was prepared. Similar to the earlier studies, these compounds were also found to be stabilized in defect fluorite structure. Thermodynamic stability studies clearly indicated that incorporation of U and Ce under ambient conditions i.e. as  $\text{U}^{6+}$  and  $\text{Ce}^{4+}$  increases the stability of ceramic matrices.

Apart from these studies on ceramic matrices intended for immobilization of nuclear HLW and minor actinides, studies on the solubility of gadolinium in barium borosilicate glass matrix were also carried out. The solubility of gadolinium was found to be about 5 mol% contrary to that reported in literature (1.5 mol %). A rational and systematic study involving variation in composition of base glass constituents and processing conditions could increase the solubility limit. Moreover, the formulation was found to immobilize gadolinium at much lower processing temperature of  $950^\circ\text{C}$  which results in immobilization under economic conditions.

## 8.2. FUTURE SCOPE

In spite of the systematic and directed approach of the thesis regarding structural and thermodynamic aspects of ceramic matrices intended for immobilization of minor actinides, certain studies are also required in future to affirm use of these systems for immobilization of nuclear HLW viz.

Incorporation of uranium and minor actinide surrogates in multiphasic matrices and understand further structural deviation of the phases from constituent phases of SYNROC as observed in this thesis.

Processing of ceramic matrices is generally done under high pressure for densification of waste ensemble. Hence, moderately high pressure (~10 MPa) studies of these incorporated matrices are required for validation.

Alpha and alpha recoils from nuclear HLW can damage crystal structure of ceramic compounds. Hence, ion irradiation studies with low energy ion beams are needed to be carried out in future.

In addition to this, leachability of uranium and other actinides from ceramic matrices are needed to be carried out under accelerated condition to study the long term effects. This study also needs to be carried out for the glass system which is presented in this thesis before its validation as waste immobilization matrix.



## **SUMMARY**

As an efficient alternative to fossil fuels and minimum greenhouse emission, nuclear energy comes as a consented source. Worldwide, including India, Nuclear energy plays and is expected to play a pivotal role in the energy sector. This is being achieved by varieties of nuclear reactors. In India, currently number of nuclear reactors are serving as power source. However, immobilization of nuclear high level waste in geological repositories is an important field of ongoing research in nuclear energy industry. Ceramic matrices viz. titanates, zirconates, etc. are considered as potential matrices for immobilization of nuclear waste in repositories. In view of this, structural and thermodynamic stability studies of titanates and zirconates with zirconolite and pyrochlore structures have been investigated. Detailed structural and microstructural studies were carried out on varieties of compositions to unearth their potential use as waste matrices. A single phasic pyrochlore domain was elucidated which can incorporate up to 40 mol % of diverse ions inside the structure without undergoing phase separation. The effects of incorporation of diverse ions in to the pyrochlore structure was ascertained by detailed structural and thermodynamic stability studies (both theoretical and experimental). In addition, thermodynamic stabilities of uranium and uranium-cerium incorporated zirconate pyrochlore were also studied and it was concluded that both uranium and cerium need to be immobilized in higher oxidation state within ceramic lattice. Also, a novel glass formulation for incorporation of excess gadolinium containing waste was also designed as part of this thesis.

# **Chapter-1**

## **Introduction**

## 1.1. INTRODUCTION

Increasing consumption of power for better life choices offered by advancements in science and technology has adversely contributed a lot to the reserves of non-renewable fossil fuels such as coal, petroleum, etc. and increasing global warming. Hence, all over the world research attentions are focussing on alternate energy sources such as hydro, solar, nuclear and wind energy for power generation. Power production from nuclear reaction is considered to be one of the best methods as large amount of power can be obtained by burning a small amount of fuel inside a nuclear reactor. Moreover, zero emission of greenhouse gases also makes nuclear power a favourite choice to prevent global warming and eventually preventing drastic climate changes. A complete nuclear fuel cycle (NFC) in a nuclear energy program involves mining of uranium ores, processing of ore to get uranium oxide, suitable enrichment of uranium, fuel fabrication, transportation, installation of fuel inside nuclear power reactors, production of electricity from a controlled nuclear fission process and ultimately reprocessing of spent nuclear fuel to separate out any un-burnt uranium and plutonium. One of the toughest challenges of this cycle is the safe disposal of spent nuclear waste <sup>1</sup>. Safe nuclear waste disposal is a protocol bound multistep process which encompasses the basic aspects of protection of human health for the present as well as future generations, and protection of environment from any potential radiation hazards <sup>1</sup>. In spite of the generation of nuclear waste in almost all the steps of NFC, the prime attention is being paid to the disposal of highly radioactive nuclear High Level Waste (HLW) generated from reprocessing of spent nuclear fuel as they consist of long-lived unprocessed uranium, plutonium along with minor actinides such as neptunium, americium, etc., and they can have radioactive impacts for prolonged time period.

## 1.2. NUCLEAR ENERGY

The rate of increasing global electricity demand is almost double of that of energy production, and this mismatch is expected to escalate further resulting in a wide gap between the demand and supply <sup>2</sup>. In order to bridge the widening gap between requirement and supply, and to make energy sustainable, nuclear power needs to provide at least 25% of electrical energy by 2050. Presently, the nuclear power stations supply from a network of about 450 nuclear power reactors is around 11% of the world's energy demand. Electricity generated from nuclear power reactors is considered to be the second largest source of carbon free power generation after hydropower. In the last 50 years, the operation of nuclear power reactors has resulted in avoiding 60 Gt of CO<sub>2</sub> emissions globally, which is equivalent to five years' worth of CO<sub>2</sub> emissions from the electricity sector <sup>3</sup>. Thus, it can be envisaged that, nuclear power is inevitable to meet the demand of sustainable energy without altering of climatic conditions.

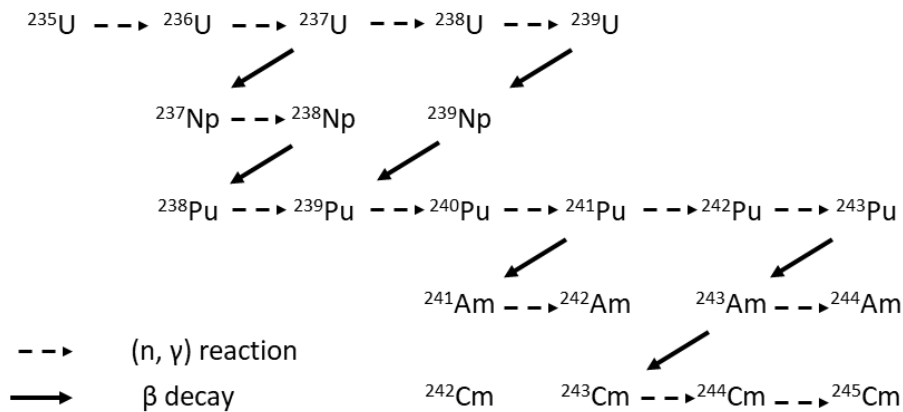
Nuclear energy is produced by fission of nucleus, usually a fissile nucleus of heavy elements. When a neutron is absorbed by a fissile nucleus viz. <sup>235</sup>U, <sup>233</sup>U and <sup>239</sup>Pu, it undergoes fission resulting two lighter nuclei and two or more neutrons which can carry out further fission. In a nuclear reactor, the extra neutrons are utilized for further fission by a controlled chain reaction <sup>4</sup>. A large amount of energy (~ 200 MeV) is released during each nuclear fission reaction. In addition to this energy, significant amounts of radioactive waste consisting of different fission products as well as long-lived transuranic elements such as <sup>237</sup>Np, <sup>241</sup>Am, <sup>243</sup>Am and <sup>245</sup>Cm are generated as activation products of (n, γ) reaction of uranium fuelled power reactors, and various nuclear reactions that lead to these long-lived transuranic elements are depicted in **Figure 1.1**.

Practically, nuclear energy is obtained by fission (burning) of uranium or other fissile nuclides inside a nuclear power reactor. The major components of nuclear fission reactors are (i) fissile and fertile radionuclides or fuel, (ii) structural materials, (iii) coolant, (iv) moderator,

reflector and blanket materials and (v) reactor control, shielding and safety system materials <sup>5</sup>.

A brief description of different types of nuclear power reactors, depending upon the nature of fuel and moderator, is given below <sup>5</sup>.

**1.2.1. Boiling Water Reactor (BWR):** This type of nuclear reactor uses 1.5 to 3% enriched uranium oxide pellets as fuel and zircaloy as cladding material. The reactor is housed inside a stainless steel containment. Here, boiling water pressurized to 70 atm to keep it liquid up to 285°C, is used as coolant as well as moderator. Good efficiency of thermal energy to electrical energy conversion is achieved in this type of reactors. However, a major drawback of this kind of reactor is radioactivity in turbine system which arises due to direct contact of radioactive water and turbine. Hence safe disposal of turbine system is required.



**Figure 1.1. Schematic diagram of the generation of transuranic radionuclides in a uranium fuelled nuclear power reactor <sup>5</sup>.**

**1.2.2. Pressurized Water Reactor (PWR):** These reactors are quite similar to BWR as far as fuel and cladding materials are concerned. The major difference is that water is pressurized at 145 atm pressure and hence it remains in liquid form even up to 310°C. As a consequence, the reactor vessels and containment materials are required to have higher mechanical strength than BWR. Here, hot and pressurized water is transported to a heat exchanger to produce steam

and the water is again sent back to the reactor assembly. Electricity is generated in PWR by moving the turbine with the generated steam. PWR's are the most prevalent among all types of nuclear reactors used worldwide.

**1.2.3. Pressurized Heavy Water Reactor (PHWR):** This reactor uses natural uranium as fuel and zircaloy as cladding material. Since heavy water ( $D_2O$ ) has low neutron absorption cross section than natural water,  $D_2O$  is used as moderator in these reactors. The fuel assembly is contained inside pressure tubes which is contained inside a large vessel termed as calandria. Heavy water circulates through the pressure tubes at 85 atm pressure and  $\sim 300^\circ C$  temperature. The heavy water is transported to heat exchanger and hence contamination of turbine does not occur in these types of reactors. These are the most prevalent types of reactors in Indian nuclear energy scenario.

**1.2.4. Gas Cooled Reactor (GCR):** In this type of reactors named as Magnox, natural uranium metal is used as fuel and magnesium is used as cladding material. Carbon dioxide is used as coolant whereas graphite is used as moderator. The coolant is kept at 20 atm pressure and  $\sim 400^\circ C$  temperature. However, advanced gas cooled reactors are also there where uranium oxide pellets kept inside stainless steel clads are used. Same material,  $CO_2$ , is used as both coolant and moderator and are kept circulating inside the reactor at 40 atm pressure and  $650^\circ C$  temperature.

**1.2.5. Vodo-Vodyanoi Energetichesky Reactor (VVER):** This is another type of PWR developed by former Soviet Union. VVER-1000 uses 2.4-4% enriched uranium oxide pellets as nuclear fuel kept inside stainless steel clads. The coolant as well as moderator is water which is circulated at 15 MPa pressure and  $\sim 250-300^\circ C$  temperature. The entire reactor assembly is placed inside a strong stainless steel vessel equipped with spray steam suppression systems. VVER designs are expounded to incorporate automatic control with passive safety and containment systems.

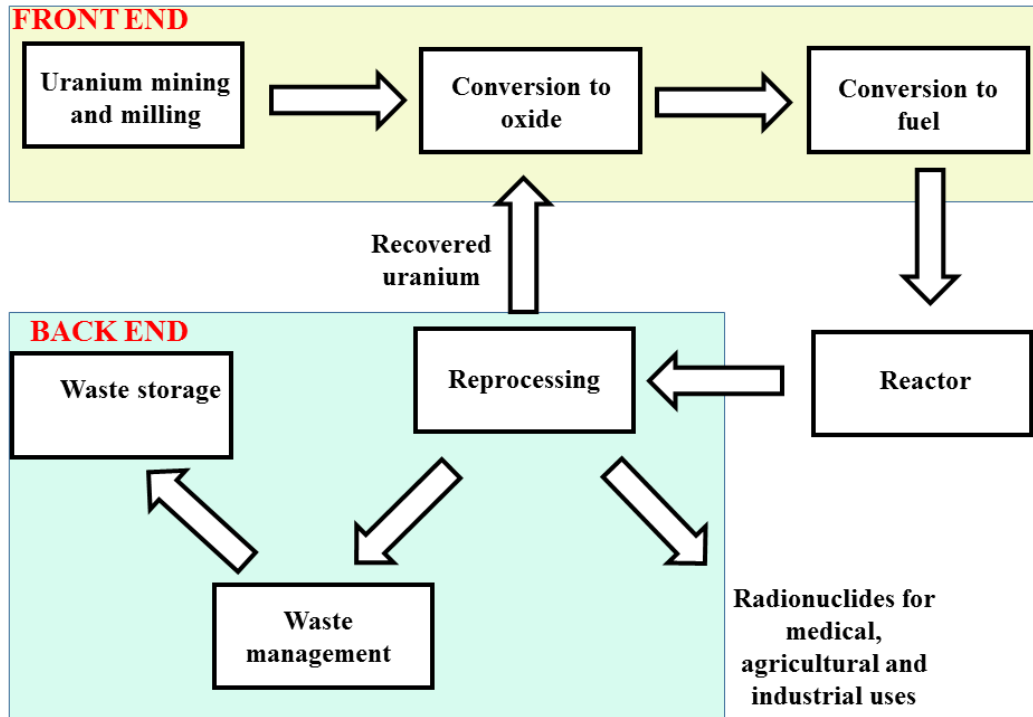
All these types of reactors described above use thermal neutrons for carrying out chain reaction. However, there are other types of reactors, termed as fast reactors which use fast neutrons for propagation of chain reaction and hence thermalization of neutron is not required. Thus, these types of reactors are devoid of moderators. A classic example in this regard is:

**1.2.6. Liquid Metal Cooled Fast Breeder Reactor (LMCFBR / FBR):** These types of reactors use mixed uranium and plutonium oxide or Mixed Oxide Fuel (MOX) as fuel. Stainless steel tubes are used as cladding materials and the fuel assembly is cooled by liquid sodium metal circulating at 3 atm pressure and  $\sim 650^{\circ}\text{C}$  temperature. The reactor core is surrounded by blankets containing fertile radionuclides such that they can be converted to fissile materials (breeding) for further use as fuel. Thus, these types of reactors are termed as breeder reactor. Plutonium or uranium generated respectively from uranium and thorium of blankets can be used further as reactor fuel in next generation of reactors. These types of reactors are very important in the context of Indian nuclear energy programme.

### **1.3. INDIAN NUCLEAR ENERGY PROGRAMME**

Limited reserves of uranium ore in India coupled with a very rich resource of thorium ore along south west coastal area has directed India to adopt a three-stage nuclear energy programme based on closed fuel cycle technologies <sup>6</sup>. The term “closed fuel cycle” refers to separation of unburnt  $^{235}\text{U}$  and  $^{239}\text{Pu}$  by chemicals means from spent fuel for further utilization as nuclear fuel leaving behind the radioactive fission products. Depending upon the half-lives and activity, the leftover radioactive fission products are categorically separated and then appropriately disposed in stable nuclear waste immobilization matrices following the principle of minimum environmental disturbance. On the other hand, “open or once-through fuel cycle” does not reprocess the spent fuel to separate any radionuclides and directly immobilize the waste in stable matrices. The closed fuel has some distinct advantages over the open fuel cycle viz.

recovery of fissile and fertile radionuclides for recycling as fuel, isolation of valuable isotopes for alternate uses, drastic reduction of radiotoxicity burden during nuclear waste immobilization, etc. A schematic diagram of closed nuclear fuel cycle practiced by India is shown in **Figure 1.2** <sup>6</sup>.

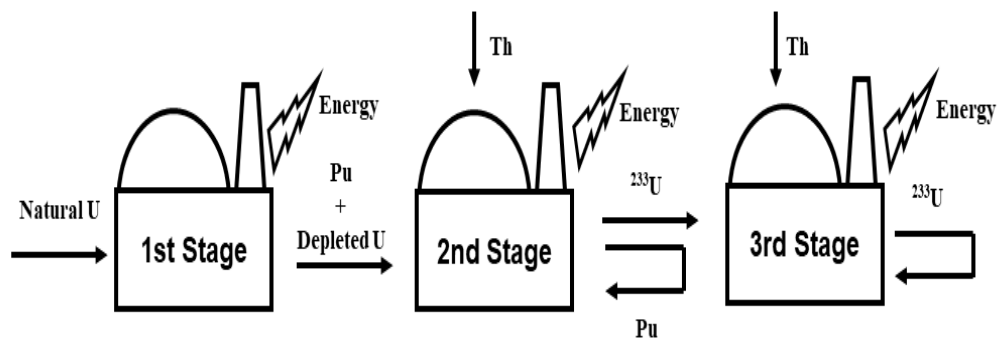


**Figure 1.2:** A schematic diagram of closed nuclear fuel cycle practiced by India <sup>5,6</sup>.

Based upon the concept of closed nuclear fuel cycle, India, under the visionary leadership of Dr. H. J. Bhabha, envisaged the three-stage nuclear power programme. The 1<sup>st</sup> stage of Indian nuclear power programme is focussed on natural uranium based fuels which are irradiated or burnt in PHWR's to generate electrical energy as well as for production of fissile  $^{239}\text{Pu}$  isotope. At present India operates 22 nuclear reactors at seven different sites with a total installed capacity of 6,780 MW to harness electrical energy <sup>7</sup>. Fissile  $^{239}\text{Pu}$  isotope produced from fertile  $^{238}\text{U}$  in the 1<sup>st</sup> stage is utilized as the fuel material for 2<sup>nd</sup> stage of Indian nuclear power programme. Attainment of criticality of 40MWth Fast Breeder Test Reactor (FBTR) constructed at Indira Gandhi Centre for Atomic Research (IGCAR), Kalpakkam is a



demonstration of the capability of India for running the 2<sup>nd</sup> stage. This test reactor uses mixed carbide of uranium and plutonium as nuclear fuel and has attained a burn up of 1,56,000 MW<sub>d</sub>/tonne. Keeping in line with this, a 500MWe capacity Prototype Fast Breeder Reactor (PFBR) is also being developed at Kalpakkam using MOX fuel. In parallel with this programme, R&D work is also being carried out for the development of 300 MWe Advanced Heavy Water Reactor (AHWR) based upon U-Pu and U-Th mixed oxide fuels. In addition, research works are also being pursued for the development of Molten Salt Breeder Reactor (MSBR) which will use mixed fluorides of U-Th as fuel. A schematic diagram of the three stage Indian nuclear power programme is depicted in **Figure 1.3**.



**Figure1.3: A schematic diagram of Indian three stage nuclear power programme.**

In addition to these above mentioned reactors, a number of coveted international programs viz. International Project on Innovative Nuclear Reactors and Fuel Cycles (INPRO)<sup>8</sup>, Generation IV International Forum (GIF), European Union led Michelangelo network (MICANET) have emerged to deliver medium and long term supports towards development of sustainable nuclear energy by covering methodology for innovative reactor systems and fuel cycles. The International Project on Innovative Nuclear Reactors and Fuel cycles (INPRO)<sup>8</sup> was set up in 2001 by International Atomic Energy Agency (IAEA) comprising of 22 member states including India <sup>9</sup>. Stress is being laid on to figure out novel and innovative approaches

to address concerns about economic competitiveness, nuclear safety, proliferation related issues and nuclear waste management.

#### **1.4. FUTURISTIC NUCLEAR FUELS IN INDIAN SCENARIO**

Generation of a large pile of plutonium is expected in future because of waste reprocessing or due to dismantling of nuclear warheads or decommissioning of nuclear reactors. However, this is not a concern for Indian nuclear industry because of its strategy of three-stage nuclear power programme. However, accumulation of several radiotoxic minor actinides having large half-lives from nuclear spent fuel leads to a concept of transmutation to stable nuclides. Inert matrix fuel (IMF) is one such concept which aims to decrease or dispose of unused plutonium as well as other minor actinides<sup>10,11</sup> while harnessing power. An Inert Matrix Fuel material need be rigorously selected based on thermophysical and neutronic properties, like good neutron economy, better thermo-physical properties like high thermal conductivity and low thermal expansion, absence of phase transition at high temperature, compatibility with cladding material, high radiation stability, etc. IMF material should consist of the matrix component, fissile component, fertile component and burnable poison. It needs to be mentioned here that most of the lanthanides act as burnable poisons for neutrons. IMF mostly stresses on single-phasic materials but composites like ceramic-metal composites (CERMET), ceramic-ceramic composites (CERCER), etc. can also be potential candidates provided they qualify the above-mentioned properties. In these context irradiation studies were carried out in  $\text{ZrO}_2\text{-UO}_2$  and  $\text{ZrO}_2\text{-PuO}_2$  since 1960s. A wide variety of ceramic host lattices were investigated by researchers worldwide for potential candidates for IMF<sup>12-16</sup>. However, it is worthwhile to mention that, actinide incorporated pyrochlore structure is also considered as one of the potential candidates for IMF applications<sup>17,18</sup>. In this context, it can be emphasized that a lot of data has been presented in this thesis using real as well as surrogate materials for actinides and minor actinides regarding their incorporation in ceramic host lattices.

## 1.5. NUCLEAR WASTE

Like India, several other countries such as France, Russia, Japan and China have also opted for closed fuel cycle while countries like USA, Canada, Finland, Sweden, etc. have chosen the path for direct disposal of spent nuclear fuel <sup>19</sup>. Since, the spent fuel of 1<sup>st</sup> stage of Indian nuclear programme generates fuel for its 2<sup>nd</sup> stage, the spent fuel is allowed to cool under specially designed pools to allow near complete decay of short-lived radionuclides. Typical spent fuel obtained from a PHWR consists of ~96% U, ~1% Pu, ~3% fission products like <sup>137</sup>Cs, <sup>90</sup>Sr, <sup>106</sup>Ru, <sup>99</sup>Tc etc, in addition to varieties of rare earths and minor actinides <sup>20</sup>.

It is well known that separation of fissile and long-lived isotopes like <sup>137</sup>Cs, <sup>90</sup>Sr, etc. not only reduces the waste volume but also drastically reduces the activity. Nuclear waste is termed as the spent fuel in liquid stage after removal of fissile and other useful radionuclides by PUREX process. In this process, chopped off spent nuclear fuel is dissolved in concentrated nitric acid (~3M). Fissile radio isotopes of uranium and plutonium are stripped by taking advantage of their multiple oxidation states using a mixture of 30% tributyl phosphate (TBP) in an organic medium like dodecane (kerosene). Uranium and plutonium in +6 oxidation state form a stable  $U/PuO_2(NO_3)_2 \cdot 2TBP$  complex and migrates from aqueous to organic phase. Uranous nitrate stabilized with hydrazine is added to the organic phase which reduces plutonium to +4 and transfer plutonium back to the aqueous phase while retaining uranium +6 in the organic TBP-dodecane phase.

Classification of nuclear waste is the most important parameter with the view of reprocessing and safe disposal. In general, nuclear wastes can be classified according to their physical state, chemical nature, radioactive dose, mechanical properties, etc. depending upon the origin of the waste. Classification of different types of nuclear waste according to their radioactivity is given in **Table-1.1**. In spite of the fact that solid, liquid and gaseous waste are generated in different process of NFC, the liquid nuclear waste requires much more attention because of their high

volume and mobility. Gaseous wastes are generated from dust particles escaping from conveyer belts during ore processing and fuel fabrication, crushing operations of ore, high temperature reprocessing processes generating fumes, etc. <sup>21</sup>. Solid nuclear waste arises from the insoluble part of the spent fuel, cladding material left in acidic medium, etc. However, highest volume of waste generated is in liquid form because of dissolution of the spent fuel. Depending upon the amount of radioactivity present in solution, liquid nuclear waste is classified into high level liquid nuclear waste (HLW), intermediate level liquid nuclear waste (ILW) and low level liquid nuclear waste (LLW).

**Table-1.1.: Classification of nuclear waste in accordance with radioactivity.**

Category	Solid Surface Dose (mGy/h)	Liquid Activity (Bq/m <sup>3</sup> )	Gaseous Activity Level (Bq/m <sup>3</sup> )
Exempt Waste <sup>4,22</sup>	<2	< 3.7×10 <sup>4</sup>	< 3.7
Low Level Waste <sup>4,22</sup>	2-20	3.7×10 <sup>4</sup> - 3.7×10 <sup>7</sup>	3.7 to 3.7×10 <sup>4</sup>
Intermediate Level Waste <sup>4</sup>	>20	3.7×10 <sup>7</sup> to 3.7×10 <sup>9</sup>	> 3.7×10 <sup>4</sup>
High Level Waste <sup>4,23</sup>	Alpha Bearing	3.7×10 <sup>9</sup> to 3.7×10 <sup>14</sup>	> 3.7×10 <sup>4</sup>

### 1.5.1. CONSTITUENTS OF LLW

LLW mostly contains short-lived radionuclides (mostly  $\beta$  and  $\gamma$  emitters) <sup>22</sup>. In addition to nuclear power reactors, they are also generated from hospitals, laboratories and industries having permission to use radioactive materials. In spite of the fact that LLW is much less hazardous compared to other types of nuclear wastes, it is concentrated by boiling and disposed of cautiously in designated sites. Solid LLW's are incinerated or compacted prior to their final burial in well designated landfills.

### 1.5.2. CONSTITUENTS OF ILW

ILW consists mostly of radionuclides with relatively longer half-lives (mostly  $\beta$  and  $\gamma$  emitters) than that of LLW constituents and very low concentration of  $\alpha$ -emitting radionuclides <sup>22</sup>. It comprises of about 7% of total waste volume and < 4% of radioactive content of the total waste. These types of wastes are solidified in concrete matrices and then disposed in proper facilities. It mainly consists of used resins, chemical sludge and components from nuclear reactors, reprocessing equipments as well as contaminated objects of weapon or reactor decommissioning.

### 1.5.3. CONSTITUENTS OF HLW

HLW mostly comprises of only 3% of total generated waste but carries radioactivity content of almost 95% of the total activity present in the waste <sup>23</sup>. High level waste gives off a large quantity of heat (due to decay of the stored radioactive elements) for several hundreds of years. The major components of HLW are <sup>4,23</sup>:

- a) Unrecovered uranium and plutonium
- b) Fission products such as <sup>90</sup>Sr, <sup>99</sup>Tc, <sup>106</sup>Ru, <sup>129</sup>I, <sup>135</sup>Cs, <sup>137</sup>Cs, <sup>144</sup>Ce, <sup>147</sup>Pm etc.
- c) Minor actinides such as <sup>237</sup>Np, <sup>241</sup>Am, <sup>243</sup>Am, <sup>242</sup>Cm, <sup>244</sup>Cm, <sup>245</sup>Cm, etc.
- d) Corrosion products of structural materials and containments (Fe, Ni, Cr, Mn etc.)
- e) Chemicals used in reprocessing plants such as nitric acid, sulphates, sodium nitrate, aluminium nitrate, chlorides, fluorides, traces of TBP and its degradation products
- f) Soluble neutron poisons such as Gadolinium, boron, cadmium, etc.

A host of diverse radionuclides present in HLW along with their respective half-lives and decay mode are given in **Table 1.2**.

**Table 1.2.: List of fission products and transuranic elements present in HLW.**

Radionuclide	Half-life	Decay mode	Radionuclide	Half-life	Decay mode
<b>Fission products</b>			<b>Fission products</b>		
<sup>99</sup> Tc	2.1 x 10 <sup>5</sup> y	β	<sup>152</sup> Eu	13.33 y	γ
<sup>90</sup> Sr	28.5 y	β	<sup>154</sup> Eu	8.8 y	γ
<sup>93</sup> Zr	1.5 x 10 <sup>6</sup> y	β	<sup>155</sup> Eu	4.96 y	β, γ
<sup>106</sup> Ru	368 d	γ	<b>Trans-uranic radionuclides</b>		
<sup>107</sup> Pb	6.5 x 10 <sup>6</sup> y	β	<sup>237</sup> Np	2.14 x 10 <sup>6</sup> y	α
<sup>125</sup> Sb	2.77 y	γ	<sup>238</sup> Pu	87.74 y	α
<sup>129</sup> I	1.57 x 10 <sup>7</sup> y	β, γ	<sup>239</sup> Pu	2.41 x 10 <sup>4</sup> y	α
<sup>134</sup> Cs	2.06 y	β, γ	<sup>240</sup> Pu	6.5 x 10 <sup>3</sup> y	α
<sup>135</sup> Cs	2 x 10 <sup>6</sup> y	β	<sup>241</sup> Pu	14.4 y	β
<sup>137</sup> Cs	30.17 y	β, γ	<sup>241</sup> Am	4.32 x 10 <sup>2</sup> y	α
<sup>144</sup> Ce	284 d	β, γ	<sup>243</sup> Am	7.3 x 10 <sup>3</sup> y	α
<sup>147</sup> Pm	2.62 y	β	<sup>244</sup> Cm	18.11 y	α
<sup>151</sup> Sm	93 y	β	<sup>245</sup> Cm	8.5 x 10 <sup>3</sup> y	α

(In this table, d=day, y= year)

## 1.6. MANAGEMENT STRATEGY OF HLW

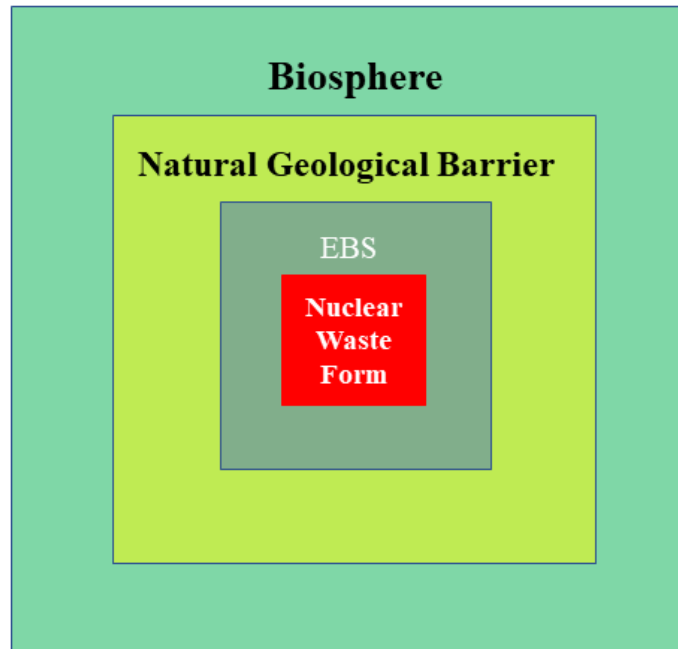
Very high stored radioactivity renders HLW to be immobilized in a suitable and durable matrix. The storage of HLW matrix needs to be carried out in an isolated locality for a considerable duration (~10<sup>6</sup> y) with systematic control and surveillance<sup>4,24</sup>. Uphill task of waste reprocessing and managing HLW generated from Fast reactors of 2<sup>nd</sup> stage of Indian nuclear programme. Higher concentration of fission products, corrosion products and minor actinides will be present in the HLW of fast reactors owing to the higher burn up and shorter cooling time. The higher α-activity and longer half-lives of minor actinides as compared to fission and corrosion products renders them for longer isolation. The policy of ‘concentrate and contain’ is utilized

for HLW management where the liquid waste is converted into suitable solid mass with high mechanical and chemical durability to sustain the long time scale required to decay of major long-lived trans actinides. Conversion to solid mass ensures enhanced safety during handling and transportation process to well designated sites. Currently, the solidified mass of HLW is being kept in interim storage facilities to allow the decay of relatively short lived radionuclides viz.  $^{90}\text{Sr}$ ,  $^{106}\text{Ru}$ ,  $^{137}\text{Cs}$ ,  $^{144}\text{Ce}$ ,  $^{147}\text{Pm}$  and  $^{244}\text{Cm}$ , which will be followed by their ultimate disposal in deep geological repositories.

## **1.7. DISPOSAL OF HLW**

Nuclear waste disposal, which involves confinement and isolation of waste from biosphere, is the ultimate step of radioactive waste management. The disposal repositories are mainly of two types: Near Surface Disposal Facility (NSDF) or Deep Geological Repository (DGR) which is selected upon the basis of half-lives and radiotoxicity of radionuclides present in HLW. The role of NSDF is to keep the radiation levels and radioactive contamination in soil, water and air in an around the disposal facilities within the permissible or safety limits as prescribed by regulatory bodies <sup>25</sup>. The global practice of long term storage of nuclear waste involves vitrification in a glass matrix encased in a stainless steel canister (~ 10 feet height and 1 feet dia). The canister is then stored at an interim storage facility for sufficient period prior to which it is to be buried deep inside a geological repository (~ 1000 m depth) with a horizontal spacing of around 10 m between successive canisters <sup>26</sup>. The major decay heat generated for around initial 300 years will be due to the decay of  $^{137}\text{Cs}$ ,  $^{90}\text{Sr}$  and their daughters followed by that of the trans-uranic radionuclides <sup>26</sup>. Hence, in order to reduce the radiotoxicity and generated heat, the waste forms are initially stored in a well-designed solid state storage and surveillance facility (SSSF)<sup>27</sup>. The nuclear waste will then be permanently disposed of in a DGR, isolated from the biosphere employing a multiple barrier approach. The multiple barrier

system includes a natural geological barrier which will be provided an engineered barrier system (EBS) and the host rock strata as depicted in **Figure 1.4**.



**Figure. 1.4: Schematic diagram of a multi-barrier system of nuclear waste storage in a DGR <sup>25</sup>.**

The EBS layer primarily involves a number of sub-barriers viz, the waste immobilization matrix, container or over-pack, repository wall and its linings. These various barriers prevent the leaking of radionuclides thereby limiting their release into the biosphere.

The main objectives of disposal in a DGR are:

- a) Seclusion of nuclear HLW from human activities and near surface accidental scenario.
- b) Protection of biosphere.
- c) Restriction of leaking of waste from degradation of EBS.
- d) Distribution and dilution of the flux of long-lived radionuclides.

The immobilized waste mass is the primary barrier to the radionuclides in the geological repositories. The container (over-pack material) will consist of a corrosion resistant metal such



as titanium or iron alloy whose rate of corrosion is very slow and happens in a predictable rate. The first back-fill layer will consist of clay materials like montmorillonite and bentonite, etc. which acts as excellent sorption material in case of accidental leaching of radioactivity. Finally, the host rock should be granite or other basaltic forms which will detain further release of radioactivity upon accidentally reaching up to the host rock layer. The design of EBS is dependent upon the disposal methodology selected and the nature of radioactive waste forms. Thus, it can be clearly envisaged a very low probability of release of radionuclides from repository to biosphere. However, environmental factors such as, natural calamities viz. earthquakes, volcanic eruptions, flood, change in groundwater movement, rock structure, erosion, etc. may contribute to diffusion of radioactivity to the biosphere. Therefore, it is immensely required to have a detailed scientific know how of the stability of the waste loading matrix under normal and off-normal situations to simulate their behaviour over a larger period of time. Moreover, no country till date has started the ultimate disposal of nuclear HLW, and studies related to proper DGR sites are being pursued all over the world.

## **1.8. NUCLEAR HLW IMMOBILIZATION MATRICES**

The prime objective of immobilization of nuclear waste is to permanently fix the radionuclides in a durable solid matrix thereby preventing their release to the biosphere over a time period of millions of years. Thus, it is quite clear to state that, the major goal of nuclear HLW immobilization relies on development of a highly stable and durable package material (waste form and container) that will ensure the long-term stability and isolation of the stored radioactivity. Moreover, the immobilization matrix is also the first barrier for the prevention of leaking of radioactivity into the surroundings.

The desired properties of immobilization matrices are:

- a) High waste loading to minimize waste volume
- b) Low leachability to minimize leaking of stored radioactivity

- c) High thermal conductivity and specific heat capacity to dissipate heat generated due to radioactive decay
- d) Low thermal expansion coefficient to avoid thermal shock and crack formation
- e) High mechanical strength for easy transportation
- f) Compatibility with storage canister

There are two distinct types of nuclear HLW immobilization matrices viz.

- i) Glass matrix (which is currently used almost all over the world) and
- ii) Ceramic matrices (which are futuristic based upon certain advantages over glass matrix).

## **1.9. GLASS MATRICES**

Glass matrices are currently used for immobilization of nuclear HLW all over the world. However, the most extensively used forms of glass matrices are phosphate based glass, borosilicate based glass and glass ceramics<sup>4,27,28</sup>.

### **1.9.1. PHOSPHATE BASED GLASSES:**

Phosphate based glasses are considered to be one of the earliest matrices being considered for immobilization of nuclear HLW. The major advantages of these matrices are:

- i) Effective incorporation of volatile molybdenum present in HLW
- ii) Promising for entrapment of sulphate bearing waste
- iii) Relatively lower temperature of formation
- iv) Main additives of these matrices are in liquid form and hence easy to homogenize during preparation.

However, in comparison to borosilicate glasses, molten phosphate glasses corrode refractory linings of the melter, thereby reducing their lifetime<sup>4</sup>. Hence, in present day, these type of glasses are used predominantly in Russia since 1987<sup>29</sup>.

The main building block for these glasses are based on the network former  $\text{PO}_4^{3-}$  groups. Network of these glasses consists of one terminal  $\text{P}=\text{O}$  and three bridging  $\text{P}-\text{O}-\text{P}$  bonds. However, the use of these matrices was quite limited because of the corrosive nature of the constituents and relatively lower glass transition temperature ( $T_g$ ). It is to be noted that  $T_g$  is the temperature above which glass becomes soft. If the stored heat inside the matrix raises its temperature above  $T_g$ , then leakage of radioactivity can take place due to softening of the glass matrix <sup>28</sup>.

### 1.9.2. BOROSILICATE BASED GLASSES

These matrices are the most widely accepted matrices for immobilization of nuclear HLW and practiced all over the world. The main reasons for their universal acceptance are as follows <sup>4,28</sup>.

- i) Higher flexibility with regards to nuclear waste loading
- ii) Ability to incorporate a variety of waste elements
- iii) Relatively higher  $T_g$  as compared to phosphate glasses making them more durable
- iv) High mechanical integrity
- v) Higher radiation stability

These types of glasses are formed in a moderate temperature range of 950-1050°C <sup>28</sup>. The main building block of these types of glasses are boron oxide ( $\text{B}_2\text{O}_3$ ) or boric acid ( $\text{H}_3\text{BO}_3$ ) and silica ( $\text{SiO}_2$ ). The glassy network structure is formed by four bridging  $\text{Si}-\text{O}-\text{Si}$  bonds and three bridging  $\text{B}-\text{O}-\text{B}$  bonds. However, depending upon the relative ratio of oxides of B/Si, an average network of  $\text{B}-\text{O}-\text{Si}$  type is observed with a coordination number in between 3 to 4. Hence, some network modifiers such as  $\text{Na}_2\text{O}$ ,  $\text{BaO}$ , etc. are added during glass formation which are subsequently then termed as sodium borosilicate glass (NBS) or barium borosilicate glass (BBS). Low concentration of alkali or alkaline earth metal oxides results in formation of  $\text{BO}_4^-$  structural units which results in formation of equally shared  $\text{BO}_4$  and  $\text{SiO}_4$  network rendering high durability

### **1.9.3.GLASS CERAMIC OR GLASS COMPOSITES:**

Glass ceramics or glass composites are the concepts and wide varieties experimental studies are being pursued worldwide in the context of nuclear HLW immobilization. The concept behind choice of these materials are incorporation of long-lived minor actinides in the ceramic phase and vitrification of other short-lived radionuclides within the glassy phase. They are obtained by controlled crystallization of desired ceramic phases within the bulk glassy medium. In order to achieve fine grained product, nucleating agents such as  $\text{TiO}_2/\text{ZrO}_2$  are sometimes added to the glassy melt for generation of desired ceramic phases. The rationale of addition of  $\text{TiO}_2/\text{ZrO}_2$  will be discussed later while discussing the ceramic matrices. Glass ceramics materials are found to be mechanically more stable and chemically more durable than glass. However, the main disadvantage of these materials lies in the crystallization of desired ceramic phases <sup>4</sup>.

### **1.10. LIMITATIONS OF GLASS MATRICES**

Glass matrices are probably the most versatile matrices used for nuclear HLW immobilization. However, it needs to be mentioned here that entire world till date is storing immobilized waste in NSDF under constant surveillance. Ultimate disposal in any geological repository is still not practiced. Since glass is thermodynamically considered as metastable material, the stability of glass matrix under geological repositories for millions of years raises concerns <sup>24,30</sup>. The crystallization of nuclear waste loaded glass (devitrification) due to energy supplied by the decay heat of the incorporated waste is also another concern. However, this in general can be circumvented by limiting the amount of radioactivity in it <sup>31</sup>. Devitrification of glass will lead to shrinkage in volume, thereby leading to generation of cracks and fissures in the surface, thereby increasing the possibility of accelerated leaching. Thus, long term chemical, thermal and radiation stability studies of glass materials need additional attention.

Moreover, the globally accepted borosilicate glasses have low solubility for sulphate, phosphate, iron oxides, sodium, molybdenum and heavy metal oxide-based wastes<sup>32,33</sup>. These shortcomings of borosilicate glass matrix necessitate the quest for alternate host matrix formulations for nuclear HLW immobilization. Moreover, in Indian context, waste of fast breeder reactors will contain even higher concentration of minor actinides, fission products, corrosion materials, etc. which are also concerns for borosilicate glass matrix. Higher amount of radionuclide can be incorporated into crystalline ceramic matrix without the need for vitrification<sup>34</sup>. However, the study of possible crystalline waste matrices is still limited to lab studies, and no commercial plants are in operation for immobilization in ceramic matrices.

### **1.11. CRYSTALLINE MATRICES**

By nature, the crystalline materials are thermodynamically stable materials as compared to glass. In addition to this, some naturally occurring crystalline minerals are found to retain high amounts radio-nuclide within their structure without undergoing any metamictization. Hence, in view of the long time periods like million years, A. E. Ringwood has proposed assemblages of mineral analogous titanates, termed as Synthetic Rock or SYNROC, for immobilization of minor actinides and nuclear HLW<sup>35</sup>. SYNROC is essentially a multiphasic composite matrix which has the ability to incorporate different cation of HLW in one or the other phases. The main ceramic phases present in SYNROC are hollandite, perovskite, pyrochlore, zirconolite and rutile. With advent of time, in addition to titanates, rock analogous monazite and zircon type of phases were also considered as potential phases for nuclear HLW immobilization<sup>36,37</sup>. Although single phasic lattice is much well suited for incorporation of particular types of radionuclides within their structure, the varieties of elements present in HLW need a composite system. The advent of Actinide Separation Demonstration Facility (ASDF) in Tarapur, India has enabled the separation of useful radioisotopes from HLW for medicinal and other commercial uses. Hence, India is at the forefront of segregation of useful radionuclides from

HLW and will need waste matrices desirable for minor actinides and other long-lived radionuclides only in future. Before going into detailed discussion about the different types of ceramic lattices mentioned above, a general comparison between glass and ceramic matrices are given in **Table 1.3**.

**Table 1.3.: General comparison between glass and ceramic matrices for nuclear HLW immobilization.**

Property	Glass	Ceramic
Incorporation ability	No crystallographic limitations	Has Crystallographic limitations
Processing temperature	Low	High
Processing cost	Low	High
Thermodynamic stability	Low	High
Radiation stability	Low	High
Leach resistance	Low	High
Solubility of actinides	Low	High
<i>In situ</i> crystallization possibility	Yes	No
Leaching rate	Decreases with time	Decreases with time
Thermal conductivity	Low	High

In spite of the fact that ceramic matrices have certain crystallographic limitations as compared to glass matrices, there are some predominant mechanisms by which radionuclides can be immobilized within their structure<sup>38–40</sup>. These are as follows:

- a) Direct substitution of iso-valent species in particular lattice sites.
- b) Aliovalent substitution followed by charge compensation in nearby sites.
- c) Insertion into open voids within the crystal lattice.
- d) Incorporation upon generation of planar defects or grain boundaries.

Some of the most promising crystalline lattices for incorporation of minor actinides are as follows:

### 1.11.1 APATITES

These types of lattices have a generic composition  $M_{10}(XO_4)_6Y_2$ , where M is a divalent cation such as  $Ca^{2+}$ ,  $Pb^{2+}$ ,  $Ba^{2+}$  etc., X is a trivalent cation such as P, V or Si, and Y is a

monovalent anion like  $F^-$ ,  $Cl^-$ ,  $Br^-$ ,  $OH^-$ , etc. These types of compounds crystallize in hexagonal structure. Calcium phosphate apatite family consisting of fluorapatite  $[Ca_{10}(PO_4)_6(F)_2]$ , hydroxyapatite  $[Ca_{10}(PO_4)_6(OH)_2]$  and chlorapatite  $[Ca_{10}(PO_4)_6(Cl)_2]$  are very much abundant mineral with higher chemical and radiation stability. Literature reports suggest them to be promising matrix for immobilization of corrosion materials and also for nuclear waste processed by pyro-processing methodology<sup>41-43</sup>.

### **1.11.2 SODIUM ZIRCONIUM PHOSPHATE (NZP)**

Sodium zirconium phosphate with composition  $NaZr_2(PO_4)_3$  allows substitution of minor actinides and actinides in Zr site. Moreover, the framework structure allows other radionuclides present in HLW to be incorporated. Three distinct types of crystallographic sites are present in the structure and hence it shows excellent compositional flexibility. However, from preparation point of view, fabrication of sintered NZP in air is difficult, and hence studies pertaining to their use in nuclear waste immobilization are limited<sup>44</sup>.

### **1.11.3. ZIRCON**

Zircon is a silicate mineral having the general composition  $(ZrSiO_4)$ . It is abundant in different types of rocks such as lunar rocks, pegmatites and meteorites. It is considered as the major ore of zirconium and contains up to 20 wt% of uranium and thorium oxides within it. It shows very high potential for immobilization of weapons-grade plutonium<sup>45,46</sup>. However, as this is an ore based mineral with limited crystallographic sites, incorporation of multiple types of radioactive cations within its structure may not be feasible and also may degrade the stability and hence accelerate the leaching of activity under acidic condition.

### **1.11.4. MONAZITE**

The general chemical composition of monazite is  $[(Ce, La, Nd, Th)PO_4]$ . It belongs to a mixed rare-earth phosphate-based mineral. This material is also considered as a very promising material for incorporation of minor actinides in accordance with its very high

chemical and radiation stability<sup>47–49</sup>. It is considered as the ore for mining of thorium in India and contains up to about 27 wt% of thorium within its structure. These lattices are mostly similar to zircon and its drawbacks are also similar to that of zircon based matrices.

### 1.11.5. HOLLANDITE

These types of compounds have the general formula  $A_2B_8O_{16}$  where A is a monovalent or divalent atom, and B has a valence between 2 and 5. A range of minerals exhibit these type of structures with difference in their B sites such as hollandite (B=Ti), ankangite (B= Ti, Cr, V), henrymeyerite (B=  $Fe^{2+}$ , Ti) priderite (B=  $Fe^{3+}$ , Ti) and redledgeite (B= Cr , Ti). Hollandites are considered as excellent host matrices for immobilization of radioactive caesium<sup>50</sup>. However, the preparation of Cs-137 pencils for blood irradiator has been taken up by Bhabha Atomic Research Centre (BARC) and hence immobilization of caesium for long term disposal is not required in Indian Scenario<sup>51</sup>.

### 1.11.6. PEROVSKITE

Perovskites are compounds with the general formula  $ABO_3$  where A is a divalent cation and B is tetravalent cation having  $AO_{12}$  and  $BO_6$  polyhedra. Perovskite structure is formed only when the Goldschmidt's tolerance factor value (t) lies in the range of 0.75 to 1.00<sup>52</sup>.

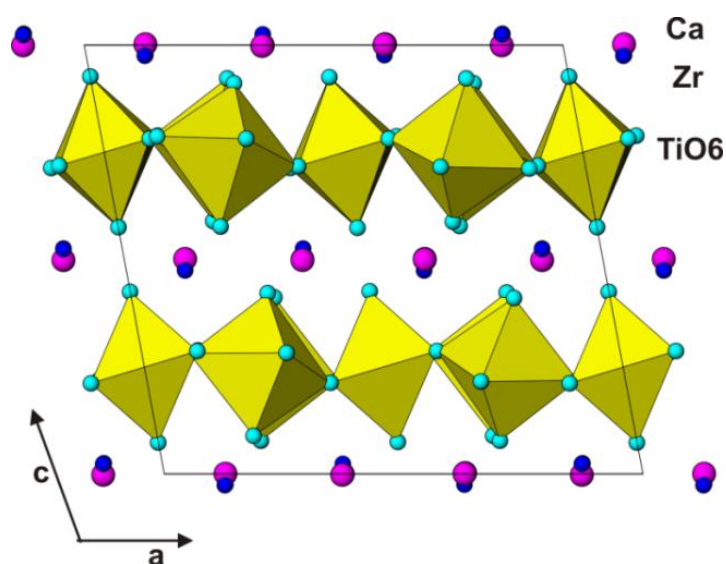
$$t = (R_A + R_O) / \sqrt{2} (R_B + R_O) \quad (\text{eqn. 1.1})$$

where  $R_A$  and  $R_B$  are the ionic radii of ions occupying A site and B site respectively and  $R_O$  is the ionic radii of oxygen. Literature reports suggest incorporation of almost 35 wt% of strontium present in HLW by substitution at A site of perovskite lattice<sup>53–55</sup>. However, again, separation of radioactive  $^{90}\text{Sr}$  is an important mandate of Bhabha Atomic Research Centre for other potential applications and hence immobilization of strontium may not be required in the near future<sup>56</sup>.



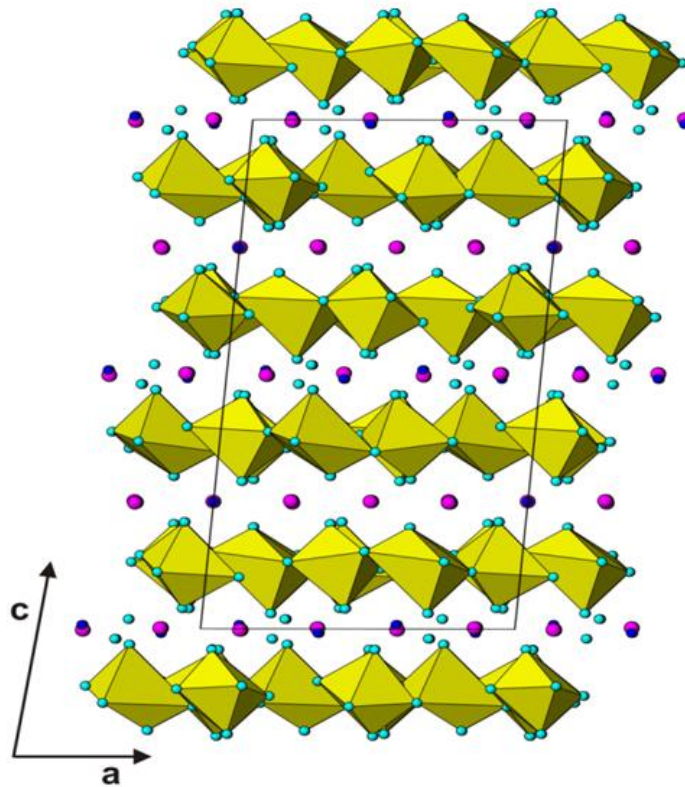
### 1.11.7. ZIRCONOLITE

The general nominal composition for zirconolite is  $\text{CaZrTi}_2\text{O}_7$ . Zirconolite is found to crystallize in monoclinic structure having  $C2/c$  space group<sup>57</sup>. The monoclinic structure is formed by stacking of multiple layers of edge-shared  $\text{TiO}_5$  trigonal pyramids and  $\text{TiO}_6$  octahedra (ideal ratio 1:2 for  $\text{CaZrTi}_2\text{O}_7$ ) with sandwiched layers of  $\text{Ca}^{2+}$  and  $\text{Zr}^{4+}$  ions in between the Ti-O polyhedra<sup>58</sup> as shown in **Figure 1.5**. The term zirconolite-2M refers to a two layered monoclinic variant of zirconolite. It is evident from the diagram that some of the Ti-O polyhedral are having coordination of 5 whereas most are having a coordination of 6. This is one of the unique feature of zirconolite to make it an immune structure to perturbations upon suitable cationic substitution. The unique ability of zirconolite structure is its ability to incorporate a wide variety of cation till the general stoichiometry  $\text{CaZr}_x\text{Ti}_{(3-x)}\text{O}_7$  where x varies from 0.80 to 1.37<sup>59–61</sup>. Moreover, it can adopt suitable alteration in the framework upon cationic incorporation resulting in crystallization of different polytypes without alteration of the basic structure or precipitation of any chemical species from the structure<sup>60–63</sup>.



**Figure 1.5:** Crystal structure of zirconolite -2M polytype ( $\text{CaZrTi}_2\text{O}_7$ ).

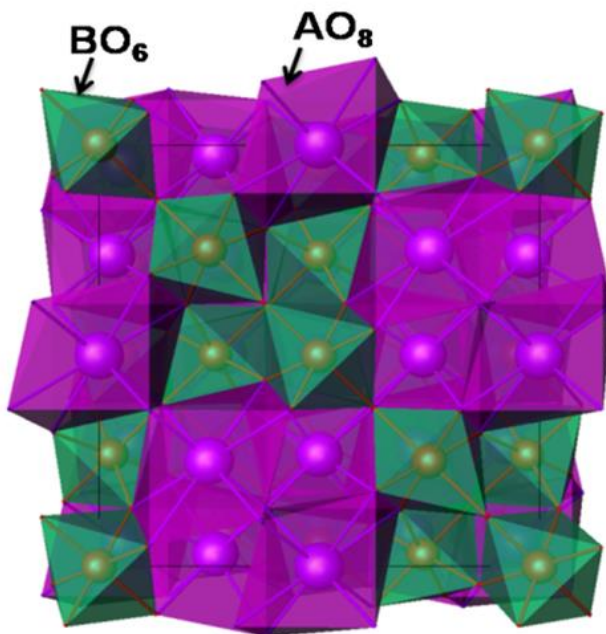
Upon higher substitution of lanthanides (surrogate for minor actinides), it was observed that zirconolite-2M transforms to zirconolite-4M structure which will be discussed in detail in chapter 4 of this thesis. 4M-zirconolite refers to a four Ti-O layered structure with  $\text{Ca}^{2+}$ ,  $\text{Zr}^{4+}$  and  $\text{RE}^{3+}$  ions (where  $\text{RE} = \text{Nd}^{3+}$ ,  $\text{Sm}^{3+}$  and  $\text{Y}^{3+}$ ) sandwiched in between them. Crystal structure of zirconolite-4M is shown in **Figure 1.6**. Substitution of different types of ions into the different cation sub-lattice of zirconolite have been reported in literature<sup>31,64,65</sup>. Caurant *et al*<sup>64</sup> investigated a series of  $\text{Nd}^{3+}$  substituted hafnium variant of zirconolite viz.  $\text{CaHfTi}_2\text{O}_7$  and demonstrated that single phase domain is available upon substitution of  $\text{Ti}^{4+}$  sites by  $\text{Al}^{3+}$  ions. The study also indicated preferential occupation of  $\text{Nd}^{3+}$  ions at  $\text{Ca}^{2+}$  site. Uranium incorporation at zirconolite lattice was also carried out by Vance et al<sup>65</sup>. In addition to phase studies, higher leach resistance and radiation stability of zirconolite is also reported in literature<sup>66-68</sup>.



**Figure 1.6: Crystal structure of zirconolite -4M polytype.**

### 1.11.8. PYROCHLORE

Pyrochlores are the compounds having the general formula  $A_2B_2O_7$ , where A = trivalent rare-earth ions and B =  $Ti^{4+}$ ,  $Zr^{4+}$  etc. A is the larger cation and B is the smaller cation in pyrochlore lattice; the  $r_A/r_B$  being the driving force for crystallization of the pyrochlore structure<sup>69</sup>. Structurally, it is an ordered form of the defect fluorite structure, and consists of distorted  $AO_8$  and  $BO_6$  polyhedra as shown in **Figure 1.7**. Literature reports have investigated the accommodation of larger proportion of minor actinides in pyrochlore structure and their stability under high radiation field without any observed segregation of secondary phases<sup>69–76</sup>. The most important parameter is that it has a wider choice of A and B cations to satisfy charge neutrality and  $r_A/r_B$ . This makes these types of lattice a very potential candidate for immobilization of minor actinides.



**Figure 1.7:** Crystal structure of pyrochlore showing distorted  $AO_8$  and  $BO_6$  polyhedra.

## 1.12. SURROGATE NUCLEAR MATERIALS

In an attempt to gain a detailed knowledge about the phase formation of actinide or minor actinide loaded ceramic matrices, the biggest roadblock is safety. It becomes very difficult to work with actinides such as plutonium or minor actinides such as americium, neptunium or curium in a common laboratory. Further, the measurement of thermo-physical properties, along with phase and microstructural studies of waste loaded matrix are the most important studies desired to certify a material as a waste immobilization matrix. The handling of radioactive materials for such studies is not possible often due to larger volume and larger activity and limited availability of isotopes. Working with so high amount of plutonium or minor actinides is really a tedious task even in a normal radiological laboratory. Hence, the concepts of using elements with closely similar chemical, physical or structural properties are in general adopted to mimic the behaviour of minor actinides.

### 1.12.1 SURROGATE FOR PLUTONIUM

A total of 15 isotopes of plutonium ranging from mass number 232 to 246 are radioactive in nature. The primary mode of decay of plutonium is by  $\alpha$  emission, the other modes being  $\beta$  emission, electron capture and spontaneous fission. Major isotopes of interest for nuclear waste immobilization viz. Pu-238, Pu-239, Pu-240 and Pu-242 are all  $\alpha$ -active. Because of small range of  $\alpha$  particles in tissues, they tend to deposit a larger amount of energy over a smaller path and hence is considered as an internal hazard. Since  $\alpha$  particles cannot penetrate skin, plutonium, especially in the form of PuO<sub>2</sub> powder, if inhaled accidentally or enter human body through any wound, gets deposited in lungs, livers or bones<sup>77</sup>. The half-life of Pu-239 is around 24,605 years which is not considered very high as 1 microgram of Pu decays more than 200 times per second. This amounts to much higher events than uranium ingestion as half-life of uranium is ~4 billion years. Moreover, solubility of uranium salts is

much more than plutonium and hence decontamination of uranium is quite easier than plutonium. Animal studies carried out using plutonium ingestion shows that few milligrams of plutonium per kilogram of tissue weight is a lethal dose. Extrapolation of this study to humans indicate and LD<sub>50</sub> for an average human of 70 kilogram weight would be about 22 milligram of plutonium. Highly sophisticated fume chambers and hot cells are required for handling of plutonium and its compounds. In addition to this, handling of the experimental waste is further involved job. However, as mentioned earlier, experimental data on PuO<sub>2</sub> is of prime importance in various aspects of nuclear research for 2<sup>nd</sup> and 3<sup>rd</sup> generation of Indian nuclear reactors. Hence, a requirement was there to find an alternative of this material which will be able to replicate its behaviour except its radioactivity. Cerium oxide (CeO<sub>2</sub>) was chosen as surrogate for PuO<sub>2</sub> for the experiments in laboratory without hot cells<sup>78</sup>. The similarity between these two species is shown in **Table 1.4**.

**Table 1.4: Table showing the similarity in properties between CeO<sub>2</sub> and PuO<sub>2</sub><sup>78</sup>.**

Properties	CeO <sub>2</sub>	PuO <sub>2</sub>
Ionic size	Ce <sup>4+</sup> <sub>6</sub> = 0.87Å Ce <sup>4+</sup> <sub>8</sub> = 0.90Å	Pu <sup>4+</sup> <sub>6</sub> = 0.86Å Pu <sup>4+</sup> <sub>8</sub> = 0.89Å
Structure	Fluorite	Fluorite
Space Group	Fm-3m	Fm-3m
Melting point	2873 K	2935 K
Density	7.30 g/cc	11.44 g/cc
Δ H <sub>298</sub> (kJ/mole)	-1090.4	-1055.8
Cp <sub>298</sub> (kJ/mole.K)	61.63	66.25
S <sub>298</sub> (J/mole.K)	62.30	66.13

### 1.12.2 SURROGATE FOR AMERICIUM

The biological half-life of Americium-241 is ~ 50 years in human bones and 20 years in human liver. Since americium does not get excreted from the gonads, contamination carries a lifetime cancer mortality risk. In addition to these risk from internal exposures, a certain risk pertaining to external exposure is also associated with americium-243. A careful peek into the decay chain of americium-243 gives neptunium-239 which is a γ emitter. However, the presence of

americium is almost the highest among the trans actinides and hence data on americium incorporated matrices are also the need of the hour for designing of suitable matrices for long term disposal of nuclear waste in DGR. Based on the cationic radii, crystal structure, phase transition temperatures, melting points and coefficients of lattice thermal expansion, literature report suggest that  $\text{CeO}_2$  can act as surrogate of  $\text{AmO}_2$  and  $\text{Nd}_2\text{O}_3$  can act as surrogate of  $\text{Am}_2\text{O}_3$ <sup>79-81</sup>. Thus, from the above discussions, it can be mentioned that surrogate chemistry for minor actinides is important for understanding chemical behaviour of any matrices intended for long term storage of nuclear waste. Lopez *et al*<sup>82</sup> have suggested for using cerium oxide or ceria as possible surrogate material for plutonium, hafnia ( $\text{HfO}_2$ ) for other tetravalent actinides such as thorium ( $\text{ThO}_2$ ) and neodymium for trivalent actinides such as curium and americium. In this thesis, surrogate elements for various studies pertaining to minor actinides.

### 1.13. SCOPE OF THE THESIS

Scope of this thesis titled “Preparation and structural investigations on zirconolite and pyrochlore based ceramics: Potential materials for nuclear back end application” is to investigate the different unanswered aspects of zirconolite and pyrochlore related materials for their qualification as nuclear matrix for long term storage of nuclear waste. Structure and thermophysical properties of two lattices based upon Ca-Zr-Ti-O system viz. calzirtite and zirconolite were evaluated in chapter 3 of this thesis. This chapter clearly indicates that not all lattices are promising for immobilization of minor actinides for long term storage. The various structural and thermodynamic parameters were evaluated to give a step-by-step guide for selection of a potential host matrix. Chapter 4 of this thesis deals with the phase evolution of zirconolite-pyrochlore type systems. This chapter envisages the gradual phase transition from zirconolite to pyrochlore type phases as a function of variation of composition. The composite phases formed were evaluated for their microstructural studies to observe their behaviour as single ensemble of SYNROC constituent phases. Variation of structure and thermodynamic

stability of aliovalent substituted pyrochlore structure is discussed in chapter 5 of this thesis. The distortion induced in the pyrochlore structure by incorporation of different sized cations and their possible site occupancy have been discussed. The variation of thermodynamic stability of pyrochlores as a function of incorporated ionic substitution is discussed. Chapter 6 deals with the phase stability, structural studies and thermodynamic stability studies of a potential matrix i.e., gadolinium zirconate as a function of processing temperature. Furthermore, the effects of incorporation of uranium in ambient as well as reducing atmosphere is discussed along with its thermodynamic implications. Finally, the structural and stability studies of uranium and cerium (surrogate for plutonium) co-doped matrix was analysed to understand its potential as a nuclear waste immobilization matrix. Chapter 7 deals with glasses and glass-ceramic based matrices for immobilization of high gadolinium containing waste pertaining to Indian nuclear energy scenario. Finally, the summary of the thesis work along with future scope of the work is presented in chapter 8.

# **Chapter 2**

## **Synthesis methods and instrumental techniques**



## 2.1. INTRODUCTION

Ceramic processing has advanced right from potter's wheel to today's age of technological innovation. Each and every ceramic material has to overcome the ladders of easy processing, fabrication, structure-property relationship to be acceptable for use in today's era. Hence, different techniques of fabrication and property evaluation need special mention.

In this thesis, ceramic materials related to zirconolite and pyrochlore type structures have been prepared for their structural characterization and thermodynamic stability analyses. The main preparation routes adopted for synthesis of materials were conventional solid state synthesis route and, solution or soft-chemical based gel-combustion route. Glass and glass-ceramic based samples were prepared by melt quench technique, which is one of the most prevalent techniques for preparation of glass materials. Basic principles of these synthesis methods are discussed in this chapter.

The products obtained were characterized by powder X-ray diffraction technique. Structural studies and unit cell parameters were calculated either by Rietveld refinement or le Bail profile refinement method. Raman spectroscopy was also used for phase identification in some of the works in this thesis. Local structure was also analysed by X-ray absorption fine structure (XAFS) technique in some of the works. Thermodynamic stability studies were carried out using calvet oxide melt solution calorimeter. Thermogravimetric analysis coupled with differential thermal analysis (TG-DTA) was also used for works related to glass and glass-ceramic materials. Other than these techniques, scanning electron microscopy (SEM), electron probe micro analyser (EPMA) were used to gain insight into microstructural and compositional details. Elucidation of oxidation state was carried out in some of the studied compositions by X-ray photoelectron spectroscopy (XPS). A brief description of all these techniques are discussed in this chapter.

## **2.2. SYNTHESIS METHODS**

Sample preparation is one of the most crucial steps for fabrication of any material intended for some technological applications. Preparation of high-quality powders with reproducible characteristics at comparatively low cost is the most important requirement for use of any ceramic material. Mainly two types of preparatory routes for ceramics viz. solid state and soft-chemical routes are conventionally used. Among the different categories of soft-chemical routes, gel combustion synthesis has been used for preparation of some compositions in this thesis and hence only the details of gel-combustions are only discussed.

### **2.2.1. SOLID STATE METHOD**

Solid state method is considered as the most widely used method for preparation of poly-crystalline ceramics owing to its simplicity in handling of reactants and scaling up of reaction for bulk synthesis. This method involves mixing together of reactants in stoichiometric ratio followed by grinding of the powders till homogenization. The basic motto of this method is mixing of the reactant powders to the maximum extent possible. Hence, this method involves mixing of reactant powders and heating at gradually elevated temperatures over long duration followed by intermittent grinding in between for better homogenization<sup>83,84</sup>. Starting temperature for heat treatment is usually based on the melting point or decomposition temperature of the solid reactants and then gradually increased to higher temperatures for successive heating. In general, for preparation of refractory materials, high temperature is required for a long duration as the reactants do not react at room or lower temperature. Materials like zirconolite and pyrochlore have melting points in excess of 1600°C and hence initial temperature for heating of samples pertaining to this thesis work has been kept at 1200°C for a long duration like 24 h for each.

Solid state reaction is diffusion-controlled reaction and follows a parabolic rate law as given below:

$$dx/dt = k \cdot x^{-1} \quad (\text{eqn. 2.1})$$

where,  $x$  is the degree of reaction (related to the thickness of the formed product layer),  $t$  is the time of reaction and  $k$  is proportionality constant. Ions present in a refractory oxide based material gains sufficient energy for migration and diffuses through the crystal lattice only at elevated temperatures. Hence, even if, the initial rate of reaction is fast, it slows down with time as the reactant ions need to diffuse through the newly formed product layer (growing with time) for further reaction.

The various factors governing the rate of a solid state reaction are:

a) **Temperature:** Refractory reactants do not react at room temperature and so it becomes necessary to heat them at elevated temperatures for prolonged time. Thus, it can be said that, solid state method encompasses both thermodynamic and kinetic considerations. Thermodynamic principles guide about the feasibility of the reaction whereas kinetics determines the rate of reaction which ultimately gives us direction for the time duration for which the sample needs to be kept at elevated temperature. Choice of elevated temperatures is mostly guided by the melting point of the reactants as for example, Fluorides being more ionic and low melting solids need relatively lower temperature for chemical reaction compared to oxides. A solid state reaction progresses in two steps viz. nucleation and growth. Nucleation step is the most difficult step because of larger structural reorganization requirements at the site of potential nucleus. Atoms or ions present in solid lattice, which are virtually immobile, need to migrate or hop towards each other into an adjacent empty site to form product layer. Hence, high temperature is a condition for solid state method which provides sufficient thermal energy to the atoms or ions to cross the lattice energy barrier for enhanced diffusion. As soon as the product nucleus formed grows, it becomes more difficult for the reactants to cross the increasing thick interface for further reaction. This is the primary reason because of which solid

state reactions are slow in nature and requires more than one heat treatment followed by intermittent grinding to break the formed product layer.

b) **Area of contact between the reactants:** The contact surface of solids guides the reactivity as it determines the area of contact for diffusion of reactants. Hence, to increase the contact surface area, the powders are finely grounded. It is always better to pelletize the ground powder as compaction helps the grains to come in close contact with each other resulting in higher rate of diffusion than unpelletized or uncompacted powders. In general, a cold pressed pellet shows a porosity in the range of ~ 20 to 40%. In view of this, for very slow reactions, hot pressing is required where the combined effect of both temperature and pressure leads to much higher densification resulting in increased rate of reaction.

c) **Defects, vacancies and interstitials:** Defects, vacancies or interstitials provide easy migration sites for the participation atoms or ions in a solid state reaction. Hence, they enhance the mobility of the species leading to a definite increase in the rate of reaction.

Taking care of all the important parameters discussed above, the reactants are ground and mixed thoroughly before each heat treatment. Well ground powders lead to increased surface area of contact and pelletizing them further enhances the contacts for reaction. After each heat treatment, the pellets are crushed into powders to separate the interface of product layer from the reactants. This process needs to be repeated till the completion of reaction takes place. Presence of adsorbed moisture or carbonates or oxycarbonates on the surface of powders, can alter the reaction process or can deviate the stoichiometry than desired. Hence, reactants are preheated at lower temperatures to make their surface free from these adsorbed impurities.

The major advantages of the solid state method of synthesis are the versatility of the method and is best suited for bulk production of refractory materials. Easy availability of the reactant oxides and low cost of production on bulk scale are the other recompenses of this method. However, the repeated heating and grindings may result in local stoichiometric

variation. Contamination from grinding media, requirement of high temperatures and longer duration of heat treatment are the other limitations of this method. Moreover, metastable materials cannot be prepared by this method as thermodynamic considerations play a big role in this method of synthesis.

### **2.2.2. GEL COMBUSTION METHOD**

Soft-chemical route or solution route of synthesis is the second most important route for preparation of technologically relevant ceramics. Soft-chemical route encompasses various methods such as co-precipitation method, hydrothermal method, sol-gel processing, pechini and citrate gel formation methods, etc. in addition to gel combustion method. Gel combustion method is a very promising route for nano-ceramic synthesis because of its simplicity, cost-efficiency and tunability of reaction processes. Moreover, certain metastable phases can also be prepared by this route as the particle size is reduced below a certain critical size during the synthesis process<sup>85</sup>.

Gel combustion process is basically a redox reaction methodology involving an oxidant (metal nitrate) and a reductant or fuel (glycine, citric acid, etc.)<sup>86</sup>. The powdered products obtained by this method of preparation has very good characteristics such as narrow size distribution, higher surface area and better sinterability<sup>87-90</sup>. The reaction method consists of two distinct processes which are: gel formation and combustion of the gel. Fuel or reductant, a very important species in gel combustion process, can be defined as a substance which is consumed or decomposed in this redox reaction producing enormous energy. The fuel is chosen such that it should be able to maintain homogeneity of composition of the reactants and undergo combustion with oxidant at low ignition temperatures. A wide variety of organic compounds such as citric acid, ascorbic acid, glycine, urea, hydrazine, hexa methylene tetra amine (HMTA), etc. can be used as fuel. Glycine, one of the most common fuel, is used in the present

work as it is one of the cheapest amino acids and acts as good complexing agent for a wide variety of metal ions<sup>91</sup>. Glycine has a zwitterionic character and hence can complex with metal ions of different sizes thereby preventing them from selective precipitation. Higher carbon containing fuels like citric acid can undergo combustion at relatively lower ignition temperatures and with greater control of combustion<sup>92-95</sup>. However, removal of carbon residues becomes slightly difficult when fuels with higher carbon content are used.

The first step of this synthesis method is gel formation which is very vital as it acts as control parameter for maintenance of phase purity of the final product. In this step, metal nitrates are mixed together in stoichiometric amounts in aqueous medium to form a transparent solution. Nitrates acts as oxidant in combustion reaction by supplying oxygen required for combustion of the fuel. A suitable fuel is then added to the transparent solution in definite amount (either stoichiometric, hypo-stoichiometric or hyper stoichiometric). In this thesis work hypo-stoichiometric or fuel deficient condition was used for controlled combustion method as reactants involved actinide nitrate solution or their surrogates. Fuel serves the dual role of complexing agent thereby binding the reacting metal ions to close proximity with each other as well as providing heat to the reaction by their decomposition. The transparent solution after addition of fuel is heated till the fuel dissolves in the medium. On further heating, the solution is converted into a viscous liquid by losing the excess water content which is termed as the gel. Removal of excess water is important as presence of traces of water in gel results in sluggish combustion, thereby deteriorating powder quality and phase purity.

The gel is heated to a higher temperature depending upon the nature of the fuel for initiating or triggering a self-propagating combustion reaction. Exothermic decomposition of fuel-oxidant precursor thereby takes place resulting in production of voluminous and fluffy powders along with release of large amount of gases. The auto ignition sustains for a very small time and can be realized upon observation of fire or flame. The fluffy nature of the powders

can be attributed to the evolution of gaseous products which dissipates the heat resulting in the fragmentation of the solid residue. The fluffy powders obtained may be either the desired phases or a semi-decomposed precursor having carbonaceous residues (evident from blackish tinge over powder surfaces). Calcination of the powders at  $\sim 600^{\circ}\text{C}$  is required to get rid of the inorganic carbon residues, undecomposed fuel (for fuel excess reaction mode) and nitrates (for fuel deficient reaction mode) to obtain chemically pure and crystalline nano powders.

The major advantages of this method are lower or no possibility of local variations (solution has to be transparent), atomic level mixing of reagents, no special intermittent processing and time saving low temperature synthesis. However, some caution is required for performing these types of reactions viz. performing reaction inside fume hood to facilitate safe ventilation and carrying out reaction in wide mouthed apparatus for easy release of generated gaseous products.

### **. 2.2.3 MELT QUENCH METHOD**

In this thesis, melt quench technique was used for the preparation of glasses and glass-ceramics materials. Melt quench method is considered to be the oldest method for preparation of glassy materials. This method comprises of calcination and melting of mostly oxides, nitrates, acetates, etc. constituents of metals required for glass formation. The melting process is carried out in non-reactive crucibles such as platinum, rhodium, alumina, zirconia, etc. followed by pouring of the molten entity directly to crucible kept at room temperature or under liquid nitrogen depending upon the requirements. The containers where the melt is poured should have to be made up of good thermal conducting materials such as copper, graphite, etc to minimise the effect of thermal shock upon pouring of the melt. Quenching process is necessitated to avoid any crystal growth over the nucleation sites created at high temperature in the melt. The rate and extent of cooling is the most important criteria for production of any

glass by this method. The cooling rate can range from a normal of  $1\text{Ks}^{-1}$  for preparation of oxide based glasses to  $10^6\text{Ks}^{-1}$  for certain compositions for metallic glasses.

The major advantage of this method is its versatility for glass preparation. Almost all types of oxide glasses can be prepared by this method. Moreover, the simple and cost-effectiveness nature of this process makes it the choice for preparation of glasses and glass-ceramics intended for immobilization of nuclear HLW. However, for preparation of glass in continuous mode by this method requires an automated intermittent stirring for better homogeneity and covering of melter crucible by lid to avoid volatilization of certain reagents leading to an error in the composition of the prepared glass. Chalcogenide glasses can also be prepared by this method provided the entire process is carried out either under inert atmosphere or in vacuum sealed crucibles <sup>96</sup>. The major disadvantage of this process lies in the decomposition of the reactant precursors as they have the potential to release  $\text{NO}_x$ , acetic acid vapours respectively which may damage or even burst the crucible.

## **2.3. INSTRUMENTAL TECHNIQUES**

Instrumental techniques play a very important role for characterization of synthesized products. Any material intended for some particular functions can be used only when it can be obtained in the desired form. Instrumental techniques play a significant role in confirming the synthesized products in their desired form. A host of experimental techniques has been used for this thesis work and their brief description is given below:

### **2.3.1 X-RAY DIFFRACTION (XRD)**

X-rays are invisible and electrically neutral electromagnetic radiations. Their frequencies lie in between ultra violet (UV) and gamma radiation respectively. Generally, X-rays have their wavelength ( $\lambda$ ) in the range of  $0.04\text{ \AA}$  to  $1000\text{ \AA}$ . The X-ray was discovered by Wilhelm Conrad Rontgen in the year 1895 for which he was awarded the Nobel prize in physics



in the year 1901. X-rays are of two types- a) characteristic radiation which are produced from core electronic transitions within an atom, and b) white radiation which are produced from acceleration or deceleration of charged particles. X-rays upon incident on a solid material (or grating) are scattered either coherently or incoherently or absorbed. Coherently scattered X-rays interfere with each other giving bright (constructive interference) and dark (destructive interference) fringes. However, the condition for scattered rays to interfere constructively arises only when the path difference between two successive rays differ by an integral multiple of their wavelength. This phenomenon is termed as X-ray diffraction (XRD) and is guided by the Bragg's law of diffraction which relates the chances of constructive interference to the interplanar spacing of a crystal lattice according to the following equation:

$$n\lambda = 2d_{hkl}\sin\theta \quad (\text{eqn. 2.2})$$

where,  $\lambda$  = wavelength of incident X-rays

$\theta$  = glancing angle (also termed as Bragg's angle)

$d$  = inter-planar spacing of crystal

$n$  = order of diffraction.

Each plane of a crystal lattice is characterized by miller indices given by (hkl). A schematic diagram of X-ray diffraction is shown in **Figure 2.1**.

The technique of X-ray diffraction is used to gain informations such as phase identification, crystal structure determination, crystallite size estimation, etc. of crystalline materials. Lattice of any crystal consists of a periodic and regular arrangement of atoms, ions or molecules throughout the crystal system. These parallel array of species present inside the crystal lattice behaves similar to parallel line of a diffraction grating. Hence, the interplanar spacing can be successfully estimated from the separations between bright fringes generated in

the diffraction pattern. Since X-rays are electromagnetic radiations, they transfer their energy via elastic collision to the electrons of the atom, which vibrates or oscillates with the same frequency as that of the X-rays. These oscillating electrons act as secondary source thereby emitting radiations of same frequency. Thus it appears as if the incident radiation is reflected or scattered by the atoms. The intensity of coherently scattered X-ray radiation from an electron is given by the classical Thomson equation and is known as the scattering power of an electron. Atoms consist of multi electron systems and thus the overall scattering factor of an atom is given by the equation:

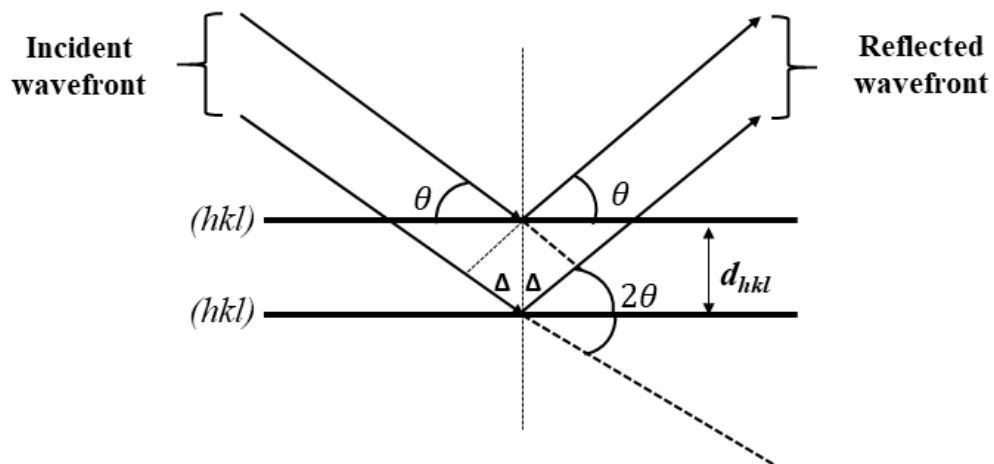
$$f = f_0 e^{\frac{-B \sin^2 \theta}{\lambda^2}} \quad (\text{eqn. 2.3})$$

$\theta$  = Bragg angle

$2\theta$  = angle of deviation between incident and reflected wavefront

$2\Delta = 2d_{hkl}\sin\theta$

= Path difference between two successive wavefront



**Figure 2.1: Schematic diagram of X-ray diffraction.**

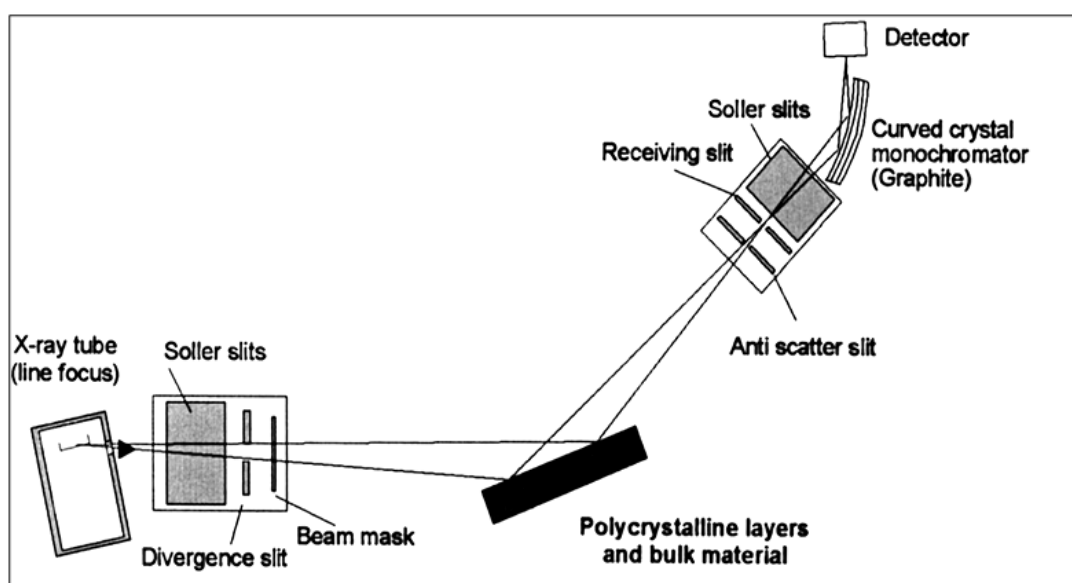
where,  $f_0$  is the scattering factor of an atom at rest and incident at  $0^\circ$ ,  $\lambda$  is the wave length of the incoming X-ray,  $\theta$  is the angle of diffraction and B is a constant or isotropic temperature factor and is related to the vibrational amplitude of an atom ( $B = 8\pi^2 u^2$ , where  $u^2$  = mean square of the displacement of the atom from its equilibrium position.). The total term in the exponential part is termed as the Debye-Waller factor. A crystal lattice consists of three-dimensional array of atomic planes which are in turn made up of numerous electrons present in the orbit of the atoms lying on the imaginary planes. The scattering power of a particular plane present in the lattice is termed as the structure factor and is given by:

$$F_{hkl} = \sum_{j=1}^{j \rightarrow N} f_j e^{2\pi i(hx_j + ky_j + lz_j)} \quad (\text{eqn. 2.4})$$

where,  $F_{hkl}$  is the amplitude of scattered radiation from hkl plane,  $f_j$  is the scattering factor of any atom j at a diffraction angle of  $\theta$ , (x, y, z) are the positional coordinates of the particular atom j and N denotes the number of atoms present in the unit cell. The term present in the exponential part represents the phase of the waves. Structure factor of a plane is related to the electron density distribution of a particular plane in the unit cell of a crystal. Experimental measurements of X-ray diffraction exhibit intensity of reflections of particular planes hkl as a function of the corresponding scattering angle ( $2\theta$ ).

X-ray diffraction (XRD) measurements require an X-ray source (kept under a sealed tube), sample to be investigated and a detector (proportional counter or scintillator based) to collect diffracted X-rays. Schematic diagram of different components of a powder X-ray diffractometer is shown in **Figure 2.2**. X-rays are produced in a laboratory equipment by thermionic emission of electrons from a tungsten source. The electrons are then attracted towards a copper target kept at a positive bias. The electrons are accelerated towards the metal target because of the bias. These accelerated electrons thus impinge the metal target and knock

out core electrons of atoms. Outer or valence electrons try to fill up those vacant sites in the core shell thereby generating characteristic X-ray radiation. However, only a small fraction of accelerated electrons produces X-ray while most of the electron energy is deposited on the target and generate large amount of heat at the target. Thus the metal target which is kept cooled by continuous flow of chilled water.

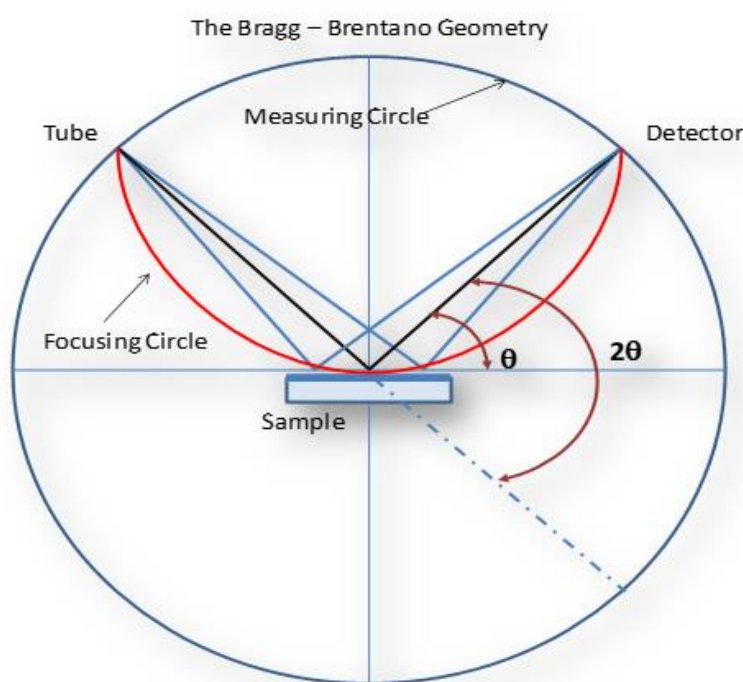


**Figure 2.2: Schematic diagram of a typical powder X-ray diffractometer <sup>78</sup>.**

The produced X-rays emerges through 360° within the sealed tube. Hence, slightly divergent X-ray radiations emitted in a particular direction is allowed to pass through a beryllium (Be) window. White radiation associated with the X-ray generation process and characteristic  $K_{\beta}$  radiation are filtered using (Z-1) metal as filters (Nickel is used for copper target). The incumbent X-ray beam passes through the soller and divergence slits before falling upon the sample which is homogenously spread over a rectangular groove in a glass slide. The diffracted (or scattered) X-ray beam passes through the soller and receiving slits before reaching the monochromator from where X-rays of a particular wavelength only reaches the detector. The role of the monochromator is to separate the stray wavelengths of inelastic

scattered radiations as well as any fluorescent radiation emitted by the sample. The details of X-ray generation and typical X-ray spectra are explained in several monographs<sup>97,98</sup>.

Powder X-ray diffractometers are usually designed based upon the Bragg-Brentano geometry as depicted in **Figure 2.3**. It can be seen from the diagram that the X-ray source, sample holder and detector subtend an angle  $\theta$  with each other and all are located along the circumference of the smaller circle termed as the focussing circle. During measurement, for a movement of  $\theta$  by the sample holder, the detector subtends an angle of  $2\theta$ . From the point of view of the measuring circle or the larger circle, the source and detector lie at the circumference whereas the sample holder lies at the centre.



**Figure 2.3: Diagram showing the schematic of Bragg-Brentano geometry<sup>78</sup>.**

Powder XRD measurements were carried out in a Panalytical Xpert pro powder diffractometer based upon the Bragg-Brentano geometry. Cu  $K_{\alpha}$  from a sealed tube was used as the source of X-ray radiation. Nickel foil was used as filter to cut off white radiation and  $K_{\beta}$ . Monochromator used consists of a curved graphite single crystal and detector is an Argon filled proportional

counter. The powder X-ray diffractometer was operated at 40 kV voltage and 30 mA operating current, and was calibrated using silicon as standard.

The output of diffraction measurement is obtained as a plot of the intensity of the diffracted rays versus  $2\theta$  (deviation of incident wavefront). Sharp and intense peaks are observed upon constructive interference of the diffracted X-rays when the incident beam subtends Bragg angle ( $\theta$ ) for a particular (hkl) plane. In general, for phase identification of a crystalline compound, a short time scan of around 30 mins scan in the  $2\theta$  range of 10 to  $70^\circ$  is sufficient whereas for structural studies a scan for around 3-4 h is required. The next step involves matching of the observed diffraction patterns with JCPDS (Joint Committee on Powder Diffraction Standards, 1974) data available for reported crystalline compositions. Unit cell parameter can be calculated easily from the recorded diffraction pattern by noting the  $2\theta$  values corresponding to peak positions and refining by a least square method using computer software “Powderx”<sup>99</sup>. Average crystallite size of the synthesized nano-crystalline compositions can also be estimated from the full width at half maximum (FWHM) value of the intense peak present in the diffraction pattern using the Scherrer’s formula, which is given by

$$t = 0.9\lambda / B\cos\theta_B \quad (\text{eqn. 2.5})$$

where  $t$  is the size of the crystal (in angstroms),  $\lambda$  is the X-ray wavelength and  $\theta_B$  the Bragg angle. The line broadening,  $B$ , is measured from the extra peak width at half the peak height and is obtained by the Warren formula:

$$B^2 = B_M^2 - B_S^2 \quad (\text{eqn. 2.6})$$

where  $B_M$  is the measured peak width of the sample in radians at half peak height and  $B_S$  is the measured peak width of a standard material (silicon).

Structural studies of unknown crystalline compounds are carried out from observed diffraction patterns using Rietveld refinement methodology<sup>100–103</sup>. This method applies to the

step scan data of a crystalline solid sample obtained from a well-aligned powder diffractometer. The basic principle of Rietveld refinement method is based upon calculation of intensity of any unknown crystalline compound by combining with all the structure factors with an assumed model unit cell and profile parameters for peaks and background. The applied standard structural model takes into account the space group, atomic position coordinates and guess unit cell parameters (which should be close to the sample). Profile data is defined by specific mathematical functions viz. Gaussian, Lorentzian or their combination termed as pseudo-Voigt function and background data by a smooth variable function.

$$Y_{ci} = y_{bi} + s \sum_{hkl} L \times P \times n \times |F_{hkl}|^2 \phi(2\mathcal{G}_i - 2\mathcal{G}_{hkl}) \times P_{hkl} \times A \quad (\text{eqn. 2.7})$$

where  $Y_{ci}$  = Calculated intensity at the  $i_{th}$  step,  $y_{bi}$  = Background intensity at  $i_{th}$  step,  $L$  = Lorentz factor,  $P$  = Polarization factor,  $|F_{hkl}|^2$  = Structure factor for  $hkl$  reflections,  $\phi(2\theta_i - 2\theta_{hkl})$  = Profile function,  $P_{hkl}$  = Preferred orientation function,  $A$  = Absorption correction,  $S$  = scale factor.

The profile functions of diffraction peaks are defined in terms of full width at half maximum ( $H_{hkl}$ ), FWHM, which is represented as a function of  $\theta$  as below:

$$H_{hkl}^2 = U \tan^2 \mathcal{G} + V \tan \mathcal{G} + W \quad (\text{eqn. 2.8})$$

Several profile functions are available in the program for fitting of the Bragg peaks. It is well known that peak shapes of XRD data are generally Lorentzian or mixed Gaussian and Lorentzian type. The best selection is mostly based up on user's judgements with logical reasoning and visual match of data with goodness of fit parameters.

Apart from Fullprof, other computer packages such as DBWS, GSAS, Rietan, Maud, etc. are also available for carrying out structural characterization by Rietveld refinement. Refinement progress remains smooth if the initial presumption of scale factor, background parameters and approximate position coordinates are closer to the real value. The guess unit

cell parameters, FWHM and mixing parameters are first refined followed by the thermal parameters, preferred orientation and asymmetry parameters. The progress of refinement is usually monitored by the difference plot of the observed and calculated diffraction profiles using Winplotr. The goodness of fit of the refinement is generally judged by the residual indicators associated with the program. Several residual indicators (termed as R parameters) shown in **Figure 2.4** are routinely calculated by Rietveld refinement programs and displayed at each cycle of refinement.

$R_p = \frac{\sum (Y_{io} - Y_{ic})}{\sum Y_{ic}}$	→	<b>R. Pattern</b>
$R_{wp} = \left[ \frac{\sum w_i (Y_{io} - Y_{ic})^2}{\sum w_i Y_{io}^2} \right]^{1/2}$	→	<b>R. Weighted pattern</b>
$R_{exp} = \left[ \frac{N - P + C}{\sum w_i Y_{io}^2} \right]^{1/2}$	→	<b>R. Expected</b>
$R_F = \frac{\sum  I_{hkl(o)}^{1/2} - I_{hkl(c)}^{1/2} }{\sum I_{hkl(o)}^{1/2}}$	→	<b>R. Structure factor</b>
$R_B = \frac{\sum  I_{hkl(o)} - I_{hkl(c)} }{\sum I_{hkl(o)}}$	→	<b>R. Bragg</b>
$S = \frac{W_{wp}}{W_{exp}} = \chi$	→	<b>Goodness of Fit</b>
$d = \frac{\sum ((\Delta_i / \sigma_i) - (\Delta_{i-1} / \sigma_{i-1}))^2}{\sum (\Delta_i / \sigma_i)^2}$	→	<b>Durbin-Watson Statistics</b>

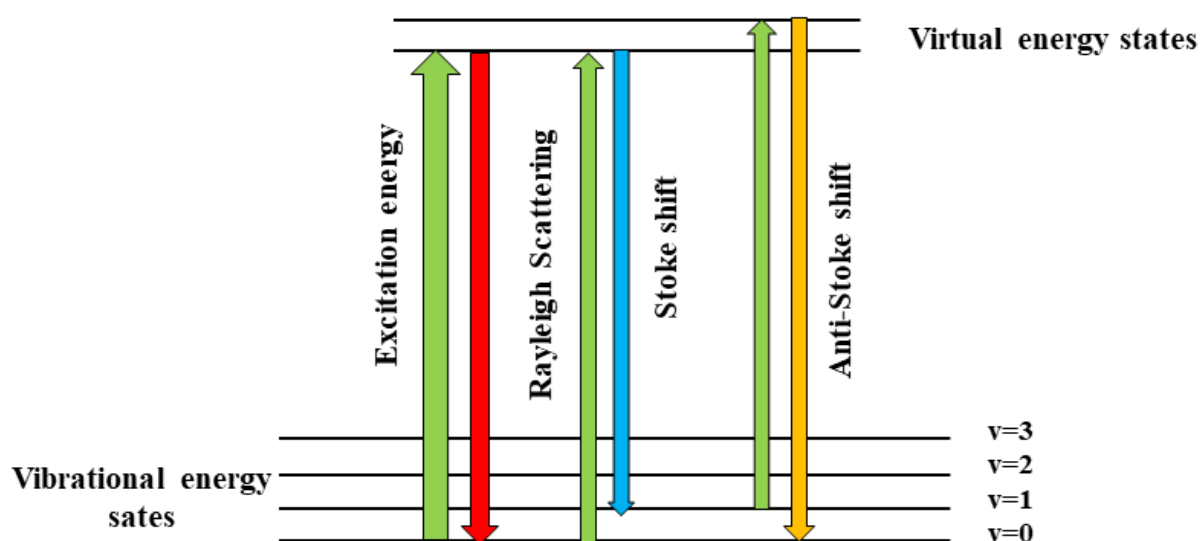
**Figure 2.4: Different goodness of fit parameters associated with Rietveld refinement.**

### 2.3.2. RAMAN SPECTROSCOPY

Raman spectroscopic technique is a vibrational spectroscopy method which is based vibration of atoms in the material. Some pyrochlore related materials pertaining to the thesis



work were characterized by this technique. Raman scattering from solid samples basically arises from quantum of lattice thermal vibrations termed as phonons. In this technique, a monochromatic incident radiation is scattered inelastically from different vibrational states of the sample being investigated. The spectrum obtained from the scattered radiation gives insight about the vibrational energy differences between the incident and the scattered radiation <sup>104–107</sup>.



**Figure 2.5: Schematic representation of Raman Scattering.**

The elastic scattering mode upon excitation is termed as Rayleigh scattering as shown in **Figure 2.5**, whereas the inelastic scattering modes constitute the phenomena of Raman scattering technique. Raman scattering or precisely called the “Raman effect” arises when an incident photon interacts with the electric dipole of a molecule. This scattering is perceived as an excitation to a virtual state (located at lower energy level to the next electronic level) followed by a real electronic transition with nearly coincident de-excitation and a change in vibrational energy. The population of electrons at vibration excited states is low at room temperature and not zero. Hence, the initial state is the ground state and the scattered photons will have lower energy than the incident radiation which is termed as the Stokes shift. However,

small fraction of molecules present in vibrationally excited state upon excitation emits radiation higher in energy than the incident photon which is termed as Anti-Stokes shift. In general, Anti-Stokes shift in Raman spectrum is always weaker than Stokes shift.

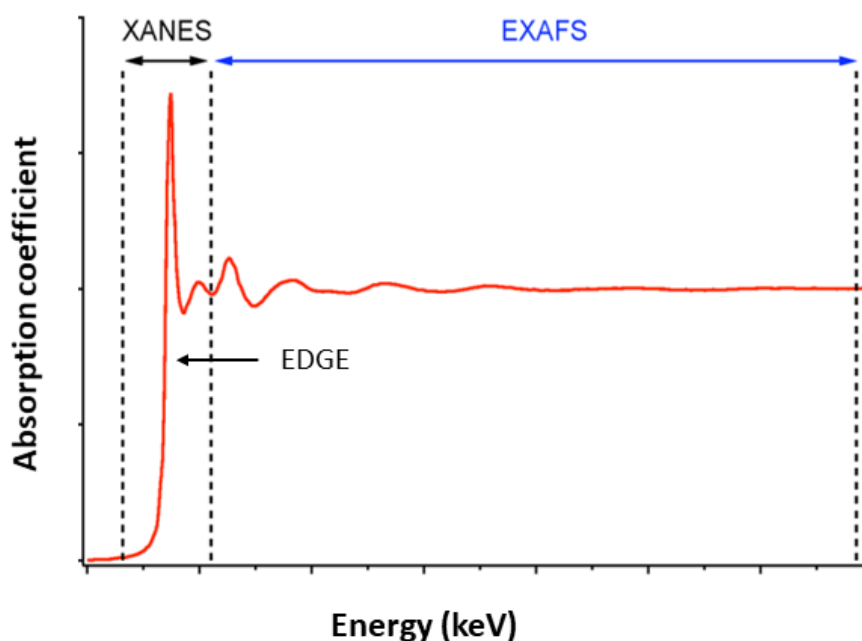
Raman scattering is one of the most popular and versatile techniques for investigation of short range ordering in crystal stabilized in disordered state such as nano crystals, alloys, impurity doped semiconductors and ion implanted substrates. The phonon energy is dependent upon the crystallographic position coordinates of the atoms present in the lattice and their local coordination with the neighbouring atoms via bond angle, bond length and bond strength. This spectroscopic technique enables one to directly identify local vibrational modes that are strongly related to the presence of impurities or some vacancies. This technique also provides detailed information about the identity and nature of various defects present in the crystal lattice. Thus, important insights can be acquired from Raman scattering for samples having chemically substituted entities, irradiation damages, etc. A Raman spectrophotometer consists of the following components:

- a) An excitation source which is mostly a laser
- b) A lens assembly to illuminate and collect the incident and scattered light.
- c) A dispersive element (which is a single, double or triple monochromator)
- d) A detector assembly which is either a photomultiplier tube or a cooled charge coupled device (CCD).

Raman spectroscopic measurements were performed with a Horiba Jobin Yvon LabRAM HR UV micro spectrometer equipped with an edge filter and thermoelectric-cooled multichannel CCD detector<sup>108</sup>. The 632.8 nm line of the HeNe laser with a power of 10mW was used as excitation source for Raman scattering measurements.

### 2.3.3. X-RAY ABSORPTION FINE STRUCTURE (XAFS)

X-ray absorption fine structure is a very promising tool for understanding of structural aspects of a host of materials ranging from crystalline to amorphous solids, glasses, polymers, etc. XAFS examines the modulation of the probability of X-ray absorption at energies around the binding energy of the core electron of the elements present in the system. The variation of X-ray absorption by any atom in the specimen depends on the chemical environment of a particular atom over short or long distance depending upon the energy. The absorption spectrum of X-ray consists of three regions: Edge region, X-ray absorption near edge structure (XANES) and extended X-ray absorption fine structure (EXAFS) as shown in **Figure 2.6**.



**Figure 2.6: Schematic diagram showing the three distinct zones of XAFS.**

The edge region gives us knowledge of the oxidation state of the investigated atoms present in the material. This can be obtained by comparing with a standard material. XANES covers over 50-100 eV energy range around the edge and imparts information about the band structure, hybridisation of molecular orbitals and tendencies of long range ordering of the

investigated material. EXAFS consists of the Kronig structure which is basically an oscillatory function spreading over 100 eV past the absorption edge which imparts knowledge about the local structure, coordination number, nearest neighbour distance and presence of disorder present in the investigated sample.

XAFS involves a process where an X-ray beam is incident on an atom causes ejection of a core electron which is filled by a valence electron. The ejection of core electron only takes place when the incident X-ray energy is higher than the binding energy of the core electron. This phenomenon is related to the X-ray absorption coefficient or  $\mu$ , which describes the relationship between incident and outgoing X-ray beam intensity and mathematically can be written as

$$\mu = -(d\ln I/dx) \quad (\text{eqn. 2.9})$$

where,  $dx$  is the traversed distance within the sample and  $I$  is the intensity of X-ray beam. In an EXAFS spectrum, various sharp peaks termed as edges are observed which corresponds to the ionization of a core orbital electron (K edge, L edge, etc.). Downward oscillations after each edge is attributed to the interactions between the ejected photoelectron and the electrons of the surrounding atom. This interference observed depends upon the nature of surrounding atoms, which in turn depends on distance from the central atom. EXAFS region is defined in terms of the absorption coefficient as

$$\chi(E) = [\mu(E) - \mu_0(E)] / \Delta\mu_0 \quad (\text{eqn. 2.10})$$

where  $[\mu(E) - \mu_0(E)]$  represents removal of background and division by  $\Delta\mu_0$  represents normalization of the curve. It is a general practice to use photoelectron wave vector  $k$  proportional to momentum during EXAFS calculation. The first step involves solution of  $k$  assuming  $E > E_0$ . The oscillations are then amplified by plotting as  $k^3$  instead of  $k$ . From Fermi's golden rule, it is known that  $\mu$  is proportional to square of the transition moment integral and

it is related to the wave function  $\psi(k)$ . The R dependence is finally calculated by using EXAFS equation and then a final Fourier transformation of the data from frequency space to the radial space gives the radial distribution function. XAFS were recorded in fluorescence mode at the ADXRD beamline (BL-12) of Indus-2 synchrotron source, RRCAT, Indore, India<sup>108</sup>. Powdered sample of thickness around 0.2 mm was placed between two kapton films. The incident photon flux was measured by an ionization chamber whereas fluorescent photon flux was measured by using a Peltier cooled energy dispersive detector (Vortex-Ex)<sup>108</sup>.

#### 2.3.4. CALVET OXIDE MELT SOLUTION CALORIMETER

Calorimetry is that branch of science which measures the change in heat or enthalpy associated with some physical or chemical changes in a material. The estimation of associated heat change in a process provides insights on the thermochemical or thermophysical properties of different compounds. Calorimetry is divided into two categories viz. reaction calorimetry and non-reaction calorimetry. Reaction calorimetry involves heat changes associated with or because of a chemical reaction whereas non-reaction calorimetry involves measurement of heat change owing to a physical process. Calorimetric measurements are generally carried out under constant pressure or constant volume conditions. Measurement under constant pressure gives the change in enthalpy of a system whereas heat change measurement under constant volume condition gives the change in internal energy of a system.

Calorimetric technique revolves around three variables viz. temperature of the calorimeter ( $T_c$ ), associated heat change ( $Q$ ) and temperature of the surroundings ( $T_s$ ). Depending upon the measuring parameter, there are four different types of calorimeters:

a) **Isothermal calorimeter:** Here  $T_c = T_s = \text{constant}$  and  $Q$  is measured by measurement of changes in physical property of surrounding materials e.g. ice calorimeter and diphenyl ether calorimeter.

**b) Adiabatic calorimeter:** Here,  $T_c = T_s$  but both are variable. The associated process changes the temperature of the calorimeter. In order to maintain  $T_c = T_s$ , measured heat flux is supplied to the system or the surrounding, and this compensated heat is measured which is related to energy change involved in the corresponding process.

**c) Heat flow calorimeter:** Here, heat flow between the system and the surrounding due to temperature difference is measured. In this calorimeter, a deliberate heat exchange takes place which is channelized through a thermopile. Voltage difference developed by the thermopile is a measurement of the heat change associated with any process. An example of these types of calorimeter is Calvet calorimeter<sup>109</sup>

**d) Isoperibol calorimeter:** Here  $T_s$  is maintained at a constant temperature and the change in  $T_c$  is monitored<sup>110</sup>. Heat exchange between calorimeter and surrounding is prevented by thermal insulation and the temperature variation is a measurement for the heat change with associated processes.

In the present work, a heat flow calorimeter was used to measure the heat of reaction and deduce their standard enthalpies of formation. Calvet melt solution calorimeter consists of two identical cylindrical holes enclosed by Pt/Pt–Rh thermopiles for measurement of any heat change associated with any process happening inside. The thermopiles are connected to the two holes in opposition to give null signal at some temperature for both the cells. Through these holes two identical alumina made one open ended tube are placed inside. The top ends of these alumina tubes are connected to a dropping mechanism set up maintained at 298.15 K. In the event of any reaction associated with the absorption or evolution of heat in one of the cells, an emf is generated in the thermopile. Integration of the total area between the emf vs time curve to the zero baseline is considered proportional to the heat effect associated with any process (endothermic or exothermic) taking place inside the calorimeter.

The electrical signal generated in nano-volt range is amplified considerably to read in milli or micro volt scale. Since these signals represent the amount of thermal energy, either absorbed or evolved, integration of that signal over the time period gives the total energy change associated with any process happening inside. Heat calibration of the instrument was carried out by using a synthetic sapphire sample [NIST SRM-720].

Calorimetric solvent used for the measurement of the samples is a eutectic mixture of sodium oxide and molybdenum oxide i.e.  $\text{Na}_2\text{O} + \text{MoO}_3$  (3:4 molar mixture) maintained at 986 K. Initially, a mixture of perfectly dried fine powders of dried  $\text{Na}_2\text{CO}_3$  (BDH, reagent grade) and  $\text{MoO}_3$  (BDH, reagent grade) in appropriate stoichiometric ratio is ground in an agate mortar and pestle. The solvent is prepared by heating the homogenized mixture in a platinum bowl at 973 K. At this temperature,  $\text{Na}_2\text{CO}_3$  decomposes to  $\text{Na}_2\text{O}$ , thereby reacting with  $\text{MoO}_3$  to form a eutectic mixture. The melt is kept at that temperature for 6 h for further homogenization. Correct stoichiometry of the melt was maintained by observing the mass loss of the melt and was compensated by mixing the required amount of volatile  $\text{MoO}_3$  followed by re-melting. On observation of no mass loss after cooling, the melt was scratched and reground again to obtain fine powders. Chemical analysis was carried out on the solvent powders to find out the stoichiometry. The atom % of Mo, Na and O estimated by chemical analysis of the solvent were found to be  $16.2 \pm 0.2$ ,  $23.4 \pm 0.3$  and  $60.4 \pm 0.4$ , respectively<sup>111</sup>. Powder X-ray diffraction studies carried out on the melt powders did not exhibit any peak corresponding to any impurity present in the melt. Calorimetric solvent prepared in the same batch was used in all the reaction enthalpy measurements to ensure reproducibility of thermodynamic data.

For measurement of the enthalpy of dissolution, the reaction tubes were equilibrated for around 10-12 h at 986 K till a steady base line for heat flux signal was observed. The slope of the base line of the differential heat flow signal was nearly ascertained to be zero as any minor and unwanted loss of volatile components will get nullified as similar effects will be

observed in sample and reference cells<sup>111</sup>. Small pellets containing few milligrams of the sample as well as their component binary oxides were dropped from room temperature maintained at the dropping mechanism set up to the calorimetric solvent maintained at 986 K. As mentioned earlier, the net effect of heat change was measured by integration of the heat flow signal with respect to time. The completion of dissolution reaction was ascertained only when a steady base line was observed after each dropping and the values of reaction enthalpy obtained as a function of time converged into a constant value. The reaction time was determined for each dissolution experiments and heat flow signals for same time period was recorded for all the experiments. For each set of experiments, fresh solvent was used to maintain the condition of infinite dilution i.e. the amount of species was dropped in such a manner that their concentration remained well below 1 atom%. Moreover, the consistency in the values of reaction per unit mass of the reactants indicate that the infinite dilution condition was maintained during the experiments. After each set of measurements, the calorimetric solvent was withdrawn from the calorimeter and cooled to room temperature<sup>111</sup>. Oxygen bubbling experiments into the solvent was avoided as it becomes very difficult to obtain a steady base line. In addition to this, solvent particles borne by oxygen may react with quartz producing undesirable and uncontrollable heat effects which may affect the reproducibility of the results. The molar enthalpy of dissolution as well as the specific heat capacity of some of the samples presented in this thesis work was measured using a Calvet calorimeter (SETARAM, Model HT-1000).

### **2.3.5. THERMOGRAVIMETRIC ANALYSIS COUPLED WITH DIFFERENTIAL THERMAL ANALYSIS (TG-DTA)**

Thermogravimetric (TG) analysis is based upon the principle of monitoring a known mass of any material or a mixture as a function of temperature during a pre-determined heating or cooling cycle. In this experimental technique, the mass loss or gain is observed by means of



a thermo balance during heating or cooling stage or as a function of time (isothermal condition) in a specified atmosphere. Loss volatile substances (such as O<sub>2</sub>, CO<sub>2</sub>, NH<sub>3</sub> etc.) or water of crystallization from sample is revealed by a weight loss in a thermogram whereas oxidation or adsorption of a gas on sample surface results in weight gain of the sample.

Differential thermal analysis (DTA) technique involves measurement of the temperature difference between the sample under study and an inert reference material as a function of temperature as both are simultaneously cooled or heated at a pre-determined rate. The DTA shows a steady base line if no thermal effect is occurring in the sample in the temperature range of measurement. If any physical or chemical change takes place in the sample which is associated by significant heat change effect, the temperature of the sample either lags behind or leads with respect to the inert reference material and this difference of temperature ( $\Delta T$ ) is observed as a peak. Area under the peak gives us an estimate of the total associated heat change. An increase in temperature indicates an exothermic reaction of the sample whereas a decrease in temperature shows an endothermic reaction and their corresponding peak appear in opposite directions.

Simultaneous TG-DTA experiments were preformed using a SETARAM simultaneous TG/DTA instrument, Model 92-16.18 to find out the glass transition temperature of some samples presented in this thesis. Flowing argon was used as the gas atmosphere and heating rate was kept at 10°C/min.

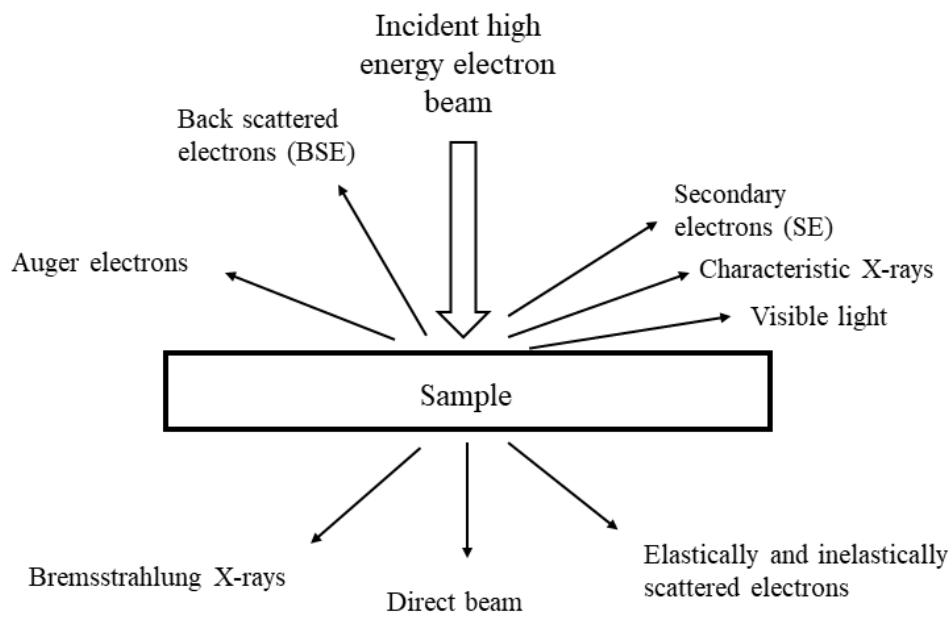
### **2.3.6. SCANNING ELECTRON MICROSCOPY (SEM)**

Electron microscopy is considered a specialized field of scientific research which employs an energetic beam of electrons as probe to form an image of the specimen sample. In comparison to light microscopy which uses visible light as probe and optical lenses for magnification, electron microscopes are operated in vacuum and electron beam focussed by electromagnetic lenses. Electron microscopy is able to garner significant information such as

morphology, crystallographic defects, composition of phases and estimation of the crystallite size etc. This technique uses shorter wavelength of electrons ( $\lambda = 0.005\text{nm}$  at an accelerating voltage of  $50\text{kV}$ ) to its advantage over wavelength of visible light ( $\lambda = 400\text{nm}$  to  $700\text{nm}$ ). SEM provides a larger depth of field which means a very small area of the sample can be brought to focus. It mainly scans a focussed and energetic beam of electrons across the sample and measures signals arising out of the electron beam-sample interaction. The most commonly used modes for imaging in SEM are secondary electron (SE) imaging and back scattered electron (BSE) imaging modes. Secondary electrons are considered as low energy electrons produced as a result of inelastic collisions of the primary electron beam with electrons of the atoms present in the sample. These electrons are readily absorbed because of their low energies and only those produced near the surface escape to the detector thereby producing detailed image corresponding to the surface topography. Apparent shadow observed in the SE images are a result of the absorption of the secondary electrons from the intermediate parts of the sample. Back scattered electrons (BSE) are relatively high energy electrons (typically greater than  $50\text{eV}$ ) which undergoes multiple elastic scattering within the sample. Greater energy of these electrons results in their larger interaction volume and lower spatial resolution compared to the secondary electrons. The extent of back scattering phenomena increases with increase in the atomic number ( $Z$ ) of the species present in the sample and thus brighter phases corresponds to the presence of higher high  $Z$  elements as compared to the darker phases. Different possible interactions of incident electron beam with sample is shown in **Figure 2.7**.

SEM requires an electron optical system, a stage for placing the sample, a secondary electron detector to collect generated secondary electrons, image display unit and an operating system. The electron optical system comprises of an electron gun, a condenser lens and an objective lens, all maintained under high vacuum. Electron gun is generally a tungsten filament, which

acts as electron source by the phenomena of thermionic emission. However, in modern microscope field emission guns (FEG) are used as electron source and they are becoming more promising for higher resolution. The generated electrons are accelerated to energies in between 20-30 KeV. Condenser lenses demagnifies the incumbent electron beam until it gets impinged upon the sample with a diameter of around 2-10nm. Ejected secondary electrons are detected



**Figure 2.7: Depiction of different phenomena occurring on interaction of electron beam with sample.**

by a scintillator coated on the tip of the detector maintained at a high voltage of around 10kV. The electrons are attracted to this high positive bias and they generate light upon impinging the scintillator material. The generated photon passes through a photo multiplier tube and gets amplified to give prominent electrical signal. Backscattered electron detectors are located above the sample in a "doughnut" type arrangement, concentric with the electron beam in order to maximize the solid angle of collection and consist of symmetrically divided parts<sup>112</sup>. However, electrons travelling only along the line of sight of the detector is collected for processing. The SEM images were recorded using FE-SEM (Zeiss, Model: Auriga, Japan).

### **2.3.7. ELECTRON PROBE MICRO ANALYZER (EPMA)**

An electron probe micro analyzer (EPMA) is a micro-beam base instrument used for non-destructive chemical analyses of solid samples. It is fundamentally quite similar to SEM but have additional capability of chemical analysis of the sample. The main importance of EPMA is its ability to gain precise insight of quantitative compositional analysis at very small spot size of 1-2 microns by wavelength dispersive spectroscopy (WDS) <sup>113</sup>. EPMA basically can give the following analysis depending upon the detectors used such as SE imaging, BSE imaging, cathodoluminescence (CL) imaging, acquiring 2D elemental mapping, compositional analysis by energy dispersive spectroscopy (EDS) or wavelength dispersive spectroscopy, etc. Modern day SEM's come with EDS mode can also be used for compositional analyses.

As mentioned earlier, electron sample interactions can lead to X-ray generation. These quantized generated X-rays are characteristic of the element and are measured using WDS assembly to give insight about the composition of the sample. EPMA instrument consists of an electron gun, a series of electromagnetic lenses a sample chamber with movable stage and a wide variety of detector assembly to cater to different needs of the user. EPMA finds its uses for problems such as chemical analysis of geological materials at small scale, identification of compositions of different phases present in a composite material like rocks, etc. <sup>113</sup>. The major advantages of EPMA lies in its ability to enable quantitative compositional analysis at very high sensitivity employing WDS technique. Imaging and quantitative analyses of the phases present in composites were performed by using Electron Probe Micro-Analyzer (CAMECA-SX 100).

### 2.3.8. X-RAY PHOTOELECTRON SPECTROSCOPY (XPS)

X-ray photoelectron spectroscopy (XPS), also known as electron spectroscopy for chemical analysis (ESCA), is considered as a semi quantitative spectroscopic tool that can give an insight into the elemental composition, empirical formula, chemical and electronic state of the elements present in a sample. XPS spectra is obtained by irradiation of sample kept under very high vacuum with a beam of aluminium or magnesium X-rays and simultaneous measurement of the kinetic energy and number of electrons escaping from the top layer (~ 1-10 nm) of the sample to the detector <sup>114</sup>. XPS techniques can be used to analyse surface chemistry of any sample either in pristine state or after cutting, scrapping, ion-beam etching, exposure to radiation, etc. XPS can detect all elements of the periodic table ranging from lithium ( $Z = 3$ ) even in parts per thousand range. Detection limits of up to parts per million is also possible with very long collection time.

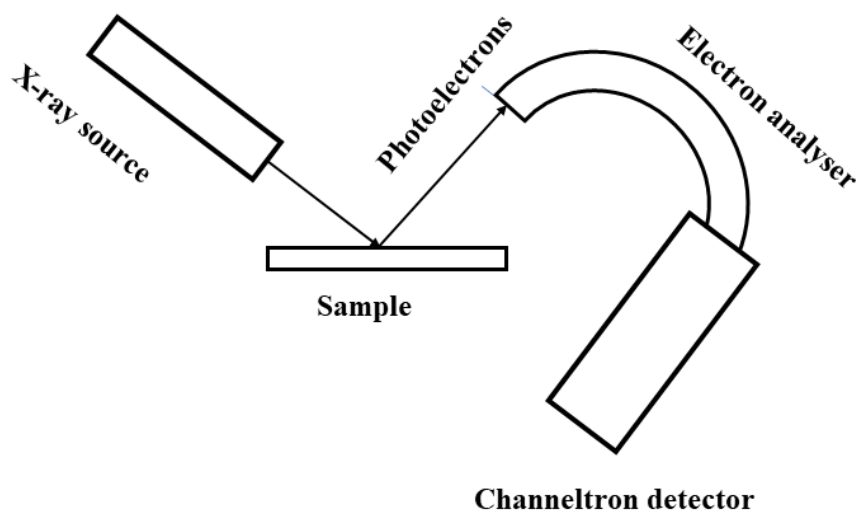
Binding energy (BE) of an electron emitted by a sample can be obtained by the equation

$$E_{\text{binding}} = E_{\text{photon}} - K_{\text{Kinetic}} - \Phi \quad (\text{eqn. 2.11})$$

Where,  $E_{\text{binding}}$  is the energy by which the electron is held in its orbit,  $E_{\text{photon}}$  is the energy of the incumbent X-ray source,  $E_{\text{kinetic}}$  is the kinetic energy of the emitted electrons and  $\Phi$  is the work function of the spectrometer.

A typical XPS spectrum is a plot of the number of electrons detected versus the binding energy of the electrons detected. Each element produces a characteristic set of binding energy values which correspond to the electronic configuration of the electrons present with the atoms. The number of detected electrons corresponding to each of the characteristic peaks is directly related to the quantity of element within the irradiated volume. Intensity of each raw XPS signal upon division by its relative sensitivity factor (RSF) and normalization over all elements detected has the potential to generate the atomic percentage content of the sample. XPS studies

are performed under ultra high vacuum as it involves electron count at different kinetic energy values with chances of minimum error and the detector assembly which is typically around one meter away from the sample holder. However, a fact to consider is that, only those electrons are detected that escapes into the vacuum and generally originates from top of the surface. Thus, XPS is considered as a versatile non-destructive technique for estimation of surface chemistry of any material. The basic components of XPS instrument are X-Ray source, sample stage and electron analyzer combined with detection system as shown in the **Figure.2.8**.



**Figure 2.8: Schematic diagram of different parts of a XPS instrument.**

Monochromatic  $K\alpha$  X-rays of aluminium are produced by diffraction and focusing of a non-monochromatic X-ray beam over crystalline quartz. The wavelength Al- $K\alpha$  is 8.3386 Å (0.83386 nm) which corresponds to a X-ray photon of energy 1486.7 eV. Similarly, monochromatic magnesium  $K\alpha$  has a wavelength of 9.89 angstroms (0.989 nm) which corresponds to photon energy of 1253 eV. X-ray photoelectron spectroscopy (XPS) studies pertaining to work related to this thesis were performed using SPECS XPS instrument with a PHOBIOS 100/150 delay line detector (DLD) with 385 W, 13.85 kV and 175.6 nA (sample

current). Al K $\alpha$  (1486.6 eV) dual anode was used as source<sup>108</sup>. C-1s peak (284.5 eV) was used as an internal reference for the absolute binding energy.

# **Chapter 3**

## **Structure and thermodynamic properties of potential waste immobilization lattices in Ca-Zr-Ti-O system: Calzirtite and Zirconolite**

The data reported in this chapter have been published in the following peer-reviewed journals:

- High temperature crystallographic and thermodynamic investigations on synthetic calzirtite ( $\text{Ca}_2\text{Zr}_5\text{Ti}_2\text{O}_{16}$ )  
M. Jafar, S. B. Phapale, S. N. Achary, R. Mishra, A. K. Tyagi  
*J Alloys Compd.* 682, (2016) 284-293.
- High temperature crystallographic and thermodynamic investigations on synthetic zirconolite ( $\text{CaZrTi}_2\text{O}_7$ )  
M. Jafar, S. B. Phapale, S. N. Achary, R. Mishra, A. K. Tyagi  
*J. Therm. Anal. Calorim.* 131(3), (2018) 2709-2718.



### 3.1. INTRODUCTION

Immobilization of separated actinides and minor actinides from the nuclear HLW in durable matrices is one of the major challenges of nuclear power technology <sup>48</sup>. Worldwide considered borosilicate glass matrix for immobilization of HLW has certain limitations such as limited stability due to their metastable nature and low solubility of actinides <sup>31</sup>. Hence as alternatives, natural rock analogue (SYNROC) composites of titanates and zirconates proposed by A. E. Ringwood <sup>38</sup> are also being considered for nuclear HLW immobilization matrices. The potential of SYNROC based matrices is based on their ability to immobilize varieties of cations of different charges and ionic radii without further segregation to any other phases or precipitation. Hence, the structural and chemical durabilities of these materials under external variables such as temperature, pressure and chemical environment i.e., in ground water conditions, are important information desired for their application.

One of the major constituent phases of SYNROC is zirconolite ( $\text{CaZrTi}_2\text{O}_7$ ). A large number of literature reports on zirconolite provides important insight about the solubility limits of actinides and formation of solid solutions under SYNROC preparation conditions as well as its structural and chemical stabilities under different temperature, pressure, radiation and hydrothermal conditions <sup>39,40,72,115,116</sup>. The low-cost processing in addition to higher chemical and structural abilities, the lower material and processing costs enable the phases in  $\text{CaO-ZrO}_2\text{-TiO}_2$  system to be primary constituents of SYNROC formulations. As a result of this, phase diagrams and phase relations in this system have been extensively investigated worldwide <sup>117</sup>. Though literature reports suggest the formation of zirconolite and perovskite related phases in these systems, Pyatenko and Pudovkina investigated a mineral analogous sample with a fluorite related structural arrangement, termed as calzirtite ( $\text{Ca}_2\text{Zr}_5\text{Ti}_2\text{O}_{16}$ ) <sup>118</sup>. It became a well-known fact that the calzirtite phase occurs with zirconolite in metasomatic calcite-forsterite-magnetite

rocks and its composition often show a variation in the Zr and Ti content but not in Ca concentration<sup>119,120</sup>.

Literature reports suggest a meagre substitution of trivalent ions like  $\text{Cr}^{3+}$ ,  $\text{Fe}^{3+}$  etc. pentavalent ions such as  $\text{Nb}^{5+}$ ,  $\text{Ta}^{5+}$ , etc. at Ti site, whereas no variation in Zr or Ca site is reported in literature<sup>120,121</sup>. However, Rossell had observed that calzirtite decomposes to zirconolite, zirconia and perovskite type phase at about 1670K which is considerably higher than SYNROC preparation temperature<sup>122</sup>. Crystallographic analysis of synthetic calzirtite confirmed the structure to be a super-structure of fluorite structure<sup>121,122</sup>. The Ca and Zr atoms have eight and seven coordinated polyhedra in both calzirtite and zirconolite but the coordination polyhedra around Ti sites show considerable differences. Moreover, the arrangements of the coordination polyhedra in these two structures are considerably different, and hence they exhibit appreciable differences in their properties. Calzirtite does not exhibit different polytype behaviour while zirconolite can exist in varieties of polytypes. Calligeri *et al.* have reported an orthorhombic variant of calzirtite wherein all the cations form similar coordination polyhedra as that in tetragonal variant, and the orthorhombic phase transforms irreversibly to tetragonal phase at higher temperature<sup>123</sup>.

In spite of a number of reports on the structural aspects of calzirtite, the high temperature behaviour and thermodynamic properties of calzirtite are not available in literature. Hence, detailed *in situ* high temperature structural studies and thermodynamic property measurements were carried out on zirconolite and calzirtite using calorimetric techniques as reported by Navrotsky *et al*<sup>124–127</sup>. Moreover, the relative stabilities of the two lattices were compared using high temperature calorimetric technique and that has been explained in this chapter.

### 3.2 EXPERIMENTAL METHODS

Calzirtite  $\text{Ca}_2\text{Zr}_5\text{Ti}_2\text{O}_{16}$  was synthesized by conventional solid state reaction of  $\text{CaCO}_3$  (Sigma Aldrich, St. Louis, MO, USA, purity > 99.9%),  $\text{ZrO}_2$  (Sigma Aldrich, purity 99.0) and  $\text{TiO}_2$  (Sigma Aldrich, purity  $\geq 99.5\%$ ).  $\text{TiO}_2$  and  $\text{ZrO}_2$  were preheated at 1173 K overnight whereas  $\text{CaCO}_3$  was dried in an oven at 473 K for 4 h. Stoichiometric amounts of  $\text{CaCO}_3$ ,  $\text{ZrO}_2$  and  $\text{TiO}_2$  in the molar ratios of 2: 5: 2 were weighed and homogenized in acetone media using agate mortar and pestle. The mixture was then pelletized and heated at 1473 K for 24 h thrice. After each treatment the sample was re-homogenized and pelletized, and then used for the next heat treatment. Finally, the pellets were sintered at 1523 K for 24 h and they were used for further studies. Similarly, zirconolite was prepared by mixing  $\text{CaCO}_3$ ,  $\text{ZrO}_2$  and  $\text{TiO}_2$  in the molar ratios of 1: 1: 2 and following a similar procedure. The final pellets of zirconolite were sintered at 1523 K for 24 h and used for structural and thermodynamic studies.

Powder X-ray diffraction measurements of calzirtite sample was carried out on a rotating anode based powder x-ray diffractometer (Rigaku, Japan) using  $\text{CuK}\alpha$  ( $\lambda = 1.5406$  and  $1.5444 \text{ \AA}$ ) radiation. Diffraction data was collected in the  $2\theta$  range of  $10$  to  $110^\circ$  with a step width of  $0.02^\circ$  and step time of 5 s. Diffraction patterns of zirconolite samples were recorded on the same diffractometer in the  $2\theta$  range of  $10$  to  $80^\circ$  using similar step width and step time as that for calzirtite.

High temperature (HT) XRD studies on calzirtite sample was carried out in the temperature range of 298 to 1473 K at a regular interval of 100 K on the same diffractometer using a high temperature attachment (Rigaku, Japan). The HT-XRD patterns corresponding to zirconolite was recorded in between 298 to 1273 K on Panalytical X-pert Pro diffractometer using an Anton Parr high temperature attachment. Platinum plate was used as sample holder in

both the cases. All the XRD patterns were analysed by Rietveld refinement method using Fullprof-2k software package <sup>103</sup>.

Standard molar enthalpies of formation of calzirtite ( $\text{Ca}_2\text{Zr}_5\text{Ti}_2\text{O}_{16,s}$ ) and zirconolite ( $\text{CaZrTi}_2\text{O}_7,s$ ) were experimentally determined from the heat of dissolution data of  $\text{Ca}_2\text{Zr}_5\text{Ti}_2\text{O}_{16}(s)$  and  $\text{CaZrTi}_2\text{O}_7(s)$ , and their binary constituent oxides such as  $\text{CaO}(s)$ ,  $\text{ZrO}_2(s)$  and  $\text{TiO}_2(s)$  in liquid  $\text{Na}_2\text{O} + \text{MoO}_3$  solvent (3:4 molar ratio) at 986 K employing a high temperature Calvet calorimeter (Setaram, Model HT-1000). Heat calibration was carried out by using a synthetic sapphire standard [NIST SRM-720]. Further details of the experimental set up and process are mentioned in chapter 2 of this thesis as well as in literature reports <sup>128,129</sup>.

Small broken pellets of  $\text{Ca}_2\text{Zr}_5\text{Ti}_2\text{O}_{16}(s)$  and  $\text{CaZrTi}_2\text{O}_7(s)$  were annealed in air at 1273 K for 50 h and stored in desiccator for  $H_T-H_{298,15}$  measurements so as to eliminate the effect of adsorbed moisture in the heat capacity of the two compositions. The enthalpy increments of the compounds were measured in the same Calvet calorimeter in the temperature range 324 to 986 K following the drop technique. The samples in the form of broken pieces of pellet maintained at 298 K in the sample holder were dropped into the sample cell maintained at a desired constant temperature. The endothermic heat flow signal accompanying the sample drop recorded under isothermal condition was evaluated to find out the enthalpy increments for the samples.

### **3.3. RESULTS AND DISCUSSIONS**

#### **3.3.1. STRUCTURAL STUDIES OF CALZIRTITE ( $\text{Ca}_2\text{Zr}_5\text{Ti}_2\text{O}_{16}$ )**

The powder X-ray diffraction data of both calzirtite and zirconolite were analysed by comparing with their reported XRD patterns and were found to be in good agreement. Structural studies of the two compositions were carried out by Rietveld refinement studies from their corresponding observed X-ray diffraction patterns. As mentioned in introduction section, calzirtite can exist in two forms with closely related structures viz. tetragonal ( $I4_1/acd$ ) and

orthorhombic (Pbca). These two structure types have almost similar coordination polyhedra around the metal ions with the exception of ordering of the cations and anions in the orthorhombic structure. Both the structural models were considered for analyses of the structural aspects of calzirtite lattice by Rietveld refinement. The peaks and background of the obtained powder XRD data were modelled using Pseudo-Voigt profile function and shifted Chebyshev polynomial function, respectively.

In case of calzirtite, all the intense peaks could be assigned to both the tetragonal ( $I4_1/acd$ ) and orthorhombic (Pbca) structural variants which may be due to minor orthorhombic distortions ( $6.97 \times 10^{-4}$ ) in the later structure. However, distinct peaks pertaining to primitive orthorhombic symmetry were found to be absent in the diffraction pattern. Keeping this in mind, further structural studies were carried out by considering the tetragonal structural variant of calzirtite. Upon consideration of the cationic compositions as a super structure of fluorite related structure, the composition of calzirtite can be explained as an anion deficient fluorite structure. The ordered arrangements of the ions could accommodate 16 anion vacancies within the structure. A close comparison between parent fluorite and calzirtite lattice rendered the vacant anion sites assigned to  $16e$  (0.25, 0.3333, 0) sites. The major difference between the calzirtite and fluorite structures lies in the fact that diverse cations of dissimilar ionic radii led to the difference of the coordination polyhedra within the structure of calzirtite. The tetragonal structure of calzirtite has two distinct crystallographic sites for  $Zr^{4+}$  viz. Zr1 and Zr2 respectively at  $16f$  and  $32g$  sites, one  $Ti^{4+}$  site (Ti1 at  $16f$ ), one  $Ca^{2+}$  site (Ca1 at  $16f$ ) and five distinct sites for  $O^{2-}$  viz. O1, O2, O3 at  $32g$  sites while O4 and O5 at  $16e$  sites. An insignificant amount of monoclinic  $ZrO_2$  phase was detected in the powder pattern and hence its structure was also considered in the Rietveld refinements. In an attempt to understand the cationic distribution at different sites, the occupancies were refined with a constraint to their concentration. Feeble distribution of cations between Ti1 and Zr1 sites was observed whereas

no intermixing of Ti with Zr2 (32g) or Ca1 (16f) was found out in accordance to other reports in literature <sup>121,122</sup>.

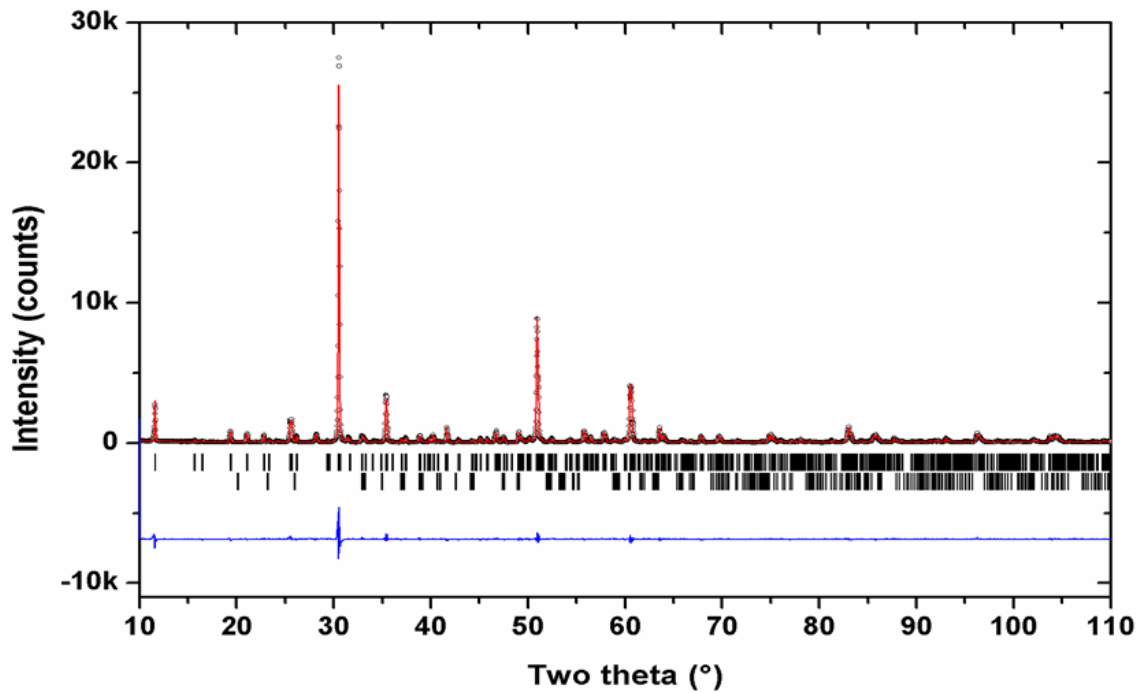
Furthermore, no occupancies of O<sup>2-</sup> at the vacant 16e sites was also concluded by refining the occupancies. These vacant sites thus formally coordinated with the Zr2 forming distorted cubical arrangement. These vacant sites were found to be linked with Ti1 sites and that lead to the formation of highly distorted cubic polyhedra around them. Hence, the coordination polyhedra of different cations can be explained like Ca1O<sub>8</sub>, Zr1O<sub>8</sub>, Zr2O<sub>7</sub> [V]<sub>1</sub> and Ti1O<sub>6</sub>[V]<sub>2</sub>, where V represents vacant 16e anionic site. These cubic polyhedra are edge shared with other polyhedra in a manner similar to a fluorite structure. Nevertheless, close analyses of the real structural parameters of the calzirtite structure shows the presence of regular Ca1O<sub>8</sub>, Zr1O<sub>8</sub>, Zr2O<sub>7</sub> and TiO<sub>6</sub> polyhedra by displacement of oxide anions from their crystallographic distinct sites of an ideal fluorite structure.

In the considered model, it was found out that the Zr1 is placed in 16f site with half occupancy resulting in a feeble displacement from the 8b site (0 0 0.25) on the 4<sub>1</sub> screw axis. The characteristic arrangement of bond around Zr1 (8b site) are: Zr1-O2 = 2.076(9) Å × 4 and Zr1-O3 = 2.494(9) Å × 4 whereas the distortion in the Zr1O<sub>8</sub> polyhedra is found out to be 83.515 × 10<sup>-4</sup>. Refinement of the XRD data by considering fully occupied 8b site by Zr1 exhibits a large displacement parameter (0.0182(16) Å<sup>2</sup>) around it. However, displacement of Zr1 atoms from the 4<sub>1</sub> screw axis severely reduces the isotopic displacement parameter to 0.006(1) Å<sup>2</sup>, whereas appreciable increase in bond distortion (Zr1-O2 = 2.088(10) Å × 2, 2.045(9) Å × 2 and Zr1-O3 = 2.313(9) Å × 2, 2.774(9) Å × 2 and distortion parameter 157.410 × 10<sup>-4</sup>) was observed. In addition to this, the residuals of refinement parameters with ordered Zr1 atoms were also found to be comparatively larger than that for disordered model [(R<sub>p</sub> = 8.90 %, R<sub>wp</sub> = 12.51 %, χ<sup>2</sup> = 3.48 (ordered model); R<sub>p</sub> = 8.29 %, R<sub>wp</sub> = 11.75 %, χ<sup>2</sup> = 3.07 (disordered model)], and hence the disordered structure was considered as the actual structure

of the tetragonal variant of calzirtite. The refined structural parameters of calzirtite at ambient temperature is given in **Table 3.1** and the corresponding Rietveld refinement plot is shown in **Figure 3.1**.

**Table 3.1: Refined structural parameters of calzirtite at ambient conditions<sup>130</sup>.**

Atoms	Sites	x	y	z	Biso ( $\text{\AA}^2$ )	Occupancy
Ca1	16f	0.3314(2)	0.5814(2)	0.12500	0.007(1)	1
Zr1(Zr/Ti)	16f	0.0125(3)	0.2625(3)	0.12500	0.006(1)	0.430(4)/0.070(4)
Ti1(Ti/Zr)	16f	0.1689(2)	0.4189(2)	0.12500	0.005(1)	0.070(4)/0.930(4)
Zr2	32g	-0.0178(1)	0.5878(1)	0.1107(1)	0.0043(4)	1
O1	32g	0.0814(7)	-0.0049(6)	-0.0432(8)	0.011(3)	1
O2	32f	0.0656(5)	0.1687(7)	-0.0029(7)	0.013(3)	1
O3	32g	0.1157(5)	0.3367(6)	-0.0006(9)	0.017(3)	1
O4	16e	0.25000	-0.0356(8)	0.00000	0.010(4)	1
O5	16e	0.25000	0.1786(9)	0.00000	0.006(4)	1



**Figure 3.1: Rietveld refinement plot of powder XRD data of calzirtite sample recorded at ambient temperature. The vertical line indicate Bragg positions for tetragonal calzirtite (1<sup>st</sup> row) and monolinic ZrO<sub>2</sub> (2<sup>nd</sup> row)<sup>130</sup>.**





**Table 3.2: The observed bond lengths (Å) of calzirtite at ambient temperature<sup>130</sup>.**

<b>Bond</b>	<b>Bond length</b>	<b>Bond</b>	<b>Bond length</b>	<b>Bond</b>	<b>Bond length</b>	<b>Bond</b>	<b>Bond length</b>
Ca1-O1	2.525(9)	Zr1-O2	2.088(9)	Zr2-O1	2.225(9)	Ti1-O1	1.949(10)
Ca1-O1	2.525(9)	Zr1-O2	2.044(9)	Zr2-O1	2.176(9)	Ti1-O1	1.949(10)
Ca1-O2	2.426(9)	Zr1-O2	2.044(9)	Zr2-O2	2.235(9)	Ti1-O3	1.957(9)
Ca1-O2	2.426(9)	Zr1-O2	2.088(9)	Zr2-O2	2.076(9)	Ti1-O3	1.957(9)
Ca1-O4	2.511(9)	Zr1-O3	2.313(9)	Zr2-O3	2.185(8)	Ti1-O4	1.898(5)
Ca1-O4	2.511(6)	Zr1-O3	2.774(9)	Zr2-O3	2.235(8)	Ti1-O4	1.898(8)
Ca1-O5	2.306(9)	Zr1-O3	2.774(9)	Zr2-O5	2.106(9)		
Ca1-O5	2.306(8)	Zr1-O3	2.313(9)				
<b>Av.</b>	2.442(3)		2.305(3)	<b>Av.</b>	2.177(3)		1.935(4)
<b>Dist.</b>	12.731× E -04		157.41× E -04	<b>Dist.</b>	7.308× E -04		1.858× E -04

In an attempt to comprehend the temperature induced structural changes of calzirtite, in situ high temperature XRD studies were carried out from ambient temperature to 1473 K at a step of 100 K each. Rossell<sup>122</sup> had reported decomposition of tetragonal calzirtite lattice to zirconolite, zirconia and calcium zirconate at around 1670 K. In order to confirm the above statement, one small pellet of calzirtite was kept at 1673 K for 24 h in furnace, cooled to room temperature, crushed into powder and analysed by powder XRD. Diffraction data did not reveal presence of any decomposed phases and thus, it could be said that, synthetic calzirtite is stable up to 1673 K. The observed XRD pattern at ambient temperature measured at high temperature set up was refined by considering the disordered structural model. The instrumental errors were corrected according to the observed structural parameters of calzirtite. XRD patterns recorded at sequentially increasing temperature were refined by Rietveld refinement method in like manner as that of the ambient temperature data. Apart from shifting of peak towards lower  $2\theta$  values with increase in temperature, no other differences were observed in the diffraction data recorded at different successive temperatures. The shifting of peaks towards lower  $2\theta$  values was attributed to the thermal expansion of lattice. However, a structural change was observed

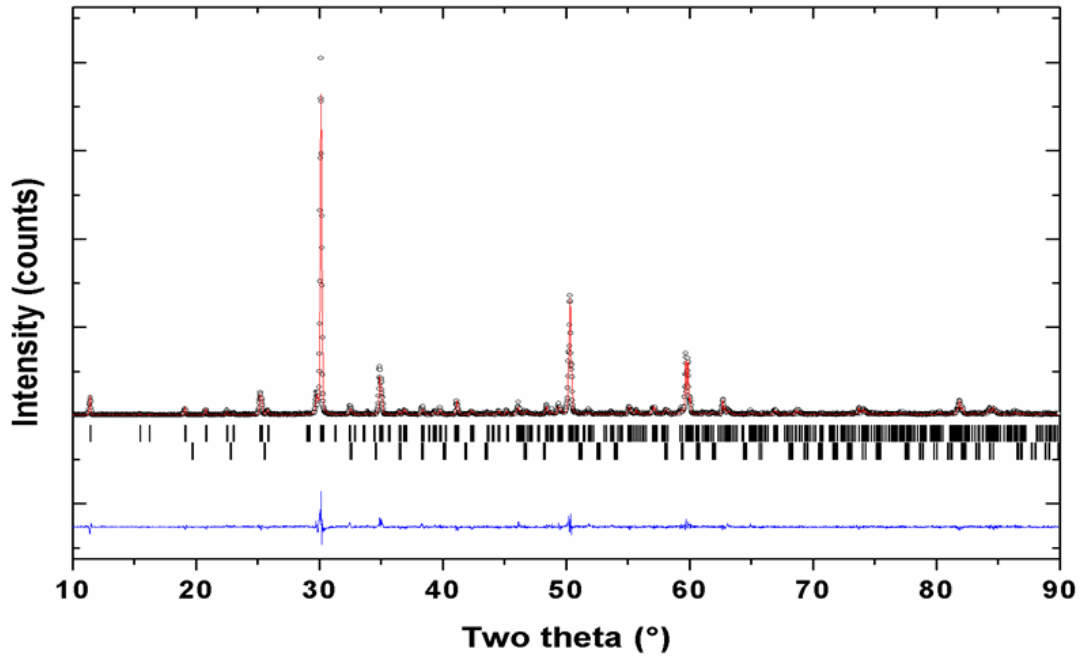
**Table 3.3: Refined structural parameters of calzirtite at 1473 K<sup>130</sup>.**

Atoms	Sites	x	y	z
Ca1	<i>16f</i>	0.3296(5)	0.5796(5)	0.125
Zr1(0.43Zr/0.07Ti)	<i>16f</i>	0.0120(7)	0.2620(7)	0.125
Ti1(0.93Ti/0.07Zr)	<i>16f</i>	0.1710(4)	0.4210(4)	0.125
Zr2	<i>32g</i>	-0.0156(2)	0.5863(3)	0.1126(3)
O1	<i>32g</i>	0.0947(14)	-0.0028(15)	-0.0414(19)
O2	<i>32f</i>	0.0648(12)	0.1627(14)	0.0037(16)
O3	<i>32g</i>	0.1266(11)	0.3438(12)	0.003(2)
O4	<i>16e</i>	0.25	-0.0260(18)	0.00000
O5	<i>16e</i>	0.25	0.1765(18)	0.00000

for the impure monoclinic zirconia phase above 1373 K which was attributed to phase transformation of the lattice from monoclinic to tetragonal lattice. The refined structural

parameters for calzirtite at 1473 K are summarized in **Table 3.3** and various inter-atomic distances are depicted in **Table 3.4**.

Typical Rietveld refinement plot for the XRD pattern of tetragonal calzirtite recorded at 1473 K is depicted in **Figure 3.3**. Temperature dependent unit cell parameters of calzirtite exhibited a gradual expansion as a function of increasing temperature as shown in **Figure 3.4**.



**Figure 3.3: Rietveld refinement plot of powder XRD data of calzirtite sample recorded at 1473 K. The vertical line indicate Bragg postions for calzirtite (1<sup>st</sup> row) and zirconia (2<sup>nd</sup> row)<sup>130</sup>.**

The unit cell parameter variation of calzirtite as a function of temperature can be represented by a second order polynomial equations as shown below:

$$a \text{ (Å)} = 15.197(1) + 1.01(3) \times 10^{-4} [T] + 3.48(2) \times 10^{-8} [T]^2 \quad (\text{eqn. 3.1})$$

$$c \text{ (Å)} = 10.094(1) + 5.6(3) \times 10^{-5} [T] + 2.1(2) \times 10^{-8} [T]^2 \quad (\text{eqn. 3.2})$$

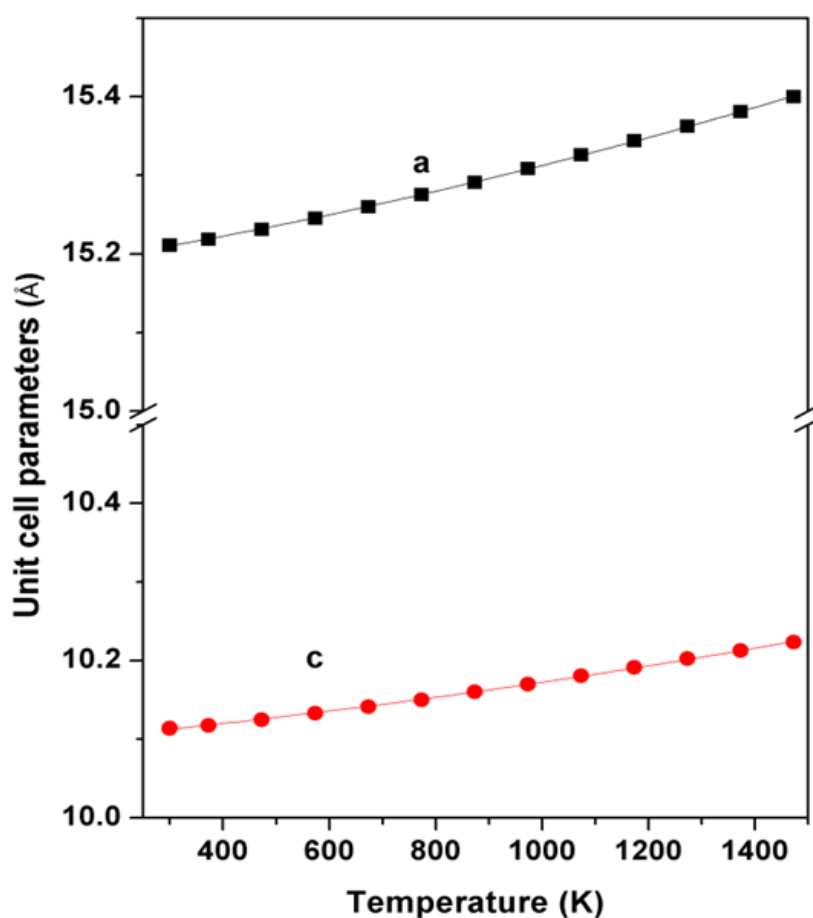
where, T is temperature in K.

Tetragonal,  $I4_1/acd$   
 $a = 15.3998(3) \text{ \AA}$ ,  $c = 10.2232(3) \text{ \AA}$   
 $V = 2424.48(10) \text{ \AA}^3$ ,  $Z = 8$   
 $R_p = 17.43 \%$ ,  $R_{wp} = 25.37 \%$ ,  $\chi^2 = 2.01$

**Table 3.4: The observed inter-atomic distances ( $\text{\AA}$ ) of calzirtite at  $1473 \text{ K}^{130}$ .**

Bond	Bond length	Bond	Bond length	Bond	Bond length	Bond	Bond length
Ca1-O1	2.421(22)	Zr1-O2	2.130(21)	Zr2-O1	2.370(21)	Ti1-O1	1.868(22)
Ca1-O1	2.421(22)	Zr1-O2	2.069(20)	Zr2-O1	2.302(22)	Ti1-O1	1.868(22)
Ca1-O2	2.412(20)	Zr1-O2	2.069(20)	Zr2-O2	2.371(19)	Ti1-O3	1.854(20)
Ca1-O2	2.412(20)	Zr1-O2	2.130(20)	Zr2-O2	2.081(18)	Ti1-O3	1.854(19)
Ca1-O4	2.404(20)	Zr1-O3	2.501(20)	Zr2-O3	2.340(18)	Ti1-O4	1.944(12)
Ca1-O4	2.404(16)	Zr1-O3	2.961(21)	Zr2-O3	2.286(19)	Ti1-O4	1.944(18)
Ca1-O5	2.316(19)	Zr1-O3	2.961(21)	Zr2-O5	2.129(18)		
Ca1-O5	2.316(16)	Zr1-O3	2.501(21)				
Av.	2.388(7)		2.415(7)	Av.	2.268(7)		1.888(8)
Distt.	$3.157 \times E-04$		$216.870 \times E-04$	Distt.	$22.689 \times E-04$		$4.414 \times E-04$

The average lattice thermal expansion coefficients of calzirtite in between the studied range of 300 K to 1473 K are  $\alpha_a = \alpha_b = 12.72 \times 10^{-6}/\text{K}$  and  $\alpha_c = 9.21 \times 10^{-6} /\text{K}$  whereas the volume thermal expansion coefficient is  $30.79 \times 10^{-6} /\text{K}$ . A closer look into the variation of bond lengths as a function of temperature depicted the elongation of bonds Zr1-O and Zr2-O whereas contraction of Ca-O and Ti-O bonds were observed. The contraction of Ca-O and Ti-O bonds and decreasing bond distortion could be related to symmetrisation of the polyhedra



**Figure 3.4: Variation of unit cell parameters of calzirtite as a function of temperature<sup>130</sup>.**

around  $\text{Ca}^{2+}$  and  $\text{Ti}^{4+}$  ions. As it was mentioned earlier, that the calzirtite structure is primarily maintained by the  $\text{Zr}_2\text{O}_7$  polyhedra leaving tunnel like empty spaces parallel to c-axis which are occupied by the fluorite like blocks of edge shared  $\text{CaO}_8$  and  $\text{TiO}_6$  octahedra and  $\text{Zr}_1\text{O}_8$  cubes as shown in **Figure 3.2**. Therefore, it can be said that, the maximum contribution to the

volume thermal expansion arises from the  $\text{Zr}_2\text{O}_7$  polyhedra expansion whereas the empty anion sites of  $\text{TiO}_6$  polyhedra along isolated  $\text{Zr}_2\text{O}_8$  chains mask the thermal expansion along the axis.

### 3.3.2. STRUCTURAL STUDIES OF ZIRCONOLITE ( $\text{CaZrTi}_2\text{O}_7$ )

In an effort to compare ambient as well as high temperature structural behaviour of zirconolite and calzirtite, similar studies were carried out with synthetic zirconolite ( $\text{CaZrTi}_2\text{O}_7$ ) sample. The ambient temperature structural studies of the prepared zirconolite compositions were carried out by Rietveld refinement of the observed powder X-ray diffraction pattern with its earlier reported structural parameters as mentioned in literature [7, 8]. The refined unit cells parameters as obtained from structural analysis are:  $a = 12.4413(2)$ ,  $b = 7.2700(1)$ ,  $c = 11.3744(2)$  Å,  $\beta = 100.557(2)^\circ$ ,  $V = 1011.38(2)$  Å<sup>3</sup> (Space group: C2/c) which were found to be in close agreement with the above mentioned literature<sup>115,116</sup>. Refined unit cell parameters of zirconolite at ambient temperature are given in **Table 3.5** and the corresponding refinement plot is depicted in **Figure 3.5**.

**Table 3.5: Refined structural parameters of zirconolite at ambient conditions<sup>131</sup>.**

Atoms		x	y	z	Biso	Occupancy
Ca1(8f)	$\text{Ca}^{2+}:\text{Zr}^{4+}$	0.3730(5)	0.1264(11)	0.4950(4)	0.022(2)	0.93(1) : 0.07(1)
Zr1(8f)	$\text{Zr}^{4+}:\text{Ti}^{4+}$	0.1230(2)	0.1241(5)	0.97432(20)	0.0048(7)	0.87(2) : 0.13(2)
Ti1(8f)	$\text{Ti}^{4+}:\text{Zr}^{4+}$	0.2487(5)	0.1223(13)	0.7450(4)	0.0152(1)	0.96(2) : 0.04(2)
Ti2(8f)	$\text{Ti}^{4+}:\text{Zr}^{4+}$	0.4700(11)	0.0520(12)	0.25000	0.046(6)	0.47(1) : 0.03(1)
Ti3(4e)	$\text{Ti}^{4+}$	0.00000	0.1293(15)	0.25000	0.016(3)	0.97(2)
O1(8f)	$\text{O}^{2-}$	0.3030(11)	0.134(3)	0.2825(12)	0.031(6)	1
O2(8f)	$\text{O}^{2-}$	0.4740(13)	0.131(2)	0.1015(12)	0.01775	1
O3(8f)	$\text{O}^{2-}$	0.2082(15)	0.086(2)	0.5718(13)	0.01775	1
O4(8f)	$\text{O}^{2-}$	0.3991(14)	0.152(3)	0.7221(13)	0.034(5)	1
O5(8f)	$\text{O}^{2-}$	0.7031(16)	0.1857(19)	0.5894(13)	0.01775	1
O6(8f)	$\text{O}^{2-}$	-0.0021(13)	0.118(2)	0.4144(13)	0.027(5)	1
O8(8f)	$\text{O}^{2-}$	0.1124(15)	0.0505(19)	0.7958(13)	0.035(6)	1

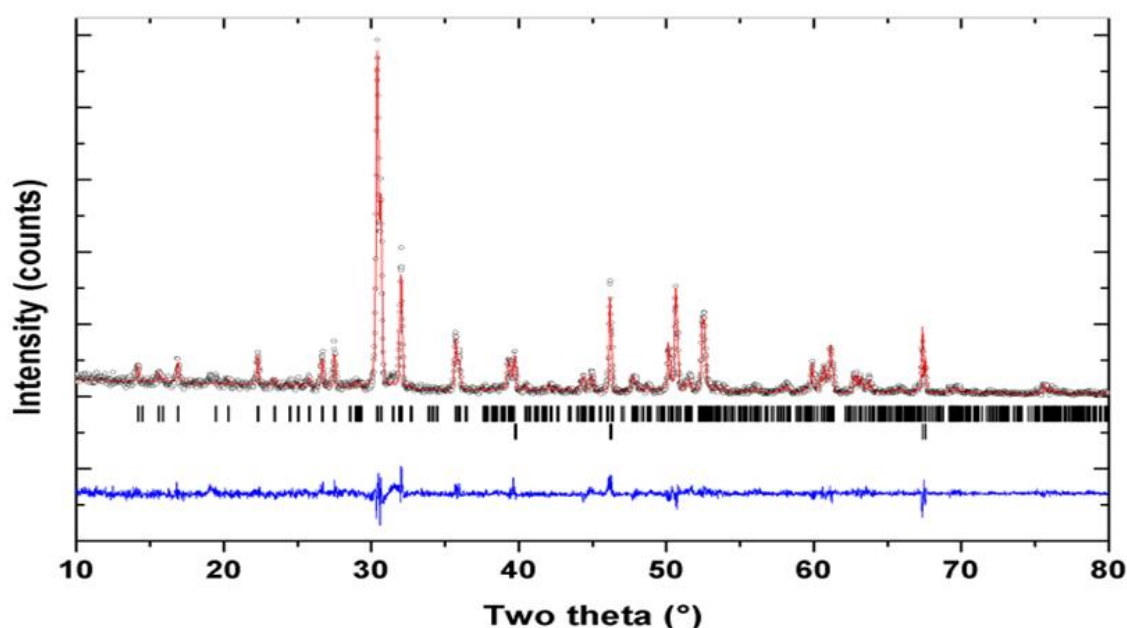
Monoclinic, C2/c

$a = 12.4413(2)$ ,  $b = 7.2700(1)$ ,  $c = 11.3744(2)$  Å,  $\beta = 100.557(2)^\circ$

$V = 1011.38(2)$  Å<sup>3</sup>,  $Z = 8$

$R_p = 9.66\%$ ,  $R_{wp} = 12.84\%$ ,  $\chi^2 = 1.89$

Zirconolite lattice contains one type of  $\text{Ca}^{2+}$  and  $\text{Zr}^{4+}$  (both  $8f$ ) site and three types of  $\text{Ti}^{4+}$  sites (two  $8f$  and one  $4e$ ). It was observed from the refinement that a partial distribution of around 7 atom % is possible in between  $\text{Ca}^{2+}$  and  $\text{Zr}^{4+}$  in the Ca1 site. Similarly, the Zr1 site also offers exchange of around 13 atom % by  $\text{Ti}^{4+}$ . The Ti1 and Ti2 sites also support limited exchange with  $\text{Zr}^{4+}$  whereas no mutual exchange of ions is observed at the Ti3 ( $4e$ ) sites. Thus it can be said that in contrast to calzirtite, a partial distribution of  $\text{Zr}^{4+}$  over the  $\text{Ca}^{2+}$  and  $\text{Ti}^{4+}$  sites

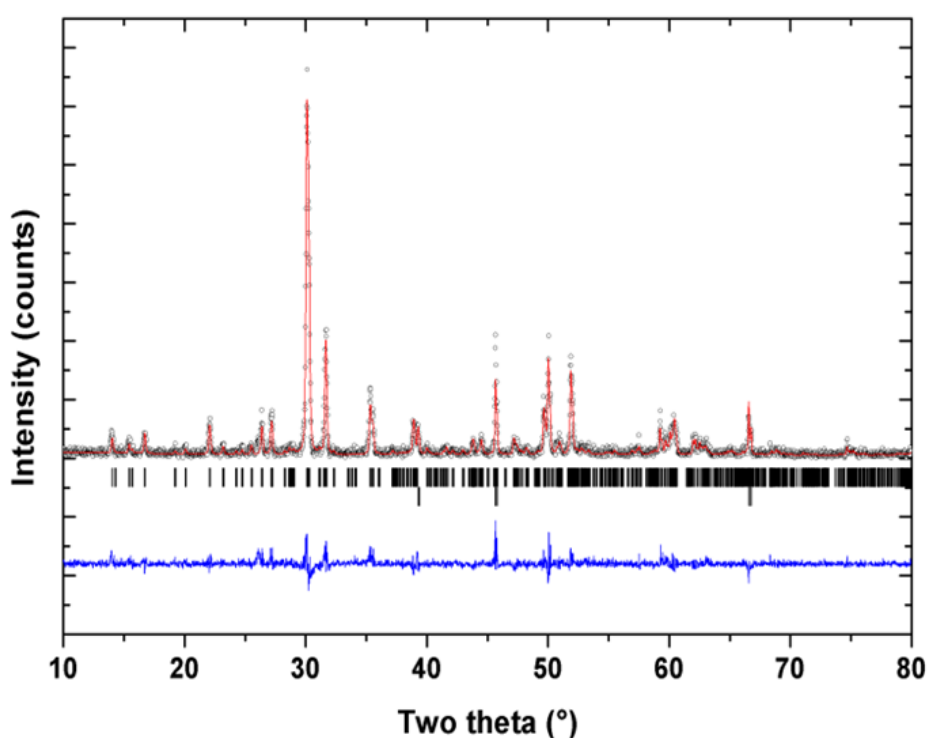


**Figure 3.5: Rietveld refinement plot of powder XRD data of zirconolite recored at 300 K. The vertical line indicate Bragg postions for zirconolite (1<sup>st</sup> row) and base metal platinum used as sample holder (2<sup>nd</sup> row)<sup>131</sup>.**

are allowed without alteration in the crystal structure of zirconolite. It may be noted that, as mentioned in chapter 1 that the backbone of zirconolite structure is formed by stacking of layers of octahedral  $\text{TiO}_6$  and trigonal bipyramidal  $\text{TiO}_5$  formed by an edge shared arrangement these polyhedra. The  $\text{Ca}^{2+}$  and  $\text{Zr}^{4+}$  ions are sandwiched in between these layers of Ti-O polyhedra. This in turn leads to eight coordinated  $\text{CaO}_8$  and seven coordinated  $\text{ZrO}_7$  polyhedra in the

structure. It is because of the flexibility of the Ti-O polyhedra that significant amount of intermixing among  $\text{Zr}^{4+}$  and  $\text{Ti}^{4+}$  ions are possible in particular at  $\text{TiO}_6$  and  $\text{ZrO}_7$  sites.

High temperature structural studies of zirconolite were carried out by Rietveld refinement of the in situ high temperature X-ray diffraction data recorded up to 1273 K. Shifting of peaks towards lower  $2\theta$  values with increase in temperature was observed and that could be attributed to the thermal expansion of lattice. Apart from that, no other change was observed in the diffraction pattern recorded as a function of temperature. This indicate for



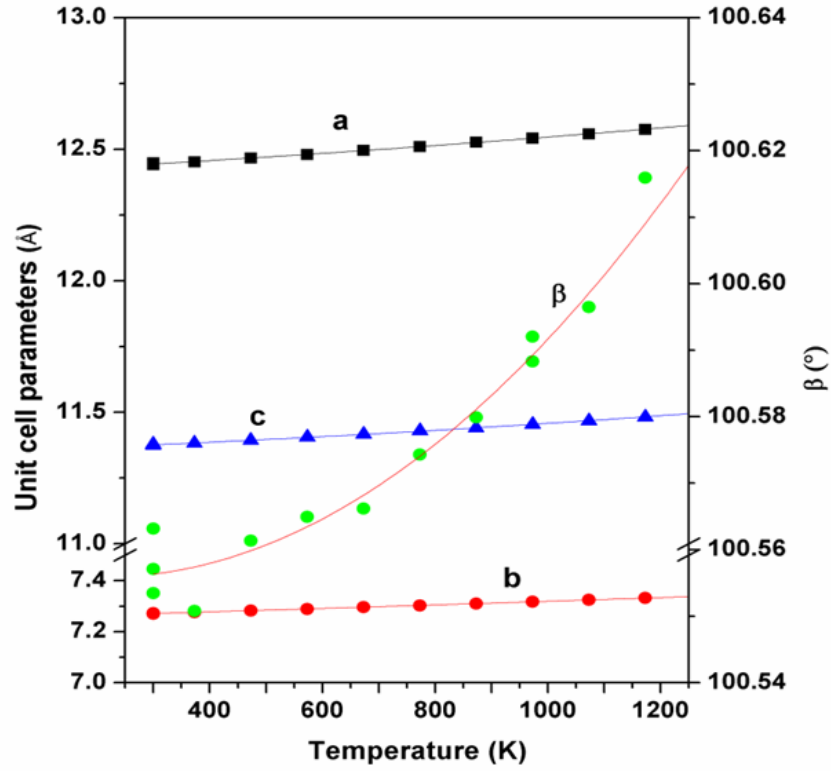
**Figure 3.6: Rietveld refinement plot of powder XRD data of zirconolite recored at 1273 K. The vertical line indicate Bragg postions for zirconolite (1<sup>st</sup> row) and base metal platinum used as sample holder (2<sup>nd</sup> row)<sup>131</sup>.**

absence of any structural transition of the sample in the studied range. The refined unit cell parameters of zirconolite at 1273 K are:  $a = 12.5951(7)$ ,  $b = 7.3381(4)$ ,  $c = 11.5004(6)$  Å and



$\beta = 100.616(6)^\circ$ ,  $V = 1044.7(1) \text{ \AA}^3$ . A typical Rietveld refinement plot of zirconolite at 1273 K is depicted in **Figure 3.6**.

The systematic variation of unit cell parameters of monoclinic zirconolite lattice as a function of temperature is shown in **Figure 3.7**. From this figure, it can be seen that unit cell



**Figure 3.7: Variation of unit cell parameters of zirconolite as a function of temperature.**

parameters show a gradual increasing trend with temperature and their temperature dependencies can be represented by second order polynomial relations as given below:

$$a (\text{\AA}) = 12.410(2) + 1.06(8) \times 10^{-4} [T] + 3.1(5) \times 10^{-8} [T]^2 \quad (\text{eqn. 3.3})$$

$$b (\text{\AA}) = 7.252(1) + 6.2(4) \times 10^{-5} [T] + 4.9(2.5) \times 10^{-9} [T]^2 \quad (\text{eqn. 3.4})$$

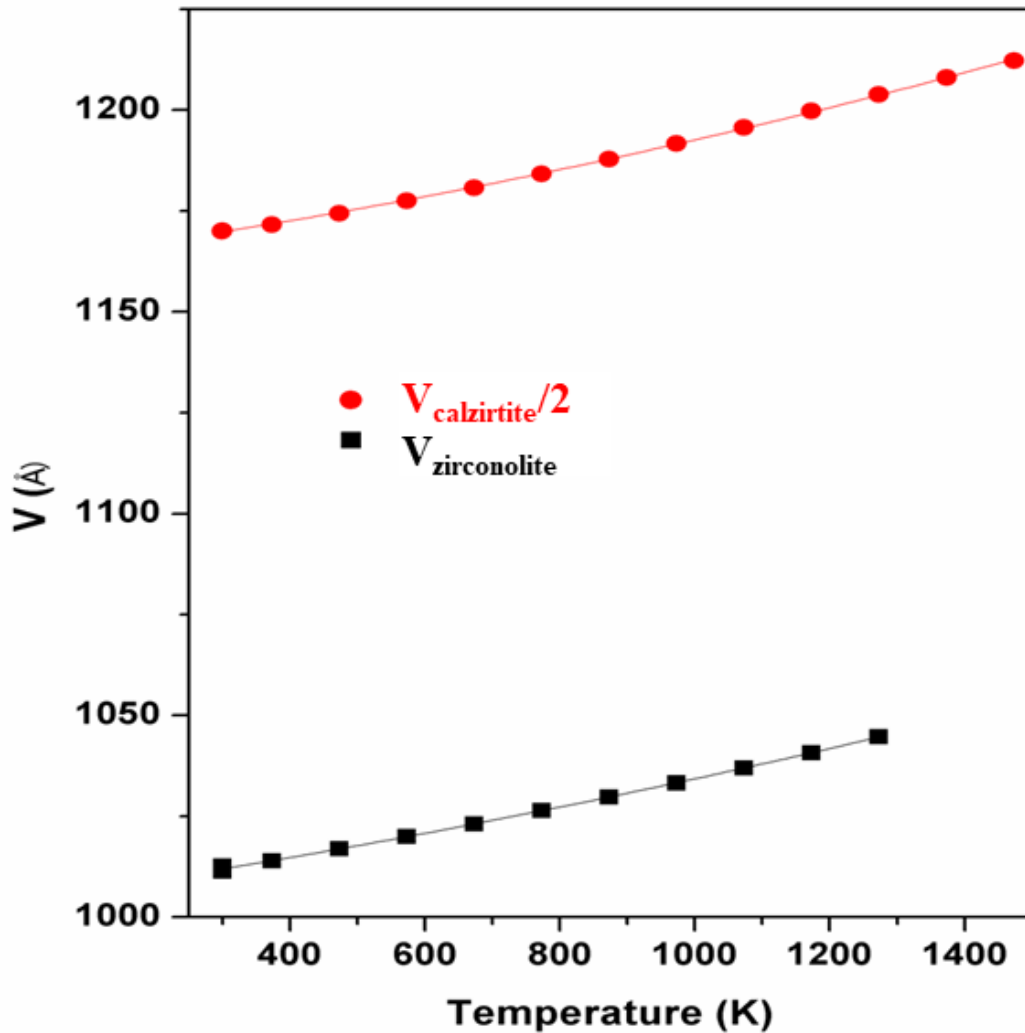
$$c (\text{\AA}) = 11.351(2) + 7.6(7) \times 10^{-5} [T] + 3.2(4) \times 10^{-8} [T]^2 \quad (\text{eqn. 3.5})$$

$$\beta (^\circ) = 100.558(6) - 2.4(1.9) \times 10^{-5} [T] + 5.7(1.2) \times 10^{-8} [T]^2 \quad (\text{eqn. 3.6})$$

Where T is temperature in K

As mentioned in Chapter 1, zirconolite is considered as a potential matrix for immobilization of actinides and minor actinides generated as nuclear waste. Therefore, high temperature structural behaviour of zirconolite has been investigated by several researchers<sup>47,65,132,133</sup>. Dilatometric studies on thermal expansion behaviour of hot-pressed zirconolite indicated that the coefficient of linear thermal expansion increases from around  $10.26 \times 10^{-6}/\text{K}$  to  $11.75 \times 10^{-6}/\text{K}$  upon the increase in temperature from 1273 to 1573K<sup>133</sup>. In like manner, drastic increment in the linear thermal expansion coefficient had been noticed by Ringwood et al.<sup>47</sup> at temperature higher than 1573 K whereas a sharp contraction was noticed around 1773 K. Vance et al.<sup>134</sup> had investigated thermal expansion of zirconolite by dilatometry and concluded that variation in thermal expansion coefficient at higher temperature can be possibly due to the movement of occluded gas bubbles present in the hot-pressed zirconolite. A combination of dilatometric and DTA studies resulted in the conclusion that temperature induced structural change is not observed in zirconolite up to 1723 K, and the coefficient of thermal expansion values was found to be around  $11 \times 10^{-6}/\text{K}$  in between 300K to 1523 K. Ball *et al*<sup>133</sup> investigated two variants of zirconolite, viz. a cation ordered structure with monoclinic unit cell and a disordered structure having hexagonal unit cell by HT-XRD in the range of around 300 K to 1523 K, and observed significantly larger coefficient of thermal expansion values for the monoclinic structure in comparison to the hexagonal structural variant. However, in the HT-XRD studies pertaining to this thesis, the observed average axial thermal expansion coefficients are:  $\alpha_a = 12.45 \times 10^{-6}/\text{K}$ ,  $\alpha_b = 9.34 \times 10^{-6}/\text{K}$  and  $\alpha_c = 11.21 \times 10^{-6}/\text{K}$ . The observed thermal expansion coefficient shows anisotropy in the order of  $\alpha_a > \alpha_c >> \alpha_b$  as reported by Ball *et al*<sup>133</sup>. However, the variation of monoclinic angle ( $\beta$ ) in the present study exhibited a smooth increasing trend with increasing temperature as compared to an anomalous variation reported by Ball *et al*<sup>133</sup>. Nevertheless, it needs to be mentioned that the studies carried out by Ball *et al*<sup>133</sup> were based on indexing selected peaks. Hence, the accuracy of  $\beta$

parameter may be limited. However, the present work exhibited a smooth expansion of the lattice indicating absence of any structural transition as reported in literature. Comparison of the unit cell volume expansion of both calzirtite and zirconolite is depicted in **Figure 3.8**.



**Figure 3.8: Variation of unit cell volume of calzirtite and zirconolite with temperature. The unit cell volume of calzirtite is divided by 2 for proper scaling.**

A smooth and gradual expansion of unit cell parameter is noticed in both the lattices. The variation of temperature dependent volume of zirconolite and calzirtite has been fitted by polynomial relations as:

$$V_{\text{calz.}} (\text{\AA})^3 = 2325.0(7) + 0.044(2) [T] + 1.7(1) \times 10^{-5} [T]^2, \quad (\text{eqn. 3.7})$$

$$V_{\text{zir.}} (\text{\AA})^3 = 1004.3(4) + 0.024(1) [T] + 6.2(8) \times 10^{-6} [T]^2 \quad (\text{eqn. 3.8})$$

Where, T is the temperature in K.

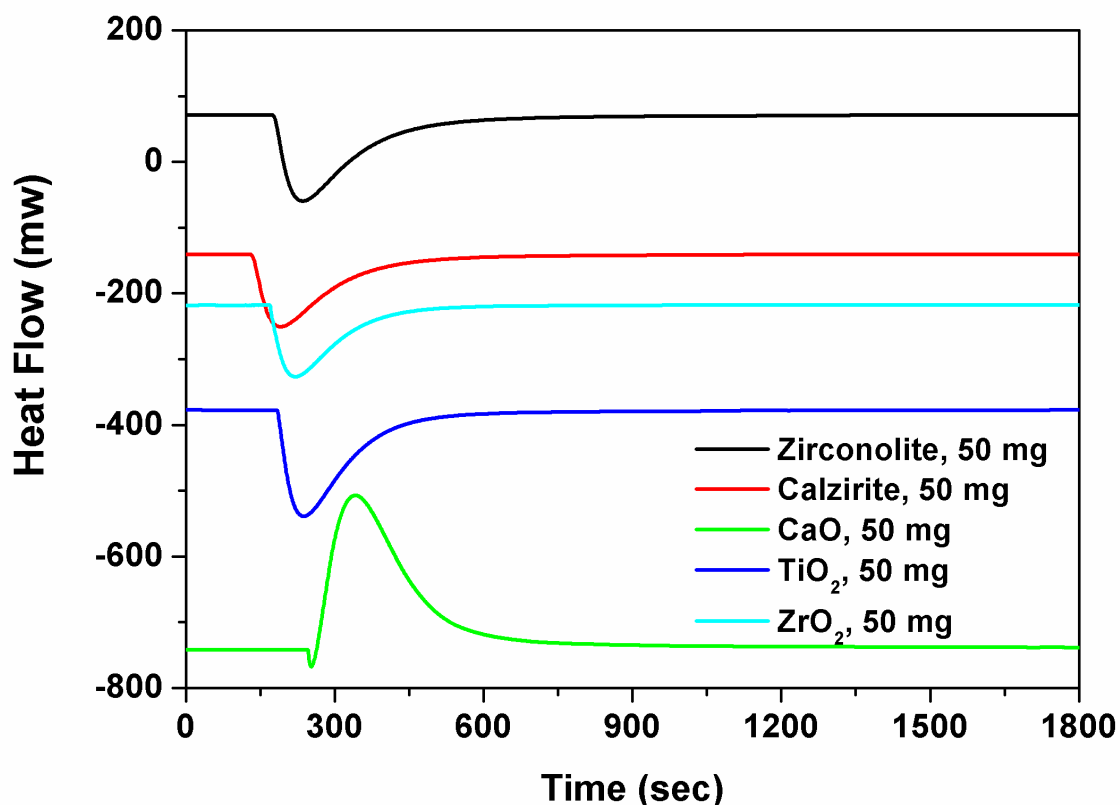
In the temperature range of 300-1273 K, the coefficient of volume thermal expansion of calzirtite ( $29.69 \times 10^{-6}/\text{K}$ ) was found to be lower compared to that of zirconolite ( $33.25 \times 10^{-6}/\text{K}$ ), which can be attributed to the close packed structure of the former compared to layered type structure of the later.

### 3.3.3. STANDARD MOLAR ENTHALPY OF FORMATION OF CALZIRTITE AND ZIRCONOLITE

Standard molar enthalpies of formation of calzirtite and zirconolite lattice were derived from the enthalpy of dissolution values of  $\text{Ca}_2\text{Zr}_5\text{Ti}_2\text{O}_{16}(\text{s})$ ,  $\text{CaZrTi}_2\text{O}_7(\text{s})$ ,  $\text{CaO}(\text{s})$ ,  $\text{ZrO}_2(\text{s})$  and  $\text{TiO}_2(\text{s})$  in liquid  $\text{Na}_2\text{O} + \text{MoO}_3$  (3:4 molar ratio) solvent maintained at 986 K under static air. Special precaution was required during dropping of the reagent CaO as it is highly reactive and absorbs carbon dioxide from air to form calcium carbonate. CaO was prepared by complete decomposition of  $\text{CaCO}_3$  at 1273 K at a furnace for 6 h under flow of argon atmosphere and then pressed to form small pellets of desired mass required for dropping experiments. Pelletized CaO (which basically had again converted to carbonates) was then transferred to a specially designed quartz crucible and heated at 1273K under dynamic vacuum. The crucible was then cooled under vacuum followed by filling it up with dry high purity argon gas. Mass of CaO inside the crucible was obtained by the mass difference of crucible filled with argon + CaO and only argon filled crucible respectively. The sample was then directly dropped from the designed crucible inside the calorimeter.

The normalized heat flow signals corresponding to the dropping of 50 mg of each of the species viz.  $\text{CaO}(\text{s})$ ,  $\text{ZrO}_2(\text{s})$ ,  $\text{TiO}_2(\text{s})$ ,  $\text{Ca}_2\text{Zr}_5\text{Ti}_2\text{O}_{16}(\text{s})$  and  $\text{CaZrTi}_2\text{O}_7(\text{s})$  samples from room temperature to liquid solvent is depicted in **Figure 3.9**. Endothermic peaks for all the

species except CaO(s) were observed. Heat flow signal upon dropping of the species to the solvent is basically the sum of the heat effects due to heat absorption of the sample as it gets heated from 298 to 986 K, dissociation of the lattice and associated lattice dissolution (solvation) energy. Absorption of heat by sample and dissociation of lattice are energy accepting process and hence they are endothermic in nature. Nevertheless, dissolution energy can be either endothermic or exothermic depending upon the nature of the solvent-solvent interactions involved. Hence, it can be said that, in case of CaO(s) the dissolution effect, which was found to be exothermic preceded over the endothermic effects because of which an exothermic peak was obtained.



**Figure 3.9: Normalized heat flow signal after dropping the sample in liquid Na<sub>2</sub>O + MoO<sub>3</sub> (3:4 molar ratio) solvent maintained at 986 K.**

Overall heat effect for dissolution in the calorimetric solvent was calculated using SETSOFT software associated with the instrument. Completion of reaction between the

dropping species and the solvent was monitored by recording heat flow signal for different time intervals. From the above diagram it was observed that a steady base line was obtained after about 1800 s beyond with no noteworthy change in heat flow was noticed. However, a waiting time of 3600 s was kept between two droppings. The molar heat of dissolution for  $\text{Ca}_2\text{Zr}_5\text{Ti}_2\text{O}_{16}(\text{s})$ ,  $\text{CaZrTi}_2\text{O}_7(\text{s})$ ,  $\text{CaO}(\text{s})$ ,  $\text{ZrO}_2$  and  $\text{TiO}_2(\text{s})$  in liquid  $\text{Na}_2\text{O} + \text{MoO}_3$  3:4 molar solvent at  $T = 986 \text{ K}$  upon plotting against respective molar concentrations showed insignificant dilution effect indicating the experiments to be under infinite dilution condition. Average value of four measurements was considered for each of the chemical species. The values of molar enthalpies of dissolution of  $\text{Ca}_2\text{Zr}_5\text{Ti}_2\text{O}_{16}(\text{s})$ ,  $\text{CaZrTi}_2\text{O}_7(\text{s})$ ,  $\text{CaO}(\text{s})$ ,  $\text{ZrO}_2(\text{s})$  and  $\text{TiO}_2(\text{s})$  in liquid  $\text{Na}_2\text{O} + \text{MoO}_3$  3:4 molar solvent at  $T = 986 \text{ K}$  are depicted in **Table 3.6**.

The enthalpy changes for each dropping experiment were determined by integration of the heat flow signal with time. The average enthalpy changes for  $\text{Ca}_2\text{Zr}_5\text{Ti}_2\text{O}_{16}(\text{s})$ ,  $\text{CaZrTi}_2\text{O}_7(\text{s})$ ,  $\text{CaO}(\text{s})$ ,  $\text{ZrO}_2(\text{s})$  and  $\text{TiO}_2(\text{s})$  were found to be  $425.80 \pm 2.70$ ,  $134.42 \pm 0.89$ ,  $-90.08 \pm 0.47$ ,  $42.83 \pm 0.85$  and  $44.89 \pm 0.49 \text{ kJ mol}^{-1}$ , respectively. Standard molar enthalpy of formation of calzirtite and zirconolite were derived from thermo-chemical cycles presented in **Table 3.7**. Molar enthalpy of dissolution values of  $\text{Ca}_2\text{Zr}_5\text{Ti}_2\text{O}_{16}(\text{s})$ ,  $\text{CaZrTi}_2\text{O}_7(\text{s})$ ,  $\text{CaO}(\text{s})$ ,  $\text{ZrO}_2(\text{s})$  and  $\text{TiO}_2(\text{s})$  were combined with auxiliary data such as standard molar enthalpies of formation of  $\text{CaO}(\text{s})$ ,  $\text{ZrO}_2(\text{s})$  and  $\text{TiO}_2(\text{s})$  from the literature<sup>135,136</sup> to derive the standard molar enthalpy of formation of  $\text{Ca}_2\text{Zr}_5\text{Ti}_2\text{O}_{16}(\text{s})$  and  $\text{CaZrTi}_2\text{O}_7(\text{s})$  at 298K. The calculated standard molar enthalpies of formation of  $\text{Ca}_2\text{Zr}_5\text{Ti}_2\text{O}_{16}(\text{s})$  and  $\text{CaZrTi}_2\text{O}_7(\text{s})$  at 298 K were found to be  $-8964.16 \pm 12.59$  and  $-3716.49 \pm 4.12 \text{ kJ mol}^{-1}$ , respectively.

**Table 3.6: The molar enthalpies of dissolution of  $\text{Ca}_2\text{Zr}_5\text{Ti}_2\text{O}_{16}(\text{s})$  (Calzirtite),  $\text{CaZrTi}_2\text{O}_7(\text{s})$ ,  $\text{CaO}(\text{s})$ ,  $\text{ZrO}_2(\text{s})$  and  $\text{TiO}_2(\text{s})$  in 6g of  $\text{Na}_2\text{O} + \text{MoO}_3$  3:4 molar ratio at  $T = 986 \text{ K}$ ; m denotes the mass of the sample dissolved;  $\Delta H$  is the measured energy change per unit mass and  $\Delta H_T$  is the molar enthalpy of solution.**

Compound	Mass m/mg	$\Delta H/\text{J.g}^{-1}$	$\Delta H_T/\text{kJ mol}^{-1}$
$\text{Ca}_2\text{Zr}_5\text{Ti}_2\text{O}_{16}(\text{s})$ (Calzirtite) Mol. Wt. = 888.05	61.4 34.4 19.1 13.3	475.68 482.74 480.86 478.65	422.43 428.70 427.03 425.06 Avr:425.80±2.70
$\text{CaZrTi}_2\text{O}_7(\text{s})$ (Zirconolite) Mol. Wt. = 339.10	31.6 40.5 29.3 33.5	399.39 393.08 395.94 397.24	135.43 133.29 134.26 134.70 Avr:134.42±0.89
$\text{CaO}(\text{s})$ Mol. Wt. = 56.08	11.7 12.4 16.0 21.5	-1506.3 -1519.4 -1512.6 -1501.2	-89.86 -90.65 -90.24 -89.56 Avr: -90.08 ±0.47
$\text{ZrO}_2(\text{s})$ Mol. Wt. = 123.22	10.8 11.0 10.5 21.5	344.47 340.48 348.95 356.6	42.44 41.95 43.00 43.94 Avr:42.83 ± 0.85
$\text{TiO}_2(\text{s})$ Mol. Wt. = 79.87	14.4 11.4 16.8 21.5	553.23 567.51 562.66 564.54	44.19 45.33 44.94 45.09 Avr:44.89±0.49

**Table 3.7: Thermo chemical cycles for derivation of standard molar enthalpies of formation of  $\text{Ca}_2\text{Zr}_5\text{Ti}_2\text{O}_{16}(\text{s}, 298\text{K})$ , Calzirtite) and  $\text{CaZrTi}_2\text{O}_7(\text{s}, 298\text{K})$ , Zirconolite)  $\text{MO}_x(\text{sln})$  = dilute solution of species  $\text{MO}_x$  in 6g liquid  $\text{Na}_2\text{O} + \text{MoO}_3$  3:4 molar solvent maintained at 986 K,  $\Delta_f H^\circ_{298}$  (Calzirtite) =  $-\Delta H_{1\text{Cal}} + 2\Delta H_2 + 5\Delta H_3 + 2\Delta H_4 + 2\Delta H_5 + 5\Delta H_6 + 2\Delta H_7$  and  $\Delta_f H^\circ_{298}$  (Zirconolite) =  $-\Delta H_{1\text{Zir}} + \Delta H_2 + \Delta H_3 + 2\Delta H_4 + \Delta H_5 + \Delta H_6 + 2\Delta H_7$ )**

Reactions	$\Delta H_i$	$\Delta H$ (kJ mol <sup>-1</sup> )
$\text{Ca}_2\text{Zr}_5\text{Ti}_2\text{O}_{16}(\text{s}, 298\text{K}) + (\text{sln}) = 2\text{CaO}(\text{sln}) + 5\text{ZrO}_2(\text{sln}) + 2\text{TiO}_2(\text{sln})$	$\Delta H_{1\text{Cal}}$	$425.80 \pm 2.70$
$\text{CaZrTi}_2\text{O}_7(\text{s}, 298\text{K}) + (\text{sln}) = \text{CaO}(\text{sln}) + \text{ZrO}_2(\text{sln}) + 2\text{TiO}_2(\text{sln})$	$\Delta H_{1,\text{Zir}}$	$134.42 \pm 0.89$
$\text{CaO}(\text{s}, 298\text{K}) + (\text{sln}) = \text{CaO}(\text{sln})$	$\Delta H_2$	$-90.08 \pm 0.47$
$\text{ZrO}_2(\text{s}, 298\text{K}) + (\text{sln}) = \text{ZrO}_2(\text{sln})$	$\Delta H_3$	$42.83 \pm 0.85$
$\text{TiO}_2(\text{s}, 298\text{K}) + (\text{sln}) = \text{TiO}_2(\text{sln})$	$\Delta H_4$	$44.89 \pm 0.49$
$\text{Ca}(\text{s}, 298\text{K}) + 0.5 \text{O}_2(\text{g}) = \text{CaO}(\text{s})$	$\Delta H_5$	$-634.29 \pm 1.67$
$\text{Zr}(\text{s}, 298\text{K}) + \text{O}_2(\text{g}) = \text{ZrO}_2(\text{s})$	$\Delta H_6$	$-1100.81 \pm 2.09$
$\text{Ti}(\text{s}, 298\text{K}) + \text{O}_2(\text{g}) = \text{TiO}_2(\text{s})$	$\Delta H_7$	$-944.75 \pm 1.67$
$2\text{Ca}(\text{s}, 298\text{K}) + 5\text{Zr}(\text{s}, 298\text{K}) + 2\text{Ti}(\text{s}, 298\text{K}) + 8\text{O}_2(\text{g}) = \text{Ca}_2\text{Zr}_5\text{Ti}_2\text{O}_{16}(\text{s}, 298\text{K})$	$\Delta_f H^\circ_{298}$	$-8964.16 \pm 12.59$
$\text{Ca}(\text{s}, 298\text{K}) + \text{Zr}(\text{s}, 298\text{K}) + 2\text{Ti}(\text{s}, 298\text{K}) + 3.5\text{O}_2(\text{g}) = \text{CaZrTi}_2\text{O}_7(\text{s}, 298\text{K})$	$\Delta_f H^\circ_{298}$	$-3716.49 \pm 4.12$

### 3.3.4. ENTHALPY INCREMENT AND HEAT CAPACITY MEASUREMENTS OF CALZIRTITE AND ZIRCONOLITE

Enthalpy increments or  $H_T - H_{298}$  values for  $\text{Ca}_2\text{Zr}_5\text{Ti}_2\text{O}_{16}(\text{s})$  and  $\text{CaZrTi}_2\text{O}_7(\text{s})$  obtained from calorimetric techniques are given in **Table 3.8**. Data reproducibility was ensured by following the principle of multiple droppings of the samples at a fixed temperature and the results were found to be vary within  $\pm 0.05\%$ . The variations of  $H_T - H_{298}$  as a function of temperature for calzirtite and zirconolite measured in the temperature range of 324 to 986 K along with the enthalpy increment data of zirconolite as reported by Poml *et al*<sup>137</sup> are plotted in **Figure 3.10**. The present enthalpy increment data for zirconolite was found to be in good agreement with the reported data<sup>137</sup>.



**Table 3.8: Enthalpy increment ( $H_T - H_{298}$ ) values for  $\text{Ca}_2\text{Zr}_5\text{Ti}_2\text{O}_{16}(\text{s})$  and  $\text{CaZrTi}_2\text{O}_7(\text{s})$ .**

<b>T/K</b>	<b>Calzirtite</b>			<b>Zirconolite</b>		
	$H_T - H_{298}$ (Measured) (J.mol <sup>-1</sup> )	$H_T - H_{298}$ (Fitted) (J.mol <sup>-1</sup> )	% Error $\frac{\text{Calc} - \text{Meas}}{\text{Calc}} \times 100$	$H_T - H_{298}$ (Measured) (J.mol <sup>-1</sup> )	$H_T - H_{298}$ Fitted (J.mol <sup>-1</sup> )	% Error $\frac{\text{Calc} - \text{Meas}}{\text{Calc}} \times 100$
324.5	16453.0	16844.9	2.33	5721.4	5930.1	3.52
350.0	29677.9	29365.1	-1.07	9942.1	11756.0	15.43
375.5	39650.5	42013.2	5.62	18571.2	17627.3	-5.35
400.5	51875.4	54537.3	4.88	23423.2	23427.7	0.02
426.0	67586.3	67438.6	-0.22	27304.8	29389.0	7.09
451.5	82305.2	80467.6	-2.28	37034.1	35395.8	-4.63
477.0	98762.5	93624.3	-5.49	42308.1	41447.8	-2.08
502.5	107728.0	106908.8	-0.77	48238.8	47545.3	-1.46
528.0	121870.7	120321.0	-1.29	54728.6	53688.2	-1.94
553.5	139074.3	133860.9	-3.89	61990.4	59876.4	-3.53
604.5	165328.5	161323.6	-2.48	70316.4	72388.8	2.86
630.0	184308.2	175246.5	-5.17	77589.0	78713.1	1.43
681.0	204072.0	203475.2	-0.29	93739.5	91497.7	-2.45
706.5	218781.5	217781.1	-0.46	97931.4	97958.0	0.03
757.5	247359.7	246775.6	-0.24	111964.3	111014.6	-0.86
783.0	264638.9	261464.3	-1.21	115914.5	117610.9	1.4
834.0	289013.0	291224.7	0.76	126953.3	130939.5	3.04
885.0	316656.0	321495.4	1.51	145102.3	144449.5	-0.45
936.0	357591.3	352276.8	-1.51	158897.2	158140.7	-0.48
986.0	378800.6	383259.3	1.16	173092.5	171876.5	-0.71

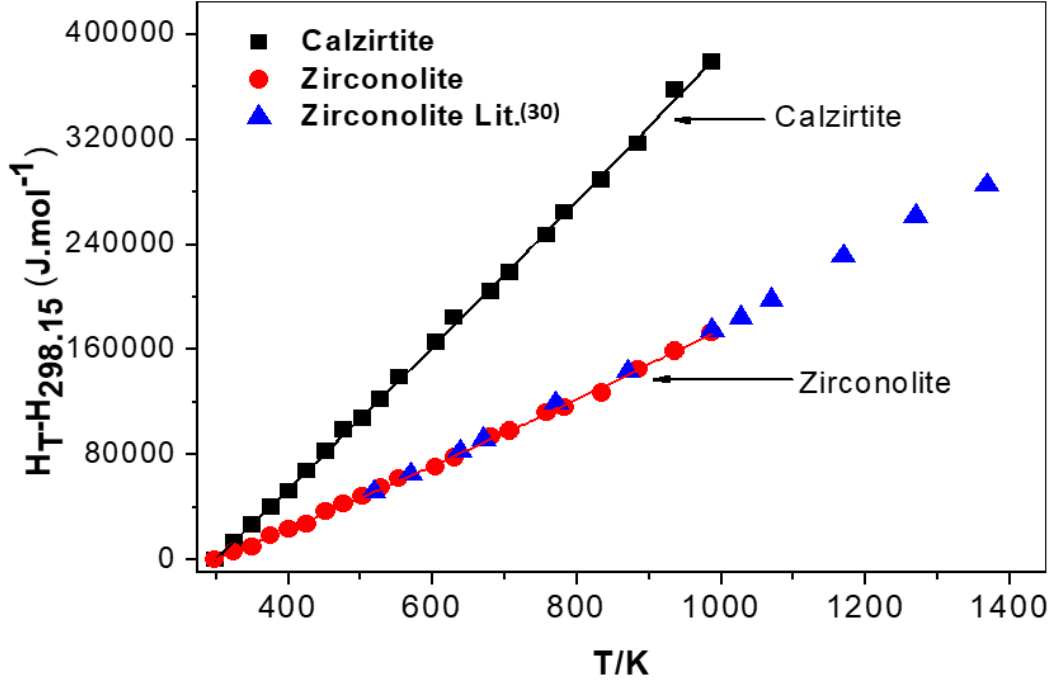
The finest least-square fitted line passing through maximum data points was extrapolated to 298 K. The measured enthalpy increment data presented in Table 3.8 was fitted applying Shomate's method<sup>138</sup> where the boundary conditions are  $H_T - H_{298\text{ K}} = 0$  at 298 K within experimental uncertainty. The generalized polynomial expressions for  $H_T - H_{298\text{ K}}$  for calzirtite ( $\text{Ca}_2\text{Zr}_5\text{Ti}_2\text{O}_{16}$ , s) and zirconolite ( $\text{CaZrTi}_2\text{O}_7$ , s) could be represented as:

$$H_T - H_{298}(\text{Cal}, \text{s}) = 424.9(\pm 5.1).T + (0.096 \pm 0.007).T^2 + \frac{50500}{T} - 129610(\pm 1484)$$

(eqn. 3.9) , and

$$H_T - H_{298}(\text{Zirc}, \text{s}) = 205.0(\pm 12.0).T + (0.0348 \pm 0.006).T^2 + \frac{4500}{T} - 64276(\pm 1371)$$

(eqn. 3.10)



**Figure 3.10:** Plot of  $H_T - H_{298.15}$  as a function of temperature for  $\text{Ca}_2\text{Zr}_5\text{Ti}_2\text{O}_{16}(\text{s})$  and  $\text{CaZrTi}_2\text{O}_7(\text{s})$  measured in the temperature range 324 to 986 K together with the enthalpy increment data for  $\text{CaZrTi}_2\text{O}_7(\text{s})$  reported by Póml et al <sup>137</sup>.

The standard molar heat capacity ( $C_p^\circ$ ) values of calzirtite and zirconolite, as derived from the enthalpy increment equations 3.9 and 3.10 could be expressed as:

$$C_{p,m}^\circ(\text{Calzirtite, s}) = 424.9 + 0.192 \cdot T - \frac{50500}{T^2} \quad (\text{eqn. 3.11})$$

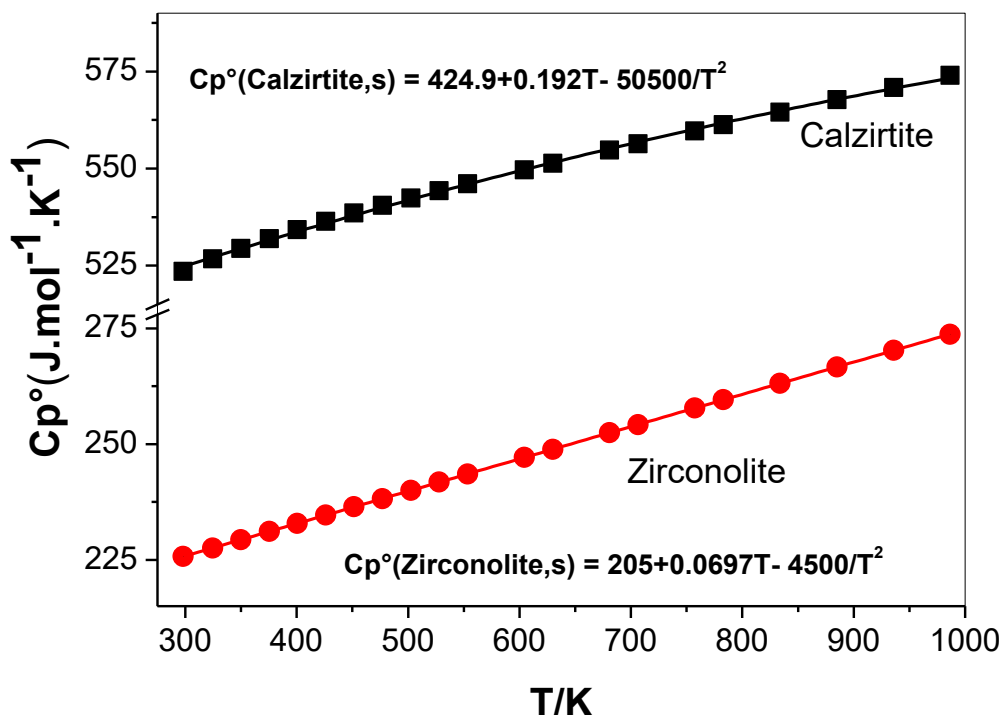
$$C_{m,298}^\circ(\text{Calzirtite, s}) = 481.58 \text{ J.mol}^{-1} \cdot \text{K}^{-1}$$

and

$$C_{p,m}^\circ(\text{Zirconolite, s}) = 205.0 + 0.0697 \cdot T - \frac{4500}{T^2} \quad (\text{eqn. 3.12})$$

$$C_{m,298}^\circ(\text{Zirconolite, s}) = 225.73 \text{ J.mol}^{-1} \cdot \text{K}^{-1}$$

The heat capacity variation of calzirtite and zirconolite as a function of temperature obtained from equations 3.11 and 3.12 are plotted in **Figure 3.11**.



**Figure 3.11. Plot of heat capacities of calzirtite  $\text{Ca}_2\text{Zr}_5\text{Ti}_2\text{O}_{16}(\text{s})$  and zirconolite  $\text{CaZrTi}_2\text{O}_7(\text{s})$  as a function of temperature.**

The respective values of heat capacity of calzirtite and zirconolite estimated from the heat capacity of the reagents  $\text{CaO}(\text{s})$ ,  $\text{ZrO}_2(\text{s})$  and  $\text{TiO}_2(\text{s})$  using Neumann–Kopp rule are found to be 473.86 and 208.13  $\text{J.mol}^{-1}.\text{K}^{-1}$ , respectively, and they are in close agreement with the measured values 481.58 and 225.73  $\text{J.mol}^{-1}.\text{K}^{-1}$ , respectively.

### 3.3.5. CONSTRUCTION OF THERMODYNAMIC TABLES FOR CALZIRTITE AND ZIRCONOLITE

Standard molar enthalpies of formation ( $\Delta_f H_{298}^0$ ) of calzirtite and zirconolite as determined from calvet calorimetric technique is presented in **Table 3.7**. Standard molar heat capacity ( $C_p^0$ ) for calzirtite and zirconolite respectively were derived from the enthalpy increment data using the above technique is tabulated in **Table 3.8**. Standard molar entropy ( $S_{298}^0$ ) values of calzirtite and zirconolite were estimated by addition of the standard molar

entropy data of component binary oxides in their respective stoichiometric ratio from literature [28, 29]. Therefore, the standard molar entropy of the two compositions at any temperature T were calculated using the relation:

$$S_{T(\text{Cal},s)}^0 = S_{298(\text{Cal},s)}^0 + \int_{298}^T \frac{Cp^0(\text{Cal},s)}{T} dT \quad (\text{eqn. 3.13})$$

$$S_{T(\text{Zirc},s)}^0 = S_{298(\text{Zirc},s)}^0 + \int_{298}^T \frac{Cp^0(\text{Zirc},s)}{T} dT \quad (\text{eqn. 3.14})$$

In like manner, the standard molar enthalpy of calzirtite and zirconolite at any temperature T can be calculated as:

$$H_T^0(\text{Cal}, s) = H_{298}^0(\text{Cal}, s) + \int_{298}^T Cp^0(\text{Cal}, s) dT \quad (\text{eqn. 3.15})$$

$$H_T^0(\text{Zirc}, s) = H_{298}^0(\text{Zirc}, s) + \int_{298}^T Cp^0(\text{Zirc}, s) dT \quad (\text{eqn. 3.16})$$

$H_{298}^0(\text{Cal}, s)$  can be equated to its standard molar enthalpy of formation ( $\Delta_f H_{298}^0, \text{Cal}, s$ ) according to the relation:

$$\Delta_f H_{298}^0, \text{Calz}, s = H_{298}^0(\text{calz}, s) - 2H_{298}^0(\text{Ca}, s) - 5H_{298}^0(\text{Zr}, s) - 2H_{298}^0(\text{Ti}, s) - 8H_{298}^0(\text{O}_2, g) \quad (\text{eqn. 3.17})$$

And

$H_{298}^0(\text{Zirc}, s)$  can be equated to its standard molar enthalpy of formation ( $\Delta_f H_{298}^0, \text{Zirc}, s$ ) according to the relation:

$$\Delta_f H_{298}^0, \text{Zirc}, s = H_{298}^0(\text{Zirc}, s) - H_{298}^0(\text{Ca}, s) - H_{298}^0(\text{Zr}, s) - 2H_{298}^0(\text{Ti}, s) - 3.5H_{298}^0(\text{O}_2, g) \quad (\text{eqn. 3.18})$$

However, it is well known that, the values of standard molar enthalpy of elements in their standard state at 298 K are zero as per convention., equation 3.15 and 3.16 will be modified as:

$$H_T^0(\text{Cal}, s) = \Delta_f H_{298}^0, \text{Cal}, s + \int_{298}^T Cp^0(\text{Cal}, s) dT \quad (\text{eqn. 3.19})$$

And

$$H_T^0(\text{Zirc}, s) = \Delta_f H_{298}^0(\text{Zirc}, s) + \int_{298}^T C_p^0(\text{Zirc}, s) dT \quad (\text{eqn. 3.20})$$

The standard molar enthalpy and entropy for calzirtite and zirconolite as a function of temperature is listed in **Table 3.9 and 3.10** respectively. Gibbs free energies of the two compounds were calculated for any temperature T from the combined values of standard molar enthalpy and standard molar entropy using the relation:

$$G_T^0 = H_T^0 - T.S_T^0 \quad (\text{eqn. 3.21})$$

The free energy function (FEF) values for the  $\text{Ca}_2\text{Zr}_5\text{Ti}_2\text{O}_{16}$  and  $\text{CaZrTi}_2\text{O}_7$  were derived from the values of  $\Delta G_T^0$  and the experimental values of standard molar enthalpy of formation of ( $\Delta_f H_{298}^0$ ) the compounds using the relation:

$$\text{FEF} = -\left(\frac{G_T^0 - H_{298}^0}{T}\right) \quad (\text{eqn. 3.22})$$

The values of free energy functions for calzirtite ( $\text{Ca}_2\text{Zr}_5\text{Ti}_2\text{O}_{16}$ ) and zirconolite ( $\text{CaZrTi}_2\text{O}_7$ ) at the experimental temperatures are listed in the **Tables 3.9 and 3.10**.

### 3.3.6. STANDARD GIBBS FREE ENERGY OF FORMATION OF CALZIRTITE AND ZIRCONOLITE

Gibbs free energy of formation of calzirtite and zirconolite were derived using the standard enthalpy of formation data of the two compounds respectively along with their respective standard change in heat capacity  $\Delta C_p^0$  and estimated entropy change  $\Delta S_{298}^0$  for the formation reaction using the relation:

$$\Delta_f G_T^0 = \Delta_f H_{298}^0 + \int_{298}^T \Delta_f C_p^0 dT - T \times \left[ \Delta_f S_{298}^0 + \int_{298}^T \frac{\Delta_f C_p^0}{T} dT \right] \quad (\text{eqn. 3.23})$$

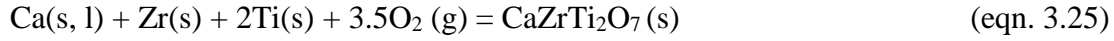
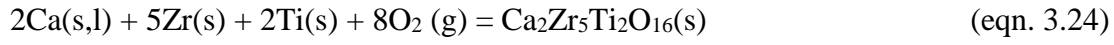
**Table 3.9: Thermodynamic data for calzirtite ( $\text{Ca}_2\text{Zr}_5\text{Ti}_2\text{O}_{16}$ , s)<sup>130</sup>.**

T/K	$\text{H}_\text{T} - \text{H}_{298}$ (J.mol <sup>-1</sup> )	$\text{Cp}_\text{m}^\circ$ (J.mol <sup>-1</sup> .K <sup>-1</sup> )	$\text{S}_\text{T}^\circ$ (J.mol <sup>-1</sup> .K <sup>-1</sup> )	$-\text{H}^\circ_\text{T}$ (kJ.mol <sup>-1</sup> )	$-\text{G}^\circ_\text{T}$ (kJ.mol <sup>-1</sup> )	$\frac{-(\text{G}^\circ_\text{T} - \text{H}^\circ_{298})}{\text{T}}$ (J.mol <sup>-1</sup> .K <sup>-1</sup> )	$\Delta_\text{f}\text{H}^\circ_\text{m}$ (kJ.mol <sup>-1</sup> )	$\Delta_\text{f}\text{G}^\circ_\text{m}$ (kJ.mol <sup>-1</sup> )
298.0	0	481.6	449.9	8964.16	9098.30	449.9	-8964.2	-8508
324.5	16453.0	486.7	490.2	8951.65	9110.72	451.6	-8963.7	-8467.7
350.0	29677.9	491.7	528.0	8938.93	9123.73	455.9	-8963.2	-8428.6
375.5	39650.5	496.6	562.8	8926.33	9137.65	462.0	-8962.8	-8389.8
400.5	51875.4	501.5	594.9	8913.85	9152.12	469.3	-8962.3	-8351.7
426.0	67586.3	506.4	626.1	8901.00	9167.69	477.8	-8961.8	-8312.9
451.5	82305.2	511.3	655.6	8888.02	9184.05	487.0	-8961.4	-8274
477.0	98762.5	516.3	683.9	8874.92	9201.14	496.8	-8960.9	-8235.2
502.5	107728.0	521.2	710.9	8861.69	9218.92	506.9	-8960.4	-8196.4
528.0	121870.7	526.1	736.8	8848.34	9237.39	517.5	-8959.9	-8157.7
553.5	139074.3	531.0	761.8	8834.86	9256.51	528.2	-8959.4	-8118.9
604.5	165328.5	540.8	809.0	8807.53	9296.58	549.9	-8958.4	-8041.5
630.0	184308.2	545.7	831.5	8793.68	9317.51	560.9	-8957.9	-8002.9
681.0	204072.0	555.5	874.3	8765.59	9361.01	582.7	-8956.8	-7925.6
706.5	218781.5	560.4	894.8	8751.37	9383.58	593.7	-8956.2	-7887
757.5	247359.7	570.2	934.2	8722.53	9430.22	615.3	-8955.1	-7809.9
783.0	264638.9	575.2	953.2	8707.93	9454.30	626.0	-8954.5	-7771.3
834.0	289013.0	585.0	989.8	8678.35	9503.86	647.1	-8953.3	-7694.3
885.0	316656.0	594.8	1024.8	8648.26	9555.23	667.9	-8952.1	-7617.4
936.0	357591.3	604.6	1058.4	8617.68	9608.37	688.2	-8950.8	-7540.5
986.0	378800.6	614.3	1090.1	8587.21	9662.63	708.0	-8949.4	-7464.4

**Table 3.10: Thermodynamic data for zirconolite (CaZrTi<sub>2</sub>O<sub>7</sub>, s)<sup>131</sup>.**

T/K	H <sub>T</sub> -H <sub>298</sub> (J.mol <sup>-1</sup> )	C <sub>p</sub> <sup>°</sup> <sub>m</sub> (J.mol <sup>-1</sup> .K <sup>-1</sup> )	S <sub>T</sub> <sup>°</sup> (J.mol <sup>-1</sup> .K <sup>-1</sup> )	-H <sup>°</sup> <sub>T</sub> (kJ.mol <sup>-1</sup> )	-G <sup>°</sup> <sub>T</sub> (kJ.mol <sup>-1</sup> )	$\frac{-(G^{\circ}_T - H^{\circ}_{298})}{T}$ (J.mol <sup>-1</sup> .K <sup>-1</sup> )	Δ <sub>f</sub> H <sub>m</sub> <sup>°</sup> (kJ.mol <sup>-1</sup> )	Δ <sub>f</sub> G <sub>m</sub> <sup>°</sup> (kJ.mol <sup>-1</sup> )
298.0	0	225.7	189.7	3716.49	3773.05	189.7	-3716.5	-3519.5
324.5	5721.4	227.6	208.9	3710.90	3778.65	191.7	-3716.0	-3502.1
350.0	9942.1	229.4	226.2	3705.41	3784.55	194.6	-3715.4	-3485.4
375.5	18571.1	231.1	242.4	3699.86	3790.85	198.1	-3715.0	-3468.6
400.5	23423.2	232.9	257.4	3694.34	3797.45	202.0	-3714.4	-3452.2
426.0	27304.8	234.7	271.8	3688.66	3804.45	206.4	-3714.0	-3435.5
451.5	37034.1	236.5	285.5	3682.91	3811.85	211.1	-3714.0	-3418.9
477.0	42308.1	238.2	298.5	3677.11	3819.55	216.0	-3713.0	-3402.3
502.5	48238.8	240.0	311.0	3671.25	3827.55	220.9	-3712.4	-3385.7
528.0	54728.58	241.8	322.9	3665.32	3835.85	226.0	-3712.0	-3369.1
553.5	61990.4	243.6	334.3	3659.35	3844.45	231.1	-3711.4	-3352.5
604.5	70316.4	247.1	356.0	3647.23	3862.45	241.4	-3710.6	-3319.5
630.0	77589.0	248.9	366.2	3641.09	3871.85	246.5	-3710.0	-3303
681.0	93739.5	252.5	385.7	3628.66	3891.35	256.7	-3709.2	-3270.1
706.5	97931.4	254.2	394.0	3622.36	3900.75	260.8	-3708.8	-3253.7
757.5	111964.3	257.8	412.9	3609.62	3922.35	271.8	-3707.8	-3220.9
783.0	115914.8	259.6	421.4	3603.17	3933.15	276.7	-3707.4	-3204.5
834.0	126953.2	263.1	437.9	3590.13	3955.35	286.4	-3706.6	-3171.7
885.0	145102.3	266.7	453.6	3576.88	3978.35	295.9	-3705.8	-3139.1
936.0	158897.2	270.2	468.7	3563.98	4002.65	305.8	-3704.8	-3106.4
986.5	173092.1	273.8	483.0	3550.08	4026.55	314.3	-3704.2	-3074.2

$\Delta_f C_p^0$  for calzirtite and zirconolite were estimated using the formation reactions



The heat capacity ( $C_p$ ) change for the above-mentioned formation reactions could be expressed as:

$$\Delta_f C_p^0(\text{Cal}) = C_p^0(\text{Cal}) - [2C_p^0(\text{Ca, s, l}) + 5C_p^0(\text{Zr, s}) + 2C_p^0(\text{Ti, s}) + 8C_p^0(\text{O}_2, \text{g})] \quad (\text{eqn. 3.26})$$

and

$$\Delta_f C_p^0(\text{Zirc}) = C_p^0(\text{Zirc}) - [C_p^0(\text{Ca, s, l}) + C_p^0(\text{Zr, s}) + 2C_p^0(\text{Ti, s}) + 3.5C_p^0(\text{O}_2, \text{g})] \quad (\text{eqn. 3.27})$$

Heat capacity values of calzirtite and zirconolite were measured for this work by calvet calorimetric technique whereas the heat capacities of the constituent elements were taken from literature <sup>135,136</sup>. In like manner, the  $\Delta_f S_{298}^0$  of calzirtite and zirconolite were calculated from the estimated  $S_{298}^0$  values for the two compounds respectively taking in accordance with it the  $S_{298}^0$  values of the constituent elements as given in equation 3.26 and 3.27, respectively. Estimated standard molar entropy of formation ( $\Delta_f S_{298}^0$ ) of calzirtite and zirconolite were found to be -1550.45 and -669.92 J. mol<sup>-1</sup>. K<sup>-1</sup>, respectively. Standard molar free energy of formation ( $\Delta_f G_T^0$ ) of calzirtite and zirconolite as a functional variation of temperature were calculated from the experimental values of standard molar enthalpy of formation ( $\Delta_f H_{298}^0$ ), the estimated standard molar entropy of formation ( $\Delta_f S_{298}^0$ ), and the calculated change in standard molar heat capacity ( $\Delta_f C_p^0$ ) for the formation of the compounds presented in **Table 3.9** and **3.10**. The



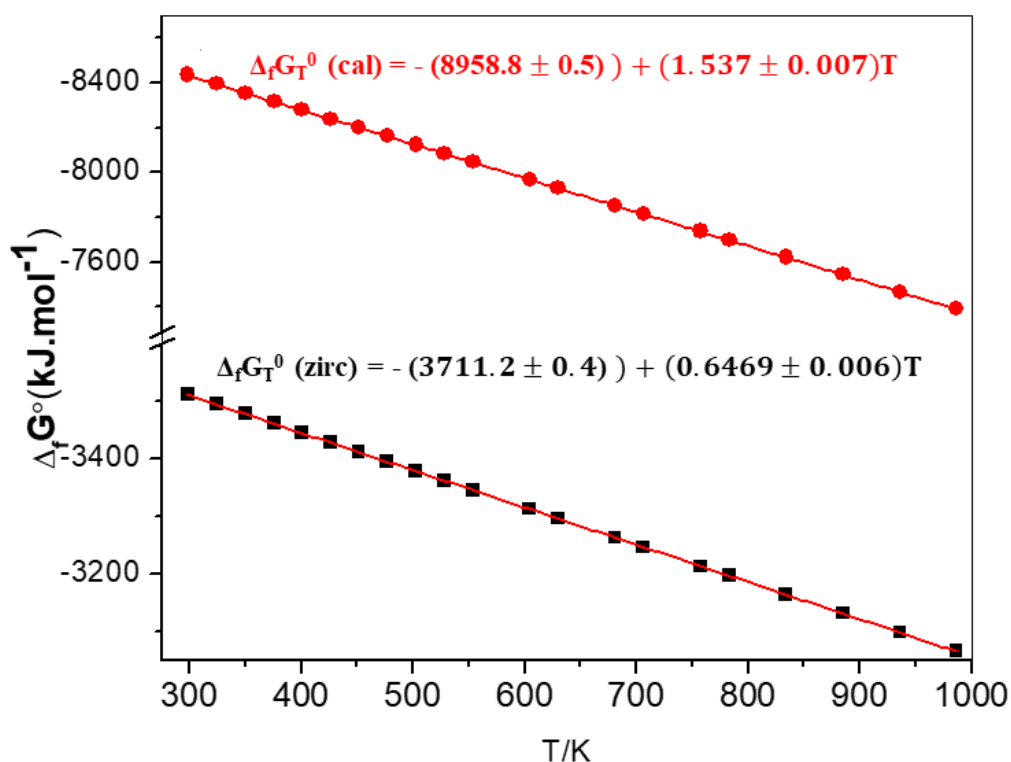
linear least square fitted equation for free energy of formation of ( $\Delta_f G_T^0$ ) of calzirtite ( $\text{Ca}_2\text{Zr}_5\text{Ti}_2\text{O}_{16}$ ) and zirconolite ( $\text{CaZrTi}_2\text{O}_7$ ) could be expressed as:

$$\Delta_f G_T^0(\text{Cal, kJ. mol}^{-1}) = -(8958.8 \pm 0.5) + (1.537 \pm 0.007) \cdot T \quad (314 \leq \frac{T}{K} \leq 986) \quad (\text{eqn. 3.28})$$

and

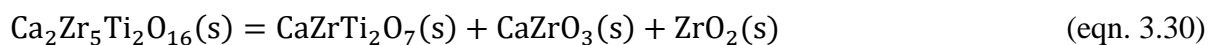
$$\Delta_f G_T^0(\text{Zirc, kJ. mol}^{-1}) = -(3711.2 \pm 0.4) + (0.6469 \pm 0.006) \cdot T \quad (314 \leq \frac{T}{K} \leq 986) \quad (\text{eqn. 3.29})$$

Comprehensive plots of free energy of formation of calzirtite  $\text{Ca}_2\text{Zr}_5\text{Ti}_2\text{O}_{16}(\text{s})$  and zirconolite  $\text{CaZrTi}_2\text{O}_7(\text{s})$  as a function of temperature are given in **Figure 3.12**.



**Figure 3.12** Plot of Standard Gibbs free energy of  $\text{Ca}_2\text{Zr}_5\text{Ti}_2\text{O}_{16}(\text{s})$  and  $\text{CaZrTi}_2\text{O}_7(\text{s})$  as a function of temperature.

Rossell<sup>122</sup> had earlier reported that above 1400 °C calzirtite decomposes into zirconolite as per the reaction:



The free energy change for the above decomposition reaction ( $\Delta G_r^0$ ) was calculated from the values of free energy of formation of calzirtite, zirconolite derived from this work and the free energy of formation of  $\text{CaZrO}_3(\text{s})$  and  $\text{ZrO}_2(\text{tetragonal})$  from literature [28, 29]. The expression for free energy change for the reaction ( $\Delta G_r^0$ ) is given by the relation:

$$\Delta G_r^0 = -186.57 + 0.1051 \times T. \quad (\text{eqn. 3.31})$$

Equating,  $\Delta G_r^0$  to zero at equilibrium, the mean decomposition temperature is found to be around 1775 K ( $\pm 100$  K). High temperature XRD results of calzirtite, reported in earlier section, suggest that the compound is stable at least up to 1673 K, which recommends that the decomposition temperature derived from free energy equation could be correct. Based on this data it can be inferred that at temperatures lower than 1775 K calzirtite is thermodynamically more stable compared to zirconolite.

### 3.4. CONCLSIONS

High temperature structural and thermodynamic properties of calzirtite and zirconolite have been determined by combination of variable temperature X-ray diffraction (XRD) and high temperature calorimetric studies. The phase and structural stability of calzirtite is concluded up to 1473 K. No decomposition of calzirtite to other phases is noticed up to 1673 K. Only a feeble intermixing of Ti and Zr sites for calzirtite is noticed while no distribution in other Zr or Ca site is observed from the structural study. Zirconolite structure shows distribution of Zr and Ti in almost all sites. A comparative analysis of the thermal expansion behaviours of both indicates lower volume thermal coefficient for calzirtite compared to zirconolite due to the close packed structure of the calzirtite lattice. The standard molar

enthalpies of formation of calzirtite ( $\text{Ca}_2\text{Zr}_5\text{Ti}_2\text{O}_{16},s$ ) and zirconolite ( $\text{CaZrTi}_2\text{O}_7, s$ ) at 298 K is found to be  $-8964.16 \pm 12.59$  and  $-3716.49 \pm 4.12 \text{ kJ mol}^{-1}$ , respectively. The standard molar heat capacity of calzirtite ( $\text{Ca}_2\text{Zr}_5\text{Ti}_2\text{O}_{16},s$ ) and zirconolite ( $\text{CaZrTi}_2\text{O}_7, s$ ) derived from the measured  $H_T - H_{298}$  values could be expressed as  $C_{p,m}^\circ(\text{Calzirtite},s) = 424.9 + 0.192 \cdot T - \frac{50500}{T^2}$  and  $C_{p,m}^\circ(\text{Zirconolite},s) = 205.0 + 0.0697 \cdot T - \frac{4500}{T^2}$ , and the corresponding standard molar Gibbs energy of formation could be expressed as

$$\Delta_f G_T^0(\text{Calzirtite}, \text{kJ. mol}^{-1})(s) = -(8958.8 \pm 0.5) + (1.537 \pm 0.007) \cdot T \quad \left(314 \leq \frac{T}{K} \leq 986\right) \quad \text{and}$$

$$\Delta_f G_T^0(\text{Zirconolite}, \text{kJ. mol}^{-1}) = -(3711.2 \pm 0.4) + (0.6469 \pm 0.006) \cdot T \quad \left(314 \leq \frac{T}{K} \leq 986\right).$$

These studies support upon the fact zirconolite can serve as a potential matrix for immobilization of nuclear waste as compared to calzirtite because of the open structure which can entrap a diverse variety of cations without undergoing subsequent alteration. Hence, phase evolution of zirconolite related systems for potential nuclear waste immobilization matrices have been further studied and they have been discussed in the next chapter.

## Chapter 4

# Phase evolution and microstructural studies in $\text{CaZrTi}_2\text{O}_7$ (zirconolite)- $\text{RE}_2\text{Ti}_2\text{O}_7$ (pyrochlore) ( $\text{RE} = \text{Nd}^{3+}, \text{Sm}^{3+}$ and $\text{Y}^{3+}$ ) related systems

The data reported in this chapter have been published in the following peer-reviewed journals:

- Phase Evolution and Microstructural Studies in  $\text{CaZrTi}_2\text{O}_7$ – $\text{Nd}_2\text{Ti}_2\text{O}_7$  System  
M. Jafar, P. Sengupta, S. N. Achary, A. K. Tyagi  
*J. Am. Ceram. Soc.* 97, (2014) 609-616.
- Phase evolution and microstructural studies in  $\text{CaZrTi}_2\text{O}_7$  (zirconolite)– $\text{Sm}_2\text{Ti}_2\text{O}_7$  (pyrochlore) system  
M. Jafar, P. Sengupta, S. N. Achary, A. K. Tyagi  
*J. Eur. Ceram. Soc.* 34, (2014) 4373-4381.
- Phase evolution studies in  $\text{CaZrTi}_2\text{O}_7$ - $\text{RE}_2\text{Ti}_2\text{O}_7$  ( $\text{RE} = \text{Nd}^{3+}, \text{Sm}^{3+}$ ) system: Futuristic Ceramic Host Matrices for Nuclear Waste Immobilization  
M. Jafar, S.N. Achary and A. K. Tyagi
- X-ray diffraction and Raman spectroscopic investigations on  $\text{CaZrTi}_2\text{O}_7$ - $\text{Y}_2\text{Ti}_2\text{O}_7$  system: Delineation of phase fields consisting of potential ceramic host materials  
M. Jafar, S. N. Achary, N. P. Salke, A. K. Sahu, R. Rao, A. K. Tyagi  
*J. Nucl. Mater.* 475, (2016) 192-199.

## 4.1. INTRODUCTION

As mentioned in the introduction sections and the previous chapter, the constituent phases of potentials of SYNROC in particular zirconolite and pyrochlore type phases, have been explored in several studies<sup>24,31,36–40,48,70,71,139</sup>. These phases constitute the major component in SYNROC compositions due to their abilities to accommodate ions having widely different oxidation states and ionic radii as well as other properties like higher leach resistance, higher radiation and thermal stabilities<sup>38,67,68,139–144</sup>

. The pyrochlore ( $A_2B_2O_7$ ; where A = trivalent rare-earth ions and B =  $Ti^{4+}$ ,  $Zr^{4+}$  etc.) type structures have been considered as one of the important phases because of the fact that they can accommodate a larger proportion of minor actinides within their crystal structure and are found to be highly stable even under very high radiation field as mentioned in literature<sup>69–74</sup>. The pyrochlore structure is closely related to anion deficient fluorite structure type and it presents a very wide choice of A and B cations in order to satisfy ionic radii and charge neutrality requirements. This is considered to be the primary reason that compounds having pyrochlore related structure can incorporate a diverse variety of radioactive cations within their crystal structure. The potential of compounds having these types of structures to immobilize radionuclides have been reviewed by Ewing *et al.*<sup>70</sup>. Compounds having the nominal composition  $A_2Ti_2O_7$ , where A = trivalent rare-earth ions, can either crystallize as monoclinic perovskite related structure or cubic pyrochlore-type structure depending on the ionic radii of  $A^{3+}$  ions<sup>70,75,144</sup>. In case of lanthanide titanates, a cubic pyrochlore type structure is favored for ions smaller than  $Sm^{3+}$ , while larger ions prefer to crystallize in perovskite related layered structure. Analogous studies carried out on zirconolite also indicates that  $CaZrTi_2O_7$  and related compositions are being considered as promising single phasic host matrices for incorporation of radionuclides having a wider variation in their valences and ionic radii<sup>48,64,65</sup>. The monoclinic crystal structure of  $CaZrTi_2O_7$  is formed upon stacking of multiple layers of edge-

shared  $\text{TiO}_6$  octahedra and  $\text{TiO}_5$  trigonal pyramids and sandwiched layers of  $\text{Ca}^{2+}$  and  $\text{Zr}^{4+}$  ions in between<sup>57–60,62,63,66,76</sup>. Zirconolite structure has the ability to incorporate a wider stoichiometry like  $\text{CaZr}_x\text{Ti}_{(3-x)}\text{O}_7$  where  $x$  varies from 0.80 to 1.37<sup>59,61,62</sup>. Moreover, zirconolite can crystallize in a number of different polytypes without significant alteration in the basic framework of the structure<sup>61,63</sup>. Apart from these, higher leach resistance<sup>66</sup> and radiation stability<sup>60,67,68,76</sup> of zirconolite and pyrochlore type structured compounds are important features which also promotes them as promising host matrices for nuclear waste immobilization. Literature reports suggest various experiments to substitute different ions in the different cation sub-lattice of zirconolite by maintaining charge balance within the crystal structure<sup>64,134,145</sup>. Caurant *et al*<sup>64</sup> investigated a series of  $\text{Nd}^{3+}$  substituted hafnium zirconolite ( $\text{CaHfTi}_2\text{O}_7$ ) to conclude that single phasicity was observed only upon co-doping of  $\text{Al}^{3+}$  ion at  $\text{Ti}^{4+}$  sites. Considering the aspects of multiphase composites also, mutual compatibility of zirconolite and pyrochlore phases among themselves as also with several other ceramic constituent phases of SYNROC formulations like hollandite, perovskite, fluorite, rutile, etc. makes them potential candidates for immobilization of minor actinides.

Keeping this in mind, these types of structures as promising for accommodation of a large proportion of actinides and minor actinides, an extensive exploration for phase fields in these systems are carried out. Since availability of rare earth elements are limited, it becomes very tedious to carry out experiments with all rare earth titanates. Hence, based upon ionic radii requirements for  $\text{RE}_2\text{Ti}_2\text{O}_7$  structure and ionic radii and nature of different actinide experiments were carried out with neodymium (surrogate of americium)<sup>79–81</sup> titanate (perovskite related monoclinic structure), samarium and yttrium titanate (cubic pyrochlore structure). Yttrium titanate was chosen to observe the effects of phase evolution upon incorporation of a rare earth element with smaller ionic radii and to simulate the effect of ionic radii on the phase evolution. Simultaneous replacement of  $\text{Ca}^{2+}$  and  $\text{Zr}^{4+}$  ions by two  $\text{RE}^{3+}$  ions was considered for charge

balance and minimum phase segregations. The details of the phase field evolutions and microstructure of composite phases are explained in this chapter.

## 4.2. EXPERIMENTAL METHODS

Nominal compositions of the series  $\text{Ca}_{1-x}\text{Zr}_{1-x}\text{RE}_{2x}\text{Ti}_2\text{O}_7$  ( $0.0 \leq x \leq 1.0$ ) where RE =  $\text{Nd}^{3+}$ ,  $\text{Sm}^{3+}$  and  $\text{Y}^{3+}$  were prepared by solid state reaction methodology using analytical grade  $\text{CaCO}_3$  (Sigma Aldrich, St. Louis, MO, USA, purity > 99.0%),  $\text{ZrO}_2$  (Sigma Aldrich, purity 99.0%),  $\text{Sm}_2\text{O}_3$ ,  $\text{Nd}_2\text{O}_3$  and  $\text{Y}_2\text{O}_3$  (Indian Rare Earths Ltd., Mumbai, India, purity 99.9%) and  $\text{TiO}_2$  (Sigma Aldrich, purity  $\geq 99.5\%$ ).  $\text{CaCO}_3$  was dried in an oven at 473 K for 4 h whereas all the other reagents were heated overnight in a furnace at 1173 K prior to weighing. Stoichiometric amount of all the reactants were weighed and homogenized in acetone medium using an agate mortar and pestle. All the nominal compositions were then pelletized and heated in a furnace at 1473 K for 24 h. Upon cooling, they were crushed to powder, homogenized again and heated at the same temperature for 24 h. This procedure was repeated once more to ensure the completion of reaction for Sm and Y containing series. The samples were then thoroughly crushed, ground pelletized and sintered at 1573 K for 24 h. However, for the Nd-containing series the third step heating was carried out at 1573 K for 24 h followed by final sintering at 1673 K for 24 h.

All the compositions belonging to the three series were characterized by powder X-ray diffraction after each step of heat treatment and final sintering. XRD patterns were recorded on a PANalytical X-Pert Pro x-ray diffractometer using  $\text{CuK}\alpha$  ( $\lambda = 1.5406$  and  $1.5444 \text{ \AA}$ ) radiation, over the two theta range of  $10\text{-}80^\circ$  with step width and time of  $0.02^\circ$  and 1.20 s, respectively. The obtained diffraction data were analysed by Rietveld refinement (for end member compositions) and Le Bail profile refinements (for non-end member compositions) using *Fullprof-2k* software package<sup>103</sup>. Microstructural Imaging studies and compositional characterizations were carried out by using Electron Probe Micro-Analyzer or EPMA

(CAMECA-SX 100) for the Nd and Sm-containing series. Sintered pellets of some selected compositions were ground on different grades of emery paper (from coarse grained to fine grained) followed by polishing on a lapping wheel setup using 0.5 $\mu$ m grain sized diamond paste. Polished sample was cleaned in an ultrasonic bath before coating them with ~100 Å thick gold coating to prevent charge accumulation. Accelerating voltage of 20keV and beam current of 4 and 20 nA respectively were used for electron imaging and X-ray analyses respectively. Quantification of chemical composition was carried out using the end member compositions as standard and raw data were corrected using depth distribution of X-rays [ $\phi(\rho z)$ ] function by Pouchou and Pichoir matrix correction procedure<sup>146</sup>. Imaging and compositional studies for Y-containing samples were carried out using a field emission scanning electron microscope (FESEM) (Auriga, ZEISS, Germany). Sample were processed in a similar manner as for EPMA. However, in this case, elemental analyses were carried out using EDS technique (OXFORD, USA attached with the instrument) as compared to WDS technique used in EPMA.

## 4.3. RESULTS AND DISCUSSIONS

### 4.3.1. PHASE EVOLUTION STUDIES

Phase formation and evolution in the series having nominal compositions  $\text{Ca}_{1-x}\text{Zr}_{1-x}\text{RE}_{2x}\text{Ti}_2\text{O}_7$  ( $0.0 \leq x \leq 1.0$ ) where  $\text{RE} = \text{Nd}^{3+}$ ,  $\text{Sm}^{3+}$  and  $\text{Y}^{3+}$  were monitored from powder X-ray diffraction patterns after each heat treatment. The powder XRD patterns after first and second heating were showing diffractions peaks corresponding to the unreacted binary oxides indicating incomplete reaction. No reactant peaks were observed in all the compositions after third round of heating. Hence samples were sintered at a temperature (1673K) higher than that of the third heating temperature, and they were used for phase evolution studies. It is to be noted that, XRD patterns for zirconolite exhibited several peaks upon first and second heating which were attributable to cubic perovskite phase. This is an evidence of the fact that formation



of quaternary zirconolite phase proceeded through a preferentially ternary intermediate  $\text{CaTiO}_3$  type phase. On the other hand, it was observed that the other end members viz.  $\text{Nd}_2\text{Ti}_2\text{O}_7$ ,  $\text{Sm}_2\text{Ti}_2\text{O}_7$  and  $\text{Y}_2\text{Ti}_2\text{O}_7$  were formed even after first round of heating only. XRD patterns corresponding to these  $\text{A}_2\text{Ti}_2\text{O}_7$  type compounds was not found to alter even after successive heat treatment.

As mentioned earlier, structural analysis of the end-member compositions was carried out by Rietveld refinement of the powder diffraction data. Typical unit cell parameters for the composition  $\text{CaZrTi}_2\text{O}_7$  ( $x=0.00$ ) as calculated from Rietveld refinement was found to be  $a = 12.4359(2) \text{ \AA}$ ,  $b=7.2668(2) \text{ \AA}$ ,  $c=11.3692(2) \text{ \AA}$ ,  $\beta=100.556(1)^\circ$  respectively [JCPDS-PDF-84-0164]. It is to be noted that no inter-cationic substitution among the sites was considered for this refinement. The refined structural parameters of zirconolite are given in **Table 4.1** and the corresponding Rietveld refinement plot is shown in **Figure 4.1**.

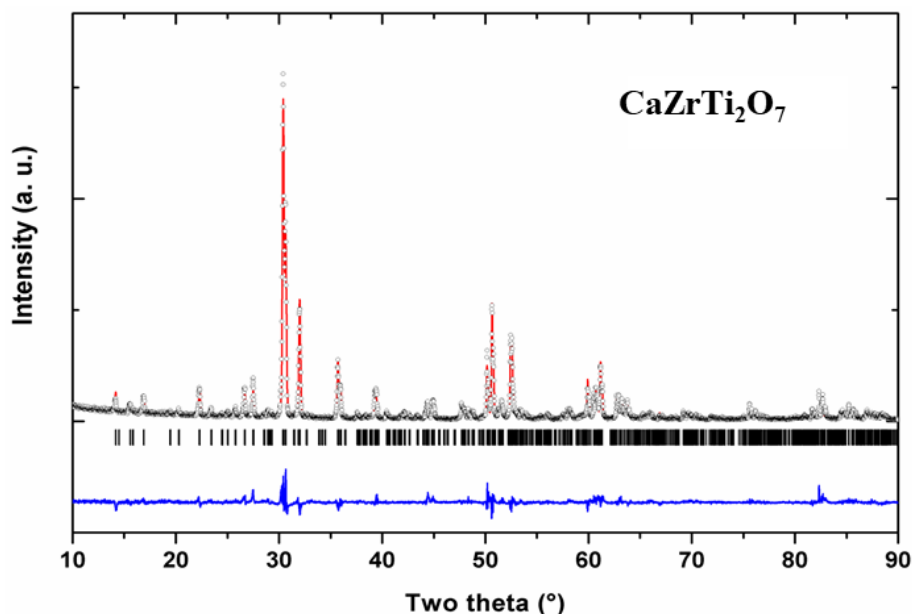
**Table 4.1: Refined structural parameters of zirconolite  $\text{CaZrTi}_2\text{O}_7$  ( $x=0.00$ ).**

Atoms	Sites	x	y	z	Occupancy
Ca	8f	0.3723(9)	0.1264(14)	0.4989(7)	1
Zr	8f	0.1228(4)	0.1262(6)	-0.0248(3)	1
Ti1	8f	0.2466(8)	0.1329(17)	0.7448(6)	1
Ti2	8f	0.4677(14)	0.0556(16)	0.2537(24)	0.5
Ti3	4e	0	0.1376(19)	0.25	1
O1	8f	0.302(2)	0.143(4)	0.283(2)	1
O2	8f	0.479(2)	0.152(3)	0.111(2)	1
O3	8f	0.214(2)	0.129(3)	0.578(2)	1
O4	8f	0.400(2)	0.155(3)	0.718(2)	1
O5	8f	0.701(2)	0.187(3)	0.589(2)	1
O6	8f	0.000(2)	0.149(3)	0.426(2)	1
O7	8f	0.117(2)	0.046(3)	0.788(2)	1

Monoclinic, Space group:  $C2/c$

$a = 12.4359(2) \text{ \AA}$ ,  $b=7.2668(2) \text{ \AA}$ ,  $c=11.3692(2) \text{ \AA}$ ,  $\beta=100.556(1)^\circ$

$R_p$ : 12.1 %,  $R_{wp}$ : 16.4 %,  $\chi^2$ : 1.51



**Figure 4.1: Final refinement plot of the powder XRD data of  $\text{CaZrTi}_2\text{O}_7$  (2M-zirconolite phase)<sup>116</sup>.**

As mentioned in earlier part, crystal structure of zirconolite exhibits different polytypes due to stacking variation and hence shows larger unit cell parameter along the  $c$  axis or the direction of stacking<sup>57,63</sup>. Polymorph of zirconolite or zirconolite-4M is characterized by low angle peaks due to enhanced periodic length and cationic ordering within the crystal structure<sup>63</sup>. No low angle peak was observed in the diffraction of data of zirconolite and hence the above pattern was refined with the zirconolite-2M model. Similarly, cation ordered superstructure for  $\text{Nd}_2\text{Ti}_2\text{O}_7$  is also reported in literature<sup>63,147–149</sup>. Usually, the cation ordered super structure of  $\text{Nd}_2\text{Ti}_2\text{O}_7$  has been reported by doubling the  $c$ -axis (sub- and super-structures of  $\text{Nd}_2\text{Ti}_2\text{O}_7$  are related as:  $a_o \sim a_d$ ,  $b_o \sim b_d$ ,  $c_o \sim 2c_d$  and  $\beta_o \sim \beta_d$ , where the subscript  $o$  and  $d$  characterizes ordered and disordered lattice). Nevertheless, the analogous rare-earth titanates like  $\text{La}_2\text{Ti}_2\text{O}_7$  and  $\text{Pr}_2\text{Ti}_2\text{O}_7$  have also been reported on the disordered structures. Therefore, the powder XRD data of this composition was refined by considering both the ordered and disordered models. All the observed peaks could be indexed assuming the disordered structural model but suitable

profile as well as intensity could be obtained only with the ordered super structure model. Hence, the ordered super structure can be assumed as the exact structure of Nd<sub>2</sub>Ti<sub>2</sub>O<sub>7</sub>. Typical refined powder XRD pattern of Nd<sub>2</sub>Ti<sub>2</sub>O<sub>7</sub> with super structure model is shown in **Figure 4.2**. The refined unit cell parameters of Nd<sub>2</sub>Ti<sub>2</sub>O<sub>7</sub> are: a=7.6755(2) Å, b=5.4624(2) Å, c=25.9865(10) Å and β=98.52(1)°, V = 1077.51(6) Å<sup>3</sup> [JCPDS-PDF-70-1691] and the detailed structural parameters are tabulated in **Table 4.2**.

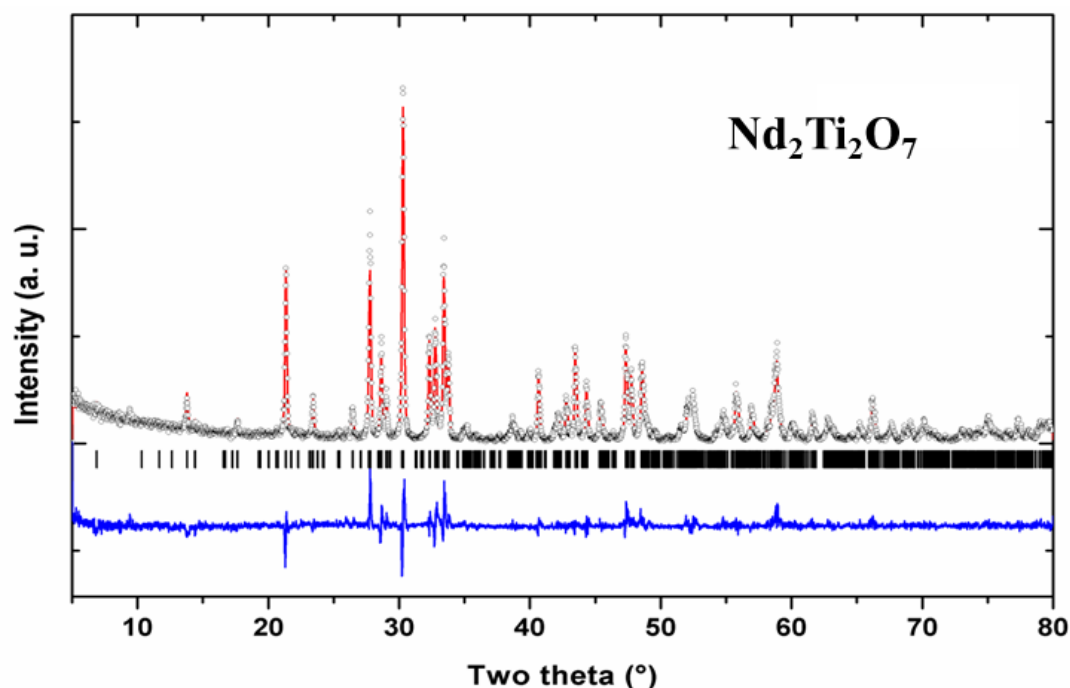
**Table 4.2: Refined structural parameters of Nd<sub>2</sub>Ti<sub>2</sub>O<sub>7</sub> (x=1.00) for RE= Nd<sup>3+</sup> series.**

Atoms	Sites	x	y	z	Occupancy
Nd1	2a	0.2282(4)	0.7551(1)	0.9069(2)	1
Nd2	2a	0.1452(4)	0.3449(1)	0.5750(2)	1
Nd3	2a	0.7194(4)	0.7468(7)	0.8814(2)	1
Nd4	2a	0.6487(7)	0.2841(9)	0.6130(3)	1
Ti1	2a	0.4702(3)	0.2580(6)	0.8794(3)	1
Ti2	2a	0.4149(6)	0.7910(8)	0.6750(3)	1
Ti3	2a	0.9667(2)	0.2594(3)	0.8820(5)	1
Ti4	2a	0.9243(1)	0.7829(2)	0.6795(3)	1
O1	2a	0.5306(8)	0.5247(1)	0.9812(3)	1
O2	2a	0.5003(3)	0.4495(3)	0.7692(2)	1
O3	2a	0.4073(7)	0.5773(3)	0.5590(1)	1
O4	2a	0.2248(1)	0.3081(2)	0.8925(6)	1
O5	2a	0.1748(6)	0.6933(4)	0.6955(5)	1
O6	2a	0.4339(4)	0.9385(2)	0.8187(3)	1
O7	2a	0.3756(2)	0.0670(1)	0.6079(7)	1
O8	2a	0.9592(2)	0.5270(3)	0.9800(9)	1
O9	2a	0.8865(3)	0.4555(6)	0.7610(1)	1
O10	2a	0.8731(1)	0.5634(2)	0.5502(7)	1
O11	2a	0.7278(8)	0.1730(2)	0.9101(3)	1
O12	2a	0.6740(4)	0.8421(8)	0.7033(6)	1
O13	2a	0.9748(3)	0.9433(4)	0.8166(1)	1
<b>O14</b>	2a	0.9227(1)	0.0518(2)	0.6040(7)	1

Monoclinic, Space group: P12<sub>1</sub>1

a=7.6755(2) Å, b=5.4624(2) Å, c=25.9865(10) Å and β=98.52(1)°

Rp = 12.6 %, Rwp= 16.7 %, χ<sup>2</sup> = 1.60



**Figure 4.2:** Final refinement plots of the powder XRD data of  $\text{Nd}_2\text{Ti}_2\text{O}_7$  composition<sup>116</sup>.

Similar structural studies were also carried out for the end member compositions i.e.,  $\text{Sm}_2\text{Ti}_2\text{O}_7$  and  $\text{Y}_2\text{Ti}_2\text{O}_7$ , of their corresponding series. Pyrochlore type structure with  $\text{Fd-}3\text{m}$  space group was used for modelling the structures of both the nominal compositions. The refined unit cell parameters for  $\text{Sm}_2\text{Ti}_2\text{O}_7$  and  $\text{Y}_2\text{Ti}_2\text{O}_7$  were found out to be:  $a=10.2321(2) \text{ \AA}$  for the former, which is in agreement with earlier reported values [JCPDS-PDF-84-0164] and  $a=10.1091(1) \text{ \AA}$  for the latter which is in close agreement with the reported values [JCPDS-PDF 73-1697]. The refined structural parameters of both of these nominal compositions are given in **Table 4.3** and **Table 4.4** and the corresponding Rietveld refinement plot is shown in **Figure 4.3** and **Figure 4.4** respectively.

Phase analyses of the intermediate compositions were carried out by comparing their powder XRD patterns with those observed for the end member compositions. XRD patterns of the sample with  $x=0.05$  for  $\text{Nd}^{3+}$  and  $\text{Sm}^{3+}$  series exhibited several extra peaks, viz. at  $2\theta \sim 33.2, 47.6, 60.0^\circ$ , which could be assigned to the evolution of the cubic perovskite-type phase.

**Table 4.3: Refined structural parameters of  $\text{Sm}_2\text{Ti}_2\text{O}_7$  ( $x=1.00$ ) for RE=  $\text{Sm}^{3+}$  series.**

Atoms	Sites	x	y	z	Occupancy
Sm	$16c$	0	0	0	1
Ti	$16d$	0.5	0.5	0.5	1
O1	$8a$	0.125	0.125	0.125	1
O2	$48f$	0.432(2)	0.125	0.125	1

Cubic, Space group: Fd-3m

$a = 10.2321(2) \text{ \AA}$ ,

$R_p$ : 16.8 %,  $R_{wp}$ : 24.5 %,  $\chi^2$ : 1.46.

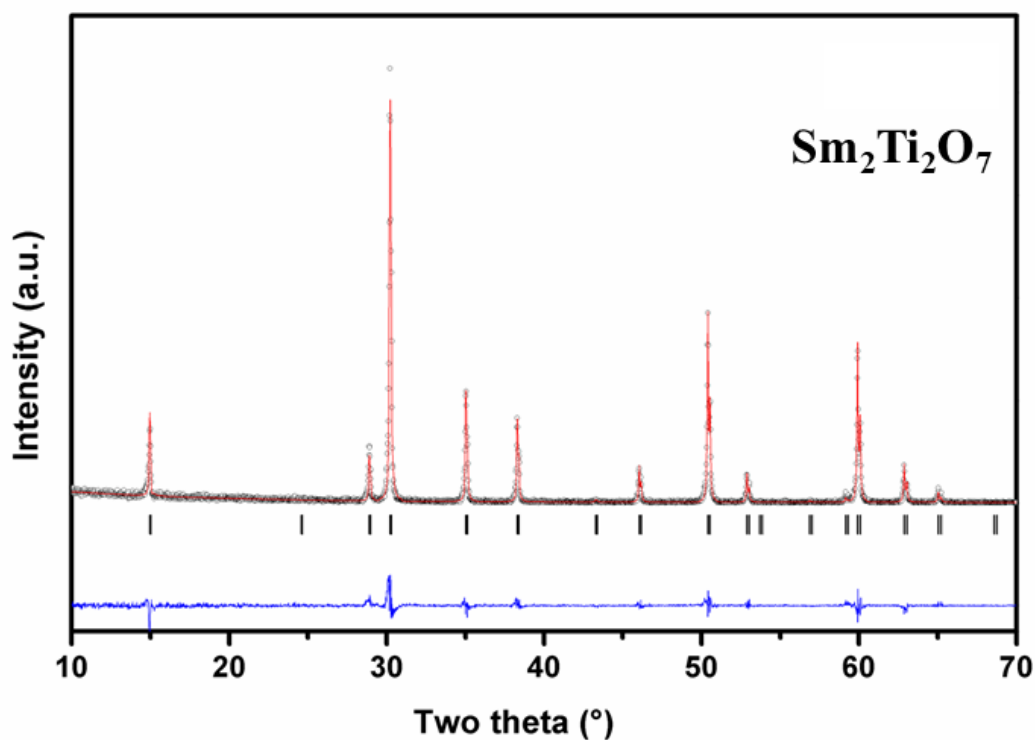
**Table 4.4: Refined structural parameters of  $\text{Y}_2\text{Ti}_2\text{O}_7$  ( $x=1.00$ ) for RE=  $\text{Y}^{3+}$  series.**

Atoms	Sites	x	y	z	Occupancy
Y	$16c$	0	0	0	1
Ti	$16d$	0.5	0.5	0.5	1
O1	$8a$	0.125	0.125	0.125	1
O2	$48f$	0.435(7)	0.125	0.125	1

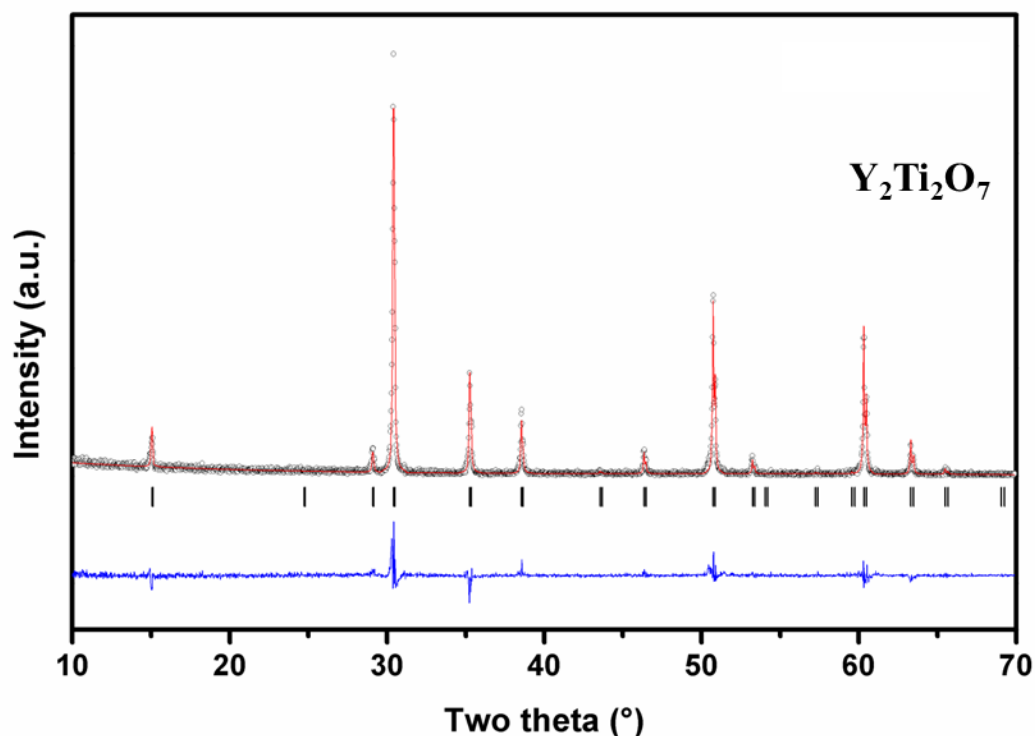
Cubic, Space group: Fd-3m

$a = 10.1091(1) \text{ \AA}$ ,

$R_p$ : 17.9 %,  $R_{wp}$ : 25.0 %,  $\chi^2$ : 1.50.



**Figure 4.3: Final refinement plots of the powder XRD data of  $\text{Sm}_2\text{Ti}_2\text{O}_7$  composition.**



**Figure 4.4: Final refinement plots of the powder XRD data of  $\text{Y}_2\text{Ti}_2\text{O}_7$  composition.**

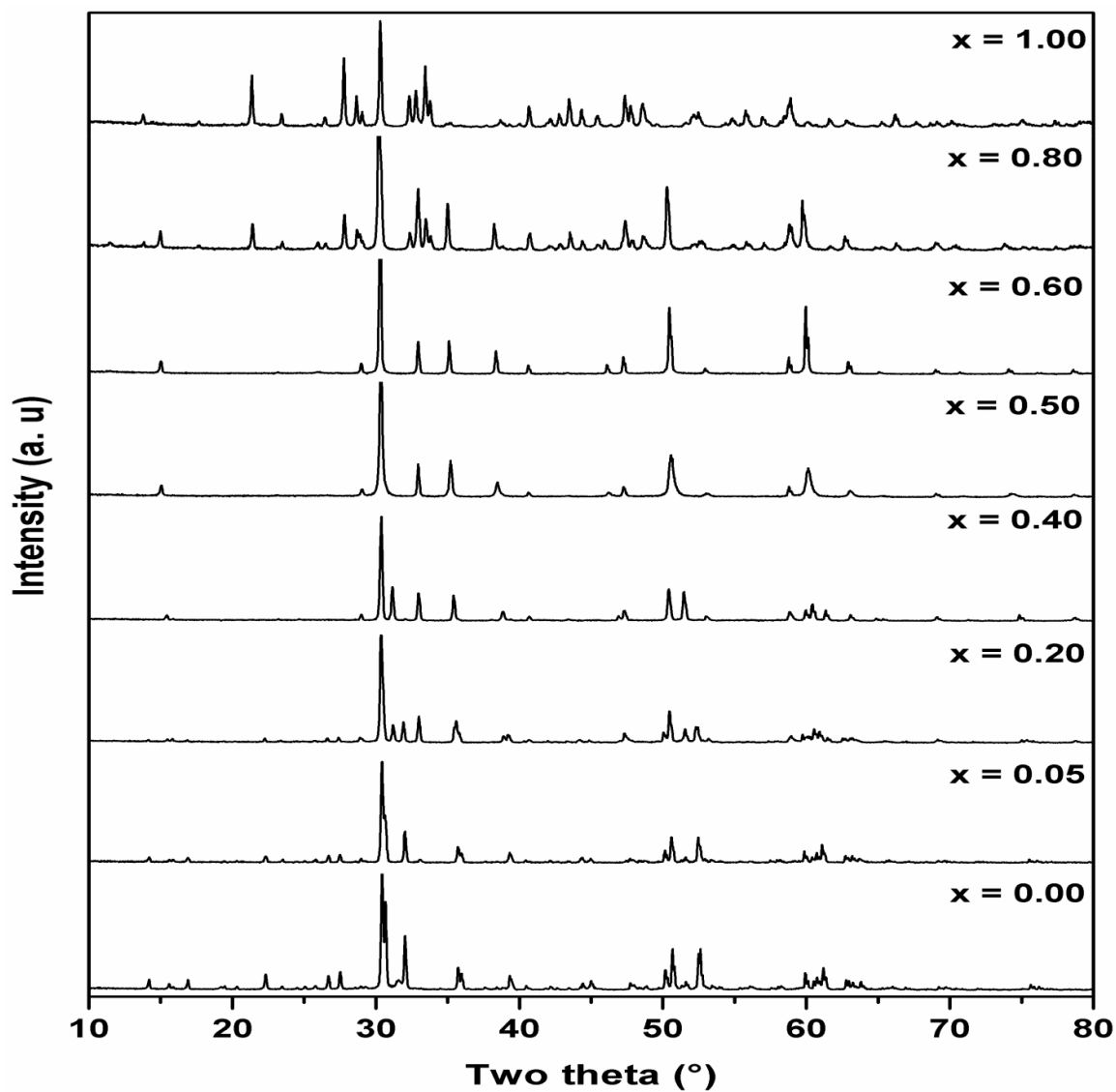
A thorough comparison of the XRD patterns of the successive  $\text{Ca}_{1-x}\text{Zr}_{1-x}\text{RE}_{2x}\text{Ti}_2\text{O}_7$  ( $\text{RE} = \text{Nd}^{3+}$  and  $\text{Sm}^{3+}$ ) compositions revealed that the intensities of the peaks attributable to perovskite-type phase systematically increase with the increase in concentration of  $\text{RE}^{3+}$  which is a clear indication that evolution of perovskite phase increases as a function of increasing  $\text{RE}^{3+}$  concentration. The separation of perovskite-type phase even in composition with  $x = 0.05$  indicates low solubility of  $\text{Nd}^{3+}$  and  $\text{Sm}^{3+}$  (<5%) in zirconolite lattice. Earlier, Rossell<sup>61,62</sup> had reported substitution of about 15 mol % of  $\text{Nd}^{3+}$  in the zirconolite lattice in a reducing condition, and concluded that  $\text{Nd}^{3+}$  substitution is enhanced by the substitution of  $\text{Ti}^{3+}$  ions at  $\text{Zr}^{4+}$  site. On the other hand, Caurant *et al*<sup>64</sup> have reported similar solubility of  $\text{Nd}^{3+}$  in zirconolite lattice by co-substitution of  $\text{Al}^{3+}$  ions at Ti sites. However, the existence of cubic perovskite phase was not observed in any composition of the series with  $\text{Y}^{3+}$  ions. This could be attributed to the preferential occupation of  $\text{Nd}^{3+}$  and  $\text{Sm}^{3+}$  at the  $\text{Ca}^{2+}$  site in zirconolite lattice due to minimum ionic radii mismatch compared to that with  $\text{Zr}^{4+}$ . The ionic radii of

$\text{Nd}^{3+}$ ,  $\text{Sm}^{3+}$ ,  $\text{Y}^{3+}$ ,  $\text{Ca}^{2+}$  and  $\text{Zr}^{4+}$  in identical coordination polyhedra are 1.11Å, 1.08Å, 1.02Å, 1.12Å and 0.84Å respectively<sup>150</sup>.

It can be inferred that ionic radii of  $\text{Nd}^{3+}$  and  $\text{Sm}^{3+}$  lies very close to  $\text{Ca}^{2+}$ , whereas ionic radii of  $\text{Y}^{3+}$  is around the average of  $\text{Ca}^{2+}$  and  $\text{Zr}^{4+}$ . It need be noted that, substitution of two  $\text{RE}^{3+}$  ions were carried out in place of one  $\text{Ca}^{2+}$  and one  $\text{Zr}^{4+}$  ions in all the series to maintain charge neutrality. The observation of phases indicate difference in substitution of  $\text{Nd}^{3+}$  and  $\text{Sm}^{3+}$  in  $\text{Ca}^{2+}$  or  $\text{Zr}^{4+}$  sites of zirconolite. However, zirconolite-2M lattice was able to incorporate  $\text{Y}^{3+}$  into the lattice without alteration of the crystal structure. The segregation of  $\text{Ca}^{2+}$  from zirconolite lattice by  $\text{Nd}^{3+}$  or  $\text{Sm}^{3+}$  ions substitution essentially led to the evolution of a perovskite phase. The unit cell parameters of the cubic perovskite phase observed in different nominal compositions show only a marginal increasing trend with the increase in  $\text{Nd}^{3+}$  concentration, viz.  $a = 3.8326(4)$  Å, at  $x = 0.05$  to  $a = 3.8445(1)$  Å at  $x = 0.70$ . At ambient temperature, the perovskite-type  $\text{CaTiO}_3$  and  $\text{CaZrO}_3$  crystallizes in the distorted orthorhombic structure. Both of them transform to cubic lattice at higher temperature<sup>151–154</sup>. The high temperature cubic  $\text{CaTiO}_3$  has a unit cell parameter,  $a = 3.895$  Å (at 1600°C). However, the high temperature structure can be stabilized at ambient temperature upon appropriate cationic substitution or creation of non-stoichiometric oxygen sub-lattice<sup>151,155–158</sup>. The expected unit cell parameters of cubic calcium titanate and calcium zirconate at ambient temperature are: 3.795 Å (JCPDS-PDF: 75-2100) and 4.020 Å (JCPDS-PDF: 75-0358), respectively. The observed unit cell parameter of the perovskite-type phases suggests a possible incorporation of  $\text{Zr}^{4+}$  in the calcium titanate lattice. It has been reported that the  $\text{CaZrO}_3$ - $\text{CaTiO}_3$  system has a mutual solubility of about 22 mol% at 1200°C<sup>117</sup>. Hence, appreciable solubility of  $\text{Zr}^{4+}$  and  $\text{Nd}^{3+}$  ions in  $\text{CaTiO}_3$  is also expected.

Representative XRD patterns for the three different series, viz.  $\text{RE} = \text{Nd}^{3+}$ ,  $\text{Sm}^{3+}$  and  $\text{Y}^{3+}$  are depicted in **Figure 4.5, 4.6 and 4.7**, respectively. The phase analyses of all the nominal

compositions along with their unit cell parameters as calculated from Le Bail profile refinements are given in **Table 4.5**, **4.6** and **4.7** for  $\text{RE}^{3+} = \text{Nd}^{3+}$ ,  $\text{Sm}^{3+}$  and  $\text{Y}^{3+}$ , respectively.



**Figure 4.5:** Representative XRD patterns of  $\text{Ca}_{1-x}\text{Zr}_x\text{Nd}_{2x}\text{Ti}_2\text{O}_7$  compositions<sup>116</sup>.



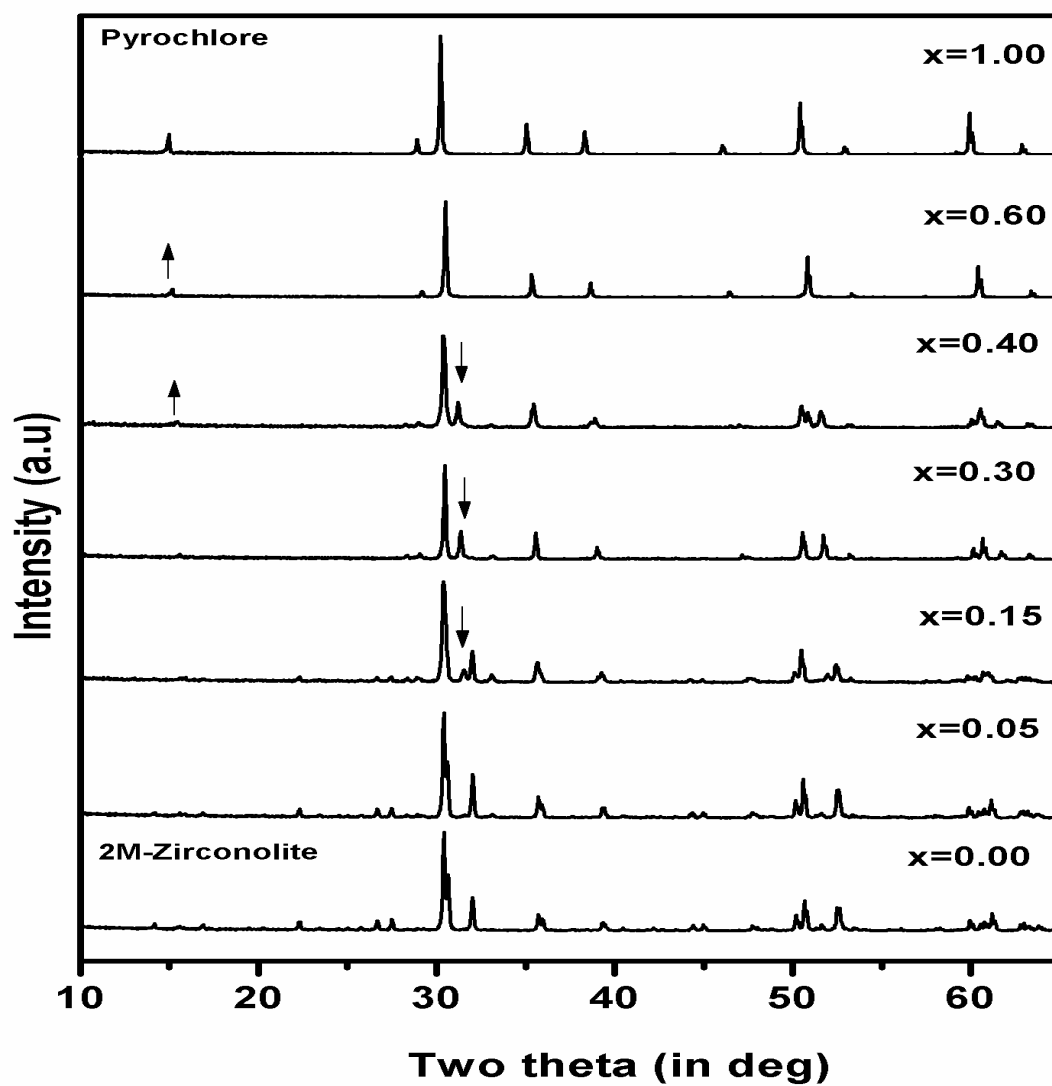
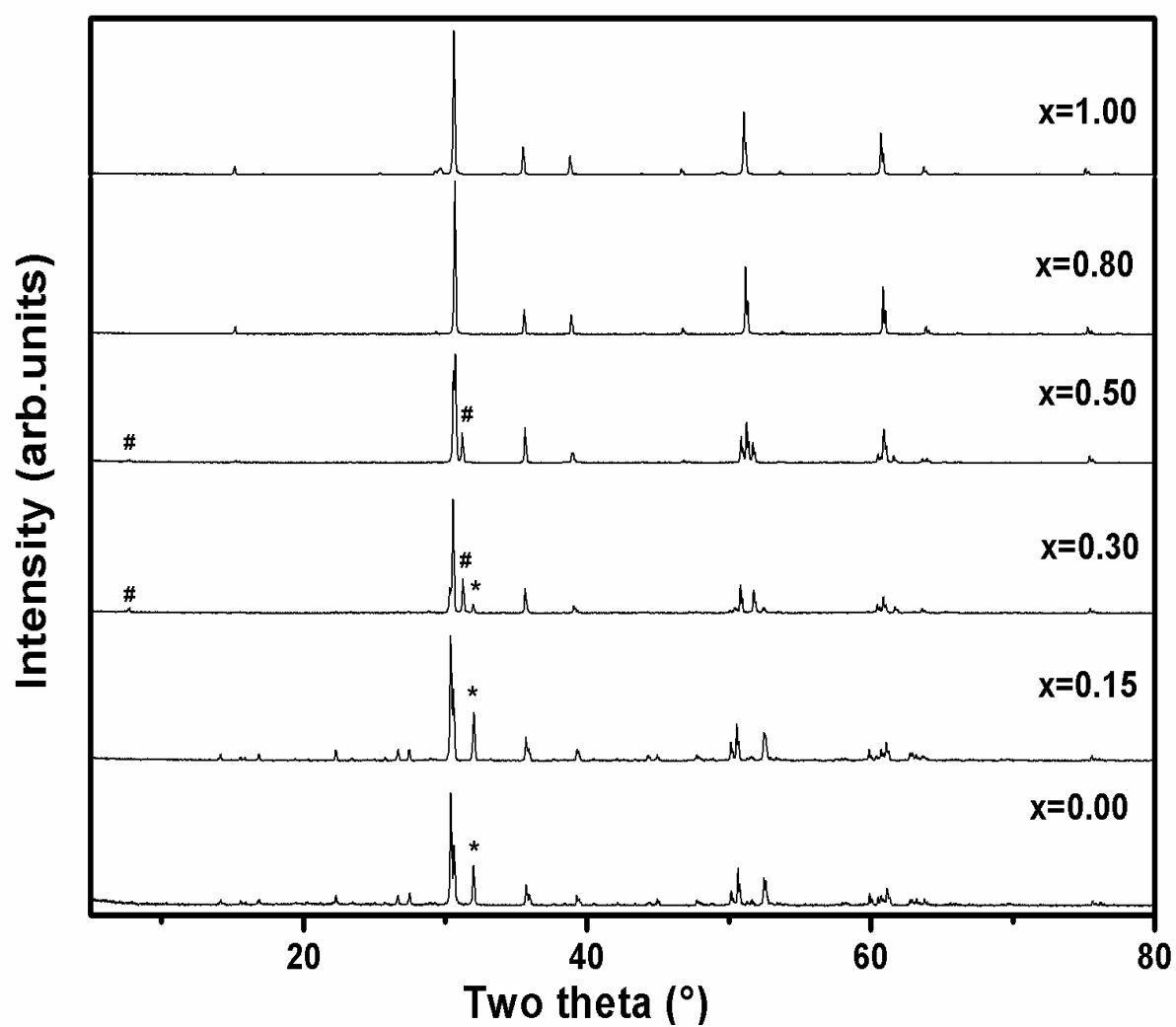


Figure 4.6: Representative XRD patterns of  $\text{Ca}_{1-x}\text{Zr}_x\text{Sm}_{2x}\text{Ti}_2\text{O}_7$  compositions<sup>115</sup>. Signature peaks are marked in figure as “up arrow” pyrochlore and “down arrow” 2M-zirconolite.



**Figure 4.7:** Representative XRD patterns of  $\text{Ca}_{1-x}\text{Zr}_x\text{Y}_{2x}\text{Ti}_2\text{O}_7$  ( $0.00 \leq x \leq 1.00$ ) compositions<sup>159</sup>. Signature peaks are marked in figure as “\*” 2M-zirconolite and “#” 4M-zirconolite.

**Table 4.5: Summary of phases identified in  $\text{Ca}_{1-x}\text{Zr}_{1-x}\text{Nd}_{2x}\text{Ti}_2\text{O}_7$  and their unit cell parameters.**

x	Composition	Phases	Zirconolite (2M or 4M) and $\text{Nd}_2\text{Ti}_2\text{O}_7$ (NT)					Perovskite (P1)		Pyrochlore (P2)	
			a (Å)	b (Å)	c (Å)	$\beta$ (°)	V (Å) <sup>3</sup>	a (Å)	V (Å) <sup>3</sup>	a (Å)	V (Å) <sup>3</sup>
<b>0.00</b>	$\text{CaZrTi}_2\text{O}_7$	2M	12.4359(2)	7.2668(2)	11.3692(2)	100.556(2)	1010.05(3)	-	-		
<b>0.05</b>	$\text{Ca}_{0.95}\text{Zr}_{0.95}\text{Nd}_{0.10}\text{Ti}_2\text{O}_7$	2M+P1	12.4571(3)	7.2763(2)	11.3789(3)	100.555(2)	1013.95(4)	3.8326(4)	56.30(1)		
<b>0.10</b>	$\text{Ca}_{0.90}\text{Zr}_{0.90}\text{Nd}_{0.20}\text{Ti}_2\text{O}_7$	2M+P1	12.4742(3)	7.2812(2)	11.3911(2)	100.573(2)	1017.05(4)	3.8360(2)	56.45(1)		
<b>0.15</b>	$\text{Ca}_{0.85}\text{Zr}_{0.85}\text{Nd}_{0.30}\text{Ti}_2\text{O}_7$	2M+P1	12.4885(3)	7.2841(2)	11.4083(3)	100.575(3)	1020.16(1)	3.8392(1)	56.59(1)		
<b>0.20</b>	$\text{Ca}_{0.80}\text{Zr}_{0.80}\text{Nd}_{0.40}\text{Ti}_2\text{O}_7$	2M+4M+P1	12.4977(5)	7.2855(3)	11.4097(4)	100.557(4)	1021.29(7)	3.8388(1)	56.57(1)		
			12.516(3)	7.225(1)	23.018(1)	84.86(1)	2073.1(5)				
<b>0.25</b>	$\text{Ca}_{0.75}\text{Zr}_{0.75}\text{Nd}_{0.50}\text{Ti}_2\text{O}_7$	4M +P1	12.4754(4)	7.2544(3)	23.1437(9)	85.103(3)	2086.9(1)	3.8373(2)	56.50(1)		
<b>0.30</b>	$\text{Ca}_{0.70}\text{Zr}_{0.70}\text{Nd}_{0.60}\text{Ti}_2\text{O}_7$	4M +P1	12.4937(3)	7.2553(2)	23.1847(9)	85.035(3)	2093.7(1)	3.8397(2)	56.61(1)	-	-
<b>0.35</b>	$\text{Ca}_{0.65}\text{Zr}_{0.65}\text{Nd}_{0.70}\text{Ti}_2\text{O}_7$	4M +P1	12.5315(4)	7.2468(2)	23.1044(2)	84.813(5)	2089.6(1)	3.8425(1)	56.73(1)	-	-
<b>0.40</b>	$\text{Ca}_{0.60}\text{Zr}_{0.60}\text{Nd}_{0.80}\text{Ti}_2\text{O}_7$	4M +P1+P2	12.5151(3)	7.2496(2)	23.0990(4)	84.793(2)	2087.1(1)	3.8412(2)	56.68(2)	10.2077(6)	1063.6(2)
<b>0.45</b>	$\text{Ca}_{0.55}\text{Zr}_{0.55}\text{Nd}_{0.90}\text{Ti}_2\text{O}_7$	4M +P1+P2	12.5237(6)	7.2490(2)	23.0944(5)	84.775(3)	2087.9(1)	3.8440(1)	56.80(1)	10.2077(5)	1063.6(2)
<b>0.50</b>	$\text{Ca}_{0.50}\text{Zr}_{0.50}\text{Nd}_{1.00}\text{Ti}_2\text{O}_7$	P1+P2	-	-	-	-	-	3.8447(2)	56.82(1)	10.2037(3)	1062.4(1)
<b>0.60</b>	$\text{Ca}_{0.40}\text{Zr}_{0.40}\text{Nd}_{1.20}\text{Ti}_2\text{O}_7$	P1+P2	-	-	-	-	-	3.8450(1)	56.85(1)	10.2240(1)	1068.7(1)
<b>0.70</b>	$\text{Ca}_{0.30}\text{Zr}_{0.30}\text{Nd}_{1.40}\text{Ti}_2\text{O}_7$	P1+P2	-	-	-	-	-	3.8445(1)	56.82(1)	10.2612(2)	1080.4(1)
<b>0.80</b>	$\text{Ca}_{0.20}\text{Zr}_{0.20}\text{Nd}_{1.60}\text{Ti}_2\text{O}_7$	P1+P2+NT	7.6801(3)	5.4511(3)	25.9374(7)	98.76(1)	1070.76(5)	*		10.2591(2)	1079.9(1)
<b>0.90</b>	$\text{Ca}_{0.10}\text{Zr}_{0.10}\text{Nd}_{1.80}\text{Ti}_2\text{O}_7$	NT	7.6697(3)	5.4519(2)	25.9488(5)	98.69(1)	1072.56(4)			10.2673(3)	1082.5(1)
<b>1.00</b>	$\text{Nd}_2\text{Ti}_2\text{O}_7$	NT	7.6755(2)	5.4624(2)	25.9865(10)	98.54(1)	1077.34(6)				

2M = zirconolite-2M; 4M=zirconolit-4M; P1= perovskite; P2=cubic pyrochlore; NT= $\text{Nd}_2\text{Ti}_2\text{O}_7$

**Table 4.6: Summary of phases identified in  $\text{Ca}_{1-x}\text{Zr}_{1-x}\text{Sm}_{2x}\text{Ti}_2\text{O}_7$  and their unit cell parameters.**

x	Composition	Phases	Zirconolite (2M or 4M)					Pyrochlore (P2)	
			a (Å)	b (Å)	c (Å)	$\beta$ (°)	V (Å) <sup>3</sup>	a (Å)	V (Å) <sup>3</sup>
<b>0.00</b>	$\text{CaZrTi}_2\text{O}_7$	2M	12.4385(3)	7.2674(2)	11.3679(3)	100.556(3)	1010.22(5)	-	-
<b>0.05</b>	$\text{Ca}_{0.95}\text{Zr}_{0.95}\text{Sm}_{0.10}\text{Ti}_2\text{O}_7$	2M-P1*	12.4607(4)	7.2722(2)	11.3700(4)	100.588(3)	1012.77(5)	-	-
<b>0.10</b>	$\text{Ca}_{0.90}\text{Zr}_{0.90}\text{Sm}_{0.20}\text{Ti}_2\text{O}_7$	2M-P1	12.4888(4)	7.2813(2)	11.3804(4)	100.596(4)	1017.23(6)	-	-
<b>0.15</b>	$\text{Ca}_{0.85}\text{Zr}_{0.85}\text{Sm}_{0.30}\text{Ti}_2\text{O}_7$	2M+4M+P1	12.4888(8)	7.2813(6)	11.3804(7)	100.596 (9)	1017.23(12)	-	-
			12.5248(7)	7.2293(5)	23.0315(6)	84.873(5)	2077.0(2)		
<b>0.20</b>	$\text{Ca}_{0.80}\text{Zr}_{0.80}\text{Sm}_{0.40}\text{Ti}_2\text{O}_7$	2M+4M+P1	12.5028(12)	7.2814(6)	11.3895(9)	100.604(11)	1019.2(2)	-	-
			12.5128(11)	7.2262(5)	22.8972(10)	84.882(5)	2062.1(3)	-	-
<b>0.25</b>	$\text{Ca}_{0.75}\text{Zr}_{0.75}\text{Sm}_{0.50}\text{Ti}_2\text{O}_7$	2M+4M+P1	12.4934(27)	7.2747(14)	11.3919(17)	100.637(25)	1017.6(3)	-	-
			12.5031(14)	7.2212(7)	22.9065(8)	84.838(7)	2059.8(3)		
<b>0.30</b>	$\text{Ca}_{0.70}\text{Zr}_{0.70}\text{Sm}_{0.60}\text{Ti}_2\text{O}_7$	4M+P1	12.5275(9)	7.2252(5)	22.9612(9)	84.860(6)	2069.9(2)	-	-
<b>0.35</b>	$\text{Ca}_{0.65}\text{Zr}_{0.65}\text{Sm}_{0.70}\text{Ti}_2\text{O}_7$	4M+P1	12.5189(33)	7.2256(18)	22.9948(15)	84.772(31)	2071.4(8)	-	-
<b>0.40</b>	$\text{Ca}_{0.60}\text{Zr}_{0.60}\text{Sm}_{0.80}\text{Ti}_2\text{O}_7$	4M+P2	12.5252(29)	7.2283(15)	23.0160(13)	84.852(16)	2075.3(6)	10.1536(5)	1046.8(1)
<b>0.45</b>	$\text{Ca}_{0.55}\text{Zr}_{0.55}\text{Sm}_{0.90}\text{Ti}_2\text{O}_7$	4M+P2	12.5348(30)	7.2334(16)	23.0707(16)	84.740(18)	2082.9(7)	10.1621(3)	1049.4(1)
<b>0.50</b>	$\text{Ca}_{0.50}\text{Zr}_{0.50}\text{Sm}_{1.00}\text{Ti}_2\text{O}_7$	4M+P2	12.5498(32)	7.2391(18)	23.1188(24)	84.710(21)	2091.4(8)	10.17239	1052.6(1)
<b>0.60</b>	$\text{Ca}_{0.40}\text{Zr}_{0.40}\text{Sm}_{1.20}\text{Ti}_2\text{O}_7$	P2	-	-	-	-	-	10.1696(3)	1051.7(1)
<b>0.70</b>	$\text{Ca}_{0.30}\text{Zr}_{0.30}\text{Sm}_{1.40}\text{Ti}_2\text{O}_7$	P2	-	-	-	-	-	10.1891(3)	1057.8(1)
<b>0.80</b>	$\text{Ca}_{0.20}\text{Zr}_{0.20}\text{Sm}_{1.60}\text{Ti}_2\text{O}_7$	P2						10.2016(3)	1061.7(1)
<b>0.90</b>	$\text{Ca}_{0.10}\text{Zr}_{0.10}\text{Sm}_{1.80}\text{Ti}_2\text{O}_7$	P2						10.2183(3)	1066.9(1)
<b>1.00</b>	$\text{Sm}_2\text{Ti}_2\text{O}_7$	P2						10.2321(2)	1071.26(4)

2M = zirconolite-2M; 4M=zirconolite-4M; P1= perovskite (cubic, a= 3.814 Å and V = 55.8 Å<sup>3</sup>); P2=cubic pyrochlore

**Table 4.7: Summary of phases identified in  $\text{Ca}_{1-x}\text{Zr}_{1-x}\text{Y}_{2x}\text{Ti}_2\text{O}_7$  and their unit cell parameters.**

x	Composition	Phases	Zirconolite (2M or 4M)					Pyrochlore (P)	
			a (Å)	b (Å)	c (Å)	$\beta$ (°)	V (Å) <sup>3</sup>	a (Å)	V (Å) <sup>3</sup>
<b>0.00</b>	$\text{CaZrTi}_2\text{O}_7$	2M	12.4377(4)	7.2681(2)	11.3692(4)	100.554(3)	1010.37(5)	-	-
<b>0.05</b>	$\text{Ca}_{0.95}\text{Zr}_{0.95}\text{Y}_{0.10}\text{Ti}_2\text{O}_7$	2M	12.4491(3)	7.2679(2)	11.3663(3)	100.574(2)	1010.96(4)	-	-
<b>0.10</b>	$\text{Ca}_{0.90}\text{Zr}_{0.90}\text{Y}_{0.20}\text{Ti}_2\text{O}_7$	2M	12.4689(4)	7.2687(2)	11.3583(4)	100.595(4)	1011.88(6)	-	-
<b>0.15</b>	$\text{Ca}_{0.85}\text{Zr}_{0.85}\text{Y}_{0.30}\text{Ti}_2\text{O}_7$	2M	12.4626(3)	7.2699(2)	11.3673(3)	100.574(3)	1012.42(5)	-	-
<b>0.20</b>	$\text{Ca}_{0.80}\text{Zr}_{0.80}\text{Y}_{0.40}\text{Ti}_2\text{O}_7$	2M+4M	12.4832(6)	7.2742(3)	11.3657(4)	100.605(6)	1014.43(7)	-	-
			12.4315(8)	7.1820(4)	22.9052(9)	84.892(6)	2036.92(20)	-	-
<b>0.25</b>	$\text{Ca}_{0.75}\text{Zr}_{0.75}\text{Y}_{0.50}\text{Ti}_2\text{O}_7$	2M+4M	12.4883(7)	7.2765(4)	11.3690(5)	100.590(7)	1015.51(9)	-	-
			12.4340(7)	7.1799(4)	22.9266(8)	84.868(4)	2038.57(2)	-	-
<b>0.30</b>	$\text{Ca}_{0.70}\text{Zr}_{0.70}\text{Y}_{0.60}\text{Ti}_2\text{O}_7$	2M+4M	12.4976(1)	7.2775(6)	11.3712(9)	100.601(1)	1016.6(2)	-	-
			12.4325(8)	7.1796(4)	22.9615(9)	84.826(5)	2041.2(2)	-	-
<b>0.35</b>	$\text{Ca}_{0.65}\text{Zr}_{0.65}\text{Y}_{0.70}\text{Ti}_2\text{O}_7$	4M	12.4292(4)	7.1814(2)	22.9746(4)	84.795(3)	2042.2(1)	-	-
<b>0.40</b>	$\text{Ca}_{0.60}\text{Zr}_{0.60}\text{Y}_{0.80}\text{Ti}_2\text{O}_7$	4M	12.4195(2)	7.1803(3)	22.9894(5)	84.791(2)	2041.6(1)	-	-
<b>0.45</b>	$\text{Ca}_{0.55}\text{Zr}_{0.55}\text{Y}_{0.90}\text{Ti}_2\text{O}_7$	4M+P*	12.4242(6)	7.1823(2)	23.0233(7)	84.793(3)	2046.0(1)	10.0728	1021.98
<b>0.50</b>	$\text{Ca}_{0.50}\text{Zr}_{0.50}\text{Y}_{1.00}\text{Ti}_2\text{O}_7$	4M+P	12.4228(2)	7.1818(2)	23.0080(4)	84.795(2)	2044.3(1)	10.0737(1)	1022.30(1)
<b>0.60</b>	$\text{Ca}_{0.40}\text{Zr}_{0.40}\text{Y}_{1.20}\text{Ti}_2\text{O}_7$	4M*+P	12.4226	7.1819	23.0108	84.795	2044.5	10.0786(1)	1023.76(1)
<b>0.70</b>	$\text{Ca}_{0.30}\text{Zr}_{0.30}\text{Y}_{1.40}\text{Ti}_2\text{O}_7$	P	-	-	-	-	-	10.0830(1)	1025.11(2)
<b>0.80</b>	$\text{Ca}_{0.20}\text{Zr}_{0.20}\text{Y}_{1.60}\text{Ti}_2\text{O}_7$	P						10.0873(1)	1026.42 (2)
<b>0.90</b>	$\text{Ca}_{0.10}\text{Zr}_{0.10}\text{Y}_{1.80}\text{Ti}_2\text{O}_7$	P						10.0946(1)	1028.66 (2)
<b>1.00</b>	$\text{Y}_2\text{Ti}_2\text{O}_7$	P						10.1091(1)	1033.10(2)

2M = zirconolite-2M; 4M=zirconolite-4M ; P=cubic pyrochlore

Powder XRD patterns of nominal compositions with  $x \geq 0.20$  exhibited peaks similar to that of zirconolite-2M and coexisting perovskite phases (for the  $\text{Nd}^{3+}$  and  $\text{Sm}^{3+}$  containing compositions). However, splitting of intense peak at  $2\theta \sim 30.3^\circ$  got reduced significantly. In addition, the intensity of the peak at  $2\theta \sim 31.2^\circ$  increases systematically with the increase in  $x$ . This indicated a possible formation of either a new ordered phase or hettotype of zirconolite structure. The decreasing trend in the splitting of intense peak and the appearance of new peak indicate the formation of a four layered monoclinic zirconolite-4M. Hence, the relative peak intensities of these two different peaks can be used as a guide for the formation of 4M phase or disappearance of 2M phase. A comparison of the observed XRD pattern with various reported structural variants of the zirconolite revealed the formation of a 4M-type  $\text{RE}^{3+}$  substituted zirconolite structure as reported Coelho *et al.*<sup>63</sup>. These powder XRD patterns could be successfully refined by considering the evolution of zirconolite-4M phase. A quick transformation to zirconolite-4M from zirconolite-2M was observed for  $\text{Nd}^{3+}$  series whereas a gradual transformation and coexistence of both phases in the range of  $0.20 \leq x \leq 0.40$  was observed for  $\text{Sm}^{3+}$  and  $\text{Y}^{3+}$  series. Therefore, it can be mentioned here that at higher  $\text{RE}^{3+}$  ion concentrations, the 2M phase has a lower stability compared to 4-M structure and that's why there is a transformation to a single phase 4-M structure at higher  $\text{RE}^{3+}$  concentration. Structure of zirconolite 2M polytype is formed by stacking of edge-shared  $\text{TiO}_6$  octahedra and  $\text{TiO}_5$  trigonal bipyramids along c-axis with intermediate layers of  $\text{Ca}^{2+}$  and  $\text{Zr}^{4+}$  ions<sup>57,59,61,62</sup>. In this structure alternate layers appear in identical position and hence this polytype is termed as 2M. Suitable cationic substitution and alteration in the formation environment can lead to variation in the periodicity of these layers leading to formation of different polytype. However, it is well established in literature report<sup>63</sup> that the basic arrangements of all the constituent ions are quite similar to that of 2M polytype. In view of the fact that the basic structural arrangements are identical and hence the strong peaks in XRD patterns of different polytypes are appeared at

similar positions. The differences in between these polytypes are the stacking of layers and hence they are reflected in larger unit cell parameter along the c-axis. From the present study on rare-earth doped zirconolite, it could be noted that zirconolite-4M can accommodate larger amounts of rare-earth ions compared to zirconolite-2M.

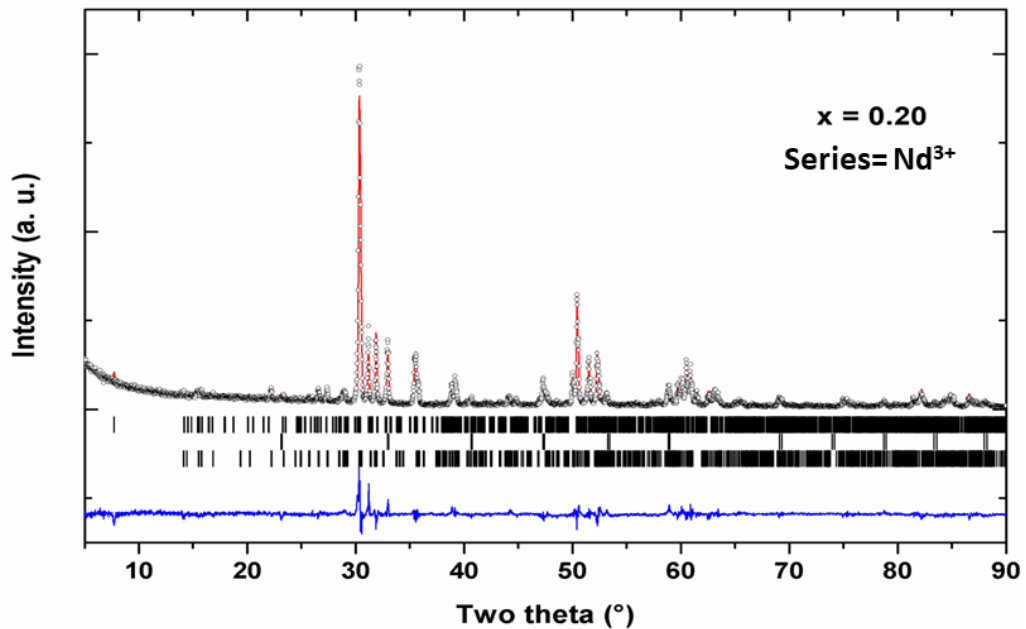
Powder XRD patterns corresponding to the composition  $x \geq 0.40$  exhibited diminished intensity of peaks corresponding to monoclinic zirconolite phase while appearance of prominent new peaks at  $2\theta \sim 15^\circ$  and  $29.8^\circ$ . These peaks are the characteristic signature for the formation of cubic pyrochlore type phase. Thus, a gradual transformation of monoclinic zirconolite-4M phase to cubic pyrochlore phase was evident with increasing  $RE^{3+}$  concentration. The powder XRD data observed at the nominal compositions with  $x = 0.45$  to  $0.70$  show peaks only from the cubic pyrochlore and perovskite-type phases. Since, unit cell volume of the perovskite-type phase observed in different compositions exhibited negligible variation with composition for the  $Nd^{3+}$  series, the rearrangement of cations of the 4M-zirconolite structure led to the cubic pyrochlore-type structure. Literature data indicate that the idealized composition  $Nd_2Zr_2O_7$  can exist either in a cation disordered fluorite-type or a cation ordered pyrochlore-type structure<sup>78,160–163</sup>. However, the monoclinic perovskite-related structure is the only stable structure for  $Nd_2Ti_2O_7$ <sup>147,149</sup>. The formation of two different structures with  $Zr^{4+}$  and  $Ti^{4+}$  ions can be related to the difference in the radii of  $Nd^{3+}$  (1.11 Å),  $Zr^{4+}$  (0.84 Å) and  $Ti^{4+}$  (0.74 Å) ions<sup>150</sup>. The formation of cubic pyrochlore-type structure in  $A_2B_2O_7$  type compositions is governed mainly by the radius of A and B cations<sup>69</sup>. A quick comparison of the unit cell parameters of cubic pyrochlore-type phases observed in the nominal compositions with  $0.4 \leq x \leq 0.5$  did not show any appreciable variation. However, a noticeable increase in unit cell parameter of pyrochlore-type phase is observed at the composition beyond  $x = 0.5$ . The increase in molar volume of the pyrochlore-type phase observed in different nominal compositions, i.e., compositions within  $0.45 \leq x \leq 0.65$  for the  $Nd^{3+}$  series, indicate

that the pyrochlore lattice has a homogeneity range. Since the ionic radius of  $\text{Nd}^{3+}$  is similar to that of  $\text{Ca}^{2+}$  ion, the increase in unit cell volume might be due to the substitution of  $\text{Nd}^{3+}$  ion at  $\text{Zr}^{4+}$  site or  $\text{Zr}^{4+}$  ions at  $\text{Ti}^{4+}$  site. However, for  $\text{Sm}^{3+}$  and  $\text{Y}^{3+}$  series, all the observed peaks in the XRD patterns of compositions with  $x \geq 0.60$  could be assigned to cubic pyrochlore type structure similar to  $\text{Sm}_2\text{Ti}_2\text{O}_7$  and  $\text{Y}_2\text{Ti}_2\text{O}_7$  of the respective series. The observation of single phase region in all the compositions spanning in the range  $0.60 \leq x \leq 1.00$  suggests that about 50 % of the A site cation of pyrochlore ( $\text{A}_2\text{B}_2\text{O}_7$ ) structure can be substituted by proper combination of cations of equivalent oxidation states. Interestingly, the weak peaks attributable to perovskite structure type phase (for  $\text{Sm}^{3+}$  series) observed along with the zirconolite type phase are not observed in the XRD patterns of compositions with  $x \geq 0.40$ . This indicates that equivalent amount of  $\text{Ca}^{2+}$  and  $\text{Zr}^{4+}$  together can replace the  $\text{Sm}^{3+}$  and  $\text{Y}^{3+}$  ions of the pyrochlore structure of  $\text{Sm}_2\text{Ti}_2\text{O}_7$  and  $\text{Y}_2\text{Ti}_2\text{O}_7$ . However,  $\text{Sm}^{3+}$  has a non-equivalent substitution in  $\text{Ca}^{2+}$  and  $\text{Zr}^{4+}$  sites of zirconolite structure as mentioned earlier. It is known that the formation of cubic pyrochlore type phase of  $\text{A}_2\text{B}_2\text{O}_7$  type composition is mainly governed by the ionic radii of the A and B site cations<sup>69</sup>. For rare-earth zirconates ( $\text{A}_2\text{Zr}_2\text{O}_7$ ), the radius ratio ( $r_{\text{A}^{3+}}/r_{\text{B}^{4+}}$ ) for lighter rare-earth ions as  $\text{A}^{3+}$  ion is suitable for fluorite type structure while that for heavier rare-earth ions as  $\text{A}^{3+}$  ion (beyond  $\text{Eu}^{3+}$ ) is suitable for pyrochlore structure. Nevertheless, in case of rare-earth titanates ( $\text{A}_2\text{Ti}_2\text{O}_7$ ), for the lighter rare-earths (up to  $\text{Nd}^{3+}$ ), the radius ratio exceeds the limit for pyrochlore structure. Hence, they have a tendency to form perovskite related structures. The cubic pyrochlore structures are generally observed for  $\text{A}_2\text{Ti}_2\text{O}_7$ , with  $\text{A} = \text{Sm}^{3+}$  to  $\text{Lu}^{3+}$ . Thus, as the  $\text{RE}^{3+}$  ions are replaced by  $\text{Ca}^{2+}$  and  $\text{Zr}^{4+}$  ( $r_{\text{av}} = 0.98 \text{ \AA}$  in coordination no 8 assuming that one  $\text{Zr}^{4+}$  and one  $\text{Ca}^{2+}$  ion is replacing two  $\text{Sm}^{3+}$  or  $\text{Y}^{3+}$  ions), the radius ratio decreases and falls to the pyrochlore structure limits.

The powder XRD patterns of the compositions towards the  $\text{Nd}_2\text{Ti}_2\text{O}_7$  end member (viz.  $x = 0.8$  and  $0.9$  for the  $\text{Nd}^{3+}$  series) show the coexistence of the cubic pyrochlore and



monoclinic  $\text{Nd}_2\text{Ti}_2\text{O}_7$  type phases. The substitution of  $\text{Ca}^{2+}$  and  $\text{Zr}^{4+}$  ions in the lattice of  $\text{Nd}_2\text{Ti}_2\text{O}_7$  favoured the existence of a pyrochlore lattice which might be due to the increase in B-site ionic radius or decrease in A-site ionic radius. The transformation of cubic pyrochlore to monoclinic  $\text{A}_2\text{Ti}_2\text{O}_7$ -type structure has been investigated in several reports [41-43]. A partial substitution of  $\text{Zr}^{4+}$  by  $\text{Ti}^{4+}$  and  $\text{Ti}^{4+}$  by  $\text{Zr}^{4+}$  have been reported in  $\text{A}_2\text{Zr}_2\text{O}_7$ - $\text{A}_2\text{Ti}_2\text{O}_7$  (where A = trivalent rare-earth ions) system<sup>147,148</sup>. In general, a continuous transition from pyrochlore to perovskite related structure was not observed because of considerable difference in these two structure types. The observed unit cell volumes of the  $\text{Nd}_2\text{Ti}_2\text{O}_7$  type phases in the compositions with  $0.80 \leq x \leq 0.90$  are almost similar and close to the parent monoclinic  $\text{Nd}_2\text{Ti}_2\text{O}_7$ . This suggests that the  $\text{Ca}^{2+}$  or  $\text{Zr}^{4+}$  ions did not have appreciable solubility in monoclinic structure of the  $\text{Nd}_2\text{Ti}_2\text{O}_7$  in the present experimental conditions. A few representative powder XRD diagrams of some selected compositions having multiple phases are given in **Figure 4. 8, 4.9 and 4.10** respectively.



**Figure 4.8:** Final refinement plots of the powder XRD data of  $\text{Ca}_{0.80}\text{Zr}_{0.80}\text{Zr}_{0.40}\text{Ti}_2\text{O}_7$  composition<sup>116</sup>. Vertical lines are Bragg positions for 4M-zirconolite, perovskite and 2M-zirconolite structures (top to bottom). ( $R_p = 11.0\%$ ,  $R_{wp} = 14.7\%$ ,  $\chi^2 = 2.63$ ).

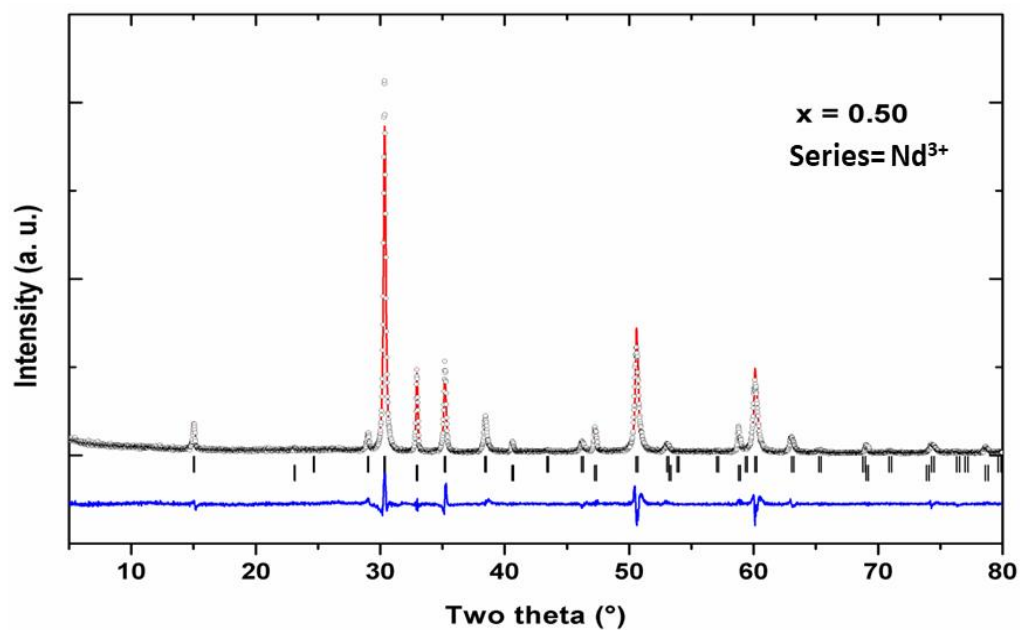


Figure 4.9: Final refinement plots of the powder XRD data of  $\text{Ca}_{0.50}\text{Zr}_{0.50}\text{Nd}_{1.00}\text{Ti}_2\text{O}_7$  composition<sup>116</sup>. Vertical lines are Bragg positions for cubic pyrochlore phase (upper) and perovskite phase (lower). ( $R_p = 12.7\%$ ,  $R_{wp} = 16.1\%$ ,  $\chi^2 = 2.51$ ).

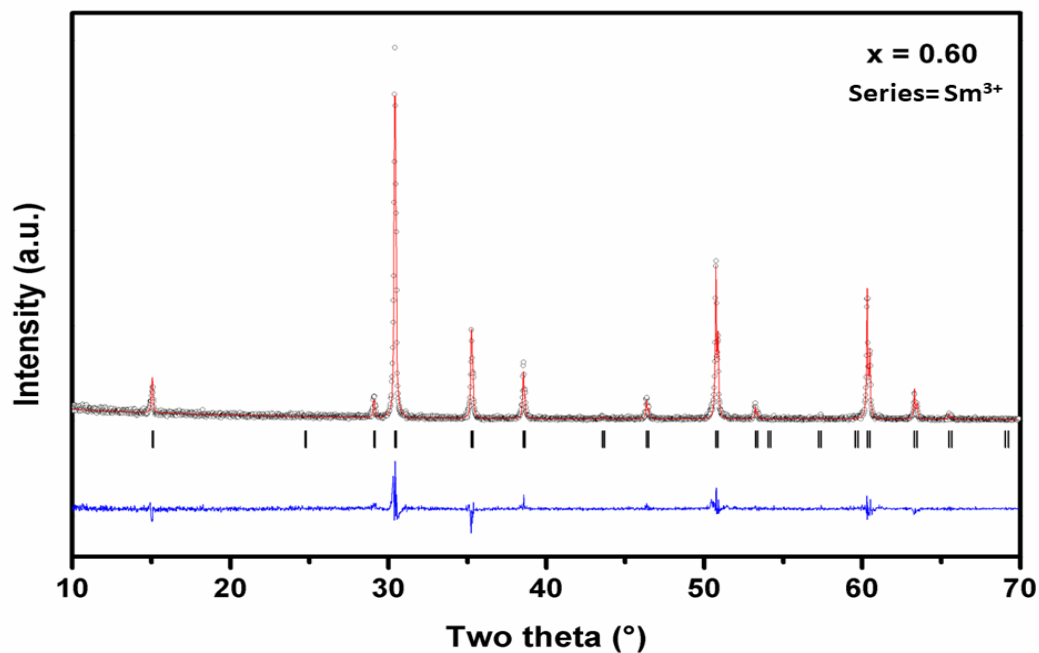
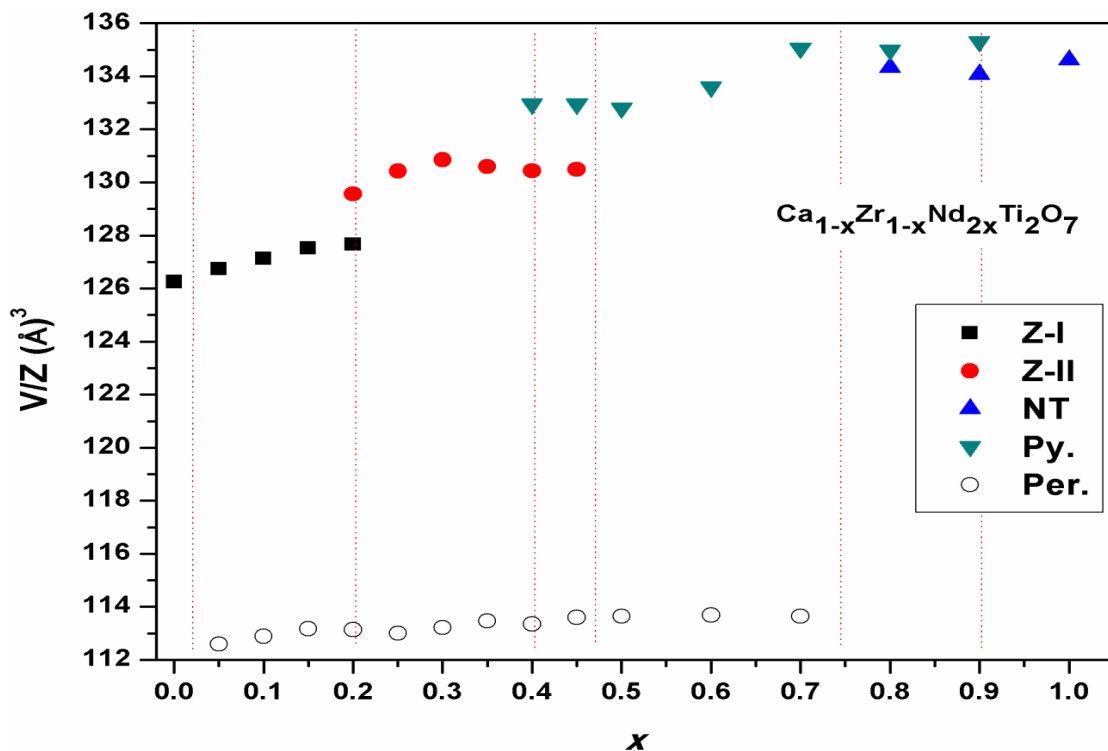


Figure 4.10: Final refinement plots of the powder XRD data of  $\text{Ca}_{0.40}\text{Zr}_{0.40}\text{Sm}_{1.20}\text{Ti}_2\text{O}_7$  composition<sup>115</sup>. ( $R_p = 17.9\%$ ,  $R_{wp} = 25.0\%$ ,  $\chi^2 = 1.50$ ).

The different phases observed in the  $\text{CaZrTi}_2\text{O}_7\text{-RE}_2\text{Ti}_2\text{O}_7$  system could be directly compared upon considering the normalized volume ( $V/Z$ ) of different phases present in the nominal compositions. Typical variation of normalized volume of the observed phases at different nominal compositions for the  $\text{Nd}^{3+}$  series is shown in **Figure 4.11**. The cubic pyrochlore ( $\text{Sm}_2\text{Ti}_2\text{O}_7$ ,  $\text{Y}_2\text{Ti}_2\text{O}_7$  and other having intermediate compositions) and monoclinic  $\text{Nd}_2\text{Ti}_2\text{O}_7$  type phases have larger molar volume as compared to zirconolite or perovskite-type phases, which can be attributed to their relatively open structures. Nevertheless, the substitution of  $\text{Ca}^{2+}$  and  $\text{Zr}^{4+}$  ions with  $\text{RE}^{3+}$  ions exhibited a small change in the molar volume in any of the observed phases. In addition to this, it can be observed from **Figure 4.11** that the molar volume increases with the 2M-zirconolite to 4M-zirconolite or 4M-zirconolite to pyrochlore-type structural transitions. All these transitions are related to the cation rearrangement following the diffusion of  $\text{Ca}^{2+}$ ,  $\text{Zr}^{4+}$  and  $\text{RE}^{3+}$  ions in the lattice.



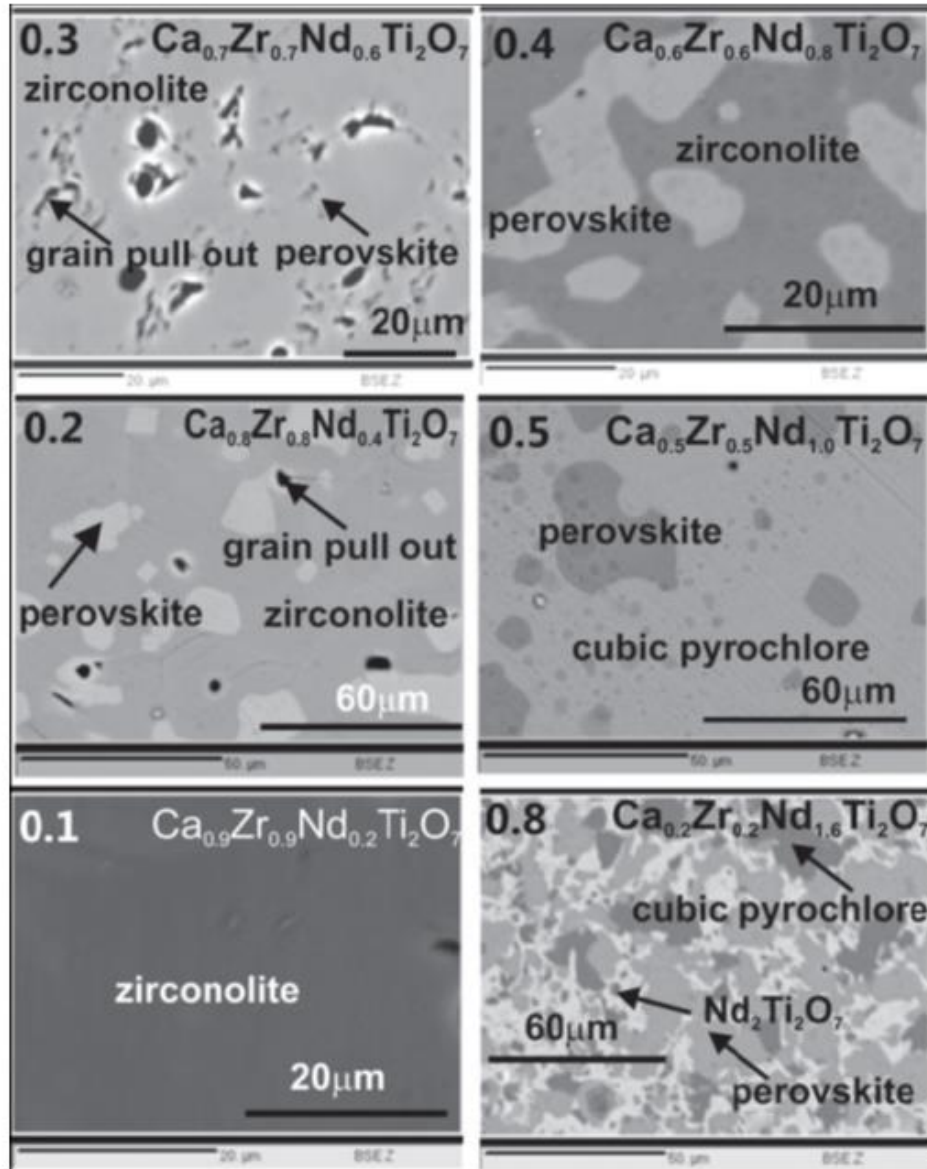
**Figure 4.11:** Variations of normalized volume ( $V/Z$ ) of different observed phases with nominal compositions<sup>116</sup>. (Z-I: Zirconolite-2M ( $Z=8$ ); Z-II: zirconolite-4M ( $Z=16$ ); Per: Perovskite ( $Z=2$ ); Py: cubic pyrochlore ( $Z=8$ ); NT: monoclinic  $\text{Nd}_2\text{Ti}_2\text{O}_7$  ( $Z=8$ ). For proper scaling of perovskite phase  $Z=2$  has been used.

The phase evolution trends obtained from powder XRD data of  $\text{Ca}_{1-x}\text{Zr}_{1-x}\text{RE}_{2x}\text{Ti}_2\text{O}_7$ , for  $x = 0.00$  to  $1.00$  system can be distinctly divided into four phase fields, namely (i) monoclinic zirconolite (comprising of 2M and 4M), (ii) cubic perovskite (not for  $\text{Y}^{3+}$  series), (iii) cubic pyrochlore, and (iv) monoclinic  $\text{Nd}_2\text{Ti}_2\text{O}_7$  types (for  $\text{Nd}^{3+}$  series). In addition to this, the zirconolite-type phase show stacking variant hettotype with the incorporation of larger  $\text{RE}^{3+}$  ions, in the lattice. The perovskite-type phase is formed on addition of large sized  $\text{RE}^{3+}$  ion in zirconolite due preferential segregation of  $\text{Ca}^{2+}$  from the lattice. Earlier, the formation of perovskite in zirconolite-type phase was observed only under reducing atmosphere<sup>57</sup>. However, later studies indicate formation of single phasic  $\text{Nd}^{3+}$  substituted zirconolite structure under reducing conditions<sup>63</sup> or by co-substitution with lower valent cations like  $\text{Al}^{3+}$  at  $\text{Ti}^{4+}$  sites<sup>64</sup>. In addition to this, the observation of coexisting perovskite-type phase in a wider range of nominal compositions suggests, the formation of perovskite phase is not solely related to annealing atmosphere but also to the temperature induced phase separation. The present observation is in accordance with the reported phase relation in  $\text{CaO-ZrO}_2\text{-TiO}_2$  system<sup>117</sup> as well as Gd substituted zirconolite system<sup>164-167</sup>. Thus, the formation of perovskite phase in zirconolite system is related to temperature induced cation rearrangement due to non-equivalent substitution of  $\text{RE}^{3+}$  ions in  $\text{Ca}^{2+}$  and  $\text{Zr}^{4+}$  sites and higher thermodynamic stability of perovskite-type phase. Similarly, the formation of cubic pyrochlore phases is also evident from this reason. Since zirconolite, pyrochlore and perovskite structures can accommodate wider range of cation compositions and disorder, the  $\text{CaZrTi}_2\text{O}_7\text{-RE}_2\text{Ti}_2\text{O}_7$  system is amenable for large variations in composition while still retaining the structures characteristic of this phase assemblage.

### 4.3.2. MICROSTRUCTURAL STUDIES

The phases identified by XRD analyses were further confirmed by the electron imaging, and qualitative as well as quantitative compositional analyses with EPMA technique. Representative back-scattered electron (BSE) images (with atomic number (Z) contrast) of selected compositions for  $\text{Nd}^{3+}$  series are shown in **Figure 4.12**, and the corresponding results of compositional analyses are presented in **Table 4.8**. Before quantitative analyses, qualitative compositional analyses were completed for each bulk compositions and a representative set of x-ray images are shown in **Figure 4.13**. The x-ray images for the bulk composition  $\text{Ca}_{0.60}\text{Zr}_{0.60}\text{Nd}_{0.80}\text{Ti}_2\text{O}_7$  show zirconolite and perovskite-type phases within the sample and the latter phase act as the sink for  $\text{Nd}^{3+}$ . A detailed assessment of the BSE images depicted in **Figure 4.12** indicated that the phase fraction having brighter contrast increases with increasing concentration of the  $\text{Nd}^{3+}$  ions, which is in accordance with the increasing phase fraction of the perovskite-type phase as concluded upon by powder XRD studies. The compositional analyses of the various parts of the BSE images revealed that small amounts of  $\text{Zr}^{4+}$  and majority of  $\text{Nd}^{3+}$  ions are preferentially substituted in the perovskite-type phase. Besides, a larger fraction of  $\text{Ca}^{2+}$  ions compared to  $\text{Zr}^{4+}$  ions are separated from the base zirconolite matrix. The analyses of the elemental stoichiometry of the phase with white contrast observed in different nominal compositions show that  $\text{Nd}^{3+}$  ion concentration exhibited a gradual increase in the perovskite-type phase. The substitution of  $\text{Ca}^{2+}$  by  $\text{Nd}^{3+}$  ions leads to a cation deficient and disordered perovskite-type phase. The BSE images observed for the nominal composition having zirconolite-2M and 4M structures along with perovskite phase, viz.  $x = 0.30$  and  $0.40$  (as inferred from XRD study) were found to be fairly comparable to those observed for zirconolite-2M and perovskite-type phase containing compositions. Thus, zirconolite-2M and 4M phases translated into indistinguishable phases in BSE image and appear as uniform grey matrix. The

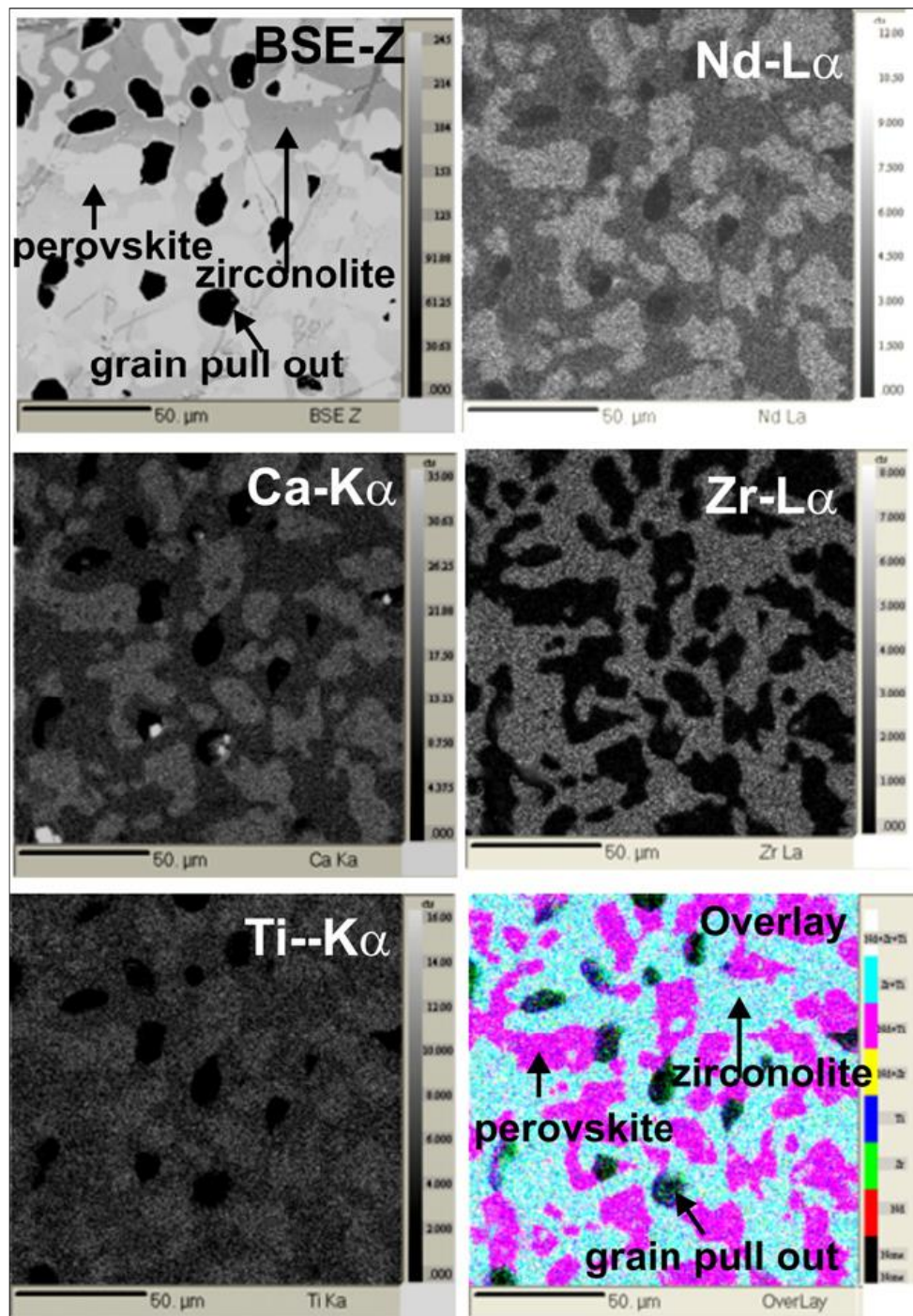
white and grey contrast phases observed in the compositions with  $x = 0.50$  and  $0.80$  exhibited  $\text{Nd}^{3+}$  rich titanate with fractional substitution of  $\text{Ca}^{2+}$  and  $\text{Zr}^{4+}$  ions. This phase could be



**Figure 4.12: Representative BSE images of 6 different bulk compositions with constituent phase assemblages<sup>116</sup>. Grain pull-outs are polishing defects.**

assumed as pyrochlore-type  $\text{Nd}_{2-x-y}\text{Ca}_x\text{Zr}_y\text{Ti}_2\text{O}_7$  phase. The increasing disorder in the cationic sub-lattice and decreasing average ionic radius at the  $\text{Nd}^{3+}$  site favoured the formation of pyrochlore phase. A comparison of the phase analyses from the XRD and EPMA studies

suggests that the zirconolite structure transform to the pyrochlore-type structure with increasing  $\text{Nd}^{3+}$  concentration. Further at higher  $\text{Nd}^{3+}$  containing compositions, the matrix is formed with



**Figure 4.13:** Representative qualitative x-ray images showing elemental distribution patterns among different phases of  $\text{Ca}_{0.60}\text{Zr}_{0.60}\text{Nd}_{0.80}\text{Ti}_2\text{O}_7$  bulk composition<sup>116</sup>.

**Table 4.8: Phase and compositions (at %) observed at various nominal bulk compositions for Nd<sup>3+</sup> series<sup>116</sup>. (balance oxygen or mention as “y”)**

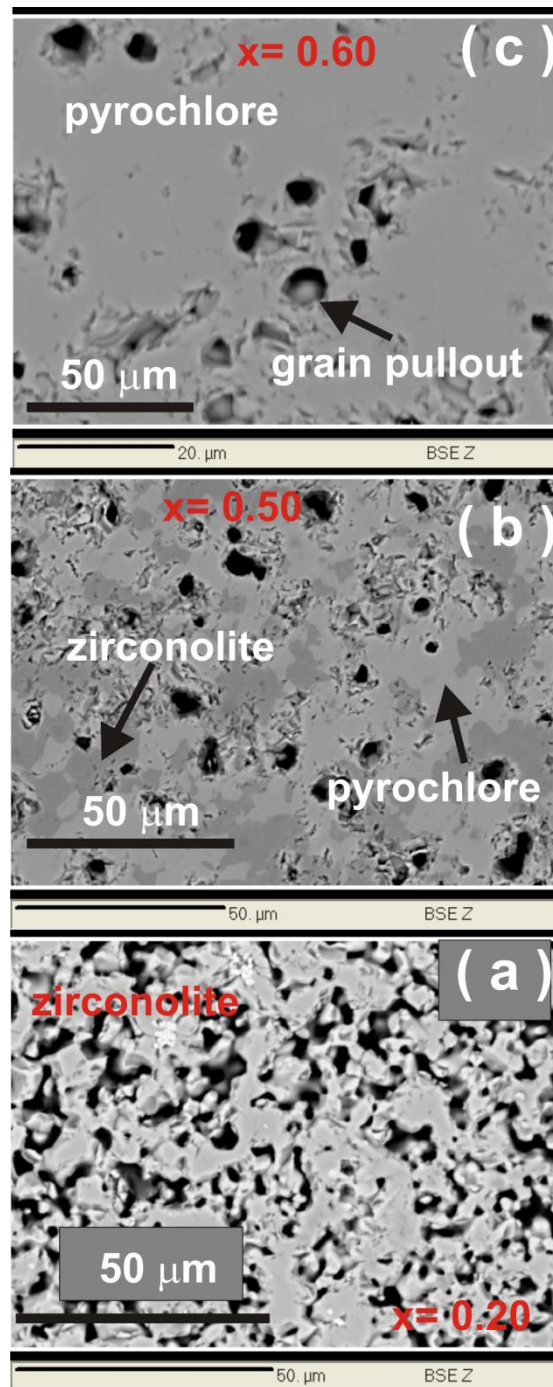
x	Composition	XR D	Phase	Zirconolite	Perovskite	Cubic Pyrochlore	Nd <sub>2</sub> Ti <sub>2</sub> O <sub>7</sub>
<b>0.10</b>	Ca <sub>0.90</sub> Zr <sub>0.90</sub> Nd <sub>0.20</sub> Ti <sub>2</sub> O <sub>7</sub>	2M	Matrix	Ca <sub>0.88</sub> Nd <sub>0.17</sub> Zr <sub>0.99</sub> Ti <sub>2.00</sub> O <sub>7</sub>	-	-	-
<b>0.20</b>	Ca <sub>0.80</sub> Zr <sub>0.80</sub> Nd <sub>0.40</sub> Ti <sub>2</sub> O <sub>7</sub>	4M P1	Matrix White	Ca <sub>0.84</sub> Nd <sub>0.24</sub> Zr <sub>1.02</sub> Ti <sub>1.87</sub> O <sub>7</sub>	Ca <sub>0.53</sub> Nd <sub>0.28</sub> Zr <sub>0.01</sub> Ti <sub>0.99</sub> O	-	-
<b>0.30</b>	Ca <sub>0.70</sub> Zr <sub>0.70</sub> Nd <sub>0.60</sub> Ti <sub>2</sub> O <sub>7</sub>	4M P1	Matrix Black	Ca <sub>0.53</sub> Nd <sub>0.49</sub> Zr <sub>0.93</sub> Ti <sub>2.05</sub> O	Ca <sub>0.44</sub> Nd <sub>0.33</sub> Zr <sub>0.06</sub> Ti <sub>1.09</sub> O		-
<b>0.40</b>	Ca <sub>0.60</sub> Zr <sub>0.60</sub> Nd <sub>0.80</sub> Ti <sub>2</sub> O <sub>7</sub>	4M P1	Matrix White	Ca <sub>0.62</sub> Nd <sub>0.50</sub> Zr <sub>1.14</sub> Ti <sub>1.73</sub> O <sub>7</sub>	Ca <sub>0.44</sub> Nd <sub>0.52</sub> Zr <sub>0.02</sub> Ti <sub>1.01</sub> O	-	-
<b>0.50</b>	Ca <sub>0.50</sub> Zr <sub>0.50</sub> Nd <sub>1.00</sub> Ti <sub>2</sub> O <sub>7</sub>	P2 P1	Matrix Gray	-	Ca <sub>0.36</sub> Nd <sub>0.53</sub> Zr <sub>0.03</sub> Ti <sub>1.07</sub> O	Nd <sub>1.06</sub> Ca <sub>0.49</sub> Zr <sub>0.63</sub> Ti <sub>1.82</sub> O	-
<b>0.80</b>	Ca <sub>0.20</sub> Zr <sub>0.20</sub> Nd <sub>1.60</sub> Ti <sub>2</sub> O <sub>7</sub>	P1 NT P2	Matrix White Gray	-	Ca <sub>0.22</sub> Nd <sub>0.60</sub> Ti <sub>1.16</sub> Zr <sub>0.02</sub> O	Nd <sub>1.20</sub> Ca <sub>0.44</sub> Zr <sub>0.06</sub> Ti <sub>2.34</sub> O	Nd <sub>1.83</sub> Ca <sub>0.07</sub> Ti <sub>2.05</sub> Zr <sub>0.05</sub> O

2M= zirconolite-2M ; 4M= zirconolite-4M; P1=perovskite; P2=cubic pyrochlore; NT=Nd<sub>2</sub>Ti<sub>2</sub>O<sub>7</sub>

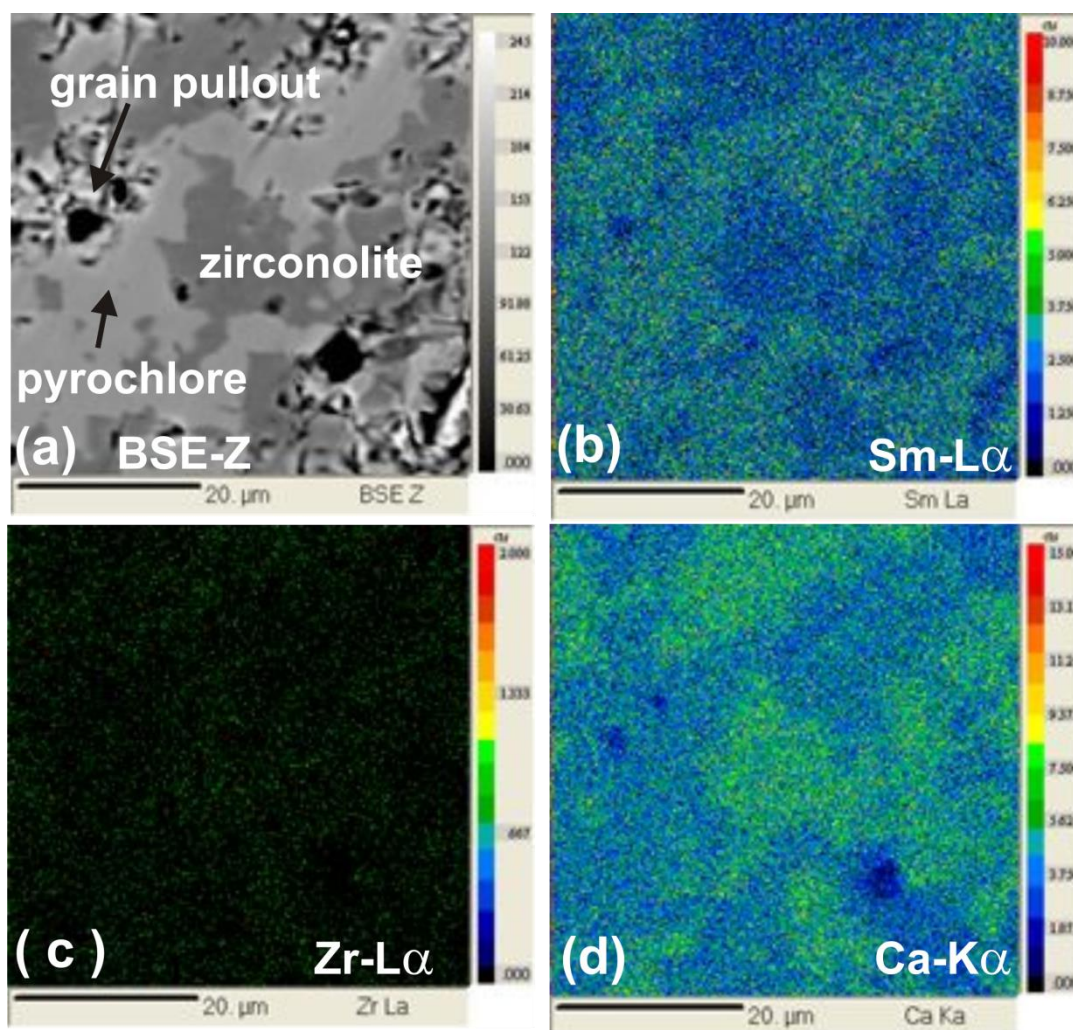


mainly  $\text{Nd}_2\text{Ti}_2\text{O}_7$  with a small fraction of cubic pyrochlore-type phase. Poorly crystalline micro-structural features are observed for the  $\text{Nd}^{3+}$  rich compositions. The bulk white matrix compositions observed at  $x = 0.90$  are poorly crystalline and show only a feeble ( $\sim 0.1\%$ ) substitution of Ca and Zr. The higher Ca and Zr containing phases are observed as segregated phase which correspond to cubic pyrochlore-type phase.

Representative back-scattering electron images (BSE) of representative compositions for  $\text{Sm}^{3+}$  series are illustrated in **Figure 4.14 (a-c)**. The X-ray mapping for one representative composition  $\text{Ca}_{0.50}\text{Zr}_{0.50}\text{Sm}_{1.00}\text{Ti}_2\text{O}_7$  ( $x = 0.50$ ) is shown in **Figure 4.15 (a-d)**. Presence of minor segregated perovskite type phase could not be observed in any of the BSE images, The BSE image (**Figure 4.14.a**) of the nominal composition  $\text{Ca}_{0.90}\text{Zr}_{0.90}\text{Sm}_{0.20}\text{Ti}_2\text{O}_7$  (i.e.,  $x=0.10$ ) exhibited homogeneous zirconolite type phase only. Likewise, the existence of a uniform single phase is conformed from the BSE image of the  $\text{Ca}_{0.40}\text{Zr}_{0.40}\text{Sm}_{1.20}\text{Ti}_2\text{O}_7$  composition (**Figure 1.14.c**). However, the coexistence of two phases (zirconolite-4M and cubic pyrochlore) at the composition with  $x = 0.50$  (i.e.  $\text{Ca}_{0.50}\text{Zr}_{0.50}\text{Sm}_{1.00}\text{Ti}_2\text{O}_7$ ) is reflected in the phase contrast BSE images (**Figure 4.14.b**). The minor zirconolite-4M phase is observed as darker contrast while the cubic pyrochlore phase appeared with lighter contrast within the BSE images. The analyses of the compositions of the phases from the emitted x-rays (**Figure 4.15**) backing the coexistence of zirconolite and pyrochlore type phase in that particular nominal composition. Both the BSE and x-ray images show that the minor zirconolite-4M phase is distributed within the matrix of cubic pyrochlore phase. Compositions of the different phases observed in other compositions are given in **Table 4.9**. Elemental compositions of different phases are also in close agreement with the nominal compositions of both single and biphasic systems.



**Figure 4.14:** Representative BSE images for  $\text{Ca}_{1-x}\text{Zr}_{1-x}\text{Sm}_{2x}\text{Ti}_2\text{O}_7$  compositions<sup>115</sup>. ( $x = 0.10$  (a).  $0.50$  (b) and  $0.60$  (c)). Dark black regions are polishing grain pull-outs defect.



**Figure 4.15:** X-ray images of  $\text{Ca}_{0.50}\text{Zr}_{0.50}\text{Sm}_{1.00}\text{Ti}_2\text{O}_7$  ( $x=0.50$ )<sup>115</sup>. (Two phase system consisting of zirconolite and pyrochlore).

**Table 4.9:** Phase and compositions (at %) observed at various representative compositions for  $\text{Sm}^{3+}$  series<sup>115</sup>.

x	Composition	XRD	Phase	Zirconolite	Cubic Pyrochlore
0.10	$\text{Ca}_{0.90}\text{Zr}_{0.90}\text{Sm}_{0.20}\text{Ti}_2\text{O}_7$	M1	Matrix	$\text{Ca}_{0.73}\text{Zr}_{0.76}\text{Sm}_{0.15}\text{Ti}_2\text{O}_{6.48}$	-
0.50	$\text{Ca}_{0.50}\text{Zr}_{0.50}\text{Sm}_{1.00}\text{Ti}_2\text{O}_7$	P2 M2	Matrix Gray	$\text{Ca}_{0.49}\text{Zr}_{0.53}\text{Sm}_{0.72}\text{Ti}_2\text{O}_{6.63}$	$\text{Ca}_{0.38}\text{Zr}_{0.38}\text{Sm}_{1.04}\text{Ti}_2\text{O}_{6.70}$
0.60	$\text{Ca}_{0.40}\text{Zr}_{0.40}\text{Nd}_{1.20}\text{Ti}_2\text{O}_7$	P2	Matrix	-	$\text{Ca}_{0.35}\text{Zr}_{0.35}\text{Sm}_{1.22}\text{Ti}_2\text{O}_{6.88}$

The microstructure and elemental details for some nominal compositions for  $\text{Y}^{3+}$  series were carried out by SEM and EDS studies. Typical SEM images of some compositions are shown in **Figure 4.16**. Well sintered characteristics with near spherical or irregular grains were

observed in the SEM images of the nominal compositions. However, it may be noted that the microstructures were found to be almost similar for both single phase ( $x = 0.40$ ) and multiphase ( $x = 0.25$  and  $0.50$ ) nominal compositions. Elemental analyses were carried out by EDS on some random selected points and is depicted in **Table 4.10**. Despite the closer atomic numbers (Z) of the elements, like Ca/Ti and Zr/Y, the estimated compositions are closer to that expected for the nominal compositions. The estimated compositions were found out to be in close agreement with the nominal compositions in single phase samples. Attempts to find the compositions of phases in multiphase samples indicated an overall composition due to poor Z contrast of different phases as well as individual phases.

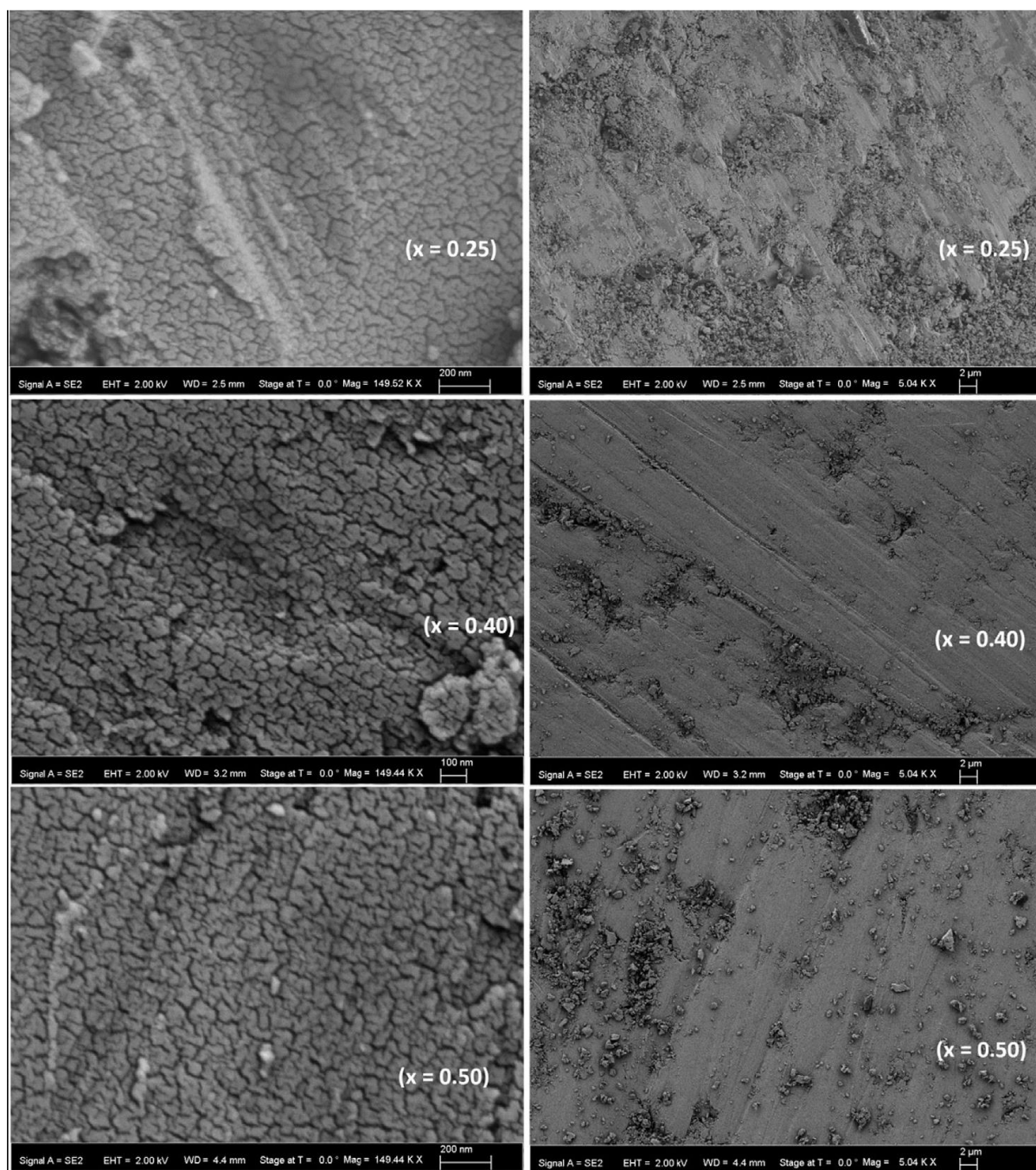
**Table 4.10: Atomic (metal) ratio as estimated from point mode EDX analyses of some representative compositions<sup>159</sup>.**

x	Nominal composition		Atomic ratio (metal ions)			
			Ca	Zr	Y	Ti
0.25	$\text{Ca}_{0.75}\text{Zr}_{0.75}\text{Y}_{0.50}\text{Ti}_2\text{O}_7$	Expected	0.1875	0.1875	0.125	0.5
		EDX-1	0.2068	0.1999	0.1442	0.4430
		EDX-2	0.2038	0.1984	0.1405	0.4458
0.4	$\text{Ca}_{0.60}\text{Zr}_{0.60}\text{Y}_{0.80}\text{Ti}_2\text{O}_7$	Expected	0.1500	0.1500	0.2000	0.5000
		EDX-1	0.1574	0.1686	0.2358	0.4004
		EDX-2	0.1574	0.1653	0.2376	0.4021
0.5	$\text{Ca}_{0.50}\text{Zr}_{0.50}\text{Y}_{1.00}\text{Ti}_2\text{O}_7$	Expected	0.1250	0.1250	0.2500	0.5
		EDX-1	0.1507	0.1661	0.2479	0.4219
		EDX-2	0.1505	0.1673	0.2493	0.4320
0.8	$\text{Ca}_{0.20}\text{Zr}_{0.20}\text{Y}_{1.60}\text{Ti}_2\text{O}_7$	Expected	0.0500	0.0500	0.4000	0.5000
		EDX-1	0.0462	0.0632	0.3837	0.4607
		EDX-2	0.0474	0.0590	0.3987	0.4721
		EDX-3	0.0452	0.0591	0.3941	0.4699

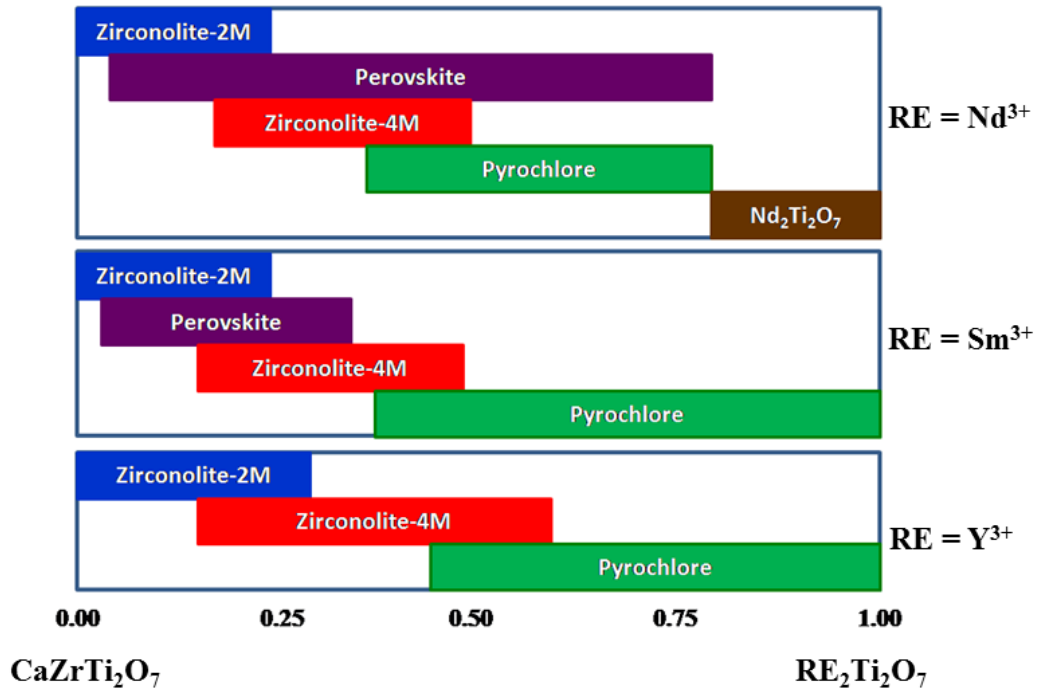
## 4.4. CONCLUSIONS

From powder XRD and microstructure studies on the  $\text{CaZrTi}_2\text{O}_7$  (zirconolite)- $\text{RE}_2\text{Ti}_2\text{O}_7$  (pyrochlore) ( $\text{RE} = \text{Nd}^{3+}$ ,  $\text{Sm}^{3+}$  and  $\text{Y}^{3+}$ ) systems, it is evident that the systems consist of four phase fields, namely (i) monoclinic zirconolite (comprising of 2M and 4M), (ii) cubic

perovskite (not for  $Y^{3+}$  series), (iii) cubic pyrochlore and (iv) monoclinic  $Nd_2Ti_2O_7$  types (for  $Nd^{3+}$  series). A representation of phase field in the above system is represented in **Figure 4.17**



**Figure 4.16: SEM images of compositions with  $x = 0.25$ ,  $0.40$  and  $0.50$  in two different resolutions (left column: 150 KX and right column: 5 KX magnifications)<sup>159</sup>.**



**Figure 4.17: Phase evolution in  $\text{CaZrTi}_2\text{O}_7$  (zirconolite)- $\text{RE}_2\text{Ti}_2\text{O}_7$  (pyrochlore) ( $\text{RE} = \text{Nd}^{3+}$ ,  $\text{Sm}^{3+}$  and  $\text{Y}^{3+}$ ) system.**

It is also found that the existence of cubic perovskite phase decreases with decreasing ionic radii of  $\text{RE}^{3+}$  ion. It is also concluded that the solubility of trivalent ions in zirconolite lattice increases with decreasing ionic radii of  $\text{RE}^{3+}$  ion. Molar volumes of each phases are found to increase with increasing  $\text{RE}^{3+}$  content, which is in accordance with the slightly larger ionic radii of  $\text{RE}^{3+}$  than that of  $\text{Ca}^{2+}$ - $\text{Zr}^{4+}$  couple. In all the three studied systems, a cubic pyrochlore structure was observed which can be able to accommodate a larger amount of heterovalent cation without any phase separation. Hence, a detailed structural and thermodynamic stability studies have been carried out on aliovalent substituted cubic pyrochlore structure and the results are discussed in the next chapter of this thesis.



# **Chapter 5**

## **Structure and thermodynamic stability of Ca and Zr co-substituted $\text{Gd}_2\text{Ti}_2\text{O}_7$ pyrochlore system: Experimental and theoretical study**

The data reported in this chapter have been published in the following peer-reviewed journal:

- Implication of aliovalent cation substitution on structural and thermodynamic stability of  $\text{Gd}_2\text{Ti}_2\text{O}_7$ : Experimental and theoretical investigations  
M. Jafar, S. B. Phapale, S. Nigam, S. N. Achary, R. Mishra, C. Majumder, A. K. Tyagi,  
*J Alloys Compd.* (Accepted)

Theoretical studies presented in this chapter have been carried out in collaboration.

## 5.1. INTRODUCTION

Longer half-lives of minor actinides present in nuclear high level waste (HLW) such as Np, Am, Cf, etc is the main reason for its long term radio toxicity. Hence, nuclear HLW needs to be immobilized in very stable and long-lasting materials which are also called as waste immobilization matrices<sup>48</sup>. Presently, most countries throughout the world uses borosilicate glass as the primary waste immobilization matrices<sup>4</sup>. Nevertheless, glass being a metastable material has its own set of limitations such as possible devitrification and low solubility of minor actinides to name a few<sup>31,143,168</sup>. In view of these shortcoming of glass matrix, Ringwood et al proposed composites or assemblages of mineral analogous titanates, termed as SYNROC as futuristic and potential matrix for immobilization of nuclear HLW<sup>38</sup>. SYNROC is a composite material and mostly consists of zirconolite, perovskite, hollandite, pyrochlore and rutile type phases<sup>38,65,70,72</sup>. Among the constituent phases of SYNROC, major emphasis on research has been on the study of these constituent phases in isolation or as an ensemble<sup>65,70</sup>.

Pyrochlore phase, one of the most important constituent phases of SYNROC, is expressed by the general formula  $A_2B_2O_7$  where A and B cations respectively form  $AO_8$  and  $BO_6$  polyhedra with oxygen atom<sup>69</sup>. The pyrochlore structure can exist in two different forms viz. either an ordered structure with Fd-3m symmetry or a disordered one having Fm-3m symmetry (defect-fluorite type) structure depending upon the  $r_A/r_B$  ratio where  $r_A$  and  $r_B$  represents the ionic radii of the cations in their respective co-ordination numbers<sup>115,116,159</sup>. In general, for  $A_2Ti_2O_7$  where A is a rare earth ion, ionic radii smaller than  $Sm^{3+}$  form ordered cubic pyrochlore structures whereas ions having greater ionic radii than  $Sm^{3+}$  form perovskite related monoclinic structures. The ability to accommodate a wide range of ions without significant alteration within the crystal structure makes pyrochlore a potential candidate for immobilization of minor actinides present in nuclear HLW<sup>67,71</sup>. Several reports indicating the structural and thermodynamic stability of pyrochlore type compounds under extreme



conditions such as temperature, pressure, higher radiation field, etc. are available in literature<sup>131,169–178</sup>. However, most of studies are limited to host lattices or uranium incorporated lattices. Structural perturbations induced by doping of diverse cations into pyrochlore lattice are still limited in literature. The effects of aliovalent substitution and multi cation substitution is an important field in nuclear waste immobilization as it required to understand the effects of dopants in pyrochlore lattices before qualifying them as waste immobilization matrices. Hence, incorporation of one divalent ion ( $\text{Ca}^{2+}$ ) and one tetravalent cation ( $\text{Zr}^{4+}$ ) in place of two trivalent cations ( $\text{Gd}^{3+}$ ) were carried out in this work. The idea of the planned work was to carry out a detailed analysis on structural and thermodynamic stability of diverse cation doped pyrochlore structure along with their theoretical validations. The choice of the system to probe was based on our earlier studies in zirconolite-pyrochlore based systems<sup>115,116,159</sup> and the results are presented in the chapter.

## 5.2. EXPERIMENTAL METHODS

Solid state synthetic route was chosen to prepare a series of nominal compositions having the general stoichiometry  $\text{Gd}_{2-2x}\text{Ca}_x\text{Zr}_x\text{Ti}_2\text{O}_7$  ( $0.0 \leq x \leq 0.4$ ). Binary oxides such as  $\text{ZrO}_2$  (Sigma Aldrich, purity 99.0%),  $\text{TiO}_2$  (Sigma Aldrich, purity  $\geq 99.5\%$ ),  $\text{Gd}_2\text{O}_3$  (Indian Rare Earths Ltd., purity 99.9%) were preheated overnight at 1173K to remove adsorbed water and oxy-carbonate residues.  $\text{CaCO}_3$  (Sigma Aldrich, St. Louis, MO, USA, purity  $> 99.0\%$ ) was dehydrated at 473K for 4 h. Stoichiometric amount of the dried reactants required to prepare desired compositions were weighed, homogenised in acetone medium, pelletized and then heated at 1473K for 24 h. The heated pellets were crushed, homogenized and again kept at the same temperature for 24 h. The above process was repeated again and the pellets were finally sintered at 1573K for 24 h. Products obtained after each heat treatment were characterized by powder x-ray diffraction (XRD) technique on a Panalytical X-pert Pro diffractometer using Cu

$K\alpha$  ( $\lambda = 1.5406$  and  $1.5444$  Å) radiation, in the two theta range of  $10$ - $90^\circ$  with step width and time of  $0.02^\circ$  and  $1.20$ s, respectively as mentioned in literatures<sup>115,116,159</sup>. Structural investigations of the nominal compositions were carried out using Fullprof-2000 program<sup>103</sup>. Raman spectra of the nominal compositions were recorded using He-Ne laser having a wavelength of  $632$  nm. Powder samples were smeared on a glass slide and the scattered radiation was collected at  $180^\circ$  scattering geometry using a CCD (Synapse) based monochromator (LabRAM HR800, Horiba Jobin Yvon, France) together with an edge filter. The operating power of the laser was kept at  $10$  mW and spot size of the sample was  $0.5$  mm in diameter. Raman band at  $520\text{ cm}^{-1}$  corresponding to a silicon wafer was used for calibration of the instrument. The resolution of spectral measurement was estimated to be close to  $\sim 1\text{ cm}^{-1}$ . Standard molar enthalpy of formation of the nominal compositions  $\text{Gd}_{2-2x}\text{Ca}_x\text{Zr}_x\text{Ti}_2\text{O}_7$  ( $0.0 \leq x \leq 0.4$ ) were calculated by measuring the enthalpy of dissolution of the compounds in liquid  $\text{Na}_2\text{O} + \text{MoO}_3$  solvent (3:4 molar ratio) at  $986$  K as well as the binary oxide reactants by employing a high-temperature Calvet calorimeter (Setaram model HT-1000). The calorimeter consists of an isothermal alumina block containing two equal alumina tubes surrounded by a series of thermopiles composed of Pt–Pt 10 % Rh thermocouple having a measurement accuracy of  $\pm 0.1$  K. Calibration of heat flow in the instrument was carried out by a synthetic sapphire [NIST SRM-720] and the detailed experimental process is mentioned in our earlier reports<sup>130,131,178</sup>.

Theoretical calculations were carried out using spin-polarized density functional theory (DFT) associated with a plane-wave basis set implemented in the Vienna Ab-initio Simulation Package (VASP)<sup>179–182</sup>. Electron–ion interactions were designated by the projector augmented wave (PAW) method<sup>182</sup>. In order to calculate the exchange–correlation energy, the spin-polarized generalized gradient approximation using the Perdew–Burke–Ernzerhof (PBE) functional has been used<sup>183</sup>. The cut-off energy for the plane-wave basis set was fixed at  $400$

eV. Geometry optimization was carried out by ionic relaxation using a conjugate gradient minimization. Geometries were considered to be converged when the force on each ion became less than or equal to 0.01 eV. Total energy convergence was verified with respect to the sizes of the plane-wave basis set, the simulation cell and the total energy was found to be accurate within 1 meV. A Monkhorst–Pack k-point grid of 2 x 2 x 2 was employed for mapping of the first Brillouin zone.

## 5.3. RESULTS AND DISCUSSIONS

### 5.3.1. STRUCTURAL STUDIES

Progress of Phase formation in  $\text{Gd}_{2-2x}\text{Ca}_x\text{Zr}_x\text{Ti}_2\text{O}_7$  ( $0.0 \leq x \leq 0.4$ ) were inspected upon analysis of powder XRD patterns of the nominal compositions obtained after each heat treatment. In accordance with our earlier studies<sup>115,116,159</sup>, reaction completion was observed after sintering at 1573K. Hence, the structural analysis of the nominal compositions was carried out from the powder XRD pattern obtained after final sintering at 1573K. Powder XRD patterns of the nominal compositions  $\text{Gd}_{2-2x}\text{Ca}_x\text{Zr}_x\text{Ti}_2\text{O}_7$  ( $0.0 \leq x \leq 0.4$ ) are shown in **Figure 5.1**. Powder XRD pattern for the parent compound,  $\text{Gd}_2\text{Ti}_2\text{O}_7$  ( $x=0.0$ ), matched fairly well with the standard cubic pyrochlore type structure (Fd-3m symmetry, PCPDF card no. 73-1698) exhibiting the superstructure peaks for pyrochlore at  $2\theta \sim 15.06^\circ$ ,  $29.09^\circ$ ,  $46.30^\circ$  and  $65.39^\circ$  corresponding to (111), (311), (511) and (711) planes, respectively.

Presence of these superstructure peaks throughout the entire studied range is an indication that all the compositions exist in cubic pyrochlore structure. Moreover, relative lowering of intensity of the superstructure peak with respect to the main peak is also observed with increasing substitution of  $\text{Ca}^{2+}$  and  $\text{Zr}^{4+}$  ions and is depicted in **Figure 5.2**. This observation can be accounted to the increasing randomization of ions incorporated into the pyrochlore structure.

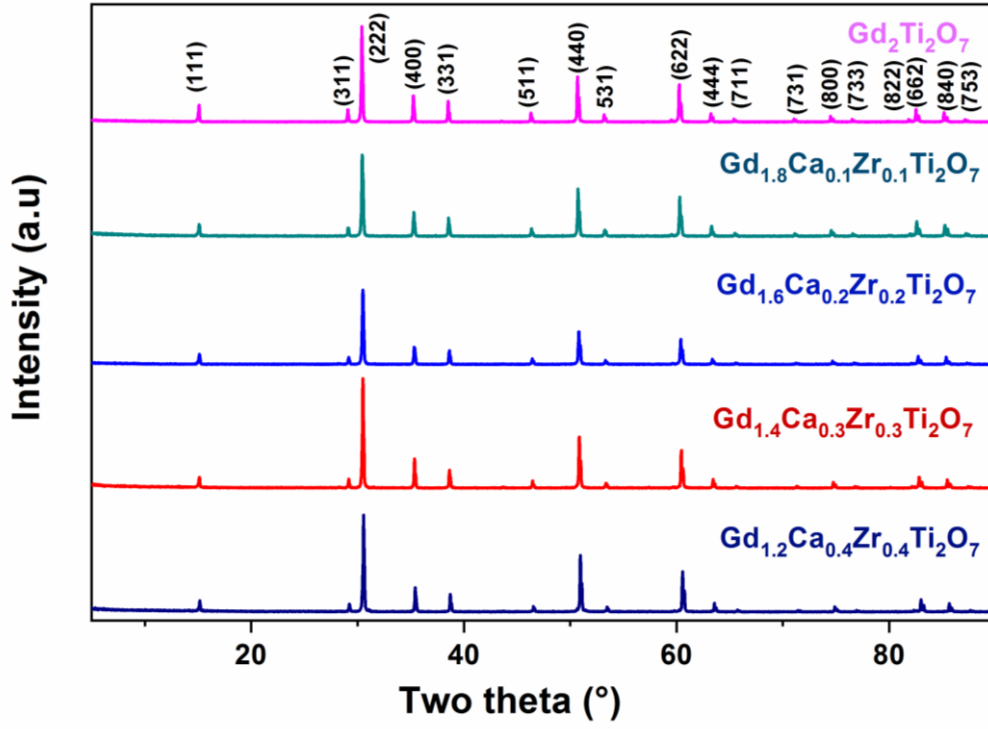


Figure 5.1: Powder X-ray diffraction patterns of the series  $\text{Gd}_{2-2x}\text{Ca}_x\text{Zr}_x\text{Ti}_2\text{O}_7$  ( $0.0 \leq x \leq 0.4$ )<sup>184</sup> (PCPDF-73-1698).

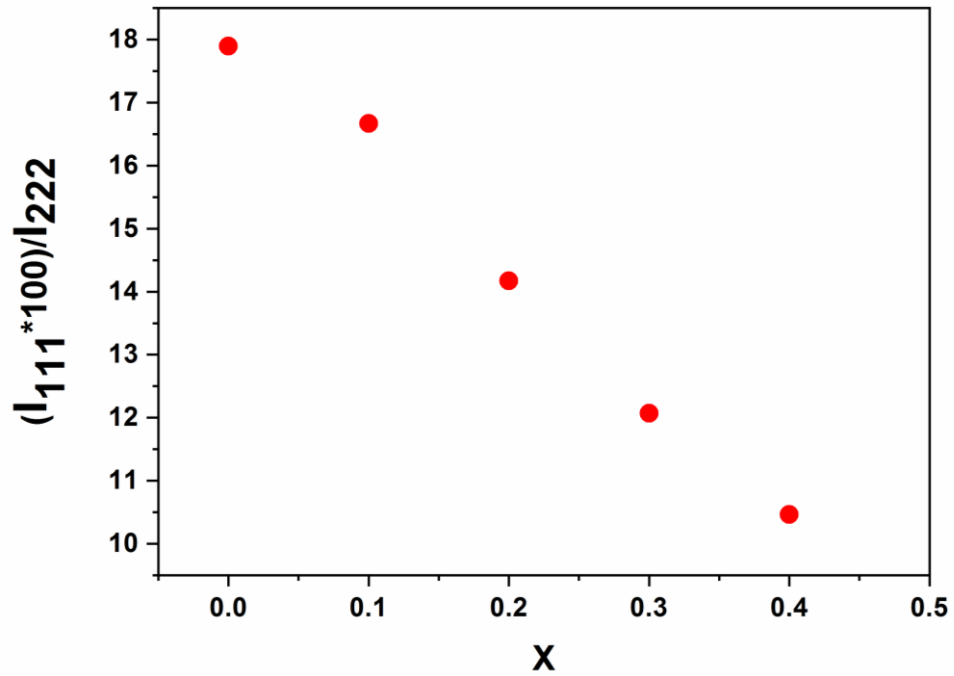


Figure 5.2: Relative peak intensity (%) of (111) superstructure peak with respect to the strongest (222) peak of pyrochlore structure<sup>184</sup>.

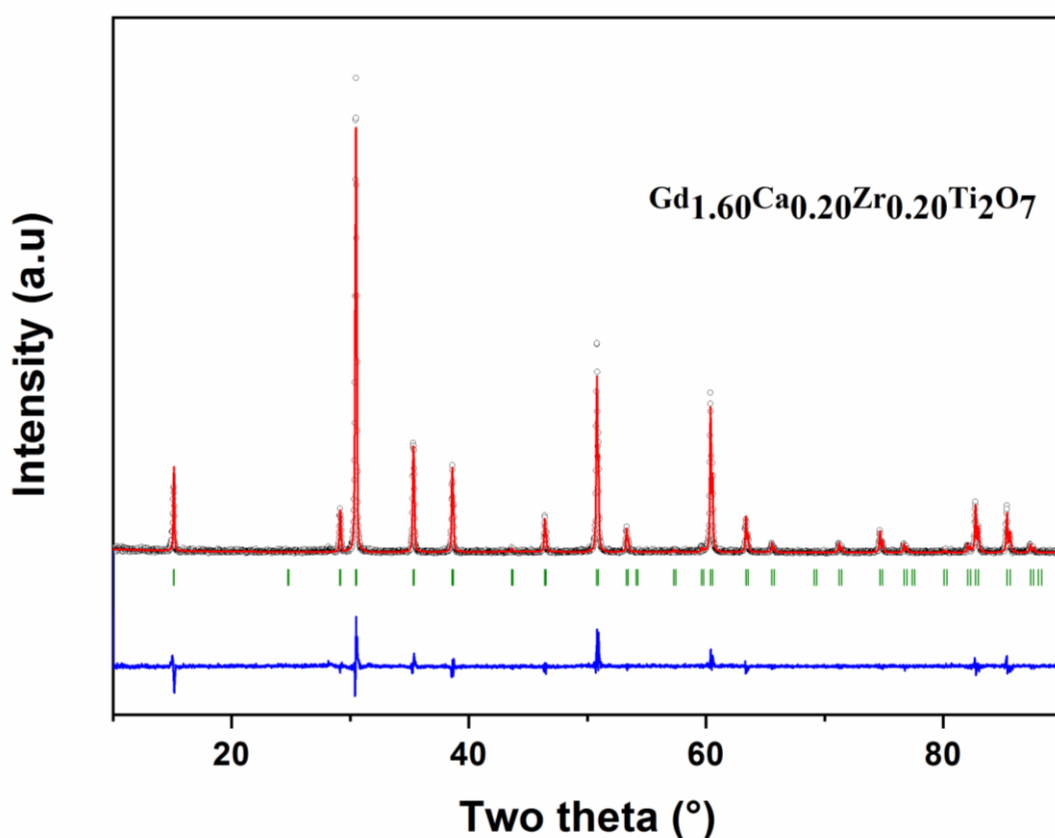
Structural analysis of all the nominal compositions was carried out using Rietveld refinement program. The background of obtained XRD data was fitted with a sixth order polynomial relation followed by adjustment of scale factor. All the observed diffraction peaks were fitted with pseudo-Voigt profile function followed by refinement of the u, v, w parameters. Absorption parameter and displacement factor were not considered in the refinements. In accordance with these conditions, unit cell parameter obtained for  $\text{Gd}_2\text{Ti}_2\text{O}_7$  ( $x=0.0$ ) were calculated as:  $a = 10.1841(1) \text{ \AA}$  and  $V = 1056.25(2) \text{ \AA}^3$ . Since all the other nominal compositions exhibited superstructure peaks, all the patterns were refined considering the substitution of both  $\text{Ca}^{2+}$  and  $\text{Zr}^{4+}$  ions into  $\text{Gd}^{3+}$  site only leaving  $\text{Ti}^{4+}$  site untouched. The rationale of considering the above assumption is based on the size of ionic radii of the different constituent ions present in the system at different coordination number<sup>150</sup> and is given in **Table 5.1**.

**Table 5.1: Ionic radii of the constituent ions at different coordination number<sup>150</sup>.**

Atoms	Coordination No.	Ionic radii ( $\text{\AA}$ )
$\text{Gd}^{3+}$	8	1.053
	6	0.938
$\text{Zr}^{4+}$	8	0.84
	6	0.72
$\text{Ti}^{4+}$	8	0.74
	6	0.605
$\text{Ca}^{2+}$	8	1.12
	6	1.00

From the table, it can be observed that ionic radii of two  $\text{Gd}^{3+}$  comes to be  $2.106 \text{ \AA}$  whereas the addition of the substituent ions ( $\text{Ca}^{2+} + \text{Zr}^{4+}$ ) is  $1.96 \text{ \AA}$ . Therefore, a negative deviation of ionic radii from the combined substituent ions at A site of pyrochlore structure comes out to be  $\sim 6\%$ . In accordance with this, Rietveld refinement of the non-end member compositions exhibited a decreasing trend in unit cell parameters and unit cell volume with increase in substituent concentration or x values. The details of phase analyses and unit cell parameters observed are given in **Table 5.2**. Unit cell parameter as calculated from Rietveld refinement

steadily decreased from  $a = 10.1841(1) \text{ \AA}$ ,  $V = 1056.25(2) \text{ \AA}^3$  for  $\text{Gd}_2\text{Ti}_2\text{O}_7$  ( $x=0.0$ ) to  $a = 10.1356(1) \text{ \AA}$ ,  $V = 1041.24(2) \text{ \AA}^3$  for  $\text{Gd}_{1.20}\text{Ca}_{0.40}\text{Zr}_{0.40}\text{Ti}_2\text{O}_7$  ( $x=0.4$ ) respectively. “X” coordinate for 48f oxygen atoms also remains almost similar ( $\sim 0.43$ ) from  $x=0.0$  to  $x=0.3$  showing just slight alteration to 0.425 (for  $x=0.4$ ) indicating tendency towards randomization of the pyrochlore structure into some disordered form which results in segregating of secondary phase. Representative Rietveld refinement plot of  $\text{Gd}_{1.6}\text{Ca}_{0.2}\text{Zr}_{0.2}\text{Ti}_2\text{O}_7$  ( $x=0.2$ ) is shown in **Figure 5.3**.



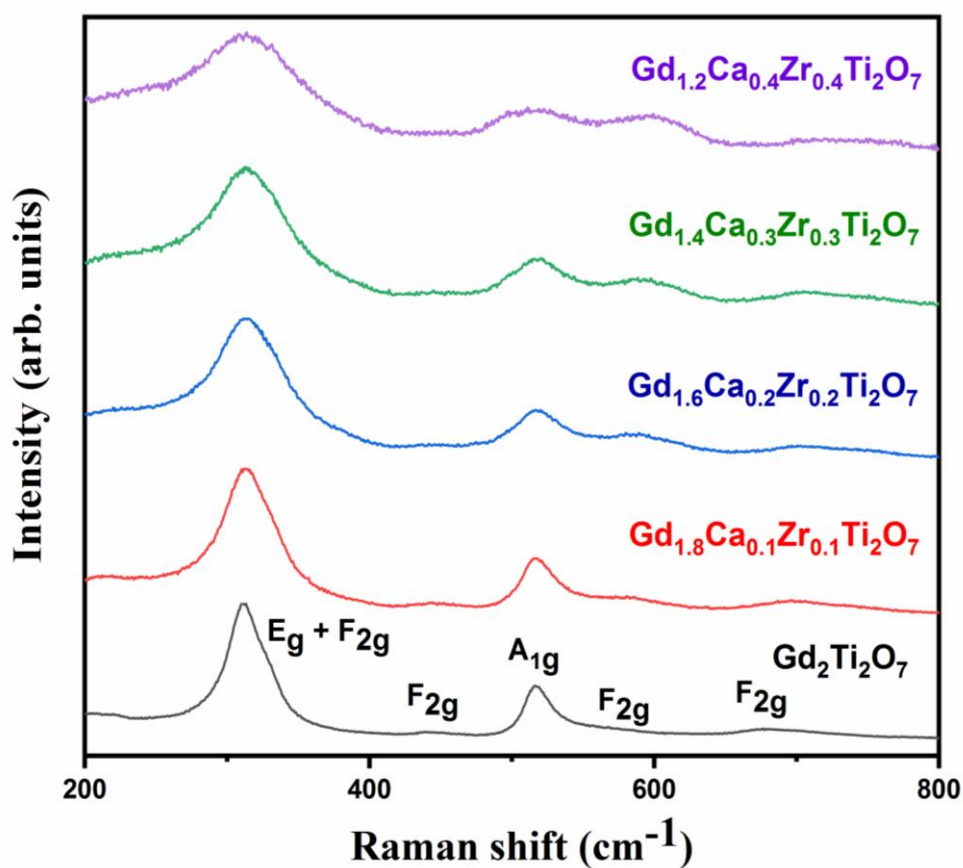
**Figure 5.3: Rietveld refinement plot of  $\text{Gd}_{1.6}\text{Ca}_{0.2}\text{Zr}_{0.2}\text{Ti}_2\text{O}_7$  ( $x=0.2$ ).**

Raman spectra of the prepared nominal compositions  $\text{Gd}_{2-2x}\text{Ca}_x\text{Zr}_x\text{Ti}_2\text{O}_7$  ( $0.0 \leq x \leq 0.4$ ) were recorded in the range of  $200\text{--}800 \text{ cm}^{-1}$ . Raman spectra of the parent compound  $\text{Gd}_2\text{Ti}_2\text{O}_7$  ( $x=0.0$ ) showed five discrete bands centred at  $\sim 310\text{cm}^{-1}$ ,  $\sim 450\text{cm}^{-1}$ ,  $\sim 520 \text{ cm}^{-1}$ ,  $\sim 570 \text{ cm}^{-1}$  and  $\sim 690 \text{ cm}^{-1}$ , and is displayed in **Figure 5.4**. The strongest band centred around  $310 \text{ cm}^{-1}$  could be assigned to O—Gd—O bending mode which is an amalgamation of two Raman modes ( $E_g$

**Table 5.2: Refinement parameters of the series  $\text{Gd}_{2-2x}\text{Ca}_x\text{Zr}_x\text{Ti}_2\text{O}_7$  ( $0.0 \leq x \leq 0.4$ )<sup>184</sup>.**

<b>x</b>	<b>0.00</b>	<b>0.10</b>	<b>0.20</b>	<b>0.30</b>	<b>0.40</b>
Composition	$\text{Gd}_{2.00}\text{Ti}_2\text{O}_7$	$\text{Gd}_{1.80}\text{Ca}_{0.10}\text{Zr}_{0.10}\text{Ti}_2\text{O}_7$	$\text{Gd}_{1.60}\text{Ca}_{0.20}\text{Zr}_{0.20}\text{Ti}_2\text{O}_7$	$\text{Gd}_{1.40}\text{Ca}_{0.30}\text{Zr}_{0.30}\text{Ti}_2\text{O}_7$	$\text{Gd}_{1.20}\text{Ca}_{0.40}\text{Zr}_{0.40}\text{Ti}_2\text{O}_7$
a (Å)	10.1841(1)	10.1762(2)	10.1629(1)	10.1533(1)	10.1356(1)
V (Å <sup>3</sup> )	1056.25(2)	1053.79(3)	1049.68(2)	1046.71(2)	1041.24(2)
X parameter	0.433(1)	0.431(2)	0.432(1)	0.432(1)	0.425(1)
u	0.0214(4)	0.057(8)	0.033(7)	0.0400(5)	0.045(6)
v	-0.021(4)	-0.070(9)	-0.042(8)	-0.036(5)	-0.055(6)
w	0.012(1)	0.034(3)	0.027(2)	0.015(1)	0.024(2)
Rp	12.2	16.2	17.5	14.6	16.3
Rwp	19.5	27.0	24.8	20.4	22.0
Chi <sup>2</sup>	1.99	1.99	1.65	1.60	1.90
M-O1 (Å)	$2.2049 \times 2$	$2.2032 \times 2$	$2.2003 \times 2$	$2.1983 \times 2$	$2.1944 \times 2$
M-O2 (Å)	$2.593(6) \times 4$	$2.577(6) \times 4$	$2.577(8) \times 4$	$2.579(5) \times 4$	$2.525(5) \times 4$
	$2.593(8) \times 2$	$2.577(10) \times 2$	$2.577(6) \times 2$	$2.579(7) \times 2$	$2.525(7) \times 2$
Distortion ( $\times 10^{-4}$ )	45.414	42.435	43.170	44.060	34.307
Ti-O (Å)	$1.924(8) \times 4$	$1.930(10) \times 4$	$1.926(7) \times 4$	$1.922(7) \times 4$	$1.944(7) \times 4$
	$1.924(4) \times 2$	$1.930(6) \times 2$	$1.926(4) \times 2$	$1.922(4) \times 2$	$1.944(4) \times 2$
Distortion ( $\times 10^{-4}$ )	-0.001	0.000	0.001	-0.001	0.001

and  $F_{2g}$ )<sup>162,162,185</sup>. The weak band at around  $450\text{ cm}^{-1}$  could be attributed to Ti—O stretching vibration. An intense band was also observed at around  $520\text{ cm}^{-1}$  which could be due to Gd—O stretching vibration ( $A_{1g}$  mode). Two weak bands around  $570\text{ cm}^{-1}$  and  $690\text{ cm}^{-1}$  were observed which are the characteristics of Ti—O stretching and vibrations of  $\text{TiO}_6$  polyhedra respectively. No new bands were observed for any of the synthesized compositions which was a clear indication of existence of pure monophasic system throughout the studied range of composition. Increase in the value of  $x$  of the nominal compositions leads to broadening of the Raman bands which can be attributed to the increasing disorder in the pyrochlore structure as



**Figure 5.4: Raman spectra of the nominal compositions of the series  $\text{Gd}_{2-2x}\text{Ca}_x\text{Zr}_x\text{Ti}_2\text{O}_7$  ( $0.0 \leq x \leq 0.4$ )<sup>184</sup>.**

evidenced from powder XRD structural studies. Decrease of wavenumbers or intensity for the O—Gd—O bending mode ( $310\text{ cm}^{-1}$ ) and Gd—O stretching vibration ( $520\text{ cm}^{-1}$ ) with respect to increasing intensity of Ti—O stretching vibration ( $570\text{ cm}^{-1}$ ) is also a clear indication of the



relative substitution of the Gd—O environment due to increasing concentration of  $\text{Ca}^{2+}$  and  $\text{Zr}^{4+}$  in the A site of the pyrochlore structure.

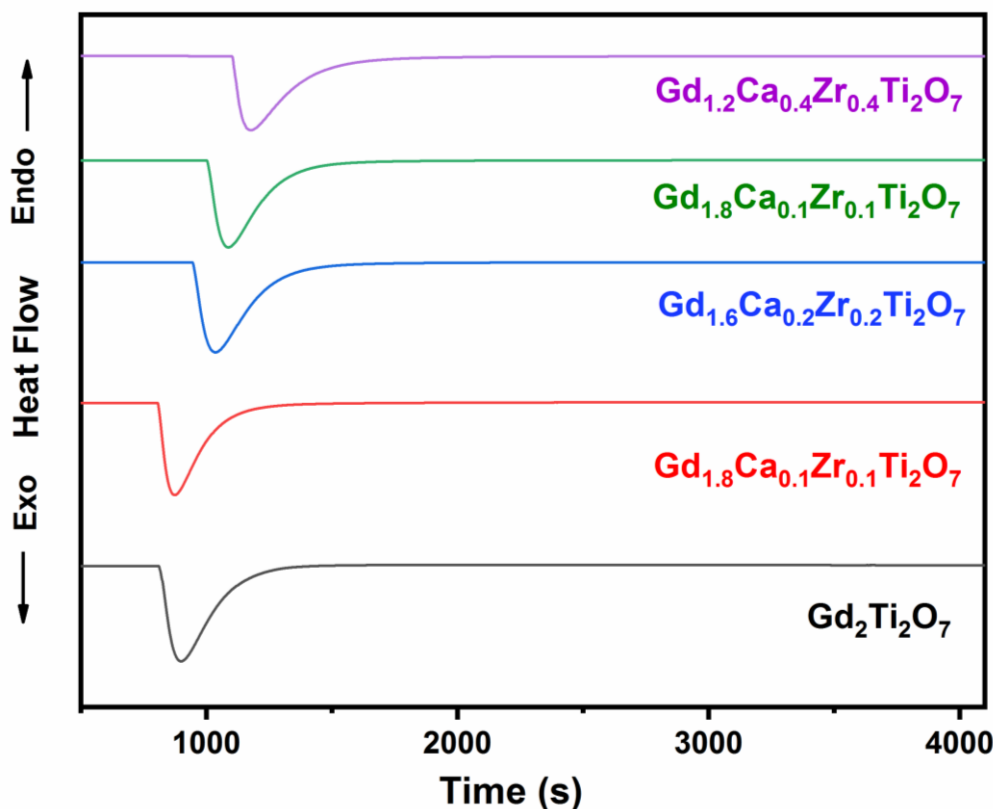
From the structural studies on the general compositions  $\text{Gd}_{2-2x}\text{Ca}_x\text{Zr}_x\text{Ti}_2\text{O}_7$  ( $0.0 \leq x \leq 0.4$ ) carried out by powder X-ray diffraction and Raman spectroscopy monophasic nature in the entire studied range could be inferred. Lower ionic radii of  $\text{Ca}^{2+} + \text{Zr}^{4+}$  couple as compared to two  $\text{Gd}^{3+}$  ions resulted in the contraction in unit cell parameter and that is observed as the shift of diffraction peaks towards higher  $2\theta$  values with increasing value of  $x$ . This is also confirmed from Rietveld refinement calculations carried out on the samples. Moreover, relative lowering of superstructure peak, which is an indication of the increasing randomization within pyrochlore structure, is also confirmed from Raman spectroscopic studies.

### 5.3.2. CALORIMETRIC STUDIES

The  $\text{Na}_2\text{O}$  and  $\text{MoO}_3$  (3:4 molar mixture) solvent for calorimetric studies was prepared by heating dried  $\text{Na}_2\text{CO}_3$  (BDH, reagent grade) and  $\text{MoO}_3$  (BDH, reagent grade) in appropriate molar ratio to a temperature of 986K. The importance of this temperature is that  $\text{Na}_2\text{CO}_3$  decomposes to  $\text{Na}_2\text{O}$  resulting in a eutectic mixture and then kept for 6 h for homogenization. The solvent powder was characterized for desired stoichiometry by chemical analysis and no impurity was observed from the powder diffraction pattern of the melt. Around 7 g of  $\text{Na}_2\text{O} + \text{MoO}_3$  solvent were added to platinum tubes, dropped inside the alumina assembly and slowly lowered into the calorimeter. The temperature was maintained at  $986 \pm 0.05$  K during the whole experiment.

Reaction tubes were equilibrated until a steady base line was obtained for heat flux. Pellets containing samples in mg amount were dropped into the solvent and the characteristic heat change effects were recorded by integrating heat flow signal with respect to time. Standard molar enthalpy of formation of the nominal compositions  $\text{Gd}_{2-2x}\text{Ca}_x\text{Zr}_x\text{Ti}_2\text{O}_7$  ( $0.0 \leq x \leq 0.4$ )

were derived from the enthalpy of dissolution values of the nominal compositions along with the constituent reagents. **Figure 5.5** exhibited the heat flow signal of the nominal compositions for a time period of 3600 s wherein a steady base line was obtained for the next dropping.

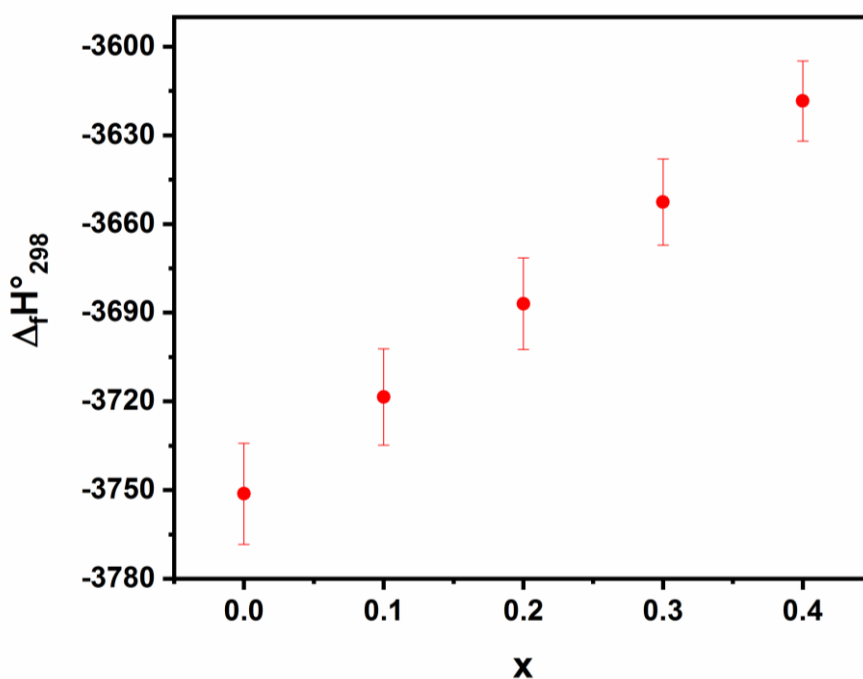


**Figure 5.5:** Normalized heat flow curves for nominal compositions of the series  $\text{Gd}_{2-2x}\text{Ca}_x\text{Zr}_x\text{Ti}_2\text{O}_7$  ( $0.0 \leq x \leq 0.4$ )<sup>184</sup>.

Dropping for each of the nominal compositions were carried out four times and heat change in J/g was calculated. Then it was transformed to kJ/mol by using molecular weight of the nominal compositions. Special precaution was taken for dropping of  $\text{CaO(s)}$  pellets into the solvent and that is mentioned in earlier report<sup>130,131</sup> and also in chapter 3 of this thesis. Change in heat flow during dropping of sample into the solvent could be due to heating of the sample from 298K to 986 K, dissociation of lattice of the species and dissolution of the species into the solvent. The first two processes are generally endothermic in nature and hence an endothermic heat change is observed. However, dissolution of chemical species in the solvent

can be either exothermic or endothermic depending upon the characteristics of solute-solvent interactions. It was observed that endothermic heat flow signals were observed for  $\text{TiO}_2(\text{s})$  and  $\text{ZrO}_2(\text{s})$ , whereas, exothermic ones were obtained for dissolution of  $\text{CaO}(\text{s})$ ,  $\text{Gd}_2\text{O}_3(\text{s})$  and the nominal compositions. Cumulative heat effect of dissolution of species in solvent was calculated using SETSOFT software. The values of molar enthalpies of dissolution of  $\text{Gd}_{2-2x}\text{Ca}_x\text{Zr}_x\text{Ti}_2\text{O}_7(\text{s})$  ( $0.0 \leq x \leq 0.4$ ),  $\text{CaO}(\text{s})$ ,  $\text{ZrO}_2(\text{s})$ ,  $\text{Gd}_2\text{O}_3(\text{s})$  and  $\text{TiO}_2(\text{s})$  in liquid  $\text{Na}_2\text{O} + \text{MoO}_3$  (3:4) melt maintained at 986K are tabulated in **Table 5.3**.

The standard molar enthalpy of formation of ( $0.0 \leq x \leq 0.4$ ) was derived using thermochemical cycles represented in **Table 5.4**. The values obtained for molar enthalpy of dissolution of  $\text{Gd}_{2-2x}\text{Ca}_x\text{Zr}_x\text{Ti}_2\text{O}_7(\text{s})$ ,  $\text{CaO}(\text{s})$ ,  $\text{ZrO}_2(\text{s})$ ,  $\text{Gd}_2\text{O}_3(\text{s})$  and  $\text{TiO}_2(\text{s})$  were combined with auxiliary data such as standard molar enthalpies of formation of  $\text{CaO}(\text{s})$ ,  $\text{ZrO}_2(\text{s})$ ,  $\text{Gd}_2\text{O}_3(\text{s})$  and  $\text{TiO}_2(\text{s})$  from reported literature values<sup>129,135,138</sup> to derive the standard molar enthalpy of formation of the nominal compositions respectively.



**Figure 5.6:** Plot of standard molar enthalpy of formation of  $\text{Gd}_{2-2x}\text{Ca}_x\text{Zr}_x\text{Ti}_2\text{O}_7$  ( $0.0 \leq x \leq 0.4$ )<sup>184</sup>.

### 5.3.3. COMPUTATIONAL RESULTS

In order to rationalize the experimental results and to get insight about the local structure and energetic due to aliovalent cationic substitution in  $\text{Gd}_2\text{Ti}_2\text{O}_7$  host lattice, theoretical calculations were performed by density functional theory (DFT) formalism. Three-dimensional periodic boundary conditions were applied for approximation of a bulk solid, i.e. the  $\text{Fd-3m}$  pyrochlore phase of  $\text{Gd}_2\text{Ti}_2\text{O}_7$ . A conventional cubic ( $\alpha = \beta = \gamma = 90^\circ$ ) unit cell containing 88 atoms (16 Gd, 16 Ti, 56 O) was used for theoretical calculations. Structural optimization was carried out with respect to atomic coordinates and unit cell parameters. The lattice parameters of the relaxed structure are  $a=b=c= 10.177 \text{ \AA}$ , which are quite close to experimental values ( $a=b=c 10.184 \text{ \AA}$ ) mentioned in earlier section. In the case of aliovalent cation incorporated  $\text{Gd}_2\text{Ti}_2\text{O}_7$ , out of the 16 Gd/Ti atoms in the unit cell, appropriate number of atoms were replaced with  $\text{Ca}^{2+}/\text{Zr}^{4+}$  to nearly approximate  $\text{Gd}_{2-2x}\text{Ca}_x\text{Zr}_x\text{Ti}_2\text{O}_7$  ( $0.0 \leq x \leq 0.4$ ) nominal compositions. As for example, to mimic the  $x=0.1$ , two Gd atoms were substituted by Ca and Zr atom leading to resultant  $x = 0.125$ . In spite of the fact that the theoretical compositions are not exactly same to that of the experimental nominal compositions, however it is believed that set nearby composition to rationalize the experimental trends. In an aim to find out the energetic preference for substitution of  $\text{Ca}^{2+}/\text{Zr}^{4+}$  at either Gd site or Ti site calculations were carried out for the scenario (1) both  $\text{Ca}^{2+}$  and  $\text{Zr}^{4+}$  replacing the  $\text{Gd}^{3+}$  ion (2)  $\text{Ca}^{2+}$  substituting the  $\text{Gd}^{3+}$  ion and  $\text{Zr}^{4+}$  replacing the  $\text{Ti}^{4+}$  ion (3) both  $\text{Ca}^{2+}$  and  $\text{Zr}^{4+}$  replacing the  $\text{Ti}^{4+}$  ion in the lattice. It was found that case (1) was found to be energetically most favourable as case (2) and case-(3) are 0.28 and 0.81 eV higher in energy. This relative stability order suggests that aliovalent substitution of  $\text{Gd}^{3+}$  by both  $\text{Ca}^{2+}$  and  $\text{Zr}^{4+}$  ions is energetically preferred over their inclusion fully at  $\text{Ti}^{4+}$  site or partially at  $\text{Gd}^{3+}$  and  $\text{Ti}^{4+}$  site. This energetic

**Table 5.3: Heat of Dissolution of  $\text{Gd}_{2-2x}\text{Ca}_x\text{Zr}_x\text{Ti}_2\text{O}_7$  ( $0.0 \leq x \leq 0.4$ ) and their component oxides<sup>184</sup>.**

Compounds	Mass (m) (mg)	$\Delta H$ (J/g)	$\Delta H_T$ (kJ mol <sup>-1</sup> )
Gd <sub>2</sub> Ti <sub>2</sub> O <sub>7</sub> (s) Mol. Wt. = 522.300 X=0.0	22.6 30.9 67.5 51.1	-189.30 -198.13 -199.11 -192.54	-98.87 -103.48 -103.99 -100.56 Avg: -101.73 ± 2.43
Gd <sub>1.8</sub> Ca <sub>0.1</sub> Zr <sub>0.1</sub> Ti <sub>2</sub> O <sub>7</sub> (s) Mol. Wt. = 503.980 X=0.1	27.8 24.7 11.5 10.9	-218.85 -208.65 -210.48 -213.46	-110.29 -105.16 -106.08 -107.58 Avg: -107.28 ± 2.25
Gd <sub>1.6</sub> Ca <sub>0.2</sub> Zr <sub>0.2</sub> Ti <sub>2</sub> O <sub>7</sub> (s) Mol. Wt. = 485.660 X=0.2	11.6 14.4 16.2 7.6	-225.96 -229.32 -239.21 -224.91	-109.74 -111.37 -116.18 -109.23 Avg: -111.63 ± 3.16
Gd <sub>1.4</sub> Ca <sub>0.3</sub> Zr <sub>0.3</sub> Ti <sub>2</sub> O <sub>7</sub> (s) Mol. Wt. = 467.340 X=0.3	24.8 12.1 8.7 12.5	-255.34 -257.26 -252.63 -251.43	-119.33 -120.23 -118.06 -117.50 Avg: -118.78 ± 1.23
Gd <sub>1.6</sub> Ca <sub>0.4</sub> Zr <sub>0.4</sub> Ti <sub>2</sub> O <sub>7</sub> (s) Mol. Wt. = 449.200 X=0.4	34.4 22.0 23.3 28.3	-279.53 -277.73 -284.12 -278.85	-125.52 -124.71 -127.58 -125.21 Avg: -125.75 ± 1.26
ZrO <sub>2</sub> (s) Mol. Wt. = 123.224	15.1 9.8 10.1 13.7	357.13 358.68 359.42 358.77	43.65 43.84 43.93 43.85 Avg: 43.82 ± 0.12
Gd <sub>2</sub> O <sub>3</sub> (s) Mol. Wt. = 362.50	15.1 21.0 17.9 12.5	-652.44 -654.98 -659.72 -658.37	-236.51 -237.43 -239.15 -238.66 Avg: -237.94 ± 1.20
CaO (s) Mol. Wt. = 56.08	11.2 18.1 15.0 9.5	-1608.95 -1599.68 -1627.14 -1619.29	-90.23 -89.71 -91.25 -90.81 Avg: -90.50 ± 0.67
TiO <sub>2</sub> (s) Mol. Wt. = 79.87	14.2 13.1 17.5 15.4	558.16 576.06 564.29 563.16	44.58 46.01 45.07 44.98 Avg: 45.16 ± 0.60

**Table 5.4: Thermochemical cycles for enthalpy of formation of  $\text{Gd}_{2-2x}\text{Ca}_x\text{Zr}_x\text{Ti}_2\text{O}_7$  ( $0.0 \leq x \leq 0.4$ )<sup>184</sup>.**

$$\Delta_f H^\circ_{298}(\text{Gd}_{2-2x}\text{Ca}_x\text{Zr}_x\text{Ti}_2\text{O}_7 (\text{s})) = -\Delta H_{1i} + x\Delta H_2 + x\Delta H_3 + (1-x) \Delta H_4 + 2\Delta H_5 + x\Delta H_6 + x\Delta H_7 + (1-x) \Delta H_8 + 2\Delta H_9$$

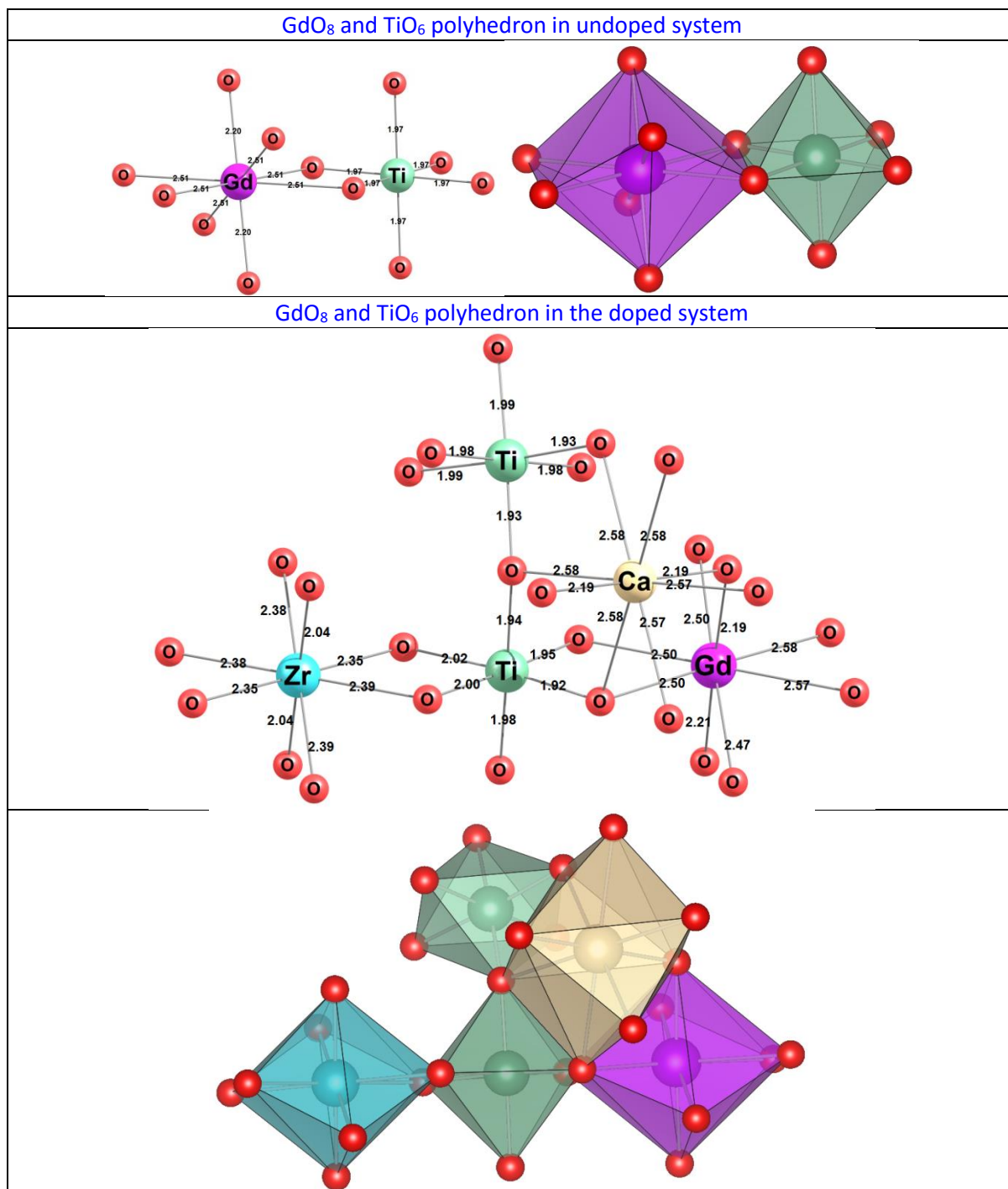
Reaction	$\Delta H_i$	$\Delta H_{\text{dissolution}}$ (kJ mol <sup>-1</sup> )
$\text{Gd}_2\text{Ti}_2\text{O}_7 (\text{s}, 298\text{K}) + (\text{sln}) = \text{Gd}_2\text{O}_3(\text{sln}) + 2\text{TiO}_2(\text{sln})$	$\Delta H_{1a}$	$-101.73 \pm 2.43$
$\text{Gd}_{1.8}\text{Ca}_{0.1}\text{Zr}_{0.1}\text{Ti}_2\text{O}_7(\text{s}) (\text{s}, 298\text{K}) + (\text{sln}) = 0.9\text{Gd}_2\text{O}_3(\text{sln}) + 0.1\text{CaO}(\text{sln}) + 0.1\text{ZrO}_2(\text{sln}) + 2\text{TiO}_2(\text{sln})$	$\Delta H_{1b}$	$-107.28 \pm 2.25$
$\text{Gd}_{1.6}\text{Ca}_{0.2}\text{Zr}_{0.2}\text{Ti}_2\text{O}_7(\text{s}) (\text{s}, 298\text{K}) + (\text{sln}) = 0.8\text{Gd}_2\text{O}_3(\text{sln}) + 0.2\text{CaO}(\text{sln}) + 0.2\text{ZrO}_2(\text{sln}) + 2\text{TiO}_2(\text{sln})$	$\Delta H_{1c}$	$-111.63 \pm 3.16$
$\text{Gd}_{1.4}\text{Ca}_{0.3}\text{Zr}_{0.3}\text{Ti}_2\text{O}_7(\text{s}) (\text{s}, 298\text{K}) + (\text{sln}) = 0.7\text{Gd}_2\text{O}_3(\text{sln}) + 0.3\text{CaO}(\text{sln}) + 0.3\text{ZrO}_2(\text{sln}) + 2\text{TiO}_2(\text{sln})$	$\Delta H_{1d}$	$-118.78 \pm 1.23$
$\text{Gd}_{1.2}\text{Ca}_{0.4}\text{Zr}_{0.4}\text{Ti}_2\text{O}_7(\text{s}) (\text{s}, 298\text{K}) + (\text{sln}) = 0.6\text{Gd}_2\text{O}_3(\text{sln}) + 0.4\text{CaO}(\text{sln}) + 0.4\text{ZrO}_2(\text{sln}) + 2\text{TiO}_2(\text{sln})$	$\Delta H_{1e}$	$-125.75 \pm 1.26$
$\text{CaO}(\text{s}, 298\text{K}) + (\text{sln}) = \text{CaO}(\text{sln})$	$\Delta H_2$	$-90.50 \pm 0.67$
$\text{ZrO}_2(\text{s}, 298\text{K}) + (\text{sln}) = \text{ZrO}_2(\text{sln})$	$\Delta H_3$	$43.82 \pm 0.12$
$\text{Gd}_2\text{O}_3(\text{s}, 298\text{K}) + (\text{sln}) = \text{Gd}_2\text{O}_3(\text{sln})$	$\Delta H_4$	$-237.94 \pm 1.20$
$\text{TiO}_2(\text{s}, 298\text{K}) + (\text{sln}) = \text{TiO}_2(\text{sln})$	$\Delta H_5$	$45.16 \pm 0.60$
$\text{Ca}(\text{s}, 298\text{K}) + 1/2\text{O}_2(\text{g}) = \text{CaO}(\text{s})$	$\Delta H_6$	$-634.29 \pm 1.67$
$\text{Zr}(\text{s}, 298\text{K}) + \text{O}_2(\text{g}) = \text{ZrO}_2(\text{s})$	$\Delta H_7$	$-1100.81 \pm 2.09$
$2\text{Gd}(\text{s}, 298\text{K}) + 3/2\text{O}_2(\text{g}) = \text{Gd}_2\text{O}_3(\text{s})$	$\Delta H_8$	$-1815.86 \pm 16.74$
$\text{Ti}(\text{s}, 298\text{K}) + \text{O}_2(\text{g}) = \text{TiO}_2(\text{s})$	$\Delta H_9$	$-944.75 \pm 1.67$
$2\text{Gd}(\text{s}, 298\text{K}) + 2\text{Ti}(\text{s}, 298\text{K}) + 3.5 \text{O}_2(\text{g}) = \text{Gd}_2\text{Ti}_2\text{O}_7 (\text{s}, 298\text{K}) (x=0.0)$	$\Delta_f H^\circ_{298}$	$-3751.25 \pm 17.14$
$1.8\text{Gd}(\text{s}, 298\text{K}) + 0.1\text{Ca}(\text{s}, 298\text{K}) + 0.1\text{Zr}(\text{s}, 298\text{K}) + 2\text{Ti}(\text{s}, 298\text{K}) + 3.5 \text{O}_2(\text{g}) = \text{Gd}_{1.8}\text{Ca}_{0.1}\text{Zr}_{0.1}\text{Ti}_2\text{O}_7 (\text{s}, 298\text{K}) (x=0.1)$		$-3718.50 \pm 16.32$
$1.6\text{Gd}(\text{s}, 298\text{K}) + 0.2\text{Ca}(\text{s}, 298\text{K}) + 0.2\text{Zr}(\text{s}, 298\text{K}) + 2\text{Ti}(\text{s}, 298\text{K}) + 3.5 \text{O}_2(\text{g}) = \text{Gd}_{1.6}\text{Ca}_{0.2}\text{Zr}_{0.2}\text{Ti}_2\text{O}_7 (\text{s}, 298\text{K}) (x=0.2)$		$-3686.95 \pm 15.46$
$1.4\text{Gd}(\text{s}, 298\text{K}) + 0.3\text{Ca}(\text{s}, 298\text{K}) + 0.3\text{Zr}(\text{s}, 298\text{K}) + 2\text{Ti}(\text{s}, 298\text{K}) + 3.5 \text{O}_2(\text{g}) = \text{Gd}_{1.4}\text{Ca}_{0.3}\text{Zr}_{0.3}\text{Ti}_2\text{O}_7 (\text{s}, 298\text{K}) (x=0.3)$		$-3652.59 \pm 14.54$
$1.2\text{Gd}(\text{s}, 298\text{K}) + 0.1\text{Ca}(\text{s}, 298\text{K}) + 0.1\text{Zr}(\text{s}, 298\text{K}) + 2\text{Ti}(\text{s}, 298\text{K}) + 3.5 \text{O}_2(\text{g}) = \text{Gd}_{1.2}\text{Ca}_{0.4}\text{Zr}_{0.4}\text{Ti}_2\text{O}_7 (\text{s}, 298\text{K}) (x=0.4)$		$-3618.42 \pm 13.57$

preference is in line with ionic radius criteria (**viz. Table 5.1**). Hence, calculations for higher dopant concentration ( $x = 0.25, 0.315, 0.375$ ) were done by considering the substitution at  $Gd^{3+}$  site only. For  $x = 0.25$  and  $0.375$  values, the calculations were performed with single unit cell having 88 atoms. However, for  $x = 0.315$  composition, the calculations were performed with a supercell having two unit cell thereby containing 178 atoms. The heat of formation ( $\Delta H_f$ ) for different aliovalent doping concentrations at Gd-sites was calculated using following equation:

$$\Delta H_f = \{E(Gd_{2-2x}Ca_xZr_xTi_2O_7) - \text{no. of Gd atoms} \times E(Gd) - \text{no. of Ti atoms} \times E(Ti) - \text{no. of Ca atoms} \times E(Ca) - \text{no. of Zr atoms} \times E(Zr)\} / \text{total number of atoms} \quad (\text{eqn. 5.1})$$

Where  $E(Gd_{2-2x}Ca_xZr_xTi_2O_7)$  is the total energy of aliovalent doped supercell while  $E(Gd)$ ,  $E(Ti)$ ,  $E(Ca)$  and  $E(Zr)$  are atom correction energy for a single Gd, Ti, Ca, and Zr atom respectively. The calculated  $\Delta H_f$  values for  $x = 0.125, 0.25, 0.315, 0.375$  compositions were found to be  $-7.14, -7.13, -7.11$  and  $-7.09$  eV/atom respectively, thereby indicating that the stability of system decrease systematically on increasing the dopant concentration. These observations are in line with the experimental observation presented in **Figure 5.7**. The steady and gradual decrease in heat of formation with increasing dopant concentration can be attributed to smaller ionic size of dopant (total ionic radius of  $Ca^{2+}$  and  $Zr^{4+}$ ) in comparison to host  $Gd^{3+}$  ion ( $2 \times$  ionic radius of  $Gd^{3+}$  ion) which leads to a significant change in the polyhedron size as depicted in **Figure 5.7**.

From the figure, it is evident that  $Ca^{2+}/Zr^{4+}$  multi cation substitution in  $Gd_2Ti_2O_7$  host lattice leads to change in nearby polyhedra, thereby leading to an increase in the average Ti-O bond lengths. These features in the DFT results were found to be in line with the experimental observation where average Ti-O bond lengths were also found to increase on doping.



**Figure 5.7:** Structure of GdO<sub>8</sub> and TiO<sub>6</sub> polyhedra in doped and undoped Gd<sub>2</sub>Ti<sub>2</sub>O<sub>7</sub><sup>184</sup>.



## 5.4. CONCLUSIONS

Single phasic solid solution compositions having pyrochlore structure with incorporation of two aliovalent cations has been stabilized. About 40 mol% of  $\text{Gd}^{3+}$  content in  $\text{Gd}_2\text{Ti}_2\text{O}_7$  can be replaced by  $\text{Ca}^{2+}$  and  $\text{Zr}^{4+}$  cations are evident from both powder X-ray diffraction and Raman spectroscopic studies. A systematic decrease in superstructure peak of pyrochlore was observed with increase in aliovalent substitution. Theoretical studies reveal that greater amount of disorder is evident around Gd-O polyhedra upon substitution of aliovalent ions. Calorimetric studies exhibit a decreasing trend in enthalpy of formation with increase in aliovalent substitution. Nevertheless, the stability decreases only by about 3.5% upon 40 mol% substitution which indicates that  $\text{Gd}_2\text{Ti}_2\text{O}_7$  type pyrochlore lattices can be considered as promising matrices for immobilization of aliovalent cations present in nuclear HLW.

# **Chapter 6**

## **Structure and thermodynamic studies on parent and actinide substituted $\text{Gd}_2\text{Zr}_2\text{O}_7$**

The data reported in this chapter have been published in the following peer-reviewed journal:

- Preparation and structure of uranium incorporated  $\text{Gd}_2\text{Zr}_2\text{O}_7$  compounds and their thermodynamic stabilities under oxidizing and reducing conditions  
M. Jafar, S. B. Phapale, B. P. Mandal, R. Mishra, A. K. Tyagi  
*Inorg. Chem.* 54, (2015) 9447-9457.

## 6.1. INTRODUCTION

Ceramic phases such as zirconolite, pyrochlore, hollandite, perovskite, etc. are considered as promising host lattices for safe disposal of nuclear HLW, which has been explained in previous chapters<sup>4,35,48,72,76,186–188</sup>. The main reason for their selection is based upon their exceptional stability in non-stoichiometric chemical compositions which makes them potentially amenable for aliovalent cationic substitution within the crystal lattice without any compromise on crystallographic stability<sup>65,66,115,116,159,189,190</sup>. The oxide pyrochlore phases comprises of general formula  $A_2B_2O_7$  where A represents a larger cation in eight-fold coordination and B represents a smaller cation having six-fold coordination, form a major part for composite ceramic host matrices. The prevalent guiding parameter for evolution of pyrochlore phase is that the radius ratio ( $r_A/r_B$ ) has to be in the range of 1.46 to 1.60<sup>69,115,184,190</sup> and hence can accommodate wide varieties of cations in them. The comparatively larger A cation can be a trivalent rare earth ion, divalent or any monovalent ion with larger ionic radii whereas the smaller B cation can be any 3d, 4d or 5d element in its suitable oxidation state<sup>69,190</sup>. The most remarkable feature of pyrochlore structure is that substitution of aliovalent cations in either or both the sites generally results in non-stoichiometric chemical composition in pyrochlore lattice without any considerable compromise on their structural stability as reported in literature<sup>125,163,184,191,192</sup> as well as chapter 5 of this thesis. Literature reports are also there which presents incorporation of surrogate minor actinides in pyrochlore matrix<sup>188,193–196</sup>.

Amongst all pyrochlore compositions,  $Gd_2Zr_2O_7$  is considered as the most promising candidate for incorporation of minor actinides present in nuclear HLW<sup>197,197</sup>. Nevertheless, it needs to be mentioned that this composition lies at borderline between pyrochlore and defect-fluorite structure because of a low  $r_A/r_B$  ratio of 1.458. The ordered form of  $Gd_2Zr_2O_7$  is the pyrochlore structure (Fd-3m symmetry) whereas the disordered form is the defect-fluorite

structure (Fm-3m symmetry)<sup>188</sup>. In both the structure, this composition exhibits extremely high radiation resistance properties under both low and high radiation environments<sup>76,191,198,199</sup>. Literature reports indicate that the ordered variant transforms into disordered variant without showing any tendency of amorphization under high irradiation scenario<sup>163,191,198</sup>.

However, it needs to be mentioned that thermodynamic stability of Gd<sub>2</sub>Zr<sub>2</sub>O<sub>7</sub> lattice as a function of processing temperature and time, which is an important parameter for its consideration for potential applications is still obscure in literature. Hence, it becomes important to study the enthalpy of formation of Gd<sub>2</sub>Zr<sub>2</sub>O<sub>7</sub> prepared in the temperature range for possible use as waste immobilization matrix. Literature reports advocate the enthalpy of formation of this compound at 1873 K (50 h)<sup>125</sup> to be around -4070 kJmol<sup>-1</sup> respectively. Hence, structural studies and enthalpy measurements of the lattice were carried out in the range of 1373K to 1673K to understand the variation with change in the crystal lattice, and they are explained in part A of this chapter. In addition to this, information regarding the structural changes and stability alteration of Gd<sub>2</sub>Zr<sub>2</sub>O<sub>7</sub> upon incorporation of uranium and plutonium is also a must requirement for their potential application as nuclear waste matrix. Hence, the effects on incorporation of uranium in both oxidized and reduced state in Gd<sub>2</sub>Zr<sub>2</sub>O<sub>7</sub> matrix are studied and they are discussed in part B. In order to study the structural and thermodynamic stability variations of Gd<sub>2</sub>Zr<sub>2</sub>O<sub>7</sub> upon simultaneous incorporation of uranium and plutonium, U and Ce substituted Gd<sub>2</sub>Zr<sub>2</sub>O<sub>7</sub> have been studied and they are explained in part C of this chapter. Studies in part C were carried out with CeO<sub>2</sub> as it is considered a promising surrogate material for PuO<sub>2</sub>, as discussed in chapter 1 of this thesis<sup>78</sup>.

## 6.2. EXPERIMENTAL METHODS

Series of compositions with the general chemical formula Gd<sub>2-x</sub>U<sub>x</sub>Zr<sub>2</sub>O<sub>7+δ</sub> (0.0 ≤ x ≤ 0.25) and Gd<sub>2-x</sub>Ce<sub>x</sub>Zr<sub>1.9</sub>U<sub>0.1</sub>O<sub>7+α</sub> (0.0 ≤ x ≤ 0.5) were prepared using gel-combustion technique using Gd<sub>2</sub>O<sub>3</sub> (Indian Rare Earths Ltd. purity 99.9%), CeO<sub>2</sub> (Indian Rare Earths Ltd. purity 99.9%),

ZrO(NO<sub>3</sub>)<sub>2</sub> (Loba Chemie and 44% metal basis), U<sub>3</sub>O<sub>8</sub> powder and glycine as fuel. Gd<sub>2</sub>O<sub>3</sub> and CeO<sub>2</sub> (for Ce-containing series) were preheated at 1073 K overnight in a furnace followed by their dissolution along with U<sub>3</sub>O<sub>8</sub> powder (for U-containing series) in stoichiometric desired amount in minimum volume of concentrated HNO<sub>3</sub> until a clear and transparent solution was observed. Stoichiometric amount of ZrO(NO<sub>3</sub>)<sub>2</sub> was slowly added into the solution under stirring till transparent followed by addition of glycine in fuel deficient ratio (1:0.6). The transparent solution was then heated till the formation a viscous gel. The temperature of the hot plate was then increased to ~ 673K for auto-ignition which resulted in the formation of white coloured fine flaky powders. Obtained powders were then calcined at 873 K to remove carbonaceous impurities present. Calcined Gd<sub>2</sub>Zr<sub>2</sub>O<sub>7</sub> powders were divided into four equal parts and sintered separately at different temperatures of 1373 K, 1473 K, 1573 K and 1673 K respectively for 8 h in air. Part of the powders with the general chemical formula Gd<sub>2-x</sub>U<sub>x</sub>Zr<sub>2</sub>O<sub>7+δ</sub> (0.0 ≤ x ≤ 0.25) were further heated at 1373 K for 8 h in flowing 92% argon-8% hydrogen atmosphere whereas another part of the products was heated at 1373 K for 8 h in static air. All compositions of the general composition Gd<sub>2-x</sub>Ce<sub>x</sub>Zr<sub>1.9</sub>U<sub>0.1</sub>O<sub>7+α</sub> (0.0 ≤ x ≤ 0.5) were heated at 1373 K for 8 h in static air.

Powder XRD patterns of the nominal compositions were recorded on a PANalytical X-Pert powder x-ray diffractometer using CuKα (λ = 1.5406 and 1.5444 Å) radiation. High temperature XRD studies on some compositions were also performed in the range of 298-1273 K in static air using same instrument. Structural characterization of the compositions was carried out using Rietveld refinement program Fullprof-2000<sup>103</sup>. Background parameters for each of the diffraction patterns for all the nominal compositions were manually added and scale factor was adjusted. Diffraction peaks were simultaneously fitted with pseudo-Voigt profile function and then unit cell parameters were refined. Absorption parameters and displacement errors were not considered during structural analyses. Microstructural studies of some of the

samples were examined by using a scanning electron microscope (SEM) (model: AIS 210, Mirero Inc., Seongnam-si, South Korea). X-ray photoelectron spectroscopy (XPS) studies were carried out using SPECS XPS instrument with a PHOBIOS 100/150 delay line detector (DLD) with 385 W, 13.85 kV and 175.6 nA (sample current). Al K $\alpha$  (1486.6 eV) dual anode was used as source. C-1s peak (284.5 eV) was used as an internal reference for the estimation of absolute binding energy. Raman spectra of the nominal compositions were recorded using He-Ne laser with a wavelength of 632 nm. Powder samples were spread on a glass slide and the scattered radiation was collected at 180° scattering geometry employing a CCD (Synapse) based monochromator (LabRAM HR800, Horiba Jobin Yvon, France) together with an edge filter. The operating power of the laser was kept at 10 mW and spot size of the sample was 0.5 mm in diameter. Raman band at 520 cm<sup>-1</sup> corresponding to a silicon wafer was used for calibration of the instrument. The accuracy of the spectral measurement was estimated to be close to ~ 1 cm<sup>-1</sup>. X-ray Absorption Spectroscopy (XAS) measurements on Zr<sub>2</sub>Gd<sub>2</sub>O<sub>7</sub> samples annealed at different temperatures have been carried out at Zr K and Gd L<sub>3</sub> edges in transmission mode at the Scanning EXAFS Beamline (BL-9) at the INDUS-2 Synchrotron Source (2.5 GeV, 100 mA) at the Raja Ramanna Centre for Advanced Technology (RRCAT), Indore, India<sup>200,201</sup>. The beamline uses a double crystal monochromator (DCM) which works in the photon energy range of 4-25 KeV with a resolution of 10<sup>-4</sup> at 10 KeV. A 1.5 m horizontal pre-mirror with meridional cylindrical curvature is used prior to the DCM for collimation of the beam and higher harmonic rejection. The second crystal of the DCM is a sagittal cylinder with radius of curvature in the range 1.28-12.91 meters which provides horizontal focusing to the beam while another Rh/Pt coated bendable post mirror facing down is used for vertical focusing of the beam at the sample position. For measurements in the transmission mode, the sample is placed between two ionization chamber detectors. The first ionization chamber measures the incident flux ( $I_0$ ) and

the second ionization chamber measures the transmitted intensity ( $I_t$ ) and the absorbance of the sample is obtained as ( $\mu = \exp(-\frac{I_t}{I_0})$ ).

The standard molar enthalpies of formation of nominal compositions  $\text{Gd}_2\text{Zr}_2\text{O}_7$  (annealed at different temperatures),  $\text{Gd}_{2-x}\text{U}_x\text{Zr}_2\text{O}_{7+\delta}$  ( $0.0 \leq x \leq 0.25$ ) (in both oxidized and reduced forms) and  $\text{Gd}_{2-x}\text{Ce}_x\text{Zr}_{1.9}\text{U}_{0.1}\text{O}_{7+\alpha}$  ( $0.0 \leq x \leq 0.5$ ) were determined by measuring the enthalpy of dissolution of  $\text{Gd}_{2-x}\text{U}_x\text{Zr}_2\text{O}_{7+\delta}$  compounds and their constituent oxides in liquid  $\text{Na}_2\text{O} + \text{MoO}_3$  solvent (3:4 molar ratio) at 986 K using a high temperature Calvet calorimeter (Setaram, Model HT-1000). The calorimeter has an isothermal alumina block containing two identical one-end closed alumina cells surrounded by a series of thermopiles. The temperature of the isothermal block was measured using a Pt–Pt 10 % Rh thermocouple ( $\pm 0.1$  K). Further details of the experimental measurements have been described elsewhere<sup>202</sup>. Synthetic sapphire sample [NIST SRM-720] was used for heat calibration.

The nominal compositions and their component oxides were found to be completely soluble in the calorimetric solvent, i.e.,  $\text{Na}_2\text{O} + \text{MoO}_3$  (3:4 molar mixture) at 986 K. This calorimetric solvent was prepared by heating mixture of dried  $\text{Na}_2\text{CO}_3$  (BDH, reagent grade) and  $\text{MoO}_3$  (BDH, reagent grade) in appropriate 3:4 molar ratio inside a platinum disk at 973 K.  $\text{Na}_2\text{CO}_3$  decomposes to  $\text{Na}_2\text{O}$  at around this temperature forming a eutectic mixture with  $\text{MoO}_3$ . This melt was then maintained at 973 K for 6 hours for further homogenization. Mass loss of the solvent was closely monitored to ensure the correct stoichiometry of the melt, which was compensated by mixing the required amount of  $\text{MoO}_3$  followed by re-melting. The entire substance was removed from the platinum disk and ground again to obtain fine uniformly mixed powder. The solvent powder was characterized by chemical analysis and XRD techniques. The atom % of Mo, Na and O obtained from the chemical analysis of the solvent were found to be  $16.2 \pm 0.2$ ,  $23.4 \pm 0.3$  and  $60.4 \pm 0.4$ , respectively. No other chemical impurity

could be detected in the melt powder.  $\text{Na}_2\text{O} + \text{MoO}_3$  powder prepared in the same batch was used in all the reaction enthalpy measurements to ensure reproducibility of thermodynamic data.

About 6 g of  $\text{Na}_2\text{O} + \text{MoO}_3$  (3:4 molar) solvent was taken in both of the two identical platinum tubes which act as a protective lining and having outer diameter matching exactly with the alumina reaction cell for proper thermal contact. The reaction cell assembly was slowly lowered into the calorimeter which was programmed up to 986 K at a heating rate of 0.5 K/min and maintained at  $986 \pm 0.05$  K during the whole experiment.

The reaction tubes were equilibrated inside the chamber for 12 h till a steady base line for heat flux signal was achieved. The slope of the base line of the differential heat flow signal was nearly zero since the heat effect due to any small loss of the volatile components is nullified due to identical effects in the sample and reference cells. Small pellets containing few milligrams of the component oxides and the nominal compositions were dropped from room temperature to the reaction cell containing calorimetric solvent maintained at 986 K. The corresponding enthalpy change was then determined by integrating the heat flow signal with respect to time. The time required for the completion of the reaction was determined by recording the heat flow signal (J/g) for different time intervals. The completion of dissolution reaction was concluded only after observation of a steady base line, and the values of enthalpy of reaction were obtained as a function of time converged into a constant value. For each dissolution experiment the reaction time was determined meticulously and the heat flow signals were recorded for the same time period for all dropping experiments. Similarly, for each experiment, fresh solvent was used. The amount of the component oxides and products dropped into solvent was chosen in such a manner that the concentration of metal ions of the nominal compositions in solvent remained well below 1 atom %. This infinite dilution condition was carefully established by repeating the dissolution experiments on same batch of the solvent.



After each measurement the sample was slowly withdrawn from the calorimeter chamber and allowed to cool to room temperature. The frozen liquid was subsequently characterized by EDS analysis to know the uniform distribution of solute in the solvent and to ascertain the infinite dilution condition of solute in solvent. Oxygen bubbling experiments into the solvent was deliberately avoided as it was becoming very tough to obtain a steady base line under oxygen bubbling conditions. In addition, the solvent particles borne by the oxygen flow often had a tendency to react with the structural material (quartz) producing undesirable heat effects which in turn could possibly affect the reproducibility of the results. Hence the calorimetric experiments were performed in static air.

### **6.3. RESULTS AND DISCUSSIONS**

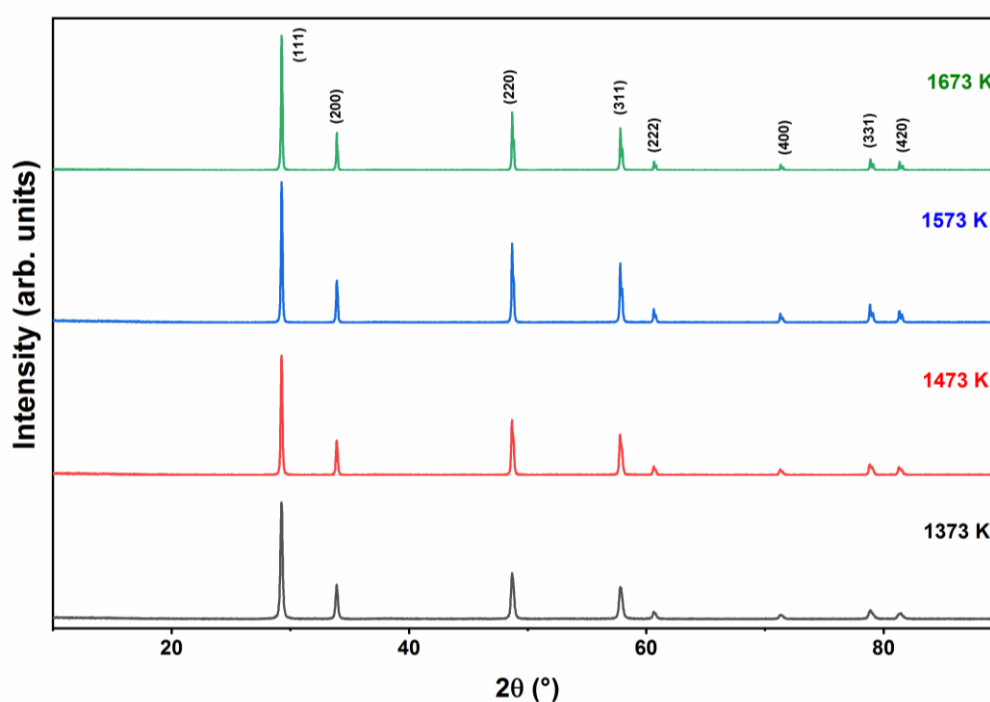
#### **PART A: Structural and thermodynamic studies on pristine $\text{Gd}_2\text{Zr}_2\text{O}_7$**

##### **(i) Powder XRD Studies**

Gel-combustion synthesis is one of the most common techniques for the preparation of nano-crystalline oxide based ceramic materials<sup>87,92</sup>. This reaction is basically a redox reaction between an oxidant (nitrate in the present case) and a reductant or fuel (glycine) which finally undergoes combustion to produce carbon dioxide and water. The enormous amount of energy released in this process eventually raises the local temperature to  $\sim 1700$  K for a very short duration which acts as the activation energy resulting in the formation of fluffy powders from the reactants present in solution. As mentioned in literature<sup>87,198</sup>, the reducing valency of glycine is calculated to be +9 whereas the oxidizing valences of  $\text{Gd}(\text{NO}_3)_3$ , and  $\text{ZrO}(\text{NO}_3)_2$  are  $-15$  and  $-10$ , respectively. The extent of exothermicity of the combustion reaction is dependent upon the oxidant to fuel ratio which was kept as 1: 0.6 or in a fuel-deficient ratio. The fluffy white powders obtained after combustion was calcined at 873 K for 1 h duration to get rid of carbonaceous remains. Powder XRD pattern of the calcined sample exhibited broad peak corresponding to the nano-crystalline nature of the sample. No reactant peaks were observed

in the XRD pattern. The XRD pattern revealed the calcined sample to crystallize in the defect fluorite form. However, due to broad nature of the peaks, possibility of overshadowing of the low intensity superstructure peaks was always there. Hence further phase characterization of the calcined sample was not carried out.

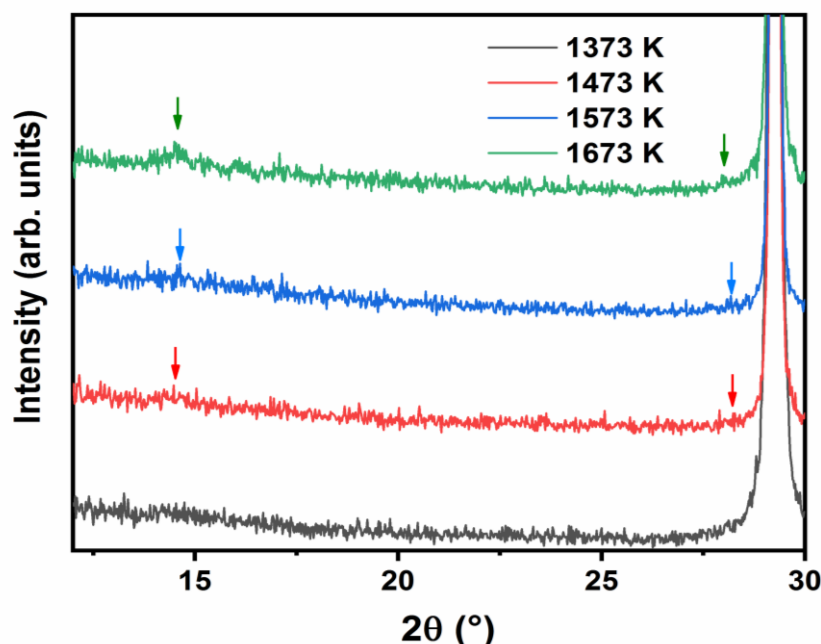
The calcined powder was divided into four parts and they were sintered separately at 1373 K, 1473 K, 1573 K and 1673 K, respectively. Powder XRD patterns of the compositions heated at different temperature is depicted in **Figure 6.1**. From the figure, it could be clearly



**Figure 6.1: Powder X-ray diffraction patterns of  $Gd_2Zr_2O_7$  sintered at 1373 K, 1473 K, 1573 K and 1673 K (PCPDF-80-0471).**

observed that there is hardly any difference in the patterns of the four samples. However close analysis revealed that weak superstructure peaks corresponding to cubic pyrochlore structure was visible on all the samples except the one sintered at 1373 K and is shown in **Figure 6.2**. From the above figure, it could be observed that with increase in the sintering temperature the powder X-ray diffraction patterns in the range of  $10-30^\circ$  show progressively increasing

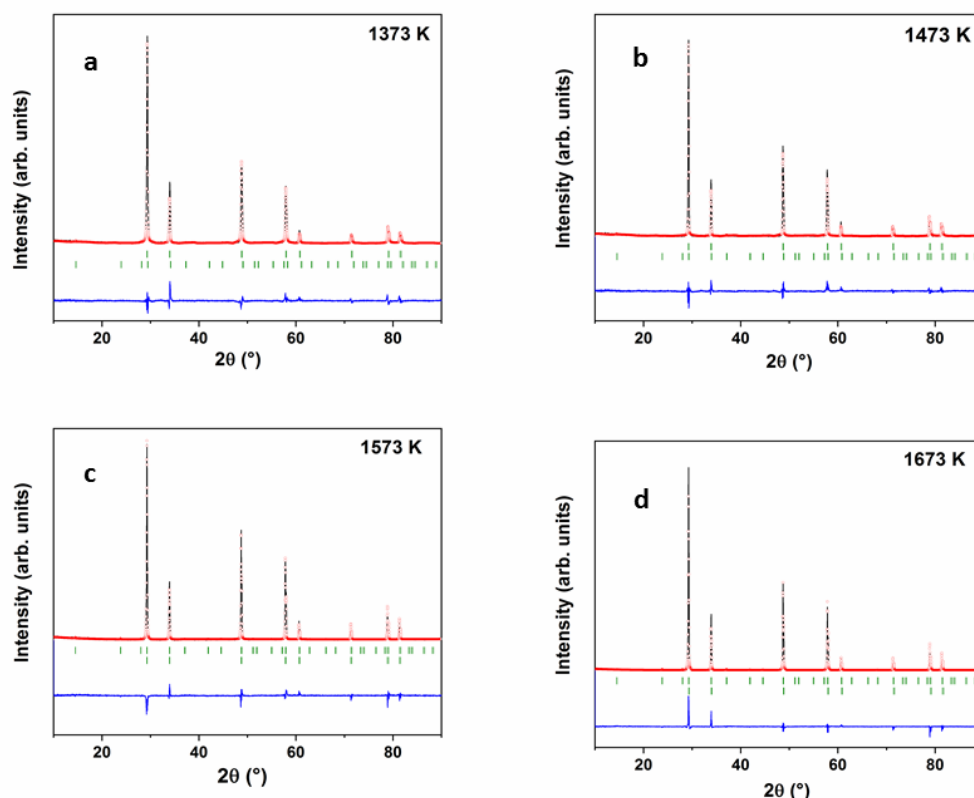
intensity of superstructure peaks at  $2\theta \sim 14.5^\circ$  and  $28.2^\circ$ . Zhou *et al*<sup>203</sup> and others<sup>204</sup> observed that  $\text{Gd}_2\text{Zr}_2\text{O}_7$  lattice undergoes transformation from a defect-fluorite to ordered pyrochlore structure at temperatures greater than 1523 K.



**Figure 6.2:** Powder X-ray diffraction patterns  $\text{Gd}_2\text{Zr}_2\text{O}_7$  sintered at 1373 K, 1473 K, 1573 K and 1673 K in the  $2\theta$  range of  $10$ – $30^\circ$ , showing superstructure peaks observed at  $2\theta \sim 14.5^\circ$  and  $28.2^\circ$ .

Keeping the above fact in mind and observed weak superstructure reflections corresponding to pyrochlore phase, two phase structural analysis was carried out on all the four samples to try and understand the evolution of ordering in the crystal system. It was concluded from structural analysis that sample sintered at 1373 K consists of  $\sim 99\%$  of defect fluorite phase and  $1\%$  ordered pyrochlore phase. Hence, for simplicity it can be said that, defect fluorite is the most adopted structure of  $\text{Gd}_2\text{Zr}_2\text{O}_7$  lattice upon preparation by gel combustion followed by 8 h sintering at 1373K. Rietveld refinement of the composition at 1473 K reveals the composition to consist of  $\sim 91\%$  defect fluorite and  $9\%$  ordered pyrochlore. Increase of sintering temperature to 1573 K induces ordered pyrochlore to constitute main phase ( $\sim 66\%$ )

whereas upon heat treatment at higher temperature i.e., 1673 K renders the calcine powder to crystallize in almost ~ 95% pyrochlore phase. Rietveld refinement plots of  $\text{Gd}_2\text{Zr}_2\text{O}_7$  sintered at 1373 K, 1473 K, 1573 K and 1673 K is shown in **Figure 6.3a, b, c and d**, respectively.



**Figure 6.3 a, b, c, d: Rietveld refinement plot of  $\text{Gd}_2\text{Zr}_2\text{O}_7$  sintered at 1373 K, 1473 K, 1573 K and 1673 K. Figure a, b: Top and bottom vertical lines indicate Bragg positions for defect fluorite and pyrochlore type phase respectively. Figure c, d: top and bottom vertical lines indicate Bragg positions for pyrochlore and defect fluorite phase respectively.**

Considering literature reports, Lee *et al.* and others<sup>205,206</sup> found out that the transition from disordered defect fluorite to ordered pyrochlore structure (F-P transition) takes place in between 1473 K to 1573 K. This report was further authenticated by Kong *et al.*<sup>207</sup> and Diaz-Guillen *et al.*<sup>208</sup> where it is reported that F-P transition depends upon both the sintering temperature and the duration of the sintering procedure. Thus, it can be explained that, at 1373 K,  $\text{Gd}_2\text{Zr}_2\text{O}_7$  primarily adopts to disordered defect fluorite structure (F). However, upon

thermal treatment at 1473 K for 8 h about 9.5% of defect fluorite phase transforms to ordered pyrochlore structure (P). Kong *et al*<sup>207</sup> observed complete F-P transition at 1473 K upon heat treatment for 50 h. Hence, it can be stated that F-P transition depends on both temperature and time of sintering. Upon further heating at 1573 K, Gd<sub>2</sub>Zr<sub>2</sub>O<sub>7</sub> primarily transforms to ordered pyrochlore structure (P) with ~ 65% phase fraction. Since the sintering duration was kept at 8 h only, complete transformation to P phase was not observed. However, drastic reduction in F phase at this temperature is a clear indication of increasing tendency of F-P transition at this particular temperature. Composition sintered at 1673 K exhibited almost pure ordered pyrochlore (P) structure with ~ 95% phase fraction. Hence, it can be stated that, F-P transition is the favoured transition in the temperature range of 1473 K to 1673 K whereby major structural changes in Gd<sub>2</sub>Zr<sub>2</sub>O<sub>7</sub> were observed. However, the comparatively shorter dwelling time of 8 h was the main reason for the incomplete structural transition in the entire temperature studied range. Unit cell parameters and typical phase fraction of Gd<sub>2</sub>Zr<sub>2</sub>O<sub>7</sub> treated at different temperatures are given in **Table 6.1**.

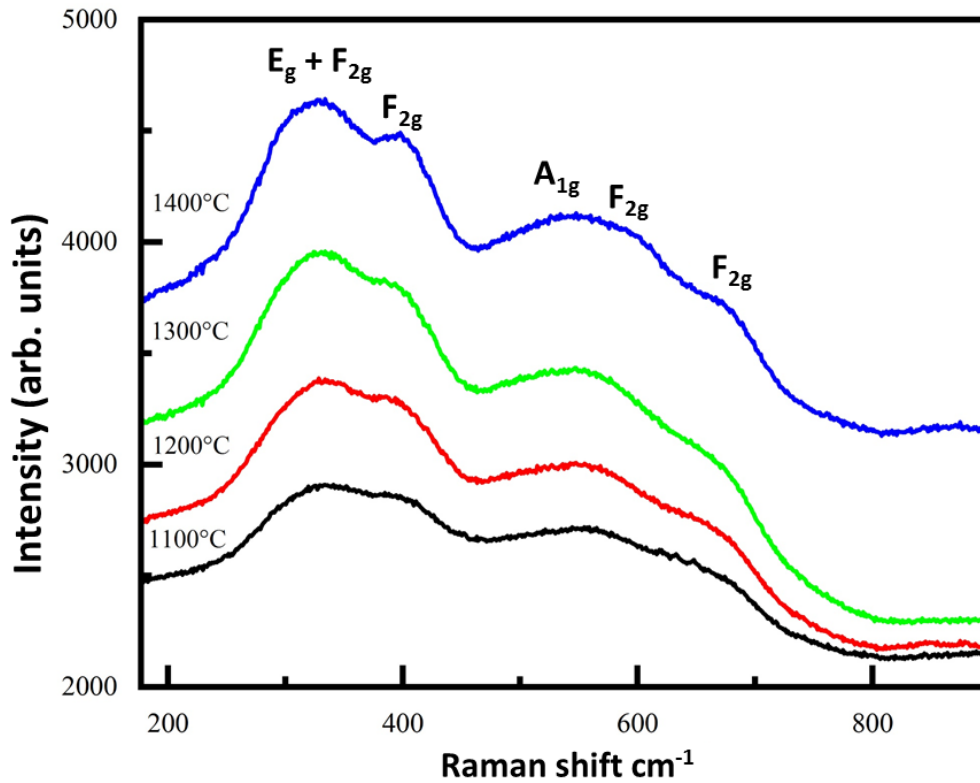
## (ii) Raman Spectroscopic Studies

Raman spectra of Gd<sub>2</sub>Zr<sub>2</sub>O<sub>7</sub> samples heat treated at 1373 K, 1473 K, 1573 K and 1673 K are depicted in **Figure 6.4**. Literature report suggests that Gd<sub>2</sub>Zr<sub>2</sub>O<sub>7</sub> prepared by annealing in the temperature 1273 K-1873 K, can exist either in the form of defect fluorite or ordered pyrochlore or a mixture of both the phases<sup>203</sup>. Gd<sub>2</sub>Zr<sub>2</sub>O<sub>7</sub> in pyrochlore phase exhibits six different Raman modes, whereas in pure fluorite phase it exhibits a single mode. In the present study it was observed that all the Raman spectra invariably exhibited broad bands centred at ~330cm<sup>-1</sup>, 400cm<sup>-1</sup>, 550cm<sup>-1</sup> and a shoulder at 670cm<sup>-1</sup> which could be assigned to the E<sub>g</sub>, F<sub>2g</sub>, A<sub>1g</sub> and F<sub>2g</sub> modes of the pyrochlore phase, respectively. Absence of any sharp peak could be attributed to the reduced domain size or formation of antiphase micro-domains in the samples (non-equilibrium method of preparation and shorter annealing duration). XRD analysis of the

**Table 6.1: Refined phase fraction and unit cell parameters of Gd<sub>2</sub>Zr<sub>2</sub>O<sub>7</sub> sintered at 1373 K, 1473 K, 1573 K and 1673 K.**

Temperature	1373 K		1473 K		1573 K		1673 K	
Phases	Defect fluorite	Pyrochlore	Defect fluorite	Pyrochlore	Defect fluorite	Pyrochlore	Defect fluorite	Pyrochlore
Space group	Fm-3m	Fd-3m	Fm-3m	Fd-3m	Fm-3m	Fd-3m	Fm-3m	Fd-3m
% fraction	99.0(1.1)	1.0(0.1)	90.6(1.0)	9.5(0.8)	34.1(0.8)	65.9(0.9)	5.6(1.2)	94.5(1.4)
a (Å)	5.2682(1)	10.5459(10)	5.2678(2)	10.5465(2)	5.2664(3)	10.5486(2)	5.2664(2)	10.5466(1)
V (Å <sup>3</sup> )	146.213(3)	1172.87(4)	146.180(6)	1173.073(9)	146.083(9)	1173.774(8)	146.083(9)	1173.11(9)
$\chi^2$	2.28		2.66		2.03		2.73	

samples also indicated the presence of both the phases in varied proportions. Increased ordering in the samples with higher annealing temperature results in increased pyrochlore phase fraction with higher annealing temperature. Hence,  $A_{1g}$  mode at  $\sim 550\text{cm}^{-1}$  assigned to the stretching vibrational mode of Gd-O in (48f) and the  $E_g$  mode at  $\sim 330\text{cm}^{-1}$  assigned to the bending vibration of O-Gd-O bonds<sup>203</sup> shifted gradually to lower wave numbers.



**Figure 6.4:** Raman spectra of  $\text{Gd}_2\text{Zr}_2\text{O}_7$  sintered at 1373 K, 1473 K, 1573 K and 1673 K respectively.

### (iii) EXAFS Studies

**Zr K edge:** EXAFS oscillations have been extracted from the X ray absorption spectra  $\mu(E)$  versus  $E$ , following the standard procedure<sup>209–211</sup>. The EXAFS oscillations,  $\chi(k)$  were weighted by  $k^2$  to amplify the oscillation at high  $k$  and the functions  $\chi(k) k^2$  are Fourier transformed using  $k$  range of  $2\text{--}10 \text{ \AA}^{-1}$  to generate the  $\chi(r)$  versus  $r$  (or FT-EXAFS) spectra in terms of the real distances from the centre of the absorbing atom. A set of data analysis program<sup>212</sup> available

within the IFEFFIT software package have been used for reduction and fitting of the experimental EXAFS data. This includes data reduction and Fourier transform to derive the  $\chi(r)$  versus  $r$  plots from the absorption spectra, generation of the theoretical EXAFS spectra starting from an assumed crystallographic structure, and finally fitting of the experimental  $\chi(r)$  versus  $r$  data with the theoretical ones using the FEFF 6.0 code. The bond distances, coordination numbers (including scattering amplitudes) and disorder (Debye-Waller) factors ( $\sigma^2$ ), which give the mean-square fluctuations in the distances, have been used as fitting parameters. The  $k$  range for Fourier transformation and the  $R$  range for data fitting have been chosen in such a way that in each case during fitting, the number of free variables were always kept below the upper limit set by Nyquist theorem ( $N_{\text{free}} = 2\Delta k \Delta r / \pi + 1$ )<sup>211</sup>. The goodness of the fit in the above process is generally expressed by the  $R_{\text{factor}}$  which is defined as:

$$R_{\text{factor}} = \sum \frac{[\text{Im}(\chi_{\text{dat}}(r_i) - \chi_{\text{th}}(r_i))]^2 + [\text{Re}(\chi_{\text{dat}}(r_i) - \chi_{\text{th}}(r_i))]^2}{[\text{Im}(\chi_{\text{dat}}(r_i))]^2 + [\text{Re}(\chi_{\text{dat}}(r_i))]^2} \quad (\text{eqn. 6.1})$$

where,  $\chi_{\text{dat}}$  and  $\chi_{\text{th}}$  refer to the experimental and theoretical  $\chi(R)$  values respectively and Im and Re refer to the imaginary and real parts of the respective quantities. The R factor of all the EXAFS fitting is less than 0.01 which ensures good fitting of the data.

The experimental  $\chi(r)$  versus  $r$  plots of the  $\text{Gd}_2\text{Zr}_2\text{O}_7$  sample annealed at different temperatures at Zr K edge have been fitted from 1-2.2 Å assuming a Zr-O shell at 2.28(×8) Å. The fitting results have been tabulated in **Table 6.2**. From the EXAFS fitting results, the Zr-O bond distance in all the samples is 2.10 Å with coordination near 7.5. This suggests the presence of pyrochlore structure (6 oxygen coordination) along with fluorite structure (8 oxygen coordination).



**Table 6.2: Table depicting average Zr-O bond length of Gd<sub>2</sub>Zr<sub>2</sub>O<sub>7</sub> sintered at 1373 K, 1473 K, 1573 K and 1673 K.**

Samples	Zr-O shell		
	$r$ (Å)	N	$\sigma^2$
1373K	2.10	7.4	0.0051
1473K	2.10	7.6	0.0054
1573K	2.10	7.5	0.0052
1673K	2.10	7.6	0.0052

**Gd L<sub>3</sub> edge:** The absorption edges of the samples lie close to that of Gd<sub>2</sub>O<sub>3</sub> standard which implies +3 oxidation state of Gd cations. However, the white line intensities of the samples are lesser than that of Gd<sub>2</sub>O<sub>3</sub> standard. The experimental  $\chi(r)$  versus  $r$  spectra have been extracted from the absorption spectra following the same procedure described earlier for Zr K edge data using a  $k$  range of 2-9 Å<sup>-1</sup>. The experimental  $\chi(r)$  versus  $r$  spectra have been fitted from 1-2.5 Å with theoretically simulated  $\chi(r)$  versus  $r$  plots generated assuming both fluorite and pyrochlore crystal structure of Gd<sub>2</sub>Zr<sub>2</sub>O<sub>7</sub>. The structural parameters for the defect fluorite and pyrochlore structure were obtained from the literature<sup>213</sup>. Following the fluorite structure, the experimental data have been fitted assuming a Gd-O shell at 2.28(×8) Å. The fitting results have been tabulated in **Table 6.3**. Similarly, the experimental data at Gd L<sub>3</sub> edge have also been fitted with the pyrochlore structure assuming two Gd-O shells at 2.28(×2) Å and 2.51(×6) Å and the fitting results have been tabulated in **Table 6.4**. From the two tables, it is evident that though both the structures fit the data, but the lower R factors are observed for the fluorite structure fitting. Also, for the pyrochlore structure fitting, the bond distance values of the Gd-O<sub>2</sub> shell are much lower than the theoretically predicted values. However, from the fluorite structure fitting results, we can see that the bond distance is higher and coordination number is

lower than the theoretical values. This may be due to presence of increasing pyrochlore phase in the samples with increasing temperature.

**Table 6.3: Table depicting average Gd-O bond length of Gd<sub>2</sub>Zr<sub>2</sub>O<sub>7</sub> sintered at 1373 K, 1473 K, 1573 K and 1673 K. [Defect fluorite model]**

Samples	Gd-O shell		
	r (Å)	N	$\sigma^2$
1373K	2.31	7.5	0.0153
1473K	2.32	8.0	0.0137
1573K	2.31	7.4	0.0159
1673K	2.32	7.3	0.0138

**Table 6.4: Table depicting average Gd-O bond length of Gd<sub>2</sub>Zr<sub>2</sub>O<sub>7</sub> sintered at 1373 K, 1473 K, 1573 K and 1673 K respectively. [Pyrochlore model]**

Samples	Gd-O1 shell			Gd-O2 shell		
	r (Å)	N	$\sigma^2$	r (Å)	N	$\sigma^2$
<b>1373K</b>	2.22	1.7	0.0022	2.38	5.2	0.0112
<b>1473K</b>	2.25	1.7	0.0014	2.39	5.4	0.0126
<b>1573K</b>	2.20	1.9	0.0024	2.37	4.5	0.0093
<b>1673K</b>	2.27	1.9	0.0036	2.39	5.7	0.0170

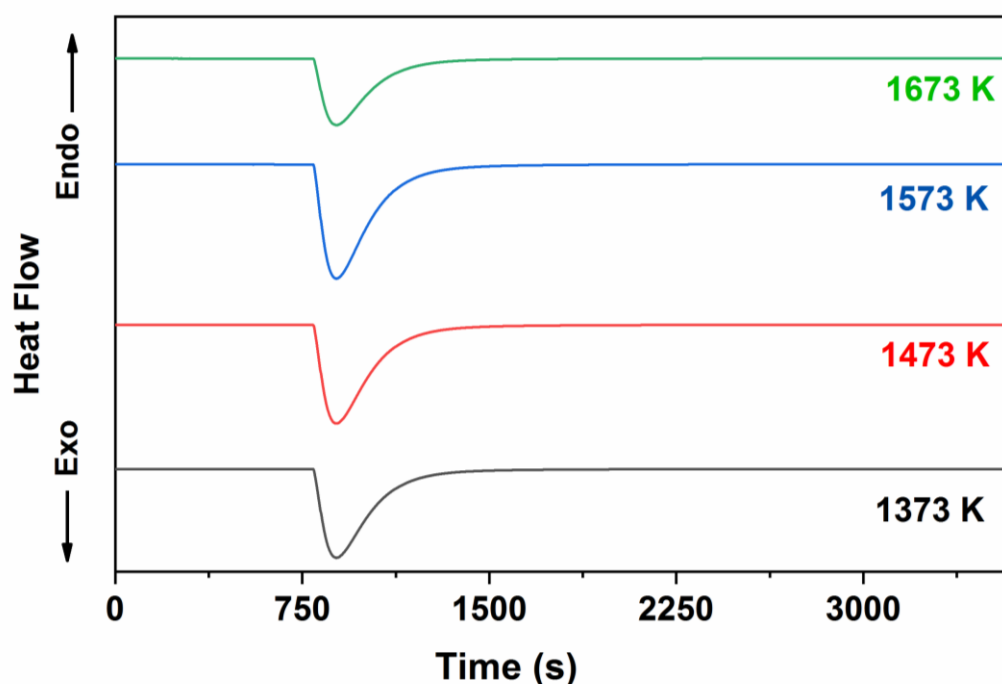
#### (iv) Calorimetric Studies

Standard molar enthalpy of formation of Gd<sub>2</sub>Zr<sub>2</sub>O<sub>7</sub> samples sintered at 1373 K, 1473 K, 1573 K and 1673 K were derived from enthalpy of dissolution values of Gd<sub>2</sub>Zr<sub>2</sub>O<sub>7</sub> samples and its component oxides such as Gd<sub>2</sub>O<sub>3</sub>(s) and ZrO<sub>2</sub>(s) in liquid Na<sub>2</sub>O + MoO<sub>3</sub> (3:4 molar ratio) solvent maintained at 986 K. The normalized plot of heat flow signal for dissolution of 10 mg Gd<sub>2</sub>Zr<sub>2</sub>O<sub>7</sub> samples versus is shown in **Figure 6.5**.

A steady base line of heat flow signal versus time was observed only after around 3600 s of sample dropping. In each measurement an exothermic heat signals were obtained. The

overall heat of dissolution was determined by integrating the area under the curve using SETSOFT software supplied along with the instrument. This method was repeated for four times for each sample and the corresponding heats of dissolution are tabulated in **Table 6.5**.

The heat effect observed in the dissolution of a sample is sum of the heat effects due to heating of the sample from 298 K to 986 K (endothermic effect), solvation of its ions in the solvent (exothermic effect) and dissociation of its crystal lattice (endothermic effect). In the present case, it was observed that dissolution of  $\text{Gd}_2\text{Zr}_2\text{O}_7$  and  $\text{Gd}_2\text{O}_3$  were exothermic, whereas  $\text{ZrO}_2$  dissolution was endothermic in nature.



**Figure 6.5:** Normalized heat flow curves for  $\text{Gd}_2\text{Zr}_2\text{O}_7$  sintered at 1373 K, 1473 K, 1573 K and 1673 K respectively.

The standard molar enthalpies of formation of  $\text{Gd}_2\text{Zr}_2\text{O}_7$  phases containing different amounts of defect fluorite and pyrochlore phases (obtained by sintering at 1373 K, 1473 K, 1573 K and 1673 K) were derived from molar enthalpy of dissolution values of  $\text{Gd}_2\text{Zr}_2\text{O}_7$  phases,  $\text{Gd}_2\text{O}_3(\text{s})$ ,  $\text{ZrO}_2(\text{s})$  together with other auxiliary data from literature<sup>135</sup> employing

thermo chemical cycle. The thermo chemical cycle used for the derivation of standard molar enthalpy of formation of  $\text{Gd}_2\text{Zr}_2\text{O}_7$  phase is depicted in **Table 6.6**. The standard molar

**Table 6.5: Heat of Dissolution of  $\text{Gd}_2\text{Zr}_2\text{O}_7$  sintered at 1373 K, 1473 K, 1573 K and 1673 K and their component oxides.**

Compounds	Mass (m) (mg)	$\Delta H$ (J/g)	$\Delta H_T$ (kJ mol <sup>-1</sup> )
$\text{Gd}_2\text{Zr}_2\text{O}_7(\text{s})$ (1373K) Mol. Wt. = 608.948	27.8 24.7 11.5 10.9	-248.39 -254.87 -250.88 -252.03	-151.26 -155.20 -152.77 -153.47 Avg: $-153.18 \pm 1.63$
$\text{Gd}_2\text{Zr}_2\text{O}_7(\text{s})$ (1473K) Mol. Wt. = 608.948	11.6 14.4 16.2 7.6	-311.33 -309.85 -313.96 -312.51	-189.58 -188.68 -191.18 -190.30 Avg: $-189.94 \pm 1.06$
$\text{Gd}_2\text{Zr}_2\text{O}_7(\text{s})$ (1573K) Mol. Wt. = 608.948	24.8 12.1 8.7 12.5	-366.93 -366.03 -367.07 -365.81	-223.44 -222.89 -223.53 -222.76 Avg: $-223.16 \pm 0.38$
$\text{Gd}_2\text{Zr}_2\text{O}_7(\text{s})$ (1673K) Mol. Wt. = 608.948	34.4 22.0 23.3 28.3	-174.64 -178.21 -180.43 -178.85	-106.35 -108.52 -109.87 -108.91 Avg: $-108.41 \pm 1.49$
$\text{ZrO}_2(\text{s})$ Mol. Wt. = 123.224	10.8 12.3 8.9 15.4	355.7 355.0 356.5 356.7	43.75 43.74 43.93 43.95 Avg: $43.84 \pm 0.11$
$\text{Gd}_2\text{O}_3(\text{s})$ Mol. Wt. = 362.50	13.8 14.2 11.3 10.8	-655.1 -657.2 -656.8 -655.9	-237.47 -238.23 -238.09 -237.76 Avg: $-237.88 \pm 0.34$

enthalpies of formation of  $\text{Gd}_2\text{Zr}_2\text{O}_7$  phase obtained by sintering at 1373 K, 1473 K, 1573 K and 1673 K are found to be  $-4014.50 \pm 17.08$ ,  $-3977.74 \pm 17.04$ ,  $-3944.52 \pm 17.01$ ,  $-4059.27 \pm 17.07$  kJ.mol<sup>-1</sup>, respectively.

**Table 6.6: Thermochemical cycles for enthalpy of formation of Gd<sub>2</sub>Zr<sub>2</sub>O<sub>7</sub> sintered at 1373 K, 1473 K, 1573 K and 1673 K.**

$$(\Delta_f H^\circ_{298} \text{Gd}_2\text{Zr}_2\text{O}_7(\text{s}) = -\Delta H_{1i} + 2\Delta H_2 + \Delta H_3 + \Delta H_4 + 2\Delta H_5)$$

Reaction	$\Delta H_i$	$\Delta H_{\text{dissolution}}$ (kJ mol <sup>-1</sup> )
Gd <sub>2</sub> Zr <sub>2</sub> O <sub>7</sub> (s,298K) + (sln) = Gd <sub>2</sub> O <sub>3</sub> (sln) + 2ZrO <sub>2</sub> (sln) [1373 K]	$\Delta H_{1a}$	-153.18 ± 1.63
Gd <sub>2</sub> Zr <sub>2</sub> O <sub>7</sub> (s,298K) + (sln) = Gd <sub>2</sub> O <sub>3</sub> (sln) + 2ZrO <sub>2</sub> (sln) [1473 K]	$\Delta H_{1b}$	-189.94 ± 1.06
Gd <sub>2</sub> Zr <sub>2</sub> O <sub>7</sub> (s,298K) + (sln) = Gd <sub>2</sub> O <sub>3</sub> (sln) + 2ZrO <sub>2</sub> (sln) [1573 K]	$\Delta H_{1c}$	-223.16 ± 0.38
Gd <sub>2</sub> Zr <sub>2</sub> O <sub>7</sub> (s,298K) + (sln) = Gd <sub>2</sub> O <sub>3</sub> (sln) + 2ZrO <sub>2</sub> (sln) [1673 K]	$\Delta H_{1d}$	-108.41 ± 1.49
ZrO <sub>2</sub> (s,298K) + (sln) = ZrO <sub>2</sub> (sln)	$\Delta H_2$	43.84 ± 0.11
Gd <sub>2</sub> O <sub>3</sub> (s,298K) + (sln) = Gd <sub>2</sub> O <sub>3</sub> (s)	$\Delta H_3$	-237.88 ± 0.34
2Gd(s,298K) + 3/2O <sub>2</sub> (g) = Gd <sub>2</sub> O <sub>3</sub> (s)	$\Delta H_4$	-1815.86 ± 16.74
Zr(s,298K) + O <sub>2</sub> (g) = ZrO <sub>2</sub> (s)	$\Delta H_5$	-1100.81 ± 2.09
2Gd(s,298K) + 2Zr(s,298K) + 3.5 O <sub>2</sub> (g) = Gd <sub>2</sub> Zr <sub>2</sub> O <sub>7</sub> (s,298K)	$\Delta_f H^\circ_{298} (1373\text{K})$	-4014.50 ± 17.08
	$\Delta_f H^\circ_{298} (1473\text{K})$	-3977.74 ± 17.04
	$\Delta_f H^\circ_{298} (1573\text{K})$	-3944.52 ± 17.01
	$\Delta_f H^\circ_{298} (1673\text{K})$	-4059.27 ± 17.07

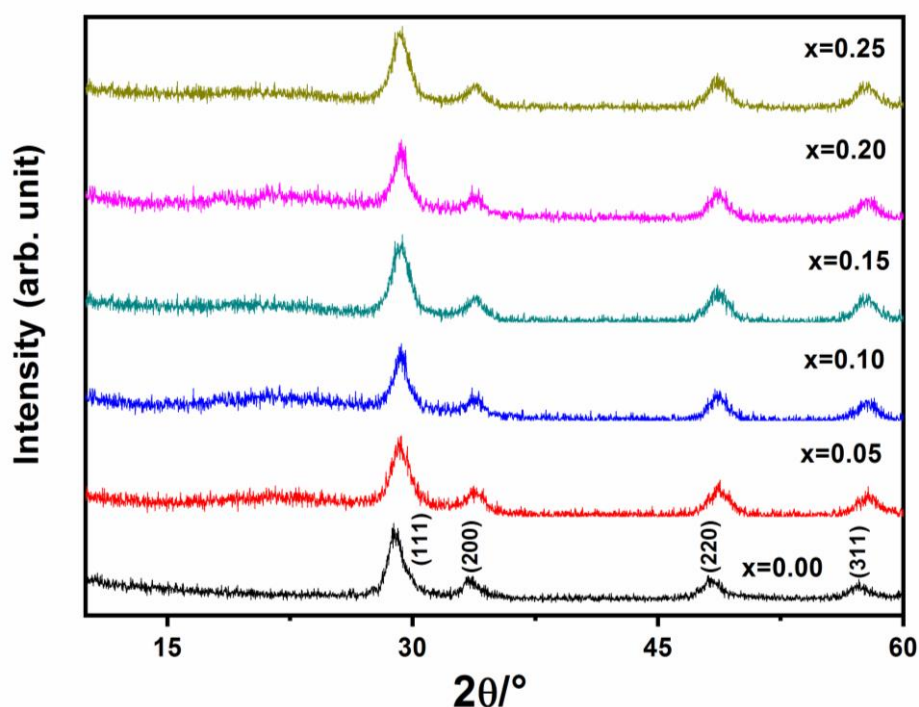
Literature report indicates that the entropy contributions for stabilization of these phases are negligible and the stability is mostly enthalpy driven<sup>125</sup>. Hence, standard molar enthalpy of formation can indirectly be equated to the thermodynamic stability for these types of systems. It was clearly observed that the enthalpy of formation of  $\text{Gd}_2\text{Zr}_2\text{O}_7$  sintered at 1373 K composition is more negative ( $-4014.5 \pm 17.1 \text{ kJ.mol}^{-1}$ ) compared to 1473 K and 1573K sintered compositions which are  $-3977.7 \pm 17.0$  and  $-3944.5 \pm 17.0 \text{ kJ.mol}^{-1}$ , respectively. Further it was also observed that, the enthalpy of formation of sample sintered at 1673K was found to be most negative ( $-4059.3 \pm 17 \text{ kJ.mol}^{-1}$ ) compared to all other samples. The lower values of standard molar enthalpy of formation for samples heated at 1373K compared to the sample heated at 1473 K could be due to increase in defect ordering onset where atoms get displaced from their usual lattice position to interstitial positions. Such arrangements tend to decrease the lattice energy, which in turn decreases standard molar enthalpy of formation values. On increase in the annealing temperature to 1673 K, the high thermodynamic stability could be explained by the evolution of pyrochlore  $\text{Gd}_2\text{Zr}_2\text{O}_7$  phase. The standard molar enthalpy of formation of pyrochlore- $\text{Gd}_2\text{Zr}_2\text{O}_7$  prepared at 1873 K reported by Navrotsky *et al*<sup>125</sup> ( $-4070 \text{ kJmol}^{-1}$ ) is in close agreement with the sample heated at sample heated at 1673 K, where the sample is partly fluorite and partly pyrochlore. The above enthalpy data supports the structural studies on evolution of  $\text{Gd}_2\text{Zr}_2\text{O}_7$  phases as a function of sintering temperature.

## **PART B: Structural and thermodynamic studies on uranium incorporated $\text{Gd}_2\text{Zr}_2\text{O}_7$**

### **(i) Powder XRD Studies**

Phase formation in the system  $\text{Gd}_{2-x}\text{U}_x\text{Zr}_2\text{O}_{7+\delta}$  ( $0.0 \leq x \leq 0.25$ ) was concluded upon characterization of the as prepared samples by powder XRD technique. Powder XRD patterns of the calcined products exhibited broad peaks due to the nano-crystalline nature of the prepared samples and is depicted in **Figure 6.6**. All the patterns showed similar fingerprint to that of the defect fluorite structure of  $\text{Gd}_2\text{Zr}_2\text{O}_7$ . As no impurity peaks corresponding to any

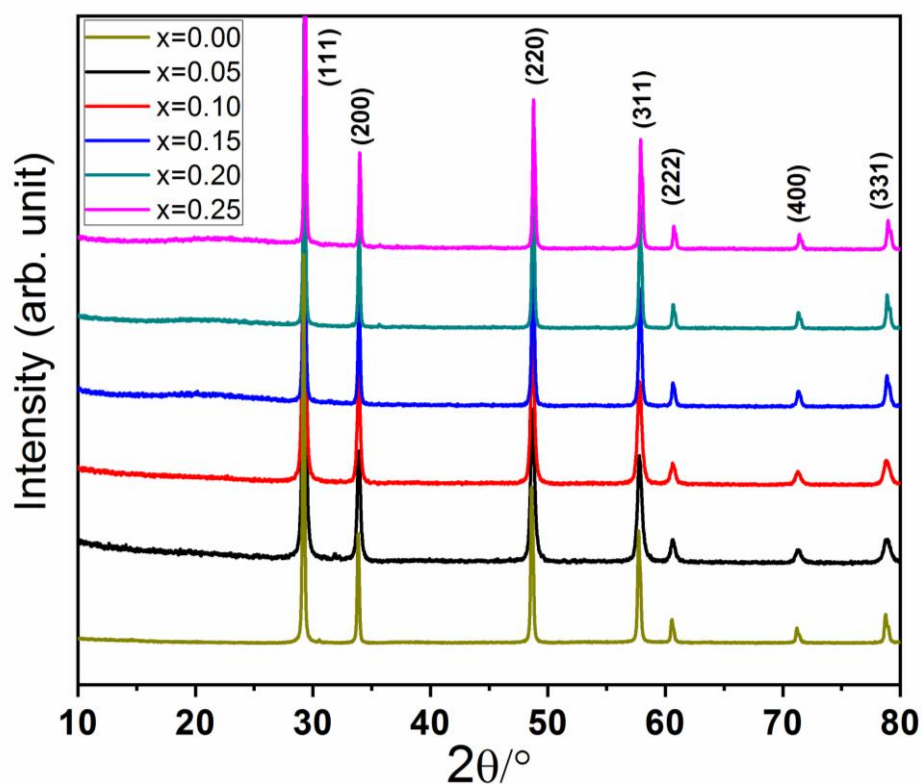
reactants were found to be present, the general composition of the samples obtained after calcinations could be represented as  $\text{Gd}_{2-x}\text{U}_x\text{Zr}_2\text{O}_{7+\delta}$ . However, due to broad nature of the peaks of the as-prepared samples, further meaningful structural characterizations of the phases present were not carried out.



**Figure 6.6: Powder XRD patterns of  $\text{Gd}_{2-x}\text{U}_x\text{Zr}_2\text{O}_{7+\delta}$  ( $0.0 \leq x \leq 0.25$ ) samples calcined at 873 K for 1 h<sup>178</sup> (PCPDF-80-0471).**

Half of the synthesized samples were reduced in presence of Ar : H<sub>2</sub> (92:8) atmosphere at 1373 K for 8 h. Powder XRD patterns of all the samples heated in reducing atmosphere in the system  $\text{Gd}_{2-x}\text{U}_x\text{Zr}_2\text{O}_{7+\delta}$  ( $0.0 \leq x \leq 0.25$ ) confirmed the formation of a single phasic defect fluorite-type structure as displayed in **Figure 6.7**. This was in line with the results mentioned in Part A of this chapter. Structural analysis was carried out using Rietveld refinement program Fullprof-2000 as mentioned earlier<sup>103</sup>. The background of the obtained diffraction patterns was fitted with sixth order polynomial relation and then scale was adjusted. Pseudo-Voigt profile function was used to fit the diffraction peak profile followed by refinement of the U, V, W parameters. Displacement and absorption factor were not considered during the refinement process. The

refined parameters have been tabulated in **Table 6.7** and some representative Rietveld refinement plots were shown in **Figure 6.8**.



**Figure 6.7: Representative Rietveld refinement plots for the nominal compositions in the series  $\text{Gd}_{2-x}\text{U}_x\text{Zr}_2\text{O}_{7+\delta}$  ( $0.0 \leq x \leq 0.25$ ) heated in reducing atmosphere<sup>178</sup> (PCPDF-80-0471).**

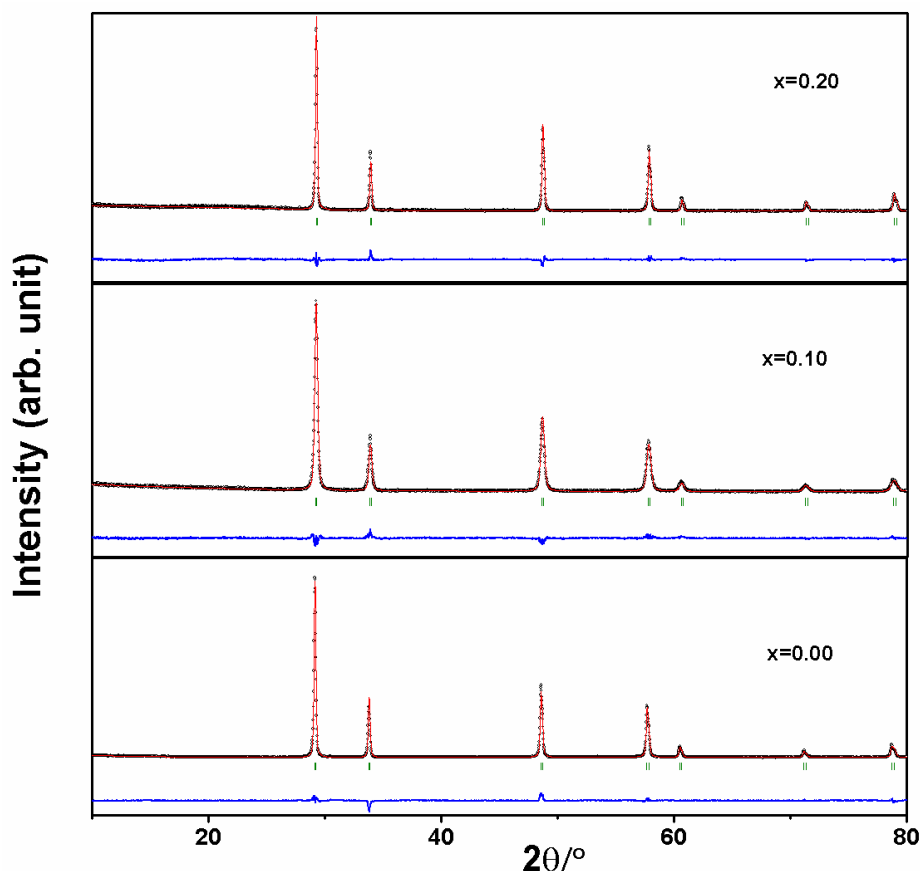
A steady decrease in lattice parameters of the compositions with increase in concentration of  $\text{U}^{4+}$  was observed. Two antagonistic factors had the potential to affect the variation in lattice parameter as a function of uranium content in this system. Firstly, the smaller ionic radius of  $\text{U}^{4+}$  (1.00 Å in eight-fold coordination) compared to that of  $\text{Gd}^{3+}$  (1.05 Å) would lead to decrease in overall lattice parameter<sup>150</sup>. On the other hand, substitution of  $\text{U}^{4+}$  in the place of  $\text{Gd}^{3+}$  would lead to unit cell dilation due to extra  $\frac{1}{2}$  incorporated oxygen atom to maintain charge balance accompanied with incorporation of each  $\text{U}^{4+}$  ion. The observed net-decrease in lattice parameter clearly indicated that the effect of smaller ionic radius of  $\text{U}^{4+}$  as compared to



**Table 6.7: Rietveld refined parameters of  $\text{Gd}_{2-x}\text{U}_x\text{Zr}_2\text{O}_{7+\delta}$  ( $0.0 \leq x \leq 0.25$ ) compositions after annealing at Ar :H<sub>2</sub> (92:8) at 1373 K for 8h<sup>178</sup>.**

Sample	$\text{Gd}_2\text{Zr}_2\text{O}_7$	$\text{Gd}_{1.95}\text{U}_{0.05}\text{Zr}_2\text{O}_{7.025}$	$\text{Gd}_{1.90}\text{U}_{0.10}\text{Zr}_2\text{O}_{7.050}$	$\text{Gd}_{1.85}\text{U}_{0.15}\text{Zr}_2\text{O}_{7.075}$	$\text{Gd}_{1.80}\text{U}_{0.20}\text{Zr}_2\text{O}_{7.100}$	$\text{Gd}_{1.75}\text{U}_{0.25}\text{Zr}_2\text{O}_{7.125}$
a (Å)	5.2621(1)	5.2601(1)	5.2591(1)	5.2578(4)	5.2569(1)	5.2559(3)
U	0.277(3)	0.931(1)	0.499(1)	0.077(3)	0.074(3)	0.086(4)
V	-0.234(2)	-0.462(1)	-0.183(9)	-0.014(7)	-0.051(3)	-0.068(2)
W	0.073(5)	0.148(2)	0.099(2)	0.031(2)	0.033(5)	0.038(1)
$\chi^2$	1.01	1.45	1.71	1.63	1.94	2.40
R <sub>p</sub> (%)	8.36	9.01	9.67	9.56	8.29	11.5
R <sub>wp</sub> (%)	11.72	12.2	12.8	12.8	10.8	14.5
R <sub>exp</sub> (%)	11.71	10.11	9.76	10.02	7.75	9.34
Space group	Fm $\bar{3}$ m	Fm $\bar{3}$ m	Fm $\bar{3}$ m	Fm $\bar{3}$ m	Fm $\bar{3}$ m	Fm $\bar{3}$ m

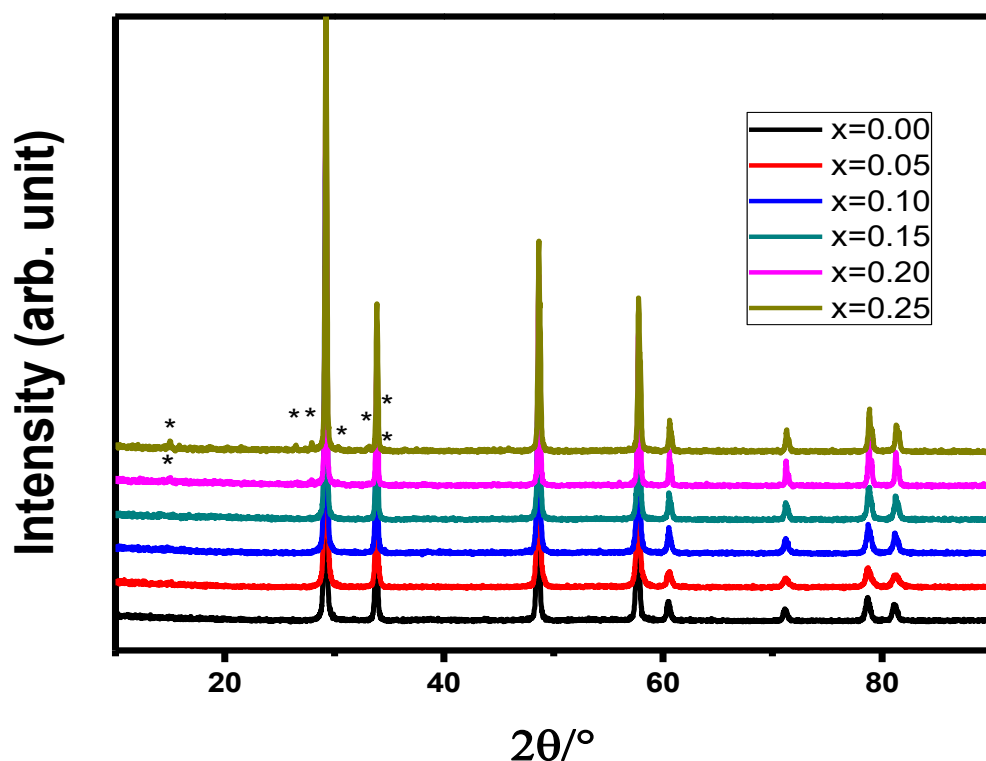
$Gd^{3+}$  is found to be predominant over the incorporated extra oxygen atom in the crystal structure.



**Figure 6.8: Powder XRD patterns of  $Gd_{2-x}U_xZr_2O_{7+\delta}$  ( $0.0 \leq x \leq 0.25$ ) samples annealed in Ar :  $H_2$  (92:8) at 1373 K for 8 h. All the compositions were found to crystallize in defect fluorite structure<sup>178</sup>.**

Other halves of the samples were annealed in air at 1373 K for 8 h to investigate the solubility of uranium in hexavalent oxidation state by powder XRD. Absence of any additional peaks apart from the signature of defect-fluorite structure in the x-ray diffraction patterns for the compositions  $x=0.0-0.15$  in  $Gd_{2-x}U_xZr_2O_{7+\delta}$  indicated that the compositions up to  $x = 0.15$  crystallize in single phase. However, the nominal compositions with  $x=0.20$  and  $0.25$  exhibited minor impurity peaks suggesting the onset of phase separation. The comparatively poor solubility of uranium into defect fluorite structure of  $Gd_2Zr_2O_7$  under oxidizing condition could

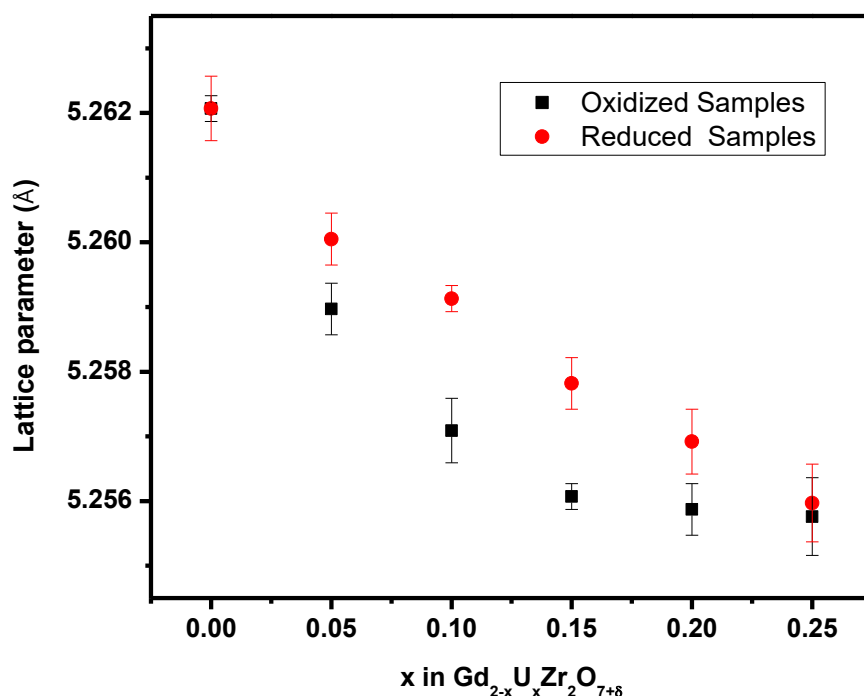
be attributed to the oxidation of  $U^{4+}$  to  $U^{6+}$  and the oxidation of  $U^{4+}$  to  $U^{6+}$  incorporated of relatively larger number of extra oxygen atoms into  $Gd_2Zr_2O_7$  lattice. Plausibly, at and after  $x = 0.15$  composition, the lattice was not able to accommodate the large amount of excess oxygen which results in segregation of secondary phase as evident from **Figure 6.9**.



**Figure 6.9:** Powder XRD patterns of  $Gd_{2-x}U_xZr_2O_{7+\delta}$  ( $0.0 \leq x \leq 0.25$ ) after heat treatment in air at 1373 K for 8 h. Asterisks indicate unidentified minor secondary phase<sup>178</sup>.

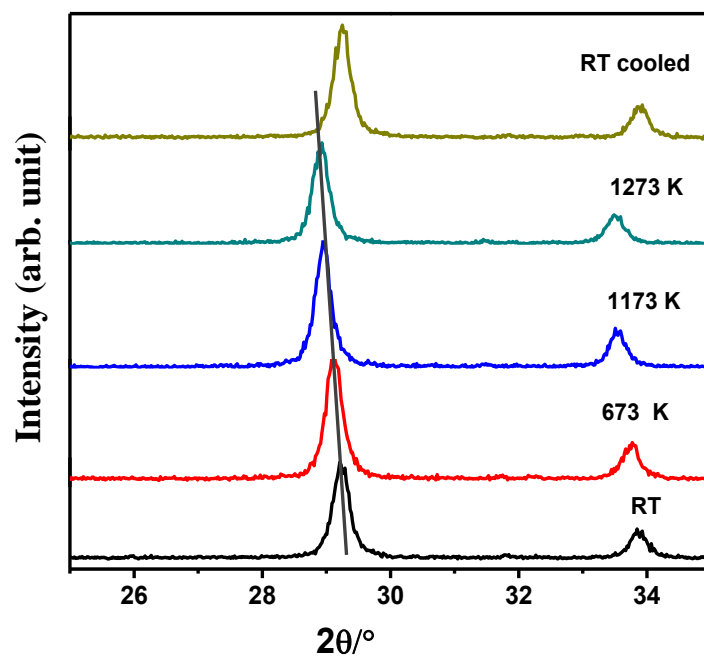
Unit cell parameter of the oxidized samples was found to decrease with increase in uranium content due to much smaller ionic radius of  $U^{6+}$  compared to that of  $Gd^{3+}$  in  $Gd_{2-x}U_xZr_2O_{7+\delta}$  system. The decrease in unit cell parameter was found to be more prominent in oxidized samples as compared to that of the samples prepared under reducing conditions because of the reason that the ionic radius of  $U^{6+}$  is much smaller than that of  $U^{4+}$  (**Figure 6.10**). The unit cell parameter of the fluorite type phase in the samples with  $x=0.20$  and  $0.25$  heated

in air was not found to vary which confirmed their biphasic nature. The amount of secondary phase was very small for its identification.

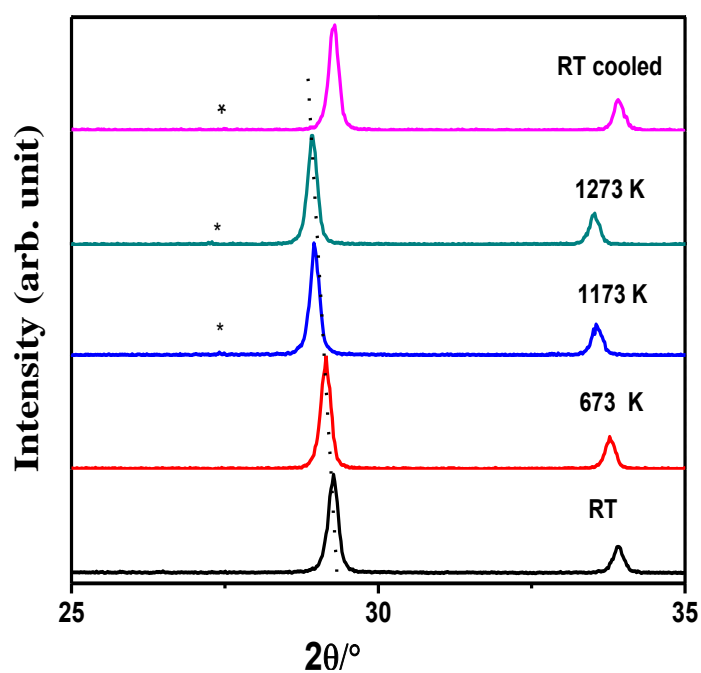


**Figure 6.10: Variation of unit cell parameter upon substitution of U at Gd site in  $Gd_{2-x}U_xZr_2O_{7+\delta}$  (reduced and oxidized samples)<sup>178</sup>.**

*In situ* high temperature XRD studies on the compositions heated under reducing atmosphere were carried out till 1273 K in static air to examine the stability of the  $U^{4+}$  substituted  $Gd_2Zr_2O_7$  samples in oxidizing environment. It was observed that all the compositions remained monophasic with the exception of  $Gd_{1.75}U_{0.25}Zr_2O_{7+\delta}$  ( $x=0.25$ ) wherein segregated secondary phase was observed from 1173 K onwards. Typical XRD patterns of  $Gd_{1.95}U_{0.05}Zr_2O_{7+\delta}$  and  $Gd_{1.75}U_{0.25}Zr_2O_{7+\delta}$ , at different temperatures are shown in **Figure 6.11a** and **b**, respectively. A systematic peak shift towards lower diffraction angle with increase in temperature was observed which clearly indicates expansion of the lattice. The intensities of the peaks of the secondary phase as observed from the XRD patterns of  $Gd_{1.75}U_{0.25}Zr_2O_{7+\delta}$  at 1173, 1273 K and RT cooled (**Figure 6.11b**) were too weak to refine. Hence, the exact



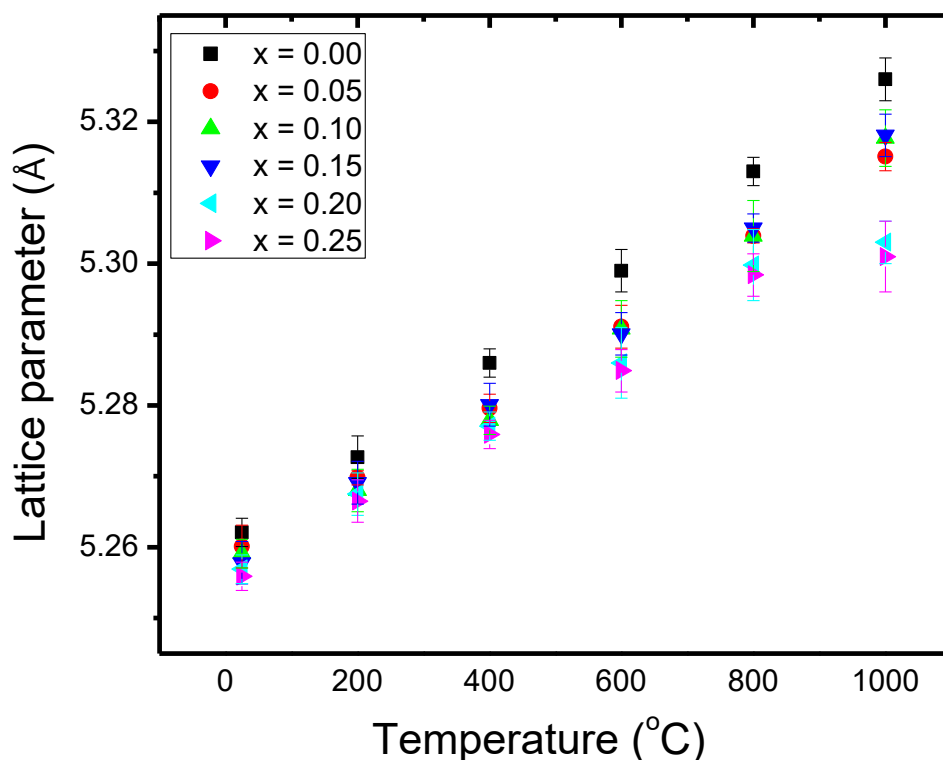
**Figure 6.11a:** High temperature-XRD pattern of  $\text{Gd}_{1.95}\text{U}_{0.05}\text{Zr}_2\text{O}_{7+\delta}$ . Solid line has been used to show the shift in peak position with variation in temperature<sup>178</sup>.



**Figure 6.11b:** High temperature-XRD pattern of  $\text{Gd}_{1.75}\text{U}_{0.25}\text{Zr}_2\text{O}_{7+\delta}$ . Asterisk indicated the segregation of secondary phase<sup>178</sup>.

identification for the impurity phase could not be carried out. All the samples showed a steady increase in cell parameter with increase in temperature as depicted in **Figure 6.12**.

Upon heating of the reduced samples in air, two contradicting phenomena occur simultaneously viz. oxidation of uranium in the substituted samples and thermal expansion of the unit cell. Under this scenario, three main controlling factors for the variation of unit cell with temperature arose viz. (a) thermal expansion of the unit cell parameters as a function of increasing temperature, (b) expansion of lattice parameters because of incorporation of additional oxygen in the lattice as a consequence of uranium oxidation and (c) contraction of unit cell parameter due to decrease in ionic radii of uranium induced by the aerial oxidation of  $U^{4+}$  to  $U^{6+}$ . It was also observed that thermal expansion of unit cell parameter of pure  $Gd_2Zr_2O_7$  was found to be more than that of the uranium substituted samples as no case of contraction is possible for the parent compound (**Figure 6.12**). Moreover, in all the uranium incorporated samples, the unit cell parameter upon cooling to room temperature was found to be lower than the cell parameters recorded initially at room temperature. This further indicated that the oxidation of uranium under static air environment causes the decrease in its ionic radius which results in shrinkage of unit cell parameter. Additionally, the extra oxygen incorporated in the lattice during in situ oxidation did not result in phase segregation up to  $x = 0.15$ . The above phenomena also exposed that the shrinkage of lattice parameters because of aerial oxidation of uranium is much more predominant factor than the lattice expansion due to incorporation of oxygen into the lattice. In addition, the samples prepared in this study were anion-deficient defect fluorites which further supports the accommodation of excess oxygen due to oxidation of  $U^{4+}$  to  $U^{6+}$ . Hence, it could be concluded with certainty that oxidation of uranium within the lattice did not result any structural rearrangement of the defect fluorite structure till  $x = 0.15$ .

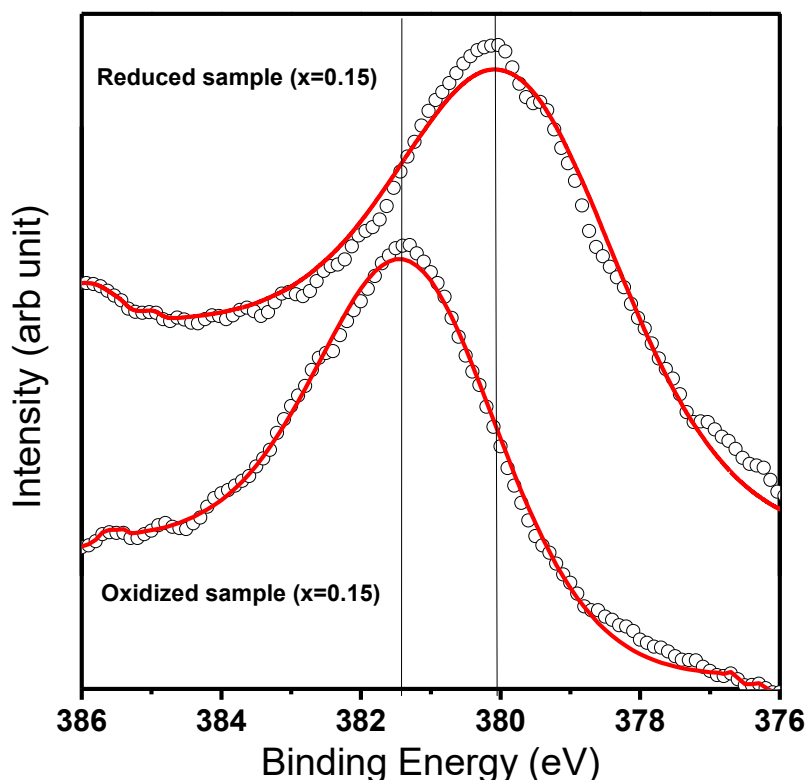


**Figure 6.12: Variation of unit cell parameters of nominal compositions  $\text{Gd}_{2-x}\text{U}_x\text{Zr}_2\text{O}_{7+\delta}$  ( $0.00 \leq x \leq 0.25$ ) with temperature<sup>178</sup>.**

## (ii) XPS Studies

Estimation of oxidation state of uranium in samples prepared under different experimental conditions (oxidized and reduced) was obligatory for ascertaining inferences drawn by powder XRD studies. The XPS spectra of two representative oxidized and reduced nominal compositions corresponding to  $x=0.15$  in  $\text{Gd}_{2-x}\text{U}_x\text{Zr}_2\text{O}_{7+\delta}$  are shown **Figure 6.13**. The position of  $4f_{7/2}$  peak in X-ray photoelectron spectrum was used to find the oxidation state of uranium. It was reported earlier that  $4f_{7/2}$  peak of  $\text{U}^{6+}$  appeared at 381.0-381.5 eV<sup>214,215</sup>. In nominal compositions heated in static air ( $x=0.15$ ), the  $4f_{7/2}$  peak appeared at 381.35 eV, which is a clear indication that the uranium in this composition is in +6 oxidation state. On the other hand, the  $4f_{7/2}$  peak was appeared at 380.05 eV in the composition heated under reducing atmosphere corresponding to  $x = 0.15$  in  $\text{Gd}_{2-x}\text{U}_x\text{Zr}_2\text{O}_{7+\delta}$ . Bera *et al.*<sup>215</sup> and Boily *et al.*<sup>216</sup> have

reported that the  $4f_{7/2}$  peak of  $U^{4+}$  appear in the range of 379.8-380.4 eV. Hence, the observed XPS data confirmed that uranium in reduced sample is in +4 oxidation state only. Since in the studied nominal compositions no XPS peak appears at 380.4 eV, hence, it can be concluded that the samples were free from any admixture of uranium in +5 oxidation state.

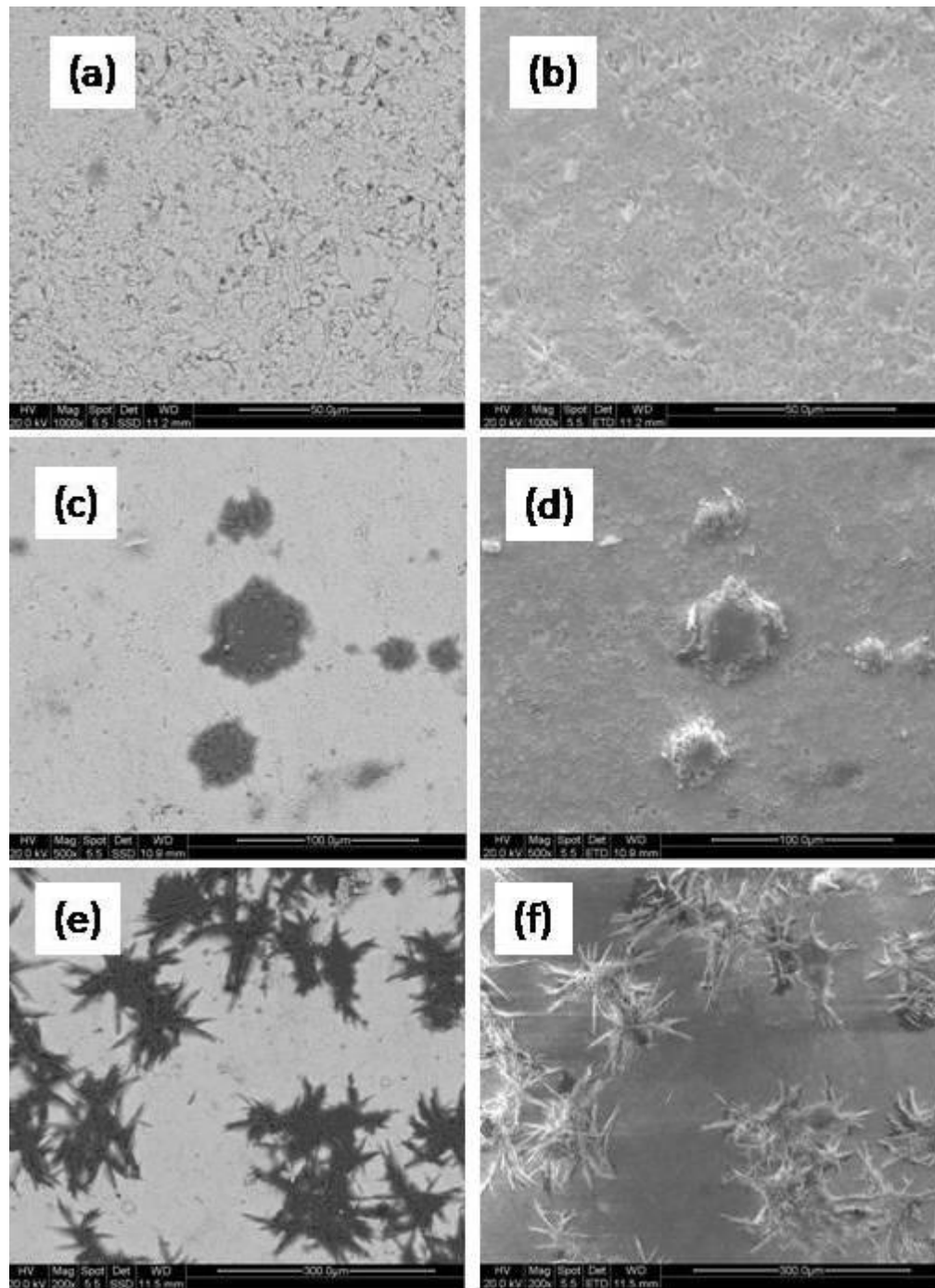


**Figure 6.13: X-ray photoelectron spectra of uranium ( $4f_{7/2}$ ) of reduced and oxidized sample having nominal composition  $Gd_{1.85}U_{0.15}Zr_2O_{7+\delta}$ .<sup>178</sup>**

### (iii) SEM Studies

Secondary electron (SE) imaging and backscattered electron (BSE) imaging has been performed on some of the nominal compositions to confirm the phase information. SE and BSE images of some of the representative nominal compositions ( $x=0.15, 0.2, 0.25$ ) heated in static air are shown in **Figure 6.14a to f**, respectively. Micrograph shown in **Figure 6.14a** for the nominal composition  $x=0.15$  clearly indicates single phasic nature of the sample. SEM micrographs of the biphasic nominal compositions were recorded by focusing the electron beam on secondary phase rich zones. Therefore, the other two BSE images **Figure 6.14c and**





**Figure 6.14: BSE images of (a)  $x=0.15$  (c)  $x=0.20$  (e)  $x=0.25$  and SE images of (b)  $x=0.15$  (d)  $x=0.20$  (f)  $x=0.25$  nominal compositions heated in static air respectively.**<sup>178</sup>

**6.14e** corresponding to the nominal compositions  $x=0.20$  and  $0.25$ , respectively, show the presence of secondary phase. Another important observation is quantitative increase of the

impurity phase from  $x=0.20$  to  $x=0.25$ . Corresponding secondary electron (SE) images for the nominal compositions  $x=0.15$ ,  $0.20$ ,  $0.25$  are shown in **Figure 6.14b**, **6.14d** and **6.14f**, respectively. Similar type of features as BSE images have been found in these images also.

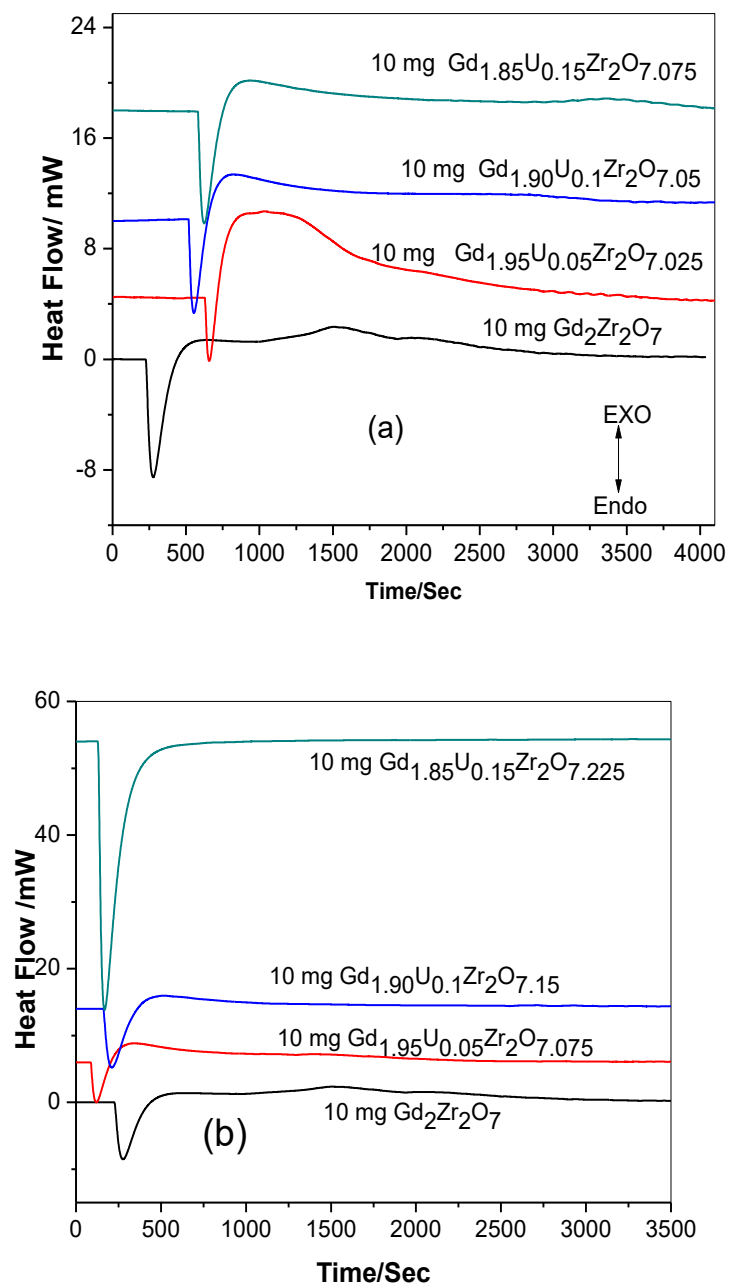
#### (iv) Calorimetric Studies

Derivation of standard molar enthalpies of nominal compositions crystallizing as single phase in both oxidizing and reducing conditions were carried out from the values of enthalpy of dissolution of  $\text{Gd}_{2-x}\text{U}_x\text{Zr}_2\text{O}_{7+\delta}$  ( $0.0 \leq x \leq 0.15$ ) samples along with their binary component oxides such as  $\text{Gd}_2\text{O}_3(\text{s})$ ,  $\text{U}_3\text{O}_8(\text{s})$  and  $\text{ZrO}_2(\text{s})$  in liquid  $\text{Na}_2\text{O} + \text{MoO}_3$  (3:4 molar ratio) solvent maintained at 986 K.

Illustrative heat flow signals for dissolution of single phasic  $\text{Gd}_{2-x}\text{U}_x\text{Zr}_2\text{O}_{7+\delta}$  ( $0.0 \leq x \leq 0.15$ ) nominal compositions heated under oxidized and reduced conditions normalized to 10 mg each in liquid  $\text{Na}_2\text{O} + \text{MoO}_3$  (3:4 molar ratio) dropped from room temperature to liquid solvent 986 K are shown in **Figure 6.15(a-b)**.

Endothermic heat flow signal was observed for all the droppings. Reaction completion between the droppings and solvent was monitored by recording a steady base line in the heat flow signal. Since, a steady base line is observed after around 3500 s, measurement time of 1 h has been selected for all the dropping experiments. The cumulative heat of dissolution in the solvent  $\text{Na}_2\text{O} + \text{MoO}_3$  (3:4 molar ratio) has been calculated upon addition of both the endothermic and exothermic effects observed using SETSOFT software supplied along with the instrument. The experimentally obtained heat of dissolution values of the single phasic nominal compositions of  $\text{Gd}_{2-x}\text{U}_x\text{Zr}_2\text{O}_{7+\delta}$  ( $0.0 \leq x \leq 0.15$ ) and their component oxides such as  $\text{Gd}_2\text{O}_3(\text{s})$ ,  $\text{UO}_2(\text{s})$  and  $\text{ZrO}_2(\text{s})$  in liquid  $\text{Na}_2\text{O} + \text{MoO}_3$  (3:4 molar ratio) solvent maintained at 986 K have been given in **Table 6.8**. The observed heat change can be attributed to the

endothermic heat effects due to the increase in enthalpy from 298 to 986 K and combined heat effects due to chemical reaction of solute with the solvent at 986 K.



**Figure 6.15: Representative heat flow signals for dissolution of  $\text{Gd}_{2-x}\text{U}_x\text{Zr}_2\text{O}_{7+\delta}$  ( $0.0 \leq x \leq 0.15$ ) nominal compositions (a) reduced and (b) oxidized compounds (normalized to 10 mg each) in liquid  $\text{Na}_2\text{O} + \text{MoO}_3$  (3:4 molar ratio) dropped from room temperature to liquid solvent 986 K.<sup>178</sup>**

**Table 6.8:** Heat of dissolution of  $Gd_{2-x}U_xZr_2O_{7+\delta}$  (oxidized/reduced) and their component oxides.

Compounds	Mass (m) (mg)	$\Delta H$ (J/g)	$\Delta H_T$ (kJ mol <sup>-1</sup> )
Gd <sub>2</sub> Zr <sub>2</sub> O <sub>7</sub> (s) Mol. Wt. = 608.948	26.5 25.2 24.7 20.1	-271.63 -266.20 -271.34 -268.42	-165.41 -162.10 -165.23 -163.45 Avr: -164.05±1.57
Gd <sub>1.95</sub> U <sub>0.05</sub> Zr <sub>2</sub> O <sub>7.025</sub> (s) (Reduced) Mol. Wt. = 613.387	35.6 22.4 13.0 21.5	-418.01 -416.23 -415.95 -417.48	-256.40 -255.31 -255.14 -256.08 Avr: -255.73±0.60
Gd <sub>1.90</sub> U <sub>0.10</sub> Zr <sub>2</sub> O <sub>7.05</sub> (s) (Reduced) Mol. Wt. = 617.826	27.9 31.6 29.4 31.5	-300.01 -298.65 -301.02 -298.03	-185.35 -184.51 -185.98 -184.13 Avr: -184.99 ±0.83
Gd <sub>1.85</sub> U <sub>0.15</sub> Zr <sub>2</sub> O <sub>7.075</sub> (s) (Reduced) Mol. Wt. = 622.265	10.3 12.5 14.5 21.3	-283.31 -287.41 -284.86 -285.91	-176.29 -178.85 -177.26 -177.91 Avr:-177.59 ±1.08
Gd <sub>1.95</sub> U <sub>0.05</sub> Zr <sub>2</sub> O <sub>7.075</sub> (s) (Oxidized) Mol. Wt. = 614.187	11.0 9.7 20.0 12.0	-263.10 -259.90 -261.52 -257.84	-161.60 -159.63 -160.62 -158.36 Avr.: -160.05±1.38
Gd <sub>1.90</sub> U <sub>0.10</sub> Zr <sub>2</sub> O <sub>7.15</sub> (s) (Oxidized) Mol. Wt. = 619.43	22.5 22.8 13.1 17.6	-164.61 -165.11 -164.10 -162.52	-101.96 -102.27 -101.65 -100.67 Avr:-101.64 ±0.69
Gd <sub>1.85</sub> U <sub>0.15</sub> Zr <sub>2</sub> O <sub>7.225</sub> (s) (Oxidized) Mol. Wt. = 624.665	5.4 5.0 5.3 4.5	413.81 407.15 405.53 409.07	258.49 254.33 253.32 255.53 Avr:255.42 ±2.24
ZrO <sub>2</sub> (s) Mol. Wt. = 123.224	11.7 13.2	356.60 357.91	43.94 44.10

	9.3 17.1	355.83 354.79	43.85 43.72 Avr: 43.90±0.16
U <sub>3</sub> O <sub>8</sub> Mol. Wt. = 842.09	31.6 26.6 25.2 13.9	87.80 88.13 87.14 88.78	73.94 74.21 73.38 74.76 Avr:74.07 ± 0.57
Gd <sub>2</sub> O <sub>3</sub> Mol. Wt. = 362.50	23.4 21.3 19.7 16.4	-656.30 -657.12 -655.03 -654.74	-237.91 -238.21 -237.45 -237.34 Avr:-237.73±0.41

The frozen products from each measurement were dissolved in distilled water and a clear solution was obtained. These phenomena clearly indicated that the droppings are completely dissolved in the solvent. The standard molar enthalpy of formation of compounds having the nominal composition  $Gd_{2-x}U_xZr_2O_{7+\delta}$  ( $0.0 \leq x \leq 0.15$ ) were derived using thermochemical cycle represented in **Table 6.9**. In order to calculate the standard molar enthalpy of formation for the nominal compositions for  $Gd_{2-x}U_xZr_2O_{7+\delta}$  ( $0.0 \leq x \leq 0.15$ ) at 298K prepared under reducing and oxidizing conditions, the molar enthalpy of dissolution values of the nominal compositions and their binary oxides such as  $Gd_2O_3(s)$ ,  $U_3O_8(s)$  and  $ZrO_2(s)$  were combined with other supplementary data such as standard molar enthalpies of formation of  $Gd_2O_3(s)$ ,  $ZrO_2(s)$  and  $U_3O_8(s)$  from the literature<sup>124,126,135,136</sup>.

It can be clearly observed from the standard molar enthalpy of formation data that the stability of nominal compositions prepared under reducing atmosphere decreases by around 84.9 kJ/mol by addition of 2.5 at %  $U^{4+}$  at  $Gd^{3+}$  site ( $x=0.05$ ) (**Figure 6.16**). However, the stability marginally improves upon addition of further amount of uranium. The decrease in stability could be attributed to the combined effects of increase in repulsive force due to incorporation of excess oxide ions (destabilizing factor) and increase in attractive force due to

**Table 6.9: Thermochemical cycle for enthalpy of formation of  $\text{Gd}_{2-x}\text{U}_x\text{Zr}_2\text{O}_{7+\delta}$  (oxidized/reduced).<sup>178</sup>**

Reaction scheme for the standard molar enthalpy of formation of  $\text{Gd}_{2-x}\text{U}_x\text{Zr}_2\text{O}_{7+\delta}(\text{s})$  (Red/Oxi), (M(sln) = dilute solution of species M in 6 g liquid  $\text{Na}_2\text{O} + \text{MoO}_3$  3:4 molar solvent maintained at 986 K,

$$\Delta_f H^\circ_{298}(\text{Gd}_2\text{Zr}_2\text{O}_7) = -\Delta H_1 + 2\Delta H_2 + \Delta H_4 + \Delta H_5 + 2\Delta H_7$$

$$\Delta_f H^\circ_{298}(\text{Gd}_{1.95}\text{U}_{0.05}\text{Zr}_2\text{O}_{7+\delta}) (\text{Red /Oxi}) = -\Delta H_{1a(\text{red/oxi})} + 2\Delta H_2 + 0.0166\Delta H_3 + 0.975\Delta H_4 + 0.975\Delta H_5 + 0.0166\Delta H_6 + 2\Delta H_7)$$

$$\Delta_f H^\circ_{298}(\text{Gd}_{1.90}\text{U}_{0.10}\text{Zr}_2\text{O}_{7+\delta}) (\text{Red /Oxi}) = -\Delta H_{1b(\text{red/oxi})} + 2\Delta H_2 + 0.0333\Delta H_3 + 0.95\Delta H_4 + 0.95\Delta H_5 + 0.0333\Delta H_6 + 2\Delta H_7)$$

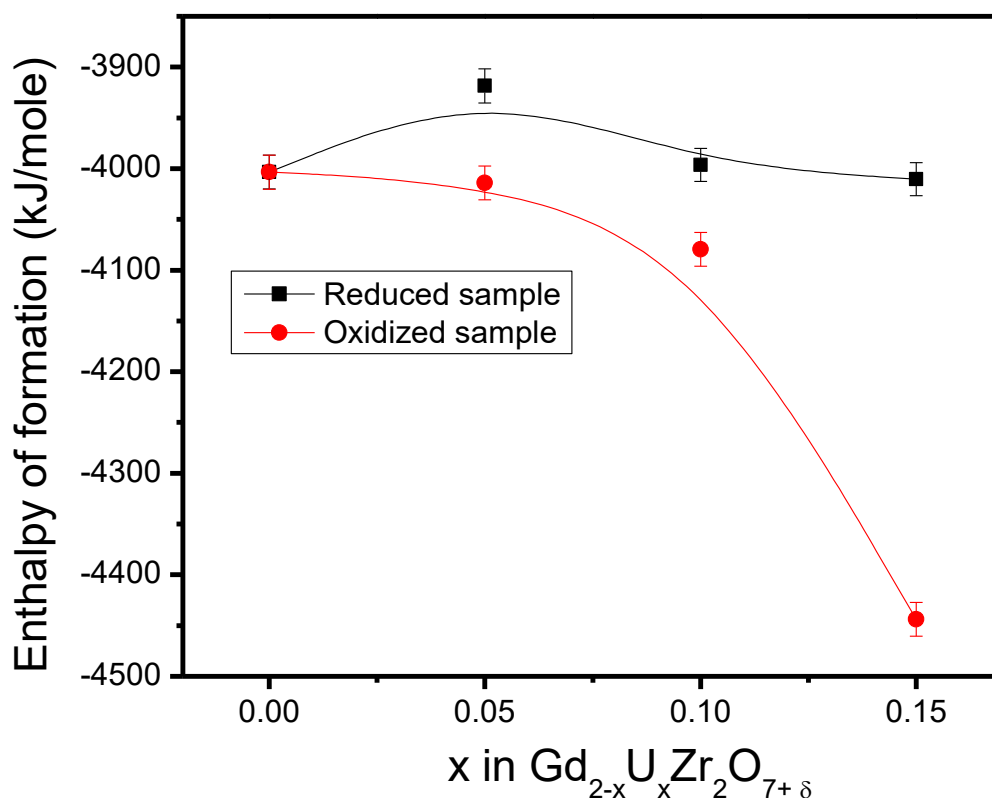
$$\Delta_f H^\circ_{298}(\text{Gd}_{1.85}\text{U}_{0.15}\text{Zr}_2\text{O}_{7+\delta})(\text{Red/Oxi}) = -\Delta H_{1c(\text{red/oxi})} + 2\Delta H_2 + 0.05\Delta H_3 + 0.925\Delta H_4 + 0.925\Delta H_5 + 0.05\Delta H_6 + 2\Delta H_7)$$

Reaction	$\Delta H_i$	$\Delta H_{\text{dissolution}}$ (kJ mol <sup>-1</sup> )
$\text{Gd}_2\text{Zr}_2\text{O}_7(\text{s}, 298\text{K}) + (\text{sln}) = \text{Gd}_2\text{O}_3(\text{sln}) + 2\text{ZrO}_2(\text{sln})$	$\Delta H_1$	-164.04±1.57
Reduced: $\text{Gd}_{1.95}\text{U}_{0.05}\text{Zr}_2\text{O}_{7.025}(\text{s}, 298\text{K}) + (\text{sln}) + 0.0167\text{O}_2(\text{g}) = 0.975\text{Gd}_2\text{O}_3(\text{sln}) + 0.0167\text{U}_3\text{O}_8(\text{sln}) + 2\text{ZrO}_2(\text{sln})$	$\Delta H_{1a(\text{red})}$	-255.73±0.60
$\text{Gd}_{1.90}\text{U}_{0.10}\text{Zr}_2\text{O}_{7.05}(\text{s}, 298\text{K}) + (\text{sln}) + 0.0333\text{O}_2(\text{g}) = 0.95\text{Gd}_2\text{O}_3(\text{sln}) + 0.0333\text{U}_3\text{O}_8(\text{sln}) + 2\text{ZrO}_2(\text{sln})$	$\Delta H_{1b(\text{red})}$	-184.99 ±0.83
$\text{Gd}_{1.85}\text{U}_{0.15}\text{Zr}_2\text{O}_{7.075}(\text{s}, 298\text{K}) + (\text{sln}) + 0.050\text{O}_2(\text{g}) = 0.925\text{Gd}_2\text{O}_3(\text{sln}) + 0.050\text{U}_3\text{O}_8(\text{sln}) + 2\text{ZrO}_2(\text{sln})$	$\Delta H_{1c(\text{red})}$	-177.59 ±1.08
Oxidized: $\text{Gd}_{1.95}\text{U}_{0.05}\text{Zr}_2\text{O}_{7.075}(\text{s}, 298\text{K}) + (\text{sln}) = 0.975\text{Gd}_2\text{O}_3(\text{sln}) + 0.0166\text{U}_3\text{O}_8(\text{sln}) + 2\text{ZrO}_2(\text{sln})$	$\Delta H_{1a(\text{oxi})}$	-160.05±1.38
$\text{Gd}_{1.90}\text{U}_{0.10}\text{Zr}_2\text{O}_{7.15}(\text{s}, 298\text{K}) + (\text{sln}) = 0.975\text{Gd}_2\text{O}_3(\text{sln}) + 0.0333\text{U}_3\text{O}_8(\text{sln}) + 2\text{ZrO}_2(\text{sln})$	$\Delta H_{1b(\text{oxi})}$	-101.64 ±0.69
$\text{Gd}_{1.85}\text{U}_{0.15}\text{Zr}_2\text{O}_{7.225}(\text{s}, 298\text{K}) + (\text{sln}) = 0.975\text{Gd}_2\text{O}_3(\text{sln}) + 0.050\text{U}_3\text{O}_8(\text{sln}) + 2\text{ZrO}_2(\text{sln})$	$\Delta H_{1c(\text{oxi})}$	255.42 ±2.24

$\text{ZrO}_2(\text{s}, 298\text{K}) + (\text{sln}) = \text{ZrO}_2(\text{sln})$	$\Delta H_2$	43.90±0.16
$\text{U}_3\text{O}_8(\text{s}, 298\text{K}) + (\text{sln}) = \text{U}_3\text{O}_8(\text{sln})$	$\Delta H_3$	74.07± 0.57
$\text{Gd}_2\text{O}_3(\text{s}, 298\text{K}) + (\text{sln}) = \text{Gd}_2\text{O}_3(\text{s})$	$\Delta H_4$	-237.73±0.41
$2\text{Gd}(\text{s}, 298\text{K}) + 3/2\text{O}_2(\text{g}) = \text{Gd}_2\text{O}_3(\text{s})$	$\Delta H_5$	-1815.86 ± 16.74
$3\text{U}(\text{s}, 298\text{K}) + 4\text{O}_2(\text{g}) = \text{U}_3\text{O}_8(\text{s})$	$\Delta H_6$	-3573.55± 3.68
$\text{Zr}(\text{s}, 298\text{K}) + \text{O}_2(\text{g}) = \text{ZrO}_2(\text{s})$	$\Delta H_7$	-1100.81±2.09
$2\text{Gd}(\text{s}, 298\text{K}) + 2\text{Zr}(\text{s}, 298\text{K}) + 3.5 \text{O}_2(\text{g}) = \text{Gd}_2\text{Zr}_2\text{O}_7 (\text{s}, 298\text{K})$ <u>Reduced:</u> $1.95\text{Gd}(\text{s}, 298\text{K}) + 0.05\text{U}(\text{s}, 298\text{K}) + 2\text{Zr}(\text{s}, 298\text{K}) + 3.5125 \text{O}_2(\text{g}) = \text{Gd}_{1.95}\text{U}_{0.05}\text{Zr}_2\text{O}_{7.025} (\text{s}, 298\text{K})$ $1.90\text{Gd}(\text{s}, 298\text{K}) + 0.10\text{U}(\text{s}, 298\text{K}) + 2\text{Zr}(\text{s}, 298\text{K}) + 3.525 \text{O}_2(\text{g}) = \text{Gd}_{1.9}\text{U}_{0.1}\text{Zr}_2\text{O}_{7.05} (\text{s}, 298\text{K})$ $1.85\text{Gd}(\text{s}, 298\text{K}) + 0.15 \text{U}(\text{s}, 298\text{K}) + 2\text{Zr}(\text{s}, 298\text{K}) + 3.588 \text{O}_2(\text{g}) = \text{Gd}_{1.85}\text{U}_{0.15}\text{Zr}_2\text{O}_{7.175} (\text{s}, 298\text{K})$ <u>Oxidised:</u> $1.95\text{Gd}(\text{s}, 298\text{K}) + 0.05\text{U}(\text{s}, 298\text{K}) + 2\text{Zr}(\text{s}, 298\text{K}) + 3.5124 \text{O}_2(\text{g}) = \text{Gd}_{1.95}\text{U}_{0.05}\text{Zr}_2\text{O}_{7.075} (\text{s}, 298\text{K})$ $1.90\text{Gd}(\text{s}, 298\text{K}) + 0.01\text{U}(\text{s}, 298\text{K}) + 2\text{Zr}(\text{s}, 298\text{K}) + 3.575 \text{O}_2(\text{g}) = \text{Gd}_{1.9}\text{U}_{0.1}\text{Zr}_2\text{O}_{7.15} (\text{s}, 298\text{K})$ $1.85\text{Gd}(\text{s}, 298\text{K}) + 0.15\text{U}(\text{s}, 298\text{K}) + 2\text{Zr}(\text{s}, 298\text{K}) + 3.663 \text{O}_2(\text{g}) = \text{Gd}_{1.85}\text{U}_{0.15}\text{Zr}_2\text{O}_{7.325} (\text{s}, 298\text{K})$	$\Delta_f H^\bullet_{298},$  $\Delta_f H^\bullet_{298, \text{Reduced}}$  $\Delta_f H^\bullet_{298},$ <b>Oxidized</b>	-4003.37±17.08  -3918.78± 16.60 -3996.27± 16.20 -4010.77± 15.81  -4014.11± 16.65 -4079.62± 16.20 -4443.78±15.93

higher positive charge of the doped  $U^{4+}$  in place of  $Gd^{3+}$  ion (stabilizing factor). The destabilizing force is found to be the major contributor for composition  $x=0.05$  whereas the stabilizing factor predominated for nominal compositions  $x=0.10$  and  $0.15$ .

However, the stability is found to steadily increase with increasing  $U^{6+}$  content up to  $x=0.15$  for samples prepared under ambient conditions. This increase in the enthalpy of formation of the nominal compositions with increasing  $U^{6+}$  content can be attributed to the higher columbic attraction between  $U^{6+}$  and  $O^{2-}$  ions which overrides the repulsion of excess oxide ion. Moreover, the existence of  $U^{6+}$  ion inside the lattice leads to contraction in unit cell parameter which consequently increases the lattice packing density which can be considered



**Figure 6.16: The enthalpy of formation of  $Gd_{2-x}U_xZr_2O_{7+\delta}$  (both oxidized and reduced samples).**<sup>178</sup>

as another probable reason for higher stability of  $U^{6+}$  substituted nominal compositions. Nevertheless, the incorporation of  $U^{6+}$  can also potentially increase the disorder in lattice which in turn increases the thermodynamic stability. However, it can be summarized that



thermodynamic stability of  $x=0.15$  sample (oxidized) is found to be around 440.16 kJ/mol higher than that of parent compound, which is an extraordinary observation from nuclear waste application point of view.

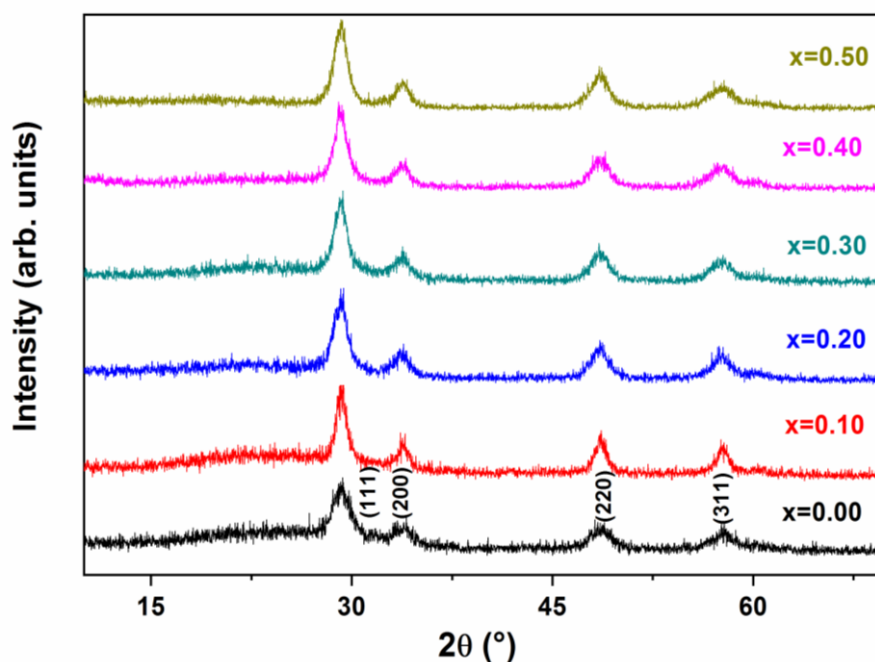
## **PART C: Structural and thermodynamic studies on uranium and cerium co-incorporated $Gd_2Zr_2O_7$**

### **(i) Powder XRD Studies**

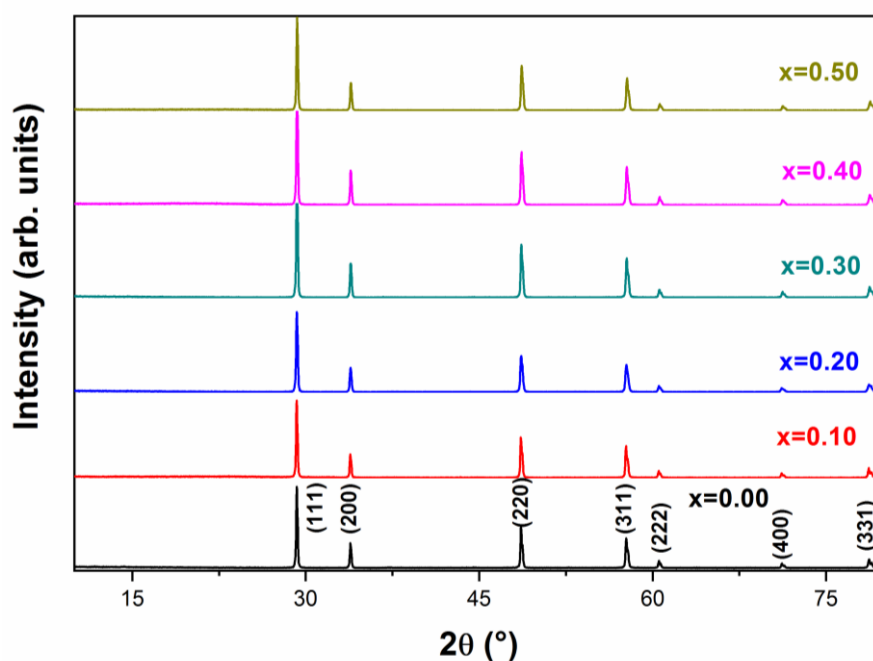
Phase formation of the nominal compositions  $Gd_{2-x}Ce_xZr_{1.9}U_{0.1}O_{7+\delta}$  ( $0.0 \leq x \leq 0.50$ ) was determined by characterization of the as prepared samples by powder XRD technique. Powder X-ray diffraction patterns of the products calcined at 873 K for 1 h shown in **Figure 6.17** indicate broad peaks due to the nano-crystalline nature of the prepared samples. XRD patterns for all the six compositions exhibited similar fingerprint as that of the defect fluorite structure of  $Gd_2Zr_2O_7$ . Since no impurity peaks of any reactants were observed, the general composition represented as  $Gd_{2-x}Ce_xZr_{1.9}U_{0.1}O_{7+\delta}$ . Further structural characterization of the phases could not be carried out due to broad nature of the peaks.

Studies carried out in part B of this chapter clearly emphasized that heating uranium based compositions in air medium yields higher stability as compared to heating in Ar : H<sub>2</sub> (92:8) atmosphere. Hence, the calcined nominal compositions  $Gd_{2-x}Ce_xZr_{1.9}U_{0.1}O_{7+\delta}$  ( $0.0 \leq x \leq 0.50$ ) were then annealed in air at 1373 K for 8 h only. All the compositions in this studied range were found to crystallize in defect-fluorite form as evident in earlier works in this chapter. Powder X-ray diffraction patterns of all the nominal compositions are depicted in **Figure 6.18**.

Fullprof-2000 software was used for Rietveld refinement of the XRD data in a bid to carry out structural analysis<sup>103</sup>. Sixth order polynomial function was used for background refinement of the collected powder diffraction data followed by adjustment of scale factor. Diffraction peaks were fitted using Pseudo-Voigt profile function. Peak profile fit was carried



**Figure 6.17:** Powder XRD patterns of  $\text{Gd}_{2-x}\text{Ce}_x\text{Zr}_{1.9}\text{U}_{0.1}\text{O}_{7+\delta}$  ( $0.0 \leq x \leq 0.50$ ) samples calcined at 873 K for 1 h (PCPDF-80-0471).



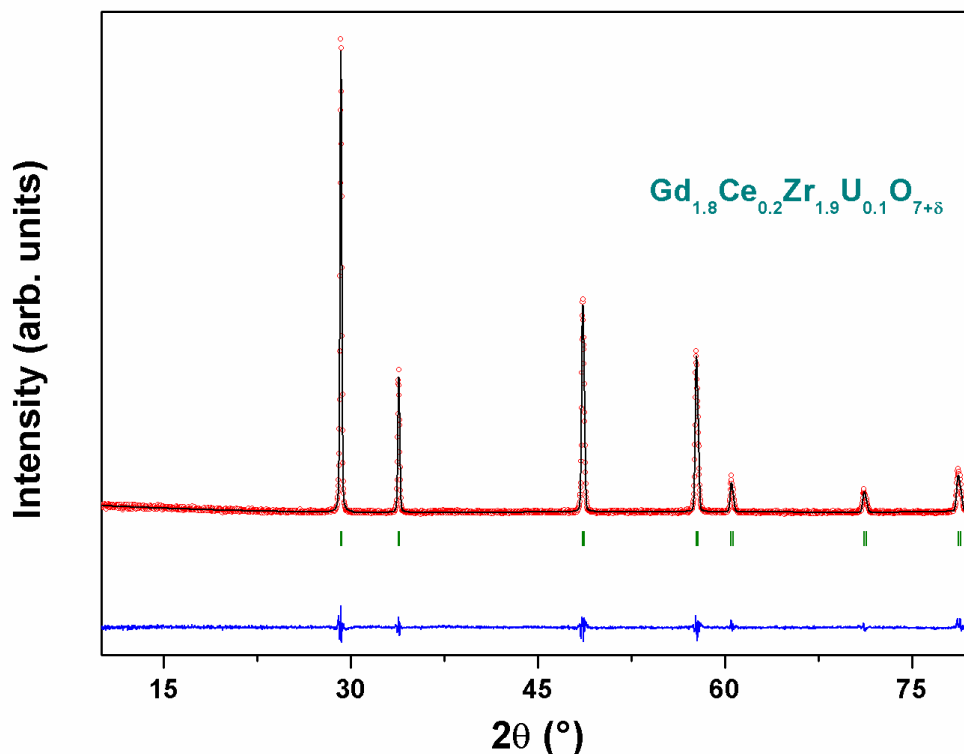
**Figure 6.18:** Powder XRD patterns of  $\text{Gd}_{2-x}\text{Ce}_x\text{Zr}_{1.9}\text{U}_{0.1}\text{O}_{7+\delta}$  ( $0.0 \leq x \leq 0.50$ ) samples annealed at 1373 K for 8 h in air (PCPDF-80-0471).

out by refinement of the U, V, W parameters. Absorption factor and displacement factor was not considered during the entire refinement cycle. A typical Rietveld refinement plot is

**Table 6.10: Rietveld refined parameters of  $\text{Gd}_{2-x}\text{Ce}_x\text{Zr}_{1.9}\text{U}_{0.1}\text{O}_{7+\delta}$  ( $0.0 \leq x \leq 0.50$ ) compositions after annealing at 1373 K for 8h in air.**

Sample	$\text{Gd}_2\text{Zr}_{1.9}\text{U}_{0.1}\text{O}_{7.10}$	$\text{Gd}_{1.9}\text{Ce}_{0.1}\text{Zr}_{1.9}\text{U}_{0.1}\text{O}_{7.15}$	$\text{Gd}_{1.8}\text{Ce}_{0.2}\text{Zr}_{1.9}\text{U}_{0.1}\text{O}_{7.20}$	$\text{Gd}_{1.7}\text{Ce}_{0.3}\text{Zr}_{1.9}\text{U}_{0.1}\text{O}_{7.25}$	$\text{Gd}_{1.6}\text{Ce}_{0.4}\text{Zr}_{1.9}\text{U}_{0.1}\text{O}_{7.30}$	$\text{Gd}_{1.5}\text{Ce}_{0.5}\text{Zr}_{1.9}\text{U}_{0.1}\text{O}_{7.35}$
a (Å)	5.2661(2)	5.2672(2)	5.2654(2)	5.2629(1)	5.2623(2)	5.2609(2)
U	0.005(2)	0.041(2)	0.129(4)	0.068(2)	0.054(3)	0.074(2)
V	-0.012(2)	-0.009(2)	-0.032(3)	-0.024(2)	-0.014(3)	-0.021(2)
W	0.008(5)	0.011(4)	0.019(6)	0.017(4)	0.008(5)	0.015(4)
$\chi^2$	2.36	1.75	1.47	1.46	1.78	1.53
R <sub>p</sub> %	7.63	11.7	11.1	10.3	10.4	9.96
R <sub>wp</sub> %	12.7	17.3	17.0	15.5	15.8	14.7
R <sub>exp</sub> %	8.28	13.07	13.98	12.8	11.8	11.9
Space group	Fm $\bar{3}$ m	Fm $\bar{3}$ m	Fm $\bar{3}$ m	Fm $\bar{3}$ m	Fm $\bar{3}$ m	Fm $\bar{3}$ m

depicted in **Figure 6.19** and the calculated refined unit cell parameters are tabulated in **Table 6.10**.

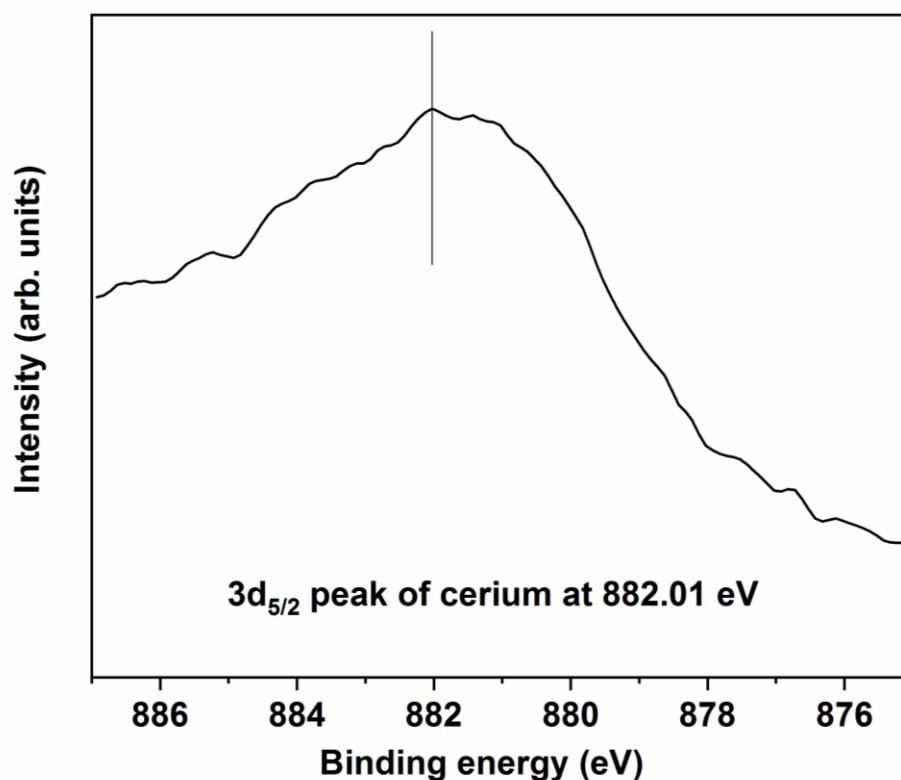


**Figure 6.19:** Powder XRD patterns of  $\text{Gd}_{1.8}\text{Ce}_{0.2}\text{Zr}_{1.9}\text{U}_{0.1}\text{O}_{7+\delta}$  ( $x=0.20$ ) samples annealed at 1373 K for 8 h in air.

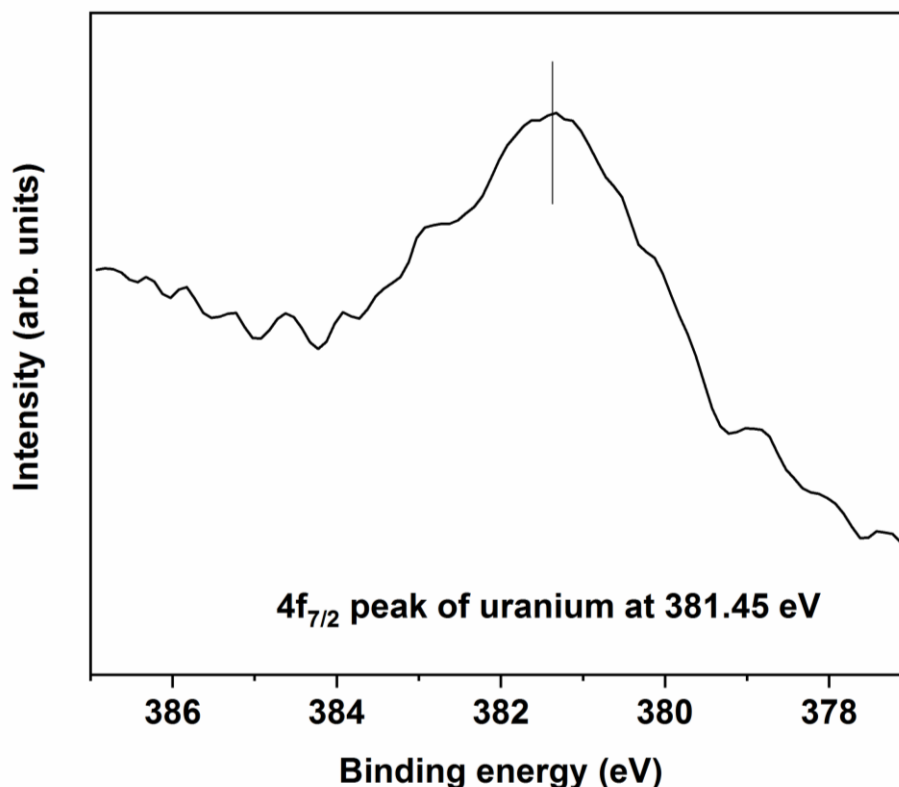
Unit cell parameters of all the nominal compositions in the series  $\text{Gd}_{2-x}\text{Ce}_x\text{Zr}_{1.9}\text{U}_{0.1}\text{O}_{7+\delta}$  were found to remain almost constant. This phenomenon can be explained by two antagonistic factors viz. (i) decrease in cell parameter with increasing cerium incorporation due to lower ionic radii of cerium as compared to gadolinium<sup>150</sup> and (ii) increase in cell parameter due to incorporation of extra oxygen in lattice with increasing cerium ( $\text{Ce}^{4+}$ ) content to maintain charge neutrality. It can therefore be concluded that both the factors almost balance each other as there is not any significant variation in unit cell parameters of the different compositions. Higher loading of cerium resulted in precipitation of minor secondary phases which could not be characterized properly due to their very low intensity.

(ii) **XPS studies**

Elucidation of oxidation state of both cerium and uranium was found to be compulsory to confirm results obtained from powder X-ray diffraction studies. XPS spectra for cerium and uranium in one representative composition  $\text{Gd}_{1.8}\text{Ce}_{0.2}\text{Zr}_{1.9}\text{U}_{0.1}\text{O}_{7+\delta}$  are shown in **Figures 6.20** and **6.21**, respectively. Cerium in +3 and +4 oxidation state is characterized by  $3d_{5/2}$  XPS peak at  $\sim 880$  eV and 882 eV, respectively<sup>217</sup>. For the nominal composition  $\text{Gd}_{1.8}\text{Ce}_{0.2}\text{Zr}_{1.9}\text{U}_{0.1}\text{O}_{7+\delta}$ , the peak maximum is observed at 882.01 eV which confirms the presence of cerium in the lattice as  $\text{Ce}^{4+}$ . Similarly, the peak maxima corresponding to uranium is observed at 381.45 eV which confirms its presence as  $\text{U}^{6+}$  inside the lattice<sup>214,215</sup>.



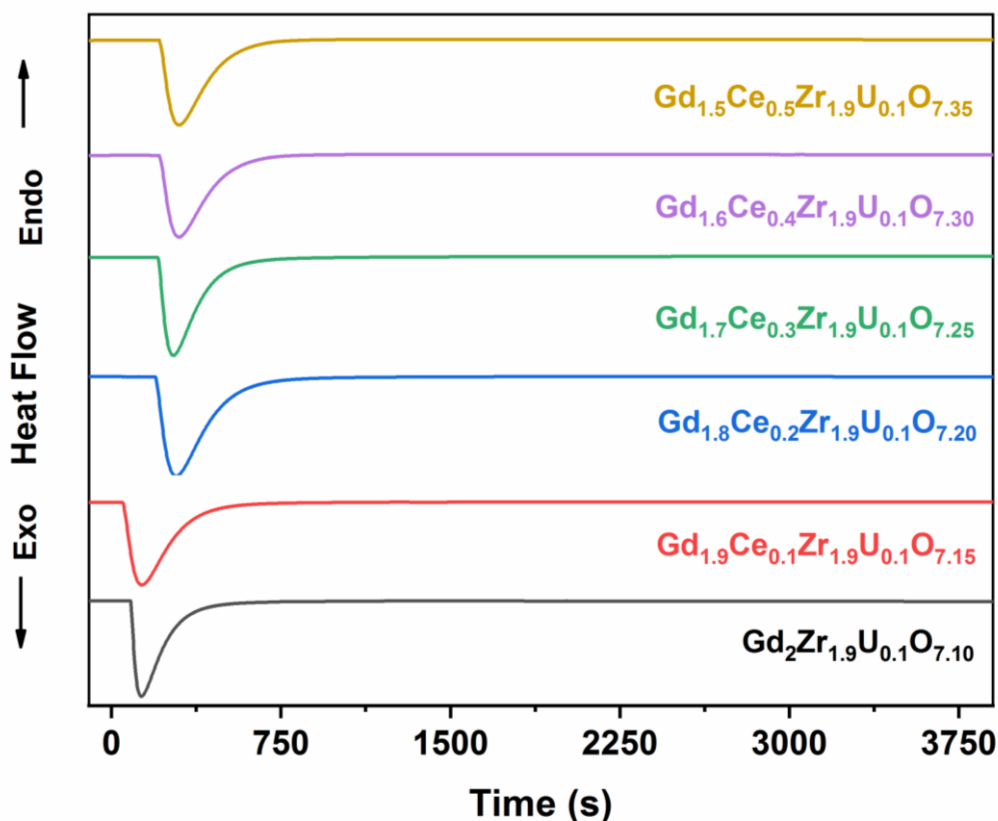
**Figure 6.20:** X-ray photoelectron spectra of cerium ( $3d_{5/2}$ ) of sample having nominal composition  $\text{Gd}_{1.8}\text{Ce}_{0.2}\text{Zr}_{1.9}\text{U}_{0.1}\text{O}_{7+\delta}$ .



**Figure 6.21: X-ray photoelectron spectra of uranium ( $4f_{7/2}$ ) of sample having nominal composition  $\text{Gd}_{1.8}\text{Ce}_{0.2}\text{Zr}_{1.9}\text{U}_{0.1}\text{O}_{7+\delta}$ .**

(iii) **Calorimetric studies**

Standard molar enthalpy of formation values of all the nominal compositions were derived from the values of enthalpy of dissolution of  $\text{Gd}_{2-x}\text{Ce}_x\text{Zr}_{1.9}\text{U}_{0.1}\text{O}_{7+\delta}$  ( $0.0 \leq x \leq 0.5$ ) samples and their binary reactant oxides such as  $\text{Gd}_2\text{O}_3(\text{s})$ ,  $\text{CeO}_2(\text{s})$ ,  $\text{U}_3\text{O}_8(\text{s})$  and  $\text{ZrO}_2(\text{s})$  in liquid  $\text{Na}_2\text{O} + \text{MoO}_3$  (3:4 molar ratio) solvent maintained at 986 K. Heat flow signals for dissolution of all the nominal compositions normalized to 10 mg each in liquid  $\text{Na}_2\text{O} + \text{MoO}_3$  (3:4 molar ratio) and dropped at liquid solvent maintained at 986 K from room temperature are shown in **Figure 6.22**.



**Figure 6.22:** Normalized heat flow signals for dissolution of  $\text{Gd}_{2-x}\text{Ce}_x\text{Zr}_{1.9}\text{U}_{0.1}\text{O}_{7+\delta}$  ( $0.0 \leq x \leq 0.5$ ) nominal compositions (normalized to 10 mg each) in liquid  $\text{Na}_2\text{O} + \text{MoO}_3$  (3:4 molar ratio) dropped from room temperature to liquid solvent 986 K.

An endothermic heat flow signal was witnessed for droppings of all the nominal compositions. Recording of a steady base line in the heat flow signal is the signal of reaction completion. As steady base line is observed after around 3600 s, measurement time of 1 h was selected for each of the droppings. Heat flow has been calculated using SETSOFT software supplied with the instrument by considering the sum of all endothermic and exothermic effects. The enthalpy of dissolution values of all the nominal compositions and their binary constituent oxides are given in **Table 6.11**. The observed enthalpy change is the sum of the effects of enthalpy increment from 298 to 986 K and other effects due to chemical reaction between solute and solvent.

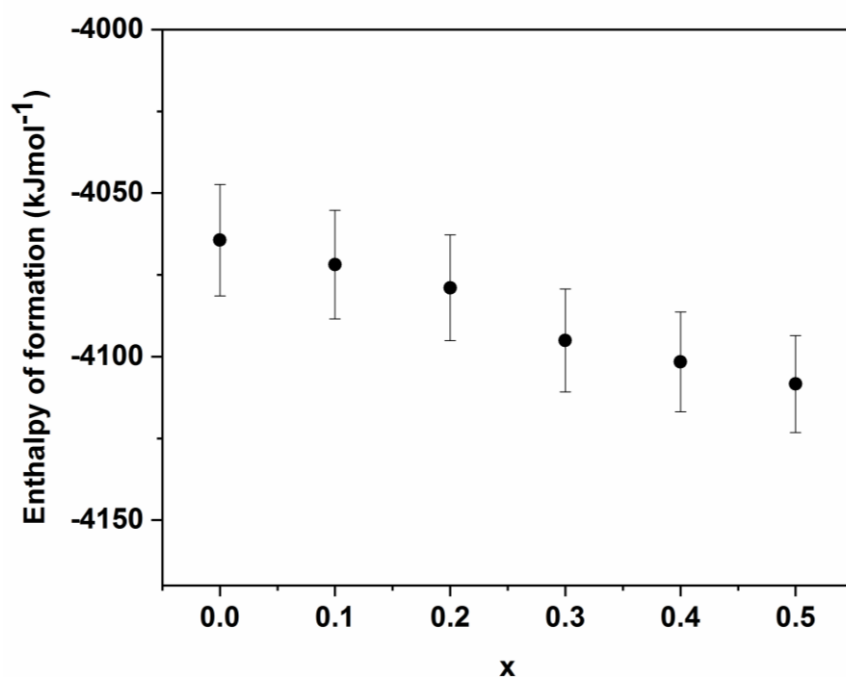
**Table 6.11:** Heat of dissolution of  $\text{Gd}_{2-x}\text{Ce}_x\text{Zr}_{1.9}\text{U}_{0.1}\text{O}_{7+\delta}$  ( $0.0 \leq x \leq 0.5$ ) and their component oxides.

Compound	Mass m (mg)	$\Delta H$ (J/g)	$\Delta H_T$ (kJ mol <sup>-1</sup> )
Gd <sub>2</sub> Zr <sub>1.9</sub> U <sub>0.1</sub> O <sub>7.10</sub> Mol. Wt. = 625.224	14.5	-185.18	-115.78
	10.0	-183.76	-114.89
	10.8	-184.76	-115.52
	21.5	-185.01	-115.67
			Avg.: -115.46 ± 0.40
Gd <sub>1.9</sub> Ce <sub>0.1</sub> Zr <sub>1.9</sub> U <sub>0.1</sub> O <sub>7.15</sub> Mol. Wt. = 624.311	15.3	-175.99	-109.87
	21.5	-175.50	-109.57
	27.0	-176.58	-110.24
	8.7	-175.26	-109.42
			Avg.: -109.78 ± 0.36
Gd <sub>1.8</sub> Ce <sub>0.2</sub> Zr <sub>1.9</sub> U <sub>0.1</sub> O <sub>7.20</sub> Mol. Wt. = 623.397	5.3	-168.77	-105.21
	13.9	-167.00	-104.11
	9.1	-167.34	-104.32
	13.3	-167.23	-104.25
			Avg.: -104.47 ± 0.50
Gd <sub>1.7</sub> Ce <sub>0.3</sub> Zr <sub>1.9</sub> U <sub>0.1</sub> O <sub>7.25</sub> Mol. Wt. = 622.484	23.4	-145.88	-90.80
	21.3	-144.55	-89.98
	19.7	-144.60	-90.01
	16.4	-144.34	-89.85
			Avg.: -90.16 ± 0.43
Gd <sub>1.6</sub> Ce <sub>0.4</sub> Zr <sub>1.9</sub> U <sub>0.1</sub> O <sub>7.30</sub> Mol. Wt. = 621.571	31.6	-137.62	-85.54
	26.6	-136.73	-84.99
	25.2	-136.62	-85.54
	13.9	-138.83	-85.67
			Avg.: -85.44 ± 0.31
Gd <sub>1.5</sub> Ce <sub>0.5</sub> Zr <sub>1.9</sub> U <sub>0.1</sub> O <sub>7.35</sub> Mol. Wt. = 620.658	23.6	-129.30	-80.25
	19.7	-130.10	-80.75
	21.3	-129.60	-80.44
	17.9	-129.46	-80.35
			Avg.: -80.45 ± 0.22
Gd <sub>2</sub> O <sub>3</sub> Mol. Wt. = 362.50	15.9	-655.64	-237.67
	24.7	-656.03	-237.81
	19.6	-659.33	-239.01
	13.7	-657.79	-238.45
			Avg.: -238.24 ± 0.52
CeO <sub>2</sub> Mol. Wt. = 172.12	22.6	263.25	45.31
	13.9	263.89	45.42
	41.3	262.72	45.22
	33.8	264.64	45.55
			Avg.: 45.38 ± 0.14
ZrO <sub>2</sub> Mol. Wt. = 123.22	15.9	350.51	43.19
	25.9	354.73	43.71
	36.1	359.11	44.25
	19.1	348.81	42.98
			Avg.: 43.53 ± 0.57
U <sub>3</sub> O <sub>8</sub> Mol. Wt. = 366.03	25.7	87.31	31.96
	19.6	87.81	32.14
	14.3	87.59	32.06
	25.1	88.11	32.25
			Avg.: 32.10 ± 0.12



Standard molar enthalpy of formation of nominal compositions  $\text{Gd}_{2-x}\text{Ce}_x\text{Zr}_{1.9}\text{U}_{0.1}\text{O}_{7+\delta}$  ( $0.0 \leq x \leq 0.5$ ) are derived from thermochemical cycle and they are presented in **Table 6.12**. Molar enthalpy of dissolution values of nominal composition and their constituent binary oxides were combined with other supplementary data viz. standard molar enthalpies of formation of  $\text{Gd}_2\text{O}_3(\text{s})$ ,  $\text{CeO}_2(\text{s})$ ,  $\text{ZrO}_2(\text{s})$  and  $\text{U}_3\text{O}_8(\text{s})$  from literature<sup>135</sup> to derive the standard molar enthalpy of formation of the nominal compositions.

The enthalpy of formation value is found to increase steadily with increasing cerium content. Increasing content of cerium in the lattice results in two antagonistic phenomena: (a) increasing  $\text{Ce}^{4+}$  in lattice results in increasing attractive force due to higher charge of Ce as compared to Gd, and (b) increase in repulsive force due to incorporation of extra oxygen ions.



**Figure 6.23: Variation of standard molar enthalpy of formation of  $\text{Gd}_{2-x}\text{Ce}_x\text{Zr}_{1.9}\text{U}_{0.1}\text{O}_{7+\delta}$  ( $0.0 \leq x \leq 0.5$ ).**

The observed results can be attributed to increased coulombic attraction between  $\text{Ce}^{4+}$  and  $\text{O}^{2-}$  ions which predominates over the repulsive force among  $\text{O}^{2-}$  ions. In addition to this, incorporation of  $\text{Ce}^{4+}$  also has the potential to increase lattice disorder which in turn increases

**Table 6.12: Thermochemical cycles for enthalpy of formation of  $\text{Gd}_{2-x}\text{Ce}_x\text{Zr}_{1.9}\text{U}_{0.1}\text{O}_{7+\delta}$  ( $0.0 \leq x \leq 0.5$ ).**

$$(\Delta_f H^\circ_{298} \text{Gd}_{2-x}\text{Ce}_x\text{Zr}_{1.9}\text{U}_{0.1}\text{O}_{7+\delta} (\text{s}) = -\Delta H_{1i} + (1-0.5x) \Delta H_2 + x\Delta H_3 + 1.9\Delta H_4 + 0.033\Delta H_5 + (1-0.5x) \Delta H_6 + x\Delta H_7 + 1.9 \Delta H_8 + 0.033\Delta H_9)$$

Reaction	$\Delta H_i$	$\Delta H_{\text{dissolution}} (\text{kJ mol}^{-1})$
$\text{Gd}_2\text{Zr}_{1.9} \text{U}_{0.1}\text{O}_{7.10} (\text{s}, 298\text{K}) + (\text{sln}) = 1.00\text{Gd}_2\text{O}_3(\text{sln}) + 1.9\text{ZrO}_2(\text{sln}) + 0.033\text{U}_3\text{O}_8(\text{sln})$	$\Delta H_{1a}$	$-115.46 \pm 0.40$
$\text{Gd}_{1.9} \text{Ce}_{0.1}\text{Zr}_{1.9} \text{U}_{0.1}\text{O}_{7.15} (\text{s}, 298\text{K}) + (\text{sln}) = 0.95\text{Gd}_2\text{O}_3(\text{sln}) + 0.1\text{CeO}_2(\text{sln}) + 1.9\text{ZrO}_2(\text{sln}) + 0.033\text{U}_3\text{O}_8(\text{sln})$	$\Delta H_{1b}$	$-109.78 \pm 0.36$
$\text{Gd}_{1.8}\text{Ce}_{0.2}\text{Zr}_{1.9} \text{U}_{0.1}\text{O}_{7.20} (\text{s}, 298\text{K}) + (\text{sln}) = 0.90\text{Gd}_2\text{O}_3(\text{sln}) + 0.2\text{CeO}_2(\text{sln}) + 1.9\text{ZrO}_2(\text{sln}) + 0.033\text{U}_3\text{O}_8(\text{sln})$	$\Delta H_{1c}$	$-104.47 \pm 0.50$
$\text{Gd}_{1.7}\text{Ce}_{0.3}\text{Zr}_{1.9} \text{U}_{0.1}\text{O}_{7.25} (\text{s}, 298\text{K}) + (\text{sln}) = 0.85\text{Gd}_2\text{O}_3(\text{sln}) + 0.3\text{CeO}_2(\text{sln}) + 1.9\text{ZrO}_2(\text{sln}) + 0.033\text{U}_3\text{O}_8(\text{sln})$	$\Delta H_{1d}$	$-90.16 \pm 0.43$
$\text{Gd}_{1.6}\text{Ce}_{0.4}\text{Zr}_{1.9} \text{U}_{0.1}\text{O}_{7.30} (\text{s}, 298\text{K}) + (\text{sln}) = 0.80\text{Gd}_2\text{O}_3(\text{sln}) + 0.4\text{CeO}_2(\text{sln}) + 1.9\text{ZrO}_2(\text{sln}) + 0.033\text{U}_3\text{O}_8(\text{sln})$	$\Delta H_{1e}$	$-85.44 \pm 0.31$
$\text{Gd}_{1.5}\text{Ce}_{0.5}\text{Zr}_{1.9} \text{U}_{0.1}\text{O}_{7.35} (\text{s}, 298\text{K}) + (\text{sln}) = 0.75\text{Gd}_2\text{O}_3(\text{sln}) + 0.5\text{CeO}_2(\text{sln}) + 1.9\text{ZrO}_2(\text{sln}) + 0.033\text{U}_3\text{O}_8(\text{sln})$	$\Delta H_{1f}$	$-80.45 \pm 0.22$
$\text{Gd}_2\text{O}_3(\text{s}, 298\text{K}) + (\text{sln}) = \text{Gd}_2\text{O}_3(\text{sln})$	$\Delta H_2$	$-238.24 \pm 0.52$
$\text{CeO}_2(\text{s}, 298\text{K}) + (\text{sln}) = \text{CeO}_2(\text{sln})$	$\Delta H_3$	$45.38 \pm 0.14$
$\text{ZrO}_2(\text{s}, 298\text{K}) + (\text{sln}) = \text{ZrO}_2(\text{sln})$	$\Delta H_4$	$43.53 \pm 0.57$
$\text{U}_3\text{O}_8(\text{s}, 298\text{K}) + (\text{sln}) = \text{U}_3\text{O}_8(\text{sln})$	$\Delta H_5$	$32.10 \pm 0.12$
$2\text{Gd}(\text{s}, 298\text{K}) + 3/2\text{O}_2(\text{g}) = \text{Gd}_2\text{O}_3(\text{s})$	$\Delta H_6$	$-1815.86 \pm 16.74$
$2\text{Ce}(\text{s}, 298\text{K}) + 2\text{O}_2(\text{g}) = 2\text{CeO}_2(\text{s})$	$\Delta H_7$	$-1090.40 \pm 0.13$
$\text{Zr}(\text{s}, 298\text{K}) + \text{O}_2(\text{g}) = \text{ZrO}_2(\text{s})$	$\Delta H_8$	$-1100.81 \pm 2.09$
$3\text{U}(\text{s}, 298\text{K}) + 4\text{O}_2(\text{g}) = \text{U}_3\text{O}_8(\text{s})$	$\Delta H_9$	$-3574.78 \pm 0.54$
$2.00\text{Gd}(\text{s}, 298\text{K}) + 1.90\text{Zr}(\text{s}, 298\text{K}) + 0.10\text{U}(\text{s}, 298\text{K}) + 3.55\text{O}_2(\text{g}) = \text{Gd}_2\text{Zr}_{1.9} \text{U}_{0.1}\text{O}_{7.10} (\text{s}, 298\text{K}) (x=0.0)$	$\Delta_f H^\circ_{298}$	$-4064.38 \pm 17.02$

$1.90\text{Gd(s,298K)} + 0.10\text{Ce(s,298K)} + 1.90\text{Zr(s,298K)} + 0.10\text{U(s,298K)} + 3.575\text{O}_2(\text{g}) = \text{Gd}_{1.9}\text{Ce}_{0.1}\text{Zr}_{1.9}\text{U}_{0.1}\text{O}_{7.15}(\text{s,298K}) \quad (\text{x}=0.1)$		$-4071.86 \pm 16.60$
$1.80\text{Gd(s,298K)} + 0.20\text{Ce(s,298K)} + 1.90\text{Zr(s,298K)} + 0.10\text{U(s,298K)} + 3.600\text{O}_2(\text{g}) = \text{Gd}_{1.8}\text{Ce}_{0.2}\text{Zr}_{1.9}\text{U}_{0.1}\text{O}_{7.20}(\text{s,298K}) \quad (\text{x}=0.2)$		$-4078.96 \pm 16.17$
$1.70\text{Gd(s,298K)} + 0.30\text{Ce(s,298K)} + 1.90\text{Zr(s,298K)} + 0.10\text{U(s,298K)} + 3.625\text{O}_2(\text{g}) = \text{Gd}_{1.7}\text{Ce}_{0.3}\text{Zr}_{1.9}\text{U}_{0.1}\text{O}_{7.25}(\text{s,298K}) \quad (\text{x}=0.3)$		$-4095.07 \pm 15.73$
$1.60\text{Gd(s,298K)} + 0.40\text{Ce(s,298K)} + 1.90\text{Zr(s,298K)} + 0.10\text{U(s,298K)} + 3.650\text{O}_2(\text{g}) = \text{Gd}_{1.6}\text{Ce}_{0.4}\text{Zr}_{1.9}\text{U}_{0.1}\text{O}_{7.30}(\text{s,298K}) \quad (\text{x}=0.4)$		$-4101.59 \pm 15.28$
$1.50\text{Gd(s,298K)} + 0.50\text{Ce(s,298K)} + 1.90\text{Zr(s,298K)} + 0.10\text{U(s,298K)} + 3.675\text{O}_2(\text{g}) = \text{Gd}_{1.5}\text{Ce}_{0.5}\text{Zr}_{1.9}\text{U}_{0.1}\text{O}_{7.35}(\text{s,298K}) \quad (\text{x}=0.5)$		$-4108.38 \pm 14.81$

the thermodynamic stability of the nominal compositions. The variation of standard molar enthalpy of formation of  $\text{Gd}_{2-x}\text{Ce}_x\text{Zr}_{1.9}\text{U}_{0.1}\text{O}_{7+\delta}$  ( $0.0 \leq x \leq 0.5$ ) is shown in **Figure 6.23**.

## 6.4. CONCLUSIONS

Structural and thermodynamic studies on pristine  $\text{Gd}_2\text{Zr}_2\text{O}_7$  revealed that phase formation and annealing temperature plays an important role as far as evolution of new phases are concerned. Formation and annihilation of defects upon ordering has been reflected in the gradual transformation from fluorite to pyrochlore phase. This work demonstrates that annealing temperature and duration is an important parameter which needs to be considered for processing of ceramic matrices intended for immobilization of nuclear HLW. It was also observed that incorporation of uranium in +6 state is always better compared to that in +4 state in terms of thermodynamic stability. It also further stated that co-incorporation of uranium and cerium under ambient conditions resulted in increased stability of the ceramic phase which is an important parameter for design of  $\text{Gd}_2\text{Zr}_2\text{O}_7$  base ceramic matrices.

# **Chapter 7**

## **Miscellaneous activities**

### **pertaining to**

## **nuclear waste immobilization**

Photoluminescence studies presented in this chapter have been carried out in collaboration.

## 7.1. INTRODUCTION

Immobilization of nuclear high level waste (HLW) is one of the most important steps in “closed nuclear fuel cycle” module which is practiced in India. Lot of experience gathered from investigations taking place worldwide concluded borosilicate glass matrices as the most promising host matrix for immobilization of HLW<sup>4,48,218–221</sup>. Sodium borosilicate (NBS) glass was identified as the most promising material as host matrices for HLW in the Indian nuclear energy scenario<sup>32</sup>. However, waste containing sulphate ions is a problem in vitrification in NBS<sup>48,222,223</sup>. Isolated sulphate domains termed as “yellow phase” appear in vitrified glass. This yellow phase consisted of water-soluble thenardite ( $\text{Na}_2\text{SO}_4$ ) phase and is found to be randomly distributed in the glass network. This yellow phase has an affinity for radioactive  $^{137}\text{Cs}$ , and the accidental breakage of stainless steel container during natural calamities such as earthquake, etc. may lead to its release to groundwater. Moreover, during plant scale production of NBS, yellow phase being lighter has a tendency to accumulate on the top of glass melt surface and that prevent the release of inactive gases and hence promote the corrosion of the electrodes<sup>224–228</sup>. Thus reformulation of glassy waste matrix became a necessity for vitrification of HLW. Significant research directed towards this problem led to the development of barium borosilicate (BBS) glass matrix<sup>229</sup>. Detailed structural studies were carried out to confirm the solubility of yellow phase in BBS<sup>230</sup>. In addition, it was also observed that thorium incorporation in BBS is much better as compared to NBS glass<sup>230</sup>. Subsequent research and developments concluded the superiority of BBS glass matrix, is currently practiced waste matrix for HLW of Indian nuclear program.

Further the transformation of nuclear power plants from uranium oxide ( $\text{UO}_2$ ) fuel to mixed oxide fuel comprising of  $\text{UO}_2\text{-PuO}_2$  as part of the start of second generation of nuclear power alerts for additional research innovations to accommodate wastes of different chemical

composition and activities. The criticality problems of plutonium in aqueous medium served as a newer challenge for the reprocessing and immobilization of these newer HLW. In view of the criticality problem, gadolinium nitrate needs to be externally added to the spent fuel during waste reprocessing. Thus, the addition of extra gadolinium nitrate results more amount of Gd in waste, which increased to almost 15 wt% in wastes of Pu bearing nuclear HLW. Thus, incorporation of excess Gd in immobilization matrices is presently one of the major challenges of the Indian nuclear waste research. A close look at international scenario points to the fact their working system consists of  $\text{Na}_2\text{O}-\text{Al}_2\text{O}_3-\text{B}_2\text{O}_3-\text{SiO}_2$  system as compared to the Indian nuclear glasses system of  $\text{Na}_2\text{O}-\text{BaO}-\text{B}_2\text{O}_3-\text{SiO}_2-\text{TiO}_2-\text{MnO}_2$ <sup>28,229,230</sup>.

Literature reports suggest very low solubility of gadolinium or rare earths in borosilicate glass matrix (around 1.6 mol%)<sup>231</sup> due to the clustering in Gd rich domains. Such clustering phenomena has been evidenced by calorimetric techniques. Studies by Li et al also stressed on the relation of  $\text{Gd}_2\text{O}_3$  solubility to the concentration of  $[\text{AlO}_{1.5}]-[\text{NaO}_{0.5}]-0.2[\text{BO}_{1.5}]$  in glass system<sup>232</sup>. However, it was a concern that the authors prepared glass formulations at 1450°C which is very high temperature for plant scale glass production. Accelerated corrosion of inconel electrodes and reaction vessel used for glass making in induction melting method starts during prolonged heating above 1000°C<sup>225–228</sup>. The Joule heated ceramic melter method also uses inconel electrodes which also limits the usability up to around 1200°C, and above which rapid corrosion of electrodes takes place. Hence, a glass formulation that can be made at lower temperature preferably below 1000°C is a current research challenge.

## 7.2. SYNTHESIS STRATEGY

One of the best features of glasses of  $\text{Na}_2\text{O}-\text{BaO}-\text{B}_2\text{O}_3-\text{SiO}_2-\text{TiO}_2-\text{MnO}_2$  system is that these glasses can be prepared around 1000°C. However, the problem persisted with the low solubility of rare earth elements in BBS. Working on the concepts of Zacharisen rules, ionic

radius, effect of network formers, network modifiers, relative ratio of network formers to network modifiers, suitable formulations by reducing the concentration of network modifiers were tried to synthesize tailor-made glasses required for Indian waste immobilization scenario.

Ionic radius of  $Gd^{3+}$  is quite large compared to the other cations present in glass forming system. In addition to this,  $Gd^{3+}$  ions mostly prefer eight-fold coordination number. Hence, it becomes difficult to fit  $Gd^{3+}$  ion within the glass framework. Larger sized ions can mostly be forced within the glass matrix without extended network formation. Thus, Gd mostly acts as a network modifier during glass preparation. High concentration of  $TiO_2$  and  $MnO_2$  along with 2.5 mol% of Gd raised the melting temperature above  $1100^\circ C$  in trial glass. Keeping this fact in mind, concentrations of  $TiO_2$  and  $MnO_2$  were reduced gradually from 6 and 10 mol%, respectively to zero<sup>218</sup> [1]. Based on several trials, the base glass was chosen by avoiding these two components while using the incorporated Gd as network modifiers.

Next important step was to choose the relative proportion of  $Na_2O$ ,  $BaO$ ,  $B_2O_3$  and  $SiO_2$ . Several trials were carried out by varying the ratio of  $SiO_2$  from 60 mol% to 30 mol%, and  $B_2O_3$  from 10 mol% to 40 mol%. Higher silica loading was found to increase the melting point of 2.5 mol%  $Gd_2O_3$  loaded glass above  $1050^\circ C$ . On the other hand, higher  $B_2O_3$  loading in base glass reduced melting temperature but reproducibility of the process was becoming an issue due to uncontrolled volatilization of boric acid ( $H_3BO_3$ ). Hence the optimum formulation of 50 mol%  $SiO_2$ , 20 mol%  $B_2O_3$ , 20 mol%  $Na_2O$  and 10 mol%  $BaO$  was chosen as the preferred formulation for  $Gd_2O_3$  incorporation for batch studies.

### 7.3. EXPERIMENTAL METHODS

50 g of glass samples of different bulk compositions were prepared in Pt-Au crucibles followed by melt-quenching technique. Stoichiometric amounts of  $NaNO_3$ ,  $Ba(NO_3)_2$ ,  $SiO_2$ ,  $H_3BO_3$  and  $Gd_2O_3$  were homogenized in agate mortar and pestle. The formulations of the



glasses prepared are given in **Table 7.1(a & b)**. The mixture was then calcined at 700°C for 2 h, melted at around 1000-1050°C for 4 h followed by pouring on steel plates from 950°C.

**Table 7.1a: Compositions in mol% of synthesized borosilicate glass.**

Code	SiO <sub>2</sub>	B <sub>2</sub> O <sub>3</sub>	Na <sub>2</sub> O	BaO	Gd <sub>2</sub> O <sub>3</sub>
Gd-0.0	50	20.0	20.0	10.0	0.0
Gd-2.5	48.75	19.5	19.5	9.75	2.5
Gd-5.0	47.5	19.0	19.0	9.5	5.0
Gd-6.0	47.0	18.8	18.8	9.4	6.0
Gd-7.5	46.25	18.5	18.5	9.25	7.5
Gd-10.0	45.0	18.0	18.0	9.0	10.0

**Table 7.1b: Compositions in wt% of synthesized borosilicate glass.**

Code	SiO <sub>2</sub>	B <sub>2</sub> O <sub>3</sub>	Na <sub>2</sub> O	BaO	Gd <sub>2</sub> O <sub>3</sub>
<b>Gd-0.0</b>	41.90	19.42	17.29	21.38	0.0
<b>Gd-2.5</b>	37.10	17.19	15.30	18.93	11.48
<b>Gd-5.0</b>	33.10	15.34	13.66	16.89	21.02
<b>Gd-6.0</b>	31.73	14.71	13.09	16.02	24.44
<b>Gd-7.5</b>	29.72	13.77	12.27	15.16	29.08
<b>Gd-10.0</b>	26.83	12.44	11.07	13.69	35.97

Amounts of the reactants taken for preparation of glass formulations were calculated based upon oxides for maintaining their chemical compositions. However, exact weights that were taken for preparation of formulations were calculated from their equivalent amounts of nitrates

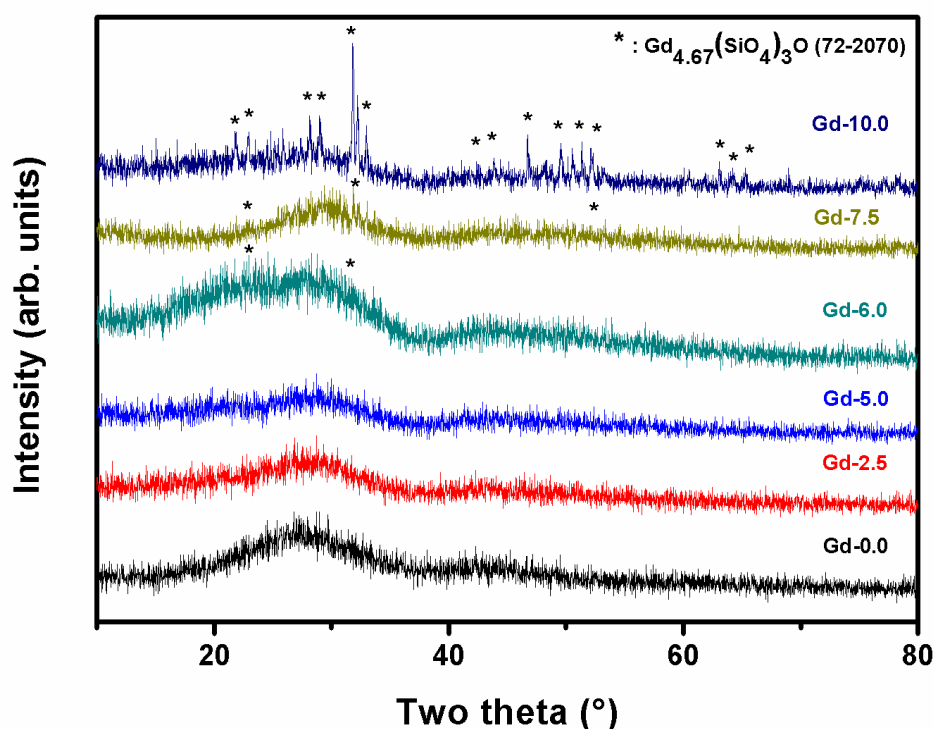
or carbonates. The weight composition information assumed significance as the requirement of solubility of  $\text{Gd}_2\text{O}_3$  in BBS matrix was required in wt% for our purpose.

All the prepared glasses were crushed using mortar and pestle to form finely ground powder. The powder obtained was passed through mesh-200 and structural characterization (apart from SEM and PL) was carried out with the powder which passed through the mesh. For SEM and PL measurements, small glass pieces were used. The presence of crystalline impurity phases was identified by powder X-ray diffraction studies on powdered glass samples. All the powder XRD patterns were recorded on PANalytical X-Pert Pro powder x-ray diffractometer using  $\text{CuK}\alpha$  ( $\lambda = 1.5406$  and  $1.5444 \text{ \AA}$ ) radiation. The powder XRD data was recorded in the  $2\theta$  range of  $10\text{--}70^\circ$  with step width of  $0.02^\circ$  and step time of 1.2s. Differential thermal analysis (DTA) studies were carried out using Setaram Setsys Evolution instrument within the range of  $400\text{--}700^\circ\text{C}$  at a scanning rate of  $10^\circ\text{C}/\text{min}$ . Photoluminescence measurements were carried out using Edinburgh Instruments FLSP 920 system attached with a 450 W Xe lamp as the excitation source. Excitation and emission slits were kept at a width of 3 nm and integration time was 0.2 s. Lifetime measurements were carried out for emission of Gd containing samples ( $\sim 310\text{--}315 \text{ nm}$ ) upon excitation by UV radiation of wavelength 275 nm. Back-scattered electron imaging studies were carried out by using scanning electron microscopy (SEM; model AIS 210, Mirero Inc., Seongnam-si, South Korea).

#### 7.4. RESULTS AND DISCUSSIONS

Initially, powder X-ray diffraction studies were carried out on the glass formulations namely Gd-0.0, Gd-2.5, Gd-5.0, Gd-7.5 and Gd-10.0. Powder pattern of base glass revealed a broad hump in the  $2\theta$  range of  $20\text{--}35^\circ$  followed by another hump in the range of  $40\text{--}55^\circ$  which is a classic signature of an amorphous or glassy material. Similar signatures were also for formulations Gd-2.5 and Gd-5.0 [Figure 7.1]. However, Gd-6.0 and Gd-7.5 showed appearance of several low intensity peaks corresponding to the formation of some ceramic

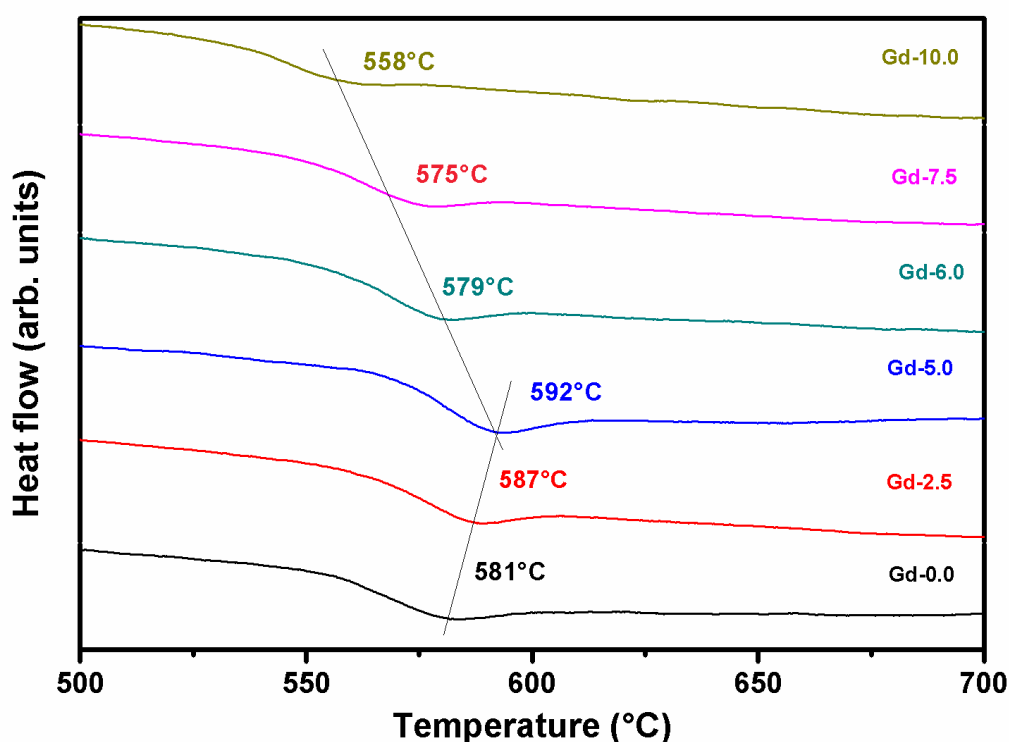
phase within the glass matrix. Higher gadolinium oxide loaded formulation Gd-10.0 exhibited several well-defined crystalline peaks which can be attributed to the ceramic phase  $\text{Gd}_{4.67}(\text{SiO}_4)_3\text{O}$  (PCPDF card no: 72-2070). Thus, it can be stated that gadolinium has high affinity for silica compared to the other constituents and that results in breaking of the amorphous glassy network followed by seeding and growth of a crystalline state within the melt. Furthermore, it can also be concluded from powder XRD patterns that the solubility of gadolinium in the synthesized glass formulations are 5 mol% or ~21 wt% which is a very satisfactory value as per the requirement.



**Figure 7.1.** Powder XRD patterns of the prepared glass formulations. “\*” marks the peaks corresponding to the crystalline phase  $\text{Gd}_{4.67}(\text{SiO}_4)_3\text{O}$ .

It became very much necessary to find out the structural implications on the glass network with incorporation of Gd. The strong magnetic nature of  $\text{Gd}^{3+}$  ion (seven unpaired electrons) restricts the characterization of glasses by  $^{29}\text{Si}$  MAS-NMR. Thus, the characterization of glasses was limited to differential thermal analyses studies. The DTA

studies on the glass formulations were carried out within the range of 400-700°C at a scanning rate of 10°C/min. DTA curves of materials exhibit an endothermic broad peak corresponding to glass transition temperature and an exothermic peak corresponding to the melting temperature. Glass transition is a very important phenomenon in glass sciences and is a strong characteristic of undergoing structural relaxations in any glassy material. It is also dependent on the nature of the constituent structural units present within the glass network<sup>229</sup>.

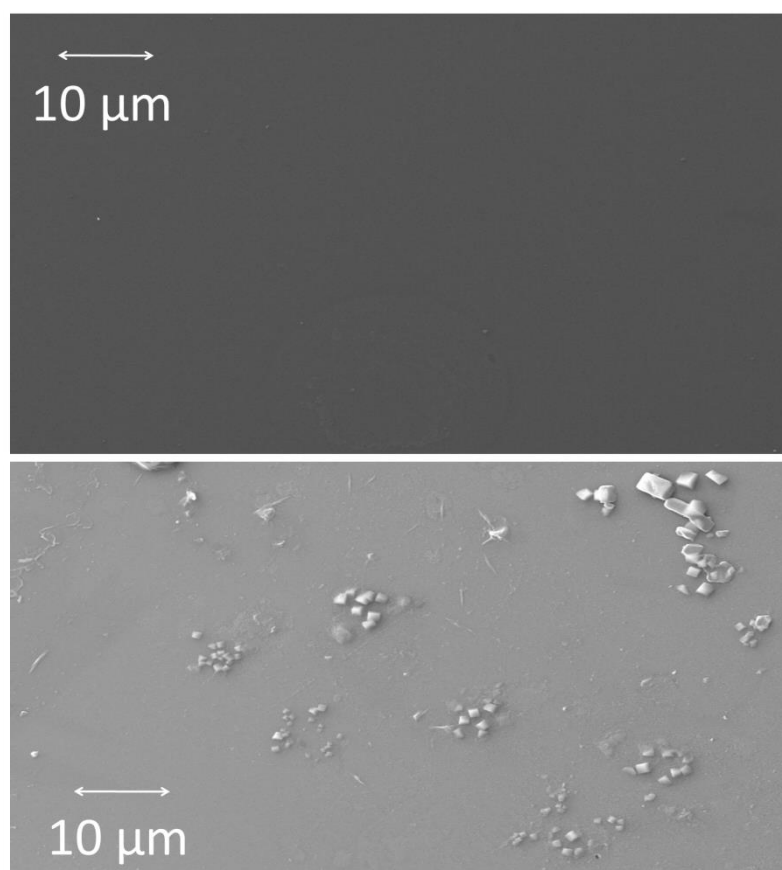


**Figure 7.2.** DTA curves of the prepared glass formulations.

It was observed from DTA curves that glass transition temperature of base glass is around 581°C. Gradual addition of gadolinium oxide into base glass matrix increased the glass transition temperature to 592°C (Gd-5.0) [Figure 7.2]. However, higher concentration of gadolinium oxide loading in glass gradually reduces the glass transition temperature to around 557°C (Gd-10.0). Hence, it can be concluded that upto Gd-5.0 gadolinium is stabilizing the glass structure by making it more rigid. On the other hand, higher loading of gadolinium has the tendency to break the glassy network which can be attributed to the separation of crystalline

$\text{Gd}_{4.67}(\text{SiO}_4)_3\text{O}$  phase as evident from powder XRD studies. Comparing these two complementary techniques, it could be inferred that effect of gadolinium in glass network is concentration dependent. At low concentration gadolinium is extending the glass network structure playing the role of a network former whereas after some critical concentration it is showing high affinity for reaction with silica and taking the role of a network modifier. This reaction initiate the seeding of crystalline phases and subsequently crystalline ceramic phases are segregated within the glass matrix.

Backscattered electron imaging studies were performed on the glass formulations to garner further light on the solubility of gadolinium inside the glass matrix. Small glass samples



**Figure 7.3. BSE images of glass formulation Gd-5.0 (top) and Gd-6.0 (bottom). Segregated phases are clearly observed in Gd-6.0.**

were mounted in bakelite discs and were ground with emery paper of different grades. Finally, the glasses were polished with 1  $\mu\text{m}$  sized diamond paste followed by cleaning in an ultrasonic bath. Thin gold coating was applied were applied BSE images of some of the selected formulations were recorded by using the polished glass sample coated with a thin film of gold [Figure 7.3].

BSE image of Gd-5.0 showed the matrix as single phasic without the presence of any segregated phase or impurities. However, Gd-6.0 showed the presence of segregated bright phase in a matrix of comparatively dark phase. Backscattering probability of any element increases with increase in its number of constituent electrons, i.e., with increase in atomic number (Z). Hence, phases having higher Z value appear brighter in BSE imaging mode. Hence, it can be concluded that the segregated phase consists of elements with higher Z and they can be attributable to the crystalline  $\text{Gd}_{4.67}(\text{SiO}_4)_3\text{O}$  phase.

In order to gain further information about the influence of gadolinium oxide on the glass structure, photoluminescence measurements were carried out on the glass formulations. A spectral scan showed the absorbance of gadolinium at around 275 nm corresponding to which an emission was observed at 311 nm. The decay in luminescence lifetime was measured in order to gain insight about the gadolinium environment. The lifetime data was fitted with exponential decay fit curve (single and multiple mode) to find out the probable mode of decay of luminescence. It can be suggested that single exponential decay mode in amorphous system (up to Gd5.0) corresponds to single chemical environment and multiple modes of decay (for Gd6.0 and beyond) are attributable to more than one chemical environments around gadolinium.

**Table 7.2: Table showing the lifetime with the mode of decay in the prepared glass formulations.**

Sample code	Lifetime	Yield	$\chi^2$
Gd-0.0	-----	-----	-----
Gd-2.5	2.700 ms	100	1.16
Gd-5.0	2.082 ms	100	0.96
Gd-6.0	1.2 ms 178 $\mu$ s	99 1	0.76
Gd-7.5	951 $\mu$ s 12 $\mu$ s	97 3	0.68
Gd-10.0	944 $\mu$ s 6 $\mu$ s	93 7	0.92

Luminescence lifetime was found to be steadily decreasing with increasing gadolinium content which can be attributed to the increasing extent of quenching among gadolinium ions. However, it was also observed that up to Gd-5.0; single exponential decay mode was observed which implies similar chemical environment whereas two modes of decay were observed from Gd-6.0 onwards. This study also confirmed that the solubility limit of gadolinium in barium borosilicate glass is ~21 wt%.

## 7.5. CONCLUSIONS

A conclusive design of borosilicate glass matrix was carried out for immobilization of added gadolinium ions in the context of immobilization of nuclear HLW from second generation of Indian nuclear power programme. Considering the waste management scenario, efficiency of gadolinium incorporation was increased almost three-fold (from 1.5 mol% to 5.0

mol%) at a much lower processing temperature of 950°C as a result of which corrosion problems of the reactants with structural material of melter i.e., Inconel can be reduced.



**Chapter 8**

**Summary**

**and**

**future scope**

## 8.1. SUMMARY

The aim of the thesis “Preparation and structural investigations on zirconolite and pyrochlore based ceramics: Potential materials for nuclear back end application” is the development of preparation methodology for zirconolite and pyrochlore based ceramics and to understand their potential for immobilization of actinides present in nuclear high level waste. Both zirconolite and pyrochlore phases are being important constituents of SYNROC, the research work in this thesis has been focused on these two phases.

, From the point of view of nuclear waste immobilization, zirconolite ( $\text{CaZrTi}_2\text{O}_7$ ) is a very important mineral analogous phase of the  $\text{CaO-ZrO}_2\text{-TiO}_2$  system. However, another mineral analogous phase with a fluorite related structural arrangement, termed as calzirtite ( $\text{Ca}_2\text{Zr}_5\text{Ti}_2\text{O}_{16}$ ) is also reported in  $\text{CaO-ZrO}_2\text{-TiO}_2$  system. Calzirtite phases are found to coexist with zirconolite in metasomatic calcite-forsterite-magnetite rocks and their nominal composition exhibits a variation in the Zr and Ti content in the lattice. Hence a detailed structural characterization and thermodynamic property evaluation of these two lattices are carried out. Structural studies carried out by combination of room temperature and high temperature X-ray diffraction studies, and revealed that only a feeble amount of Ti and Zr atoms can get exchanged within calzirtite lattice whereas the zirconolite lattice is more amenable for compositional variation. Moreover, low thermal expansion coefficient of calzirtite lattice as compared to zirconolite was observed which also justified to the closed packed nature of calzirtite lattice. These factors clearly indicated that zirconolite can act as a better nuclear waste immobilization matrix as compared to calzirtite. The open structure of zirconolite can easily accommodate cations of various charge and size. Thermodynamic studies carried out on these two lattices revealed that at  $\sim 1775$  K, calzirtite lattice can decompose to yield zirconolite, calcium zirconate and zirconium dioxide respectively.

As the above-mentioned findings ruled out the possibility of calzirtite phase to use as potential nuclear waste immobilization matrix, a detailed structural and micro-structural investigations on zirconolite-pyrochlore ( $\text{CaZrTi}_2\text{O}_7\text{-RE}_2\text{Ti}_2\text{O}_7$ , where RE= rare earth elements) based multiphasic systems were carried out to understand the mutual phase compatibility. Detailed investigations with rare earth based systems being quite tedious, due to their low availability, selected trivalent ions of different ionic radii were only used to carry out the phase evolution study. Extensive structural and microstructural studies carried out in the  $\text{CaZrTi}_2\text{O}_7$  (zirconolite)- $\text{RE}_2\text{Ti}_2\text{O}_7$  (pyrochlore) (RE=  $\text{Nd}^{3+}$ ,  $\text{Sm}^{3+}$  and  $\text{Y}^{3+}$ ) revealed the system to consists of four broad phase fields namely, (i) monoclinic zirconolite (comprising of 2M and 4M), (ii) cubic perovskite (not for  $\text{Y}^{3+}$  series), (iii) cubic pyrochlore, and (iv) monoclinic  $\text{Nd}_2\text{Ti}_2\text{O}_7$  types (for  $\text{Nd}^{3+}$  series). It could be concluded that the phase boundary of cubic perovskite increases with increasing ionic radii of  $\text{RE}^{3+}$  ion. On the contrary, it was observed that solubility of trivalent rare-earth ions in zirconolite (both 2M and 4M) lattice increases with decreasing ionic radii of  $\text{RE}^{3+}$  ion. In all the three studied systems, existence of a single phasic cubic pyrochlore phase was observed. This pyrochlore phase has the ability to incorporate a large amount of heterovalent cations without any major alteration in the crystal structure which is considered as very promising results pertaining to their usage as waste immobilization matrices.

In view of the above results, experimental and theoretical studies were carried out on  $\text{Gd}_{2-2x}\text{Ca}_x\text{Zr}_x\text{Ti}_2\text{O}_7$  ( $0.0 \leq x \leq 0.4$ ) pyrochlore system. to understand the structural perturbations induced by incorporation of one divalent ion ( $\text{Ca}^{2+}$ ) and one tetravalent cation ( $\text{Zr}^{4+}$ ) in place of two trivalent cations ( $\text{Gd}^{3+}$ ) of the titanate pyrochlore lattice. It was clearly observed that these type of titanate based pyrochlore phases are able to accommodate about 40 mol% of diverse cations without major alteration in their crystal structure. Theoretical studies carried out revealed that a small amount of disorder arises around the Gd site due to

incorporation of Ca and Zr which results in decreasing intensity of super-structure peaks with increasing incorporation of diverse cations. However, these incorporated ions are not able to destroy the cubic pyrochlore framework. Thermodynamic stability studies carried out indicates lowering of relative stability of the lattice by only about 3.5% even after incorporation of 40 mol % of heteroatom. These studies indicated that titanate pyrochlore lattices can be potential lattices in terms of their usage as waste immobilization matrices.

On the other hand,  $\text{Gd}_2\text{Zr}_2\text{O}_7$  is considered the most promising zirconate based pyrochlores for immobilization of minor actinides present in nuclear high level waste. However, the optimum processing conditions and incorporation of actinides were not substantially present in literature.  $\text{Gd}_2\text{Zr}_2\text{O}_7$  synthesized by gel-combustion technique was annealed for 8 h at 1373 K, 1473 K, 1573 K and 1673 K respectively. Powder X-ray diffraction studies revealed that transformation from defect fluorite to ordered pyrochlore structure takes place in this temperature range under the studied conditions. Phase pure defect fluorite and ordered pyrochlore structures were found to be stabilized at 1373 K and 1673 K, respectively, whereas mixed products were observed at intermediate temperatures. Thermodynamic stability studies carried out on all the compositions revealed that stability decrease from 1373 K to 1573 K before increasing again at 1673 K. It clearly indicated that  $\text{Gd}_2\text{Zr}_2\text{O}_7$  matrix needs processing at either 1373 K or 1673 K for better phase characteristics. This study helped us in optimization of process conditions for preparation of uranium loaded  $\text{Gd}_2\text{Zr}_2\text{O}_7$ , i.e.  $\text{Gd}_{2-x}\text{U}_x\text{Zr}_2\text{O}_{7+\delta}$  ( $0.0 \leq x \leq 0.25$ ). Multiple oxidation states of uranium posed a question regarding their immobilization in reduced or oxidized form in  $\text{Gd}_2\text{Zr}_2\text{O}_7$  matrix. As a result, uranium incorporation studies were carried out both in air and argon-hydrogen atmosphere at 1373K for 8 h (optimized condition from earlier study). Substantial amount of uranium ( $x=0.25$ ) could be incorporated in  $\text{Gd}_2\text{Zr}_2\text{O}_7$  lattice in reducing environment as compared to air heated samples ( $x=0.15$ ). However, higher loading samples in reducing atmosphere reverted to minor phase

precipitation during heating in ambient conditions. Thermodynamic stability studies carried out on both reducing and air heated samples revealed that immobilization of uranium in reduced state does not alter the stability of uranium incorporated  $\text{Gd}_2\text{Zr}_2\text{O}_7$  whereas the stability for samples heated in air increased significantly in the studied range of composition. These studies revealed that it is always better to immobilize uranium in +6 state in  $\text{Gd}_2\text{Zr}_2\text{O}_7$  lattice. This study was extended further towards the co-incorporation of uranium and cerium in  $\text{Gd}_2\text{Zr}_2\text{O}_7$  matrix. Keeping this in mind, a series with nominal compositions  $\text{Gd}_{2-x}\text{Ce}_x\text{Zr}_{1.9}\text{U}_{0.1}\text{O}_{7+\delta}$  ( $0.0 \leq x \leq 0.5$ ) was prepared. Similar to the earlier studies, these compounds were also found to be stabilized in defect fluorite structure. Thermodynamic stability studies clearly indicated that incorporation of U and Ce under ambient conditions i.e. as  $\text{U}^{6+}$  and  $\text{Ce}^{4+}$  increases the stability of ceramic matrices.

Apart from these studies on ceramic matrices intended for immobilization of nuclear HLW and minor actinides, studies on the solubility of gadolinium in barium borosilicate glass matrix were also carried out. The solubility of gadolinium was found to be about 5 mol% contrary to that reported in literature (1.5 mol %). A rational and systematic study involving variation in composition of base glass constituents and processing conditions could increase the solubility limit. Moreover, the formulation was found to immobilize gadolinium at much lower processing temperature of  $950^\circ\text{C}$  which results in immobilization under economic conditions.

## 8.2. FUTURE SCOPE

In spite of the systematic and directed approach of the thesis regarding structural and thermodynamic aspects of ceramic matrices intended for immobilization of minor actinides, certain studies are also required in future to affirm use of these systems for immobilization of nuclear HLW viz.

Incorporation of uranium and minor actinide surrogates in multiphasic matrices and understand further structural deviation of the phases from constituent phases of SYNROC as observed in this thesis.

Processing of ceramic matrices is generally done under high pressure for densification of waste ensemble. Hence, moderately high pressure (~10 MPa) studies of these incorporated matrices are required for validation.

Alpha and alpha recoils from nuclear HLW can damage crystal structure of ceramic compounds. Hence, ion irradiation studies with low energy ion beams are needed to be carried out in future.

In addition to this, leachability of uranium and other actinides from ceramic matrices are needed to be carried out under accelerated condition to study the long term effects. This study also needs to be carried out for the glass system which is presented in this thesis before its validation as waste immobilization matrix.



## Homi Bhabha National Institute

CHECK LIST FOR 11 CRITERIA AS PER UGC (MINIMUM  
STANDARD AND PROCEDURE FOR AWARD OF Ph.D. DEGREE)  
REGULATION 2009<sup>1</sup>

1. Name of the Student: Shri Mohsin Jafar
2. Name of the Constituent Institution: Bhabha Atomic Research Centre, Mumbai
3. Enrolment Number: CHEM01201404019
4. Board of Studies: Chemical Sciences

Sr. No.	Particular	Remark (Tick the appropriate one)
1.	Mode of selection for Ph.D. Programme	Interview
2.	Number of Ph.D. students under the guide $\leq 8$ during the period	Yes
3.	Reservation Policy applied for selection	Yes
4.	Course work done	Yes
5.	Reviews of Annual Progress held	Yes
6.	Test on Research Methodology held	Yes
7.	Pre-synopsis presentation held	Yes
8.	At least 1 journal paper published	Yes
9.	At least 2 papers in conference/ seminar presented	Yes
10.	Evaluation reports of Ph.D. Thesis from guide and two experts (one expert is out of state) received	Yes
11.	Soft copy of Thesis submitted to HBNI	Yes

*S. N. Achary*  
Dr. S. N. Achary  
(Guide)

To  
Dean, HBNI

Dean – Academic

Ph.D. student has to fulfill all the 11 criteria laid by UGC to meet eligibility criteria for employment in Indian Universities. HBNI will issue required certificate only if a student meets all the eleven criteria.

## Thesis Highlight

**Name of the Student:** Mr. Mohsin Jafar

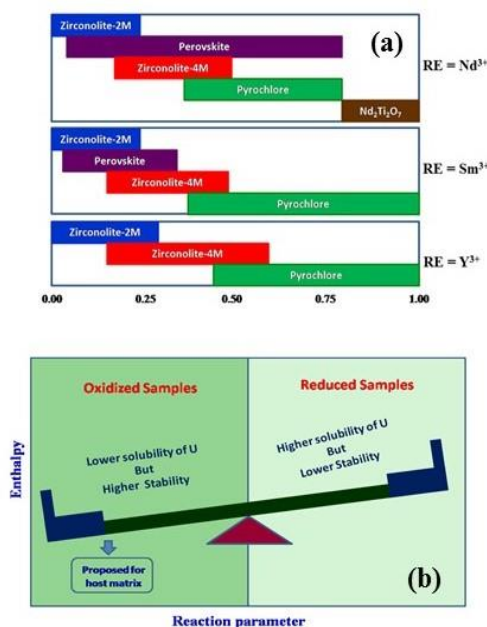
**Name of the CI/OCC:** Bhabha Atomic Research Centre **Enrolment No.:** CHEM01201404019

**Thesis Title:** Preparation and structural investigations on zirconolite and pyrochlore based ceramics: Potential materials for nuclear back end application

**Discipline:** Chemical Sciences

**Date of viva voce:** 24/04/2021

Management of nuclear High Level Waste (HLW) is a major challenge in nuclear energy sector. This is being addressed by research on wide varieties of materials in ceramic, glass and glass ceramics. In the thesis, systematic investigations on the ceramic matrices based on zirconolite and pyrochlore structure, prominent members of SYNROC formulations have been carried out. Comprehensive structural and micro-structural investigations on zirconolite-pyrochlore ( $\text{CaZrTi}_2\text{O}_7$ - $\text{RE}_2\text{Ti}_2\text{O}_7$ , where  $\text{RE} = \text{Nd}^{3+}$ ,  $\text{Sm}^{3+}$  and  $\text{Y}^{3+}$ ) based multiphasic systems were carried out. The major phase fields observed are part of the component of synroc formulation (**Figure a**). Structural characterization and stability studies on  $\text{Gd}_{2-2x}\text{Ca}_x\text{Zr}_x\text{Ti}_2\text{O}_7$  ( $0.0 \leq x \leq 0.4$ ) based pyrochlore system revealed that accommodation of about 40 mol% of aliovalent cations without major alteration in their structure. Thermodynamic stability studies on them revealed only a small (3.5%) decrease in relative stability even after incorporation of 40 mol % of heteroatom. A quick processing conditions has been developed and supported by structural characterization and thermodynamic measurements. Structural and thermodynamic investigations on urania and urania-ceria (surrogate for plutonia) incorporated  $\text{Gd}_2\text{Zr}_2\text{O}_7$  system indicated that the stabilities are higher with  $\text{U}^{6+}$  and  $\text{Ce}^{4+}$  compared to their reduced forms, like  $\text{U}^{4+}$  and  $\text{Ce}^{3+}$  (**Figure b**). In addition to this, development of novel formulation of borosilicate glass matrix was carried out where it was found that solubility of gadolinia increased almost 2.5 times i.e. from 8 wt% to ~20 wt%.



a) Figure showing representative phase fields, and b) Figure showing stability of uranium incorporated matrix